Multiscale modelling of geopolymers : from liquid to solid state

Anthony Saliou

THÈSE POUR OBTENIR LE GRADE DE DOCTEUR DE L'UNIVERSITÉ DE MONTPELLIER

En Mécanique et Génie Civil

École doctorale : Information, Structures, Systèmes

Unité de recherche : Laboratoire de Mécanique et Génie Civil (LMGC)

Modélisation Multi-Echelle de Géopolymères : Du Liquide au Solide.

Multiscale modeling of Geopolymers : From Liquid to Solide State.

Présentée par Anthony SALIOU
Le 01 Juillet 2024

Sous la direction de Katerina IOANNIDOU et Roland PELLENQ

Devant le jury composé de

Jean-François DUFRECHE, Professeur, Université de Montpellier	Président du jury
Virginie MARRY, Professeure, Sorbonne Université	Rapportrice
Jerome DELHOMMELLE, Professeur Associé, UMass Lowell	Rapporteur
Agathe ROBISSON, Professeure, Vienna University of Technology	Examinatrice
Daniel FERRY, Chargé de Recherche, CNRS, CINaM	Examinateur
Jean-Marc DELAYE, Directeur de Recherche, CEA Marcoule	Examinateur
Romain DUPUIS, Chargé de Recherche, CNRS, LMGC	Encadrant
Arnaud POULESQUEN, Directeur de Recherche, CEA Marcoule	Encadrant
Katerina IOANNIDOU, Chargée de Recherche, CNRS, LMGC	Directrice de thèse
Roland PELLENQ, Directeur de Recherche, CNRS, IEM	Directeur de thèse

UNIVERSITÉ DE MONTPELLIER

CEA Marcoule - LMGC Montpellier

Multiscale modeling of geopolymers: from liquid to solid state

Anthony Saliou

Manuscript for the degree of Doctor of Philosophy of Sciences

University of Montpellier
Montpellier, France

October 2020 – July 2024

Summary

Geopolymers are alternative binders to cement and form a promising class of materials for civil and nuclear engineering. Based on aluminosilicate, they can develop strong mechanical properties that are of great interest for the storage of radioactive wastes or isolating foams. The geo-polymerization process starts with the dissolution of a solid aluminosilicate source with an alkaline solution of high pH. Oligomers of few nanometers in size form and aggregate in a 3D percolating porous network at the mesoscale (hundreds of nm). Mechanical setting is reached in about 5h, analogous of setting in neat cement pastes. Several questions remain open regarding the complex process of geopolymerization such as : What originates cohesion ? What is the water behavior at the grain-grain interface within the gel ? How to model the complex gel phase at the atomistic level ? In this thesis, molecular simulations are used to investigate the formation mechanism of geopolymers at the atomistic ($\sim$ 1nm) and meso scale ($\sim$ 100nm), hardly reachable by experiment. The starting point of the atomistic scale simulations are aluminosilicate nano-grains generated with a reactive interaction potential. The Potential of Mean Force (PMF) quantifies the potential energy of interactions between two geopolymer oligomers. It can be computed in various charge conditions to mimic the pH effects, using either a perturbative approach or well-tempered metadynamics. Both methods are compared and their limitations are discussed in the framework of amorphous aluminosilicate nano-grains immersed in an electrolyte. Under such analysis, metadynamics is chosen for more thorough investigation of oligomers cohesion. At low deprotonation level/grain charge attraction is observed. These results shed light on the role of oligomers deprotonation that appears to be key point for the gel formation. A view of the system as "meta-grains" is proposed based on the evolution of grain geometry and ionic polarization. In this view, we decompose the global PMF into fundamental interaction terms at the grain scale, in terms of coulombic, dipole-dipole and dispersion/van der Walls interactions. Metadynamics results are recovered with water dielectric constant chosen based on the water content at the grain-grain interface. At large deprotonation level, the Poisson-Boltzmann repulsion is recovered, with a wet interface and a strong Debye screening. At very short range and low deprotonation level, we found that grain-grain attraction can be related to the formation of very local hydrogen bonds between the hydroxyls of the grains, in a dry interface. Oligomers then link through iono-covalent bonds with the release to the solution of water molecules and OH^- groups. This attracto/repulsive behavior is supported by experiments and discussed in regards to the cohesion of clays and cement hydrates. In the last part of the thesis, mesoscale models for the growth of geopolymers are proposed based on the obtained PMFs in attractive conditions. Structures resulting from Coarse-Grained Monte Carlo simulations are characterized in terms of pore size distributions and small angle neutron scattering, discussed with experimental data.

Remerciements

La thèse est souvent décrite comme un long chemin, solitaire. Il s'agirait plutôt de la voir comme une bonne randonnée : parfois les horizons nous paraissent inaccessibles et les lignes droites interminables. Pour autant, bien accompagné, ces paysages défilent et les sommets se transforment en collines.

Cette thèse a commencé dès mes années de classes préparatoires, auprès d'Adèle, Marie, Rémy et Tanguy qui m'ont toujours impressionné de leurs facultés de travail et de reflexion. Sans le savoir, vous m'avez permis de prendre le wagon qui est arrivé aujourd'hui à destination.

Les rencontres professionnelles avec Maxence, Julien mais surtout Noël auront été d'une grande richesse. Noël, tes mots ont toujours été justes et ont beaucoup raisonné en moi au cours de ces années. Car il faut des points d'ancrages pour ne pas perdre la tête durant une thèse. Duy et Yohann, vous avez su supporter mes râles et être d'un soutien énorme au cours de pauses cafés à peine trop longues. Rémy, à cette fois où je t'ai demandé comment automatiser le lancement de 6400 jobs en série... Tu m'aurais appris les joies du bash mais aussi que rien ne vaut un bon code en Python. Roman, tu étais loin, mais bon sang qu'est ce qu'est ce qu'on aurait dû être dans le même bureau ! Bon, peut-être que Genève c'était pas l'endroit le plus proche, mais finalement ces 200km de vélo auront été un déclic plus que sportif : le seul mur c'est celui que vous vous imaginez.

Les heures de travail, c'est un peu comme les kilomètres finalement, on ne les compte pas si on veut arriver à destination. Et des kilomètres, qu'est ce qu'on a pu en faire ensemble : Rémi D., Étienne, Gildas, Yohann, Camille, Yaël, Joris, Clémentine, Caroline, Timothée et Honorine. 18h08, "ça part au footing", en voilà de douces paroles d'Hugo qui nous annoncent le meilleur moment de la journée ! Souffrir à l'entraînement, c'est aussi travailler sa force mentale après tout... La force mentale, Reem et Arthur vous en faites preuve d'une grande et votre soutien au cours de ces années est indéniable.

Partir à l'aventure, c'est aussi parfois s'éloigner de ses proches. A milles kilomètres de la maison, ma famille n'a pourtant jamais été aussi proche. Mamie Mithé, Papi Serge, Tata Céline, Tonton Miguel, Enzo et Axel, l'aboutissement de ce travail je vous le dois en partie. De part vos visites et votre accueil lors de mes retours en terres bretonnes, j'ai pu garder la détermination qui m'a fait me lancer. Claudine, Michel et Marie, une armada Aïdo avec un soutien sans faille ! S'évader, décompresser, j'ai appris à prendre beaucoup de recul sur les choses avec vous. Dans les hauts comme dans les bas, Jade, maman, papa, vous avez toujours été présents pour moi et je n'en serai pas là aujourd'hui sans vous. Vous le savez, je vous aime. Ce travail n'est autre que mon intime souhait de vous rendre fiers.

Enfin, que serait un Sherlock sans Watson, un Peter Parker sans Marie Jane ou encore un Sacha sans Pikachu ? Tu m'auras suivi dans ces montagnes russes (littéralement d'ailleurs) sans lâcher. A aucun moment tu n'as douté de moi. Des bancs du lycée breton à ceux de cet amphithéâtre montpelliérain, le chemin fût long (et beau !) mais tu m'as toujours fait confiance. Grâce à toi, je ne me suis jamais senti seul. Mon ange gardien, mon amour, ma moitié, tu as été, es et seras toujours ma première source de motivation. Je t'aime.

Plutôt que d'écrire mille mercis, j'ai choisi d'en écrire un seul et unique, car il s'agit là de cinq lettres d'une profonde sincérité. Car si cette thèse est complexe, il n'y a rien de plus simple que la gratitude que j'aimerais vous exprimer pour avoir été mes compagnons de route durant ces années, et pour des années venant. Car chaque pièce du puzzle compte et ce tableau n'aurait pu être complété sans vous.

Merci,

Anthony

Contents

Introduction

Through the ages, the development of most civilizations was allowed by the evolution of its surrounding environment. Civil engineering has always been a part of humanity's progress : homes, rooms for industrialization (agriculture, factories), scientific labs and offices, buildings are everywhere and requires resources that may not be infinite.

Up to date, the most widely used materials in civil engineering is the Ordinary Portland Cement (OPC). It constitutes an accessible (from both cost and quantity point of view) way to satisfy the humans need in building materials. Moreover, it shows very good performances in terms of mechanical stress resistance and thermal isolation. Most of the concrete-built materials are able to endure earthquake or keep houses warm in winter.

Despite cement-based concrete is a material that can be easily manufactured, it has the flaw of being at the origin of strong carbon dioxides (CO_2) emissions. Cement production contributes to global warming more than aeronautics that is often referred as a dramatic green gas emission source. Still, the manufacturing of cement requires the decomposition of calcium carbonate that emits carbon dioxide proportionally to the quantity of obtained cement. From this point of view and knowingly of the current environmental situation, concrete may not constitute a viable source of building materials for the upcoming years.

Earth makes a lot of means available either at its surface and in its core. While humans have been able to exploit underground resources like oil and gas, many materials are still very abundant and may show great mechanical properties as Earth Crust constituents. Aluminum and silicon profuse under our foot and their exploitation has started many years ago. Inspired from geological systems that have survived through the years, geomaterials have been industrially manufactured, as clay, zeolites or many other granular materials. New low carbon emission cement such as Limestone Calcined Clay Cement (LC3) have also been proposed, as a blend of Portland cement (50%), calcined clay under the form of metakaolin (30%), limestone (15%) and gypsum (5%) [1, 2].

With internal structures similar to clay or zeolites, inorganic polymer materials called "geopolymers" have been designed, using residual raw materials as meta-kaolins or fly ashes. However, the path to reach such cement-like pastes is not straightforward. The use of alkali activated materials do not pretend to replace the cement but may have new specific targeted applications. For instance, in nuclear industry geopolymers are under consideration to condition reactive metals such as magnesium cladding used by the past in reactor for thermal dissipation [3]. Geopolymer as a foam also find applications for the decontamination of liquid effluent [4].

Highly depending on the raw materials properties, the manufacturing of geopolymers is a complex series of reactions happening at many scales that may not be accessible to the human eye. The purpose of this Ph. D thesis is to use molecular simulations to study the *geopolymerization* process at multiple scales. Such work contributes to the designing of a global numerical process to model the reactions happening from the atomic to the macro scale. As a triptych alongside theory and experiments, numerical simulations may open a very new path to the understanding of the multi-faceted and multi-scale processes geopolymerization is.

As a guideline towards a better comprehension of sub-processes occurring at both atomic, mesoscopic and macroscopic scales, this thesis is organized as follow. In Chapter 1, a state of art about geopoly-

mers is presented, covering the definitions of the materials from an atomic to a macroscopic point of view. Experimental results are presented, characterizing the geopolymerization process and recent modeling approaches are discussed. These are contrasted with studies on cement and clays. The literature over molecular simulations of cement and geopolymer pastes is reviewed to motivate further modeling choices. Chapter 2 stands as a methodology chapter, gathering the basics and most important principles of statistical physics that are involved in molecular simulations. It gives the technical details on most of calculations employed within this work. Chapter 3, employs the Free Energy Perturbation (FEP) technique to evaluate the Potential of Mean Force (PMF) between two aluminosilicates oligomers in solution. Such grains are defined and the calculations performed in two cases: with dry and wet interface. These results are compared to metadynamics simulations, converging to a transferable methodology for effective pair-potential calculations for aluminosilicates oligomers in solution. Applying this procedure to systems with different charges, the origin of interactions are sought in Chapter 4. Ions trajectories and grain rigidity are discussed and related to the ability of these small particles to aggregate. Under the view of larger meta-grains, as a first step to an upscaled model, meso-interactions are discussed to better describe the interactions at stake within geopolymer gels. The specific role of water is shown and related to the grains deprotonation and so, the pH of the system. Finally, Chapter 5 opens a window on mesoscale simulations, using for the first time, an effective potential of interactions based on a fully atomistic description. From fittings of the obtained PMFs and the choice of a coarse-graining length based on experimental/simulation literature, the influence of the pair-potential on the final structure is discussed. Different scenarios of aggregation are proposed, mimicking the effect of pH. Generated structures are characterized *via* an analysis of their pore size distributions and scattering intensities. This Ph.D present a path from an atomic description of a geopolymer oligomer to a porous paste with mechanical characteristics.

Chapter 1

Geopolymer materials

A geopolymer can be defined as a chain or a network of mineral silicon/aluminum-based oligomers linked together with covalent bonds. Silicon that represents 25.7% of Earth crust, is its second most abundant component right behind oxygen. Therefore, many engineering materials involving silicon are widely used in many domains such as chemical engineering, construction and nuclear industries. In the latter case, geopolymers are considered for radioactive wastes management, namely magnesium cladding and radioactive oil storage. Geopolymers that are low-calcium containing compounds (by contrast to the cement paste) are also building materials: Alkali-Activated Materials (AAM) synthesized from slags and fly ashes can be strong alternative to concrete (the mix of cement paste with mineral aggregates and sand), at lower cost and are being widely studied worldwide as a mean to reduce cement carbon footprint (which production accounts for at least 8% of the anthropogenic CO2 emissions [5]) resulting from the melting of limestone and clay at high temperature (1500°C)[6].

From the dissolution of inorganic precursor using a strong alkaline solution, AAMs are formed, as a solid aluminosilicate amorphous 3D network. With porosities around 40-50% and compressive strength around 50-60MPa, they show similar mechanical properties to that of the cement paste. While cement is based on the dissolution-precipitation reaction of clinker grains (from the cement sac), geopolymers (as a poor calcium system) forms under polycondensation reactions between aluminates and silicates. Sodium Aluminosilicate (N-A-S-H) gels are formed in a competition of both dissolution and precipitation of oligomers in solution. With such constitution, geopolymers are often seen as "Green concrete" since they present a lot of similarities with concrete in their mechanical properties and generate 80 to 90% less CO2 in their production[7].

However, the use of geopolymers as "green cement" must be nuanced[8]. So-called activating solutions needed in the geopolymerization process are not "green" since they require the use of high concentration alkaline solution at high pH values. In addition, such highly concentrated solutions could induce health hazards in their manipulation.

The denomination of geopolymers have been proposed by Davidovits in 1976[9], who proposed an accurate definition of geopolymers, depending on the Si/Al atomic ratio. It is given in Table 1.1 and allows to distinguish materials that, even if likely-constituted, can have very different structures and properties.

Si:Al ratio	Terminology
0	siloxo
1	sialate
2	sialate-siloxo
3	sialate-disiloxo
>3	sialate link

Table 1.1: Scientific terminology for geopolymers [10]

The molar ratio between silicon and aluminum also allows to define different classes of geopolymers[10] that is presented here below. Note that in this work, we will mostly focus on aluminosilicate materials activated with sodium hydroxide.

- Waterglass-based geopolymer : Si:Al=1,
- Kaolinite/Hydrosodalite-based geopolymer : Si:Al=1,
- Metakaolin MK-750-based geopolymer : Si:Al=2,
- Calcium-based geopolymer (Ca,K,Na) : Si:Al=1,2,3,
- Rock-based geopolymer : Si:Al $\in]1,5[$,
- Silica-based geopolymer, sialate link and siloxo link in poly(siloxonate) Si:Al>5,
- Fly ash-based geopolymer.

1.1 Basics of aluminosilicate structures

As mentioned earlier, geopolymers are mostly made of elementary Al and Si oxide oligomers atoms, connected with covalent bonds. There exists a wide range of such materials, with very different compositions. Silicates, aluminates and aluminosilicates are the basis components of geopolymers.

1.1.1 Silicates

Silicates are anions made of Si and O atoms, connected with covalent bonds, usually with the general formula $[SiO_{4-x}^{(4-2x)-}]_n$, $x \in [0,2[$. In most cases, silicates are formed with corner-sharing tetrahedra, 4-x also called orthosilicate anion. It has an average Si-O distance of 1.62 Å and a bond angle O-Si-O around 109.5° as shown in Fig. 1.1 (a).

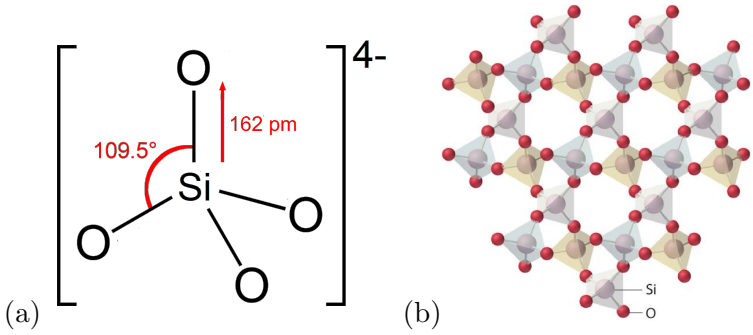

(a) (b)

Figure 1.1: (a) : Ortho-silicate anion ; (b) : Crystallizine silica (i.e. of the form $[SiO_2]_n$) : Quartz

These tetrahedra can assembly to form 3D crystal structures such as cristobalite and quartz as shown in Fig. 1.1(b). In these crystals, Si-tetrahedra share corner oxygens. In (sodium, potassium...) hydroxide solutions, the ortho-silicate $[SiO_4]^{2-}$ species can form solid hydrates of the form $[Na_{2x}Si_yO_{2y+x}]_n$ or $[(Na_2O)_x(SiO_2)_y]_n$) that result from two competing reactions: (i) the hydrolysis/condensation reaction and (ii) the protonation/deprotonation reaction, depending on pH.

$$\begin{aligned} \equiv Si - O - Si \equiv + H_2O \longleftrightarrow \equiv Si - OH + HO - Si \equiv \\ = Si - O = + H_2O \longleftrightarrow = Si(-OH)_2, \end{aligned} \tag{I}$$

$$\equiv Si - OH \longleftrightarrow Si - O^- + H^+. \tag{II}$$

The simplest silicate that exists is the orthosilicate acid : $Si(OH)_4$, a weak acid with $pK_a = 9.8$. It is stable in water as long as the concentration remains under the solubility limit (around 1mmol.L^{-1}).

Beyond this limit, it dissolves and poly-condensation begins to give a solution of oligomers which composition depends on pH. In fact, an increase of the alkaline concentration increases the de-condensation of the silicate species, allowing the formation of oligomers of various sizes. As de-condensation proceeds, smaller and smaller entities can form. At high pH, hydroxyl groups react, increasing the monomers concentration. The stability diagram for silica at ambient temperature is given in Fig. 1.2 (a), while Fig. 1.2(b) illustrates the silicate de-condensation caused by a OH^- group. There is a domain of silicate concentration/pH in which a solution of polydisperse oligomers can exist. At too low pH, silicates are not soluble while too high pH induces a strong dissolution, i.e. a bath of monomers.

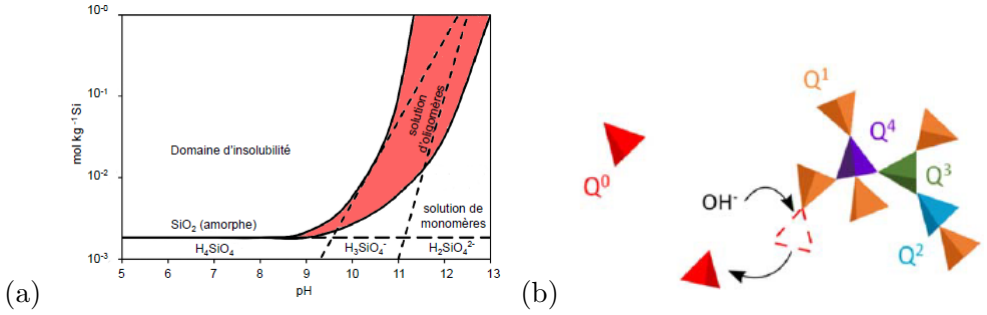

Figure 1.2: (a) Stability diagram of silica at 298 K. Reproduced from [11] ; (b) Illustration of oligomer polycondensation *via* a OH^- group in a geopolymer gel. Reproduced from [12].

Silicate oligomers in solution can be identified thanks to Nuclear Magnetic Resonance (NMR) and display very specific peaks depending on their sizes. These structures are named regarding the number of Si atoms they involve. Micro-structures with two, three, four, five or yet six atoms are referred to as dimers, trimers, tetramers, pentamers and hexamers. These oligomers are usually denoted with a Q^n notation [13], where n refers to the number of connected Si (and/or Al) atoms. Thus, Q^0 correspond to an isolated Si atom, surrounded by oxygen (O) atoms. A Q^1 species is a chain of two Si atoms, surrounded by oxygens, chained according to Si-O-Si, a Q^2 corresponds to a chain Si-O-Si-O-Si and so on. The subscript c is also often used to denote cyclic oligomers : Q^n_c (i.e. -Si-O-Si- connections forming a closed cycle, meaning that n must be at least equal to 2).

Dupuis *et al.* have modeled de-condensation in an alkali activated solution [12]. Using molecular simulations with a reactive potential (allowing bond formation and breaking), the ability for large oligomers to decompose into smaller ones was studied, presenting a size distribution of the latter and their shapes. In their work, they started from highly poly-condensed structure ($n = 2, 3$ and 4) and studied the alkaline dissolution by addition of sodium. Both initial and final simulation steps are shown in Fig. 1.3. Note that this was further extended to investigating the condensation phenomenon for both silicates and aluminosilicates, and will serve as a starting point in the present work [14, 15].

The connectivity between silicate species depends on its pK_a and arise from deprotonated bonds [16]. More precisely, an increase of the monomer and dimer charge leads to an increase of the associated pK_a as shown in Table 1.2, summarizing Sefcik *et al.*. results [16]. A pH higher than these pK_a values ensures the predominance of the associated silanols in solution. Note that to fully de-ionize a monomer, a pK_a of 18.8 is required.

Charge i	1	2	3	4	5	6
pK_a monomer	9.5	12.6	15.7	18.8	-	-
pK_a dimer	9.0	10.7	12.4	14.1	15.8	17.5

Table 1.2: pK_a of i-th ionisations of silanols for monomer $Si(OH)_4$ and dimer $Si_2O(OH)_8$. Data from [16].

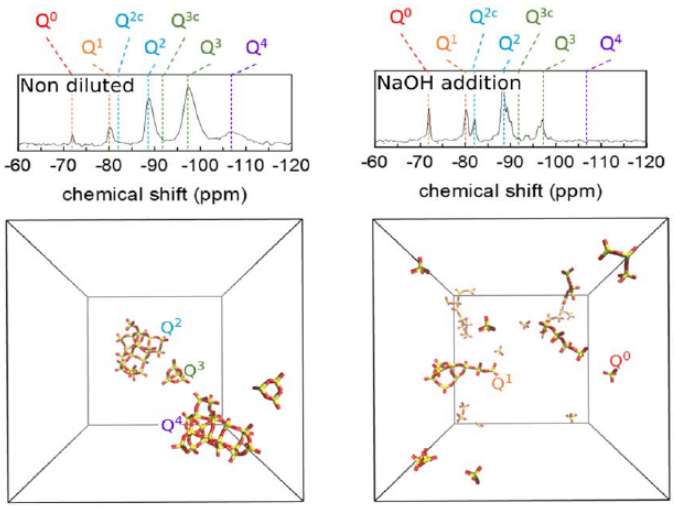

Figure 1.3: Snapshot of a geopolymer gel containing aluminosilicate oligomers of different sizes. Reproduced from [12]. It shows the influence of the addition of sodium hydroxides on the decondensation process. The left panel shows the initial simulation box containing oligomers of $n = 2, 3$ and 4 sizes. Addition of sodium and performing molecular simulations allow to reach the right panel as the final state, showing a different oligomer distribution with smaller species. NMR associated signals are displayed above.

1.1.2 Aluminates

An aluminate is a species containing an oxyanion of aluminum in solution, i.e containing elements with the formula Al O^{z-}. The most known is the tetrahedral monomer AlO_4^-. This tetrahedra has a bond angle O-Al-O around 109.5° and an average Al-O length of 1.74 Å[17]. With sodium ion it can form the Na_5AlO_4 species, or other sodium aluminates such as $NaAlO_2$ and $NaAl(OH)_4$.

1.1.3 Aluminosilicates

The nomenclature aluminosilicates encompasses many materials, either natural or synthesized as zeolites or geopolymers with Si/Al ratio higher than 1 or even imogolites with Si/Al lower than 1. An aluminosilicate species is a silicate where a few Si atoms has been replaced by Al atoms (substitution). As a consequence, a charge deficit appears which implies the presence of a counter-ion species to maintain electroneutrality. Among aluminosilicate species, one can find bi-dimensional phyllosilicates and tri-dimensional silicates structure (tectosilicates).

- Phyllosilicates are layered materials, with a $(AlSi_3O_{10})^{5-}$ basis to form, e.g., Muscovite : $(NaAl_2(OH)_2AlSi_3O$
- Tectosilicates are tridimensional crystal of $(Si,Al)_xO_{2x}$ tetrahedra, coupled with charge-compensating cations to form porous materials such as zeolites or non porous structures such as feldspaths.

1.1.4 Alkali-Activated Materials (AAM)

In civil engineering, Alkali-Activated Materials (AAM) geopolymers have attracted a lot of attention. They are also called poly-sialates, where Si and Al are 4-coordinated, with the empirical formula

$$M_n[(SiO_2)_zAlO_2]_n, wH_2O, \tag{1.1}$$

where M denotes the used cation (Na^+,K^+,Cs^+...), n the poly-condensation degree, w the water quantity and z the Si:Al ratio that lies between 1 and 5.

With this definition, all geopolymer materials can be defined according to their molar ratio H_2O/M_2O, SiO_2/M_2O and $z \equiv$ Si/Al and are referred as M-geopolymers. With this notation by ratio, the

concentrations of species in the activating solution are unknown. Still, it is the initial concentrations of silicates or alkali hydroxide that define the pH, degrees of connectivity and silicate protonation. These have a significant impact on the mobility of the species and on their reactivity with respect to aluminates, contained in the solid aluminosilicate source.

In this work, we only consider geopolymers with low calcium concentrations, precursors as class F fly ashes (spherical) or Meta-kaolin (layered) also called N-A-S-(H) gels[18]. These differ to alkali-activated gels with more calcium denoted C-A-S-H gels.

1.2 Geopolymerization : a multi step reaction

Geopolymerization describes the formation process of geopolymers as building materials. Similar to Portland Cement a solid powder phase is mixed with a liquid. The initial solid raw material is an aluminosilicate source such as Metakaolin, Slag or Fly [19]. The liquid phase, is an alkali solution at high pH (high concentration of, e.g. sodium hydroxides Na^++OH^-). The solid component gets dissolved by the basic solution, allowing its restructuring into a network of silicate/aluminosilicate species. A first step is the formation of a gel of aluminosilicate oligomers, which depends on the initially used constituents. As time passes by, up to a few minutes, oligomers will form bigger clusters[12]. Material setting then starts within a few hours. Still, the structure strengthens to acquire its final mechanical properties after more than 3 months[20].

These steps are discussed in the following with the goal of listing the different reactions involved in the formation process of geopolymer materials.

1.2.1 Dissolution, oligomerization and polymerization

The different steps as described in Fig. 1.4 of the synthesis process are presented below :

1. The aluminosilicate source is dissolved by the activating basic solution : water is consumed, silicate and aluminate species are formed;
2. An equilibrium is reached : silicates and aluminates gather to form aluminosilicate oligomers: this is called speciation;
3. The gelation starts by the oligomers growing and forming clusters with covalent bonds Si-O-Si and Si-O-Al. In the meantime, water and hydroxyl groups are released, maintaining dissolution of the initial solid.
4. Finally these gel groups polymerize and harden to form the solid material.

The reaction kinetics depends on the source and solvent concentrations, both impacting the pH but also the quantities, sizes, and types of formed oligomers. These elements play an important role in the mechanical properties of the final material.

The gelation step of geopolymerization is the key for the solidification reaction. Nevertheless, it is poorly understood as it is a complex process and it is difficult to deconvolute the experimental information. Aluminosilicates oligomers are the elementary bricks of the gel. Still, their interactions are difficult to infer. The modeling approaches of this manuscript have as starting point the formation of oligomers, then the evaluation of the effective interactions between two oligomers and a coarse-grained model that uses the effective interactions. For the interaction between oligomers two options can be considered:

1. non-reactive interactions where no chemical bonds are formed. The effective interactions are evaluated via the concept of potential of mean force (PMF) (see Chapter 3);
2. reactive interactions where oligomers could establish irreversible covalent bonds, corresponding to an infinite interaction potential, forming a continuous network akin to porous networks or glasses.

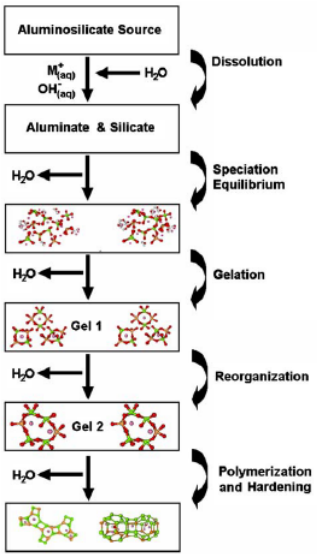

Figure 1.4: Geopolymerization process. Reproduced from [21]. Note that not only H_2O is released in the solution, but also OH^-, enhancing dissolution.

1.2.2 Reaction parameters

Geopolymers are amorphous thermo-metastable monolith while zeolites are stable crystalline powders. Conditions on temperature and Al and Si ratio for zeolites and geopolymer synthesis are given in Fig. 1.5, showing that geopolymers are formed at lower temperature. These differences in the formation process necessarily leads to differences in mechanical properties and in the overall micro-structure. However, it is interesting to note that zeolites can be formed from geopolymerization after a sufficiently long time.

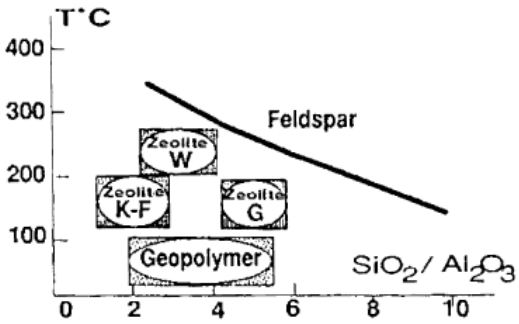

Figure 1.5: Zeolites and geopolymers formation domains. Reproduced from [22]

Even though the speciation process is still triggering a lot of research, several parameters are known to directly influence the macro-structure[19, 23, 24] and especially the porosity of the final product[25, 26, 27].

- Type of alkali cations;
- Silicate and water concentration in the activating solution;
- Al/Si ratio in the aluminosilicate source;
- Ambient conditions (humidity, temperature).

Fig. 1.6 displays both Pore Size Distributions (PSDs) and nitrogen sorption isotherms for different geopolymer pastes, changing water contents and with potassium (K) and sodium (Na) as alkaline ions. An increase of the water content leads to larger pore sizes until a certain ratio (15 H_2O/M_2O

ratio, M=Na or K). The use of a heavier ion leads to an increase of the specific surface and the accessible porous volume. The pore diameter is estimated around 100Å, the actual values depending on materials constitution. PSDs ranges from 30Å to almost 0.1μm according to mercury intrusion porosimetry data.

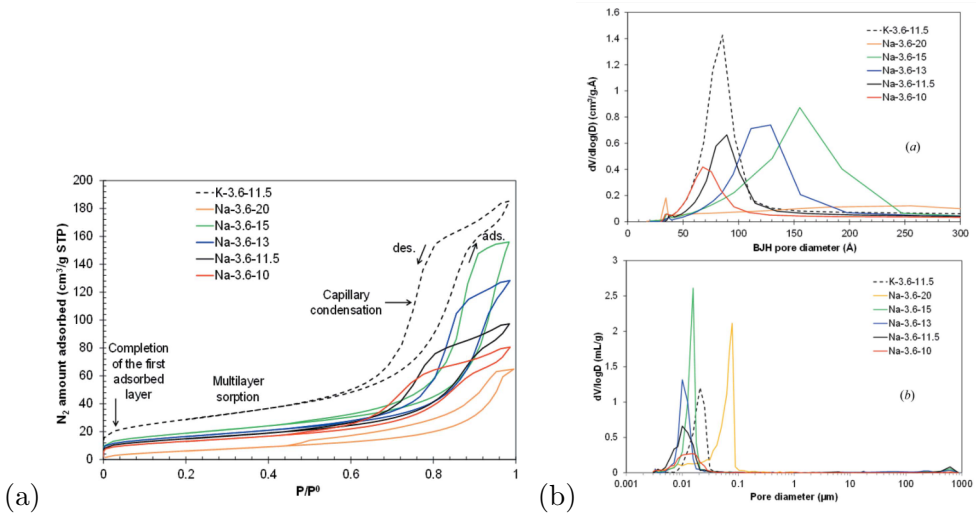

Figure 1.6: Porous network characterization. (a) Nitrogen sorption isotherms and (b) pore size distributions for different geopolymer compositions (alkaline ion and water content). Each color corresponds to a paste composition that reads as M-SiO_2/M_2O-H_2O/M_2O, M being the alkaline ion of the activating solution. Top and bottom panels show the PSD from nitrogen sorption porosimetry and mercury intrusion porosimetry respectively. Reproduced from [28].

1.2.3 Aging of geopolymers

The setting of geopolymers occurs with few hours, however the micro-structure and mechanical properties are evolving for several days and months[20, 23]. Covering a wide range of aluminosilicates sources (meta-kaolin, fly ashes, red mud,...) with different Al:Si contents and concentrations of the alkaline solution, the influence of aging parameters has been fully demonstrated by experiments[28, 29]. As an example, Fig. 1.7 displays how the scattering varies between a few hour up to 180 days. This proves that the aging of geopolymers involves very long time scales and that the final structure is highly dependent on the activating ion, as shown in the (d) panel. These results suggest that the use of heavier alkaline ions leads to smaller aggregate sizes and so, smaller porosity. For the three used alkaline ions, a Porod regime (q^{-4}) is found, accounting for a smooth interface over the range of [0.1,2-3]nm.

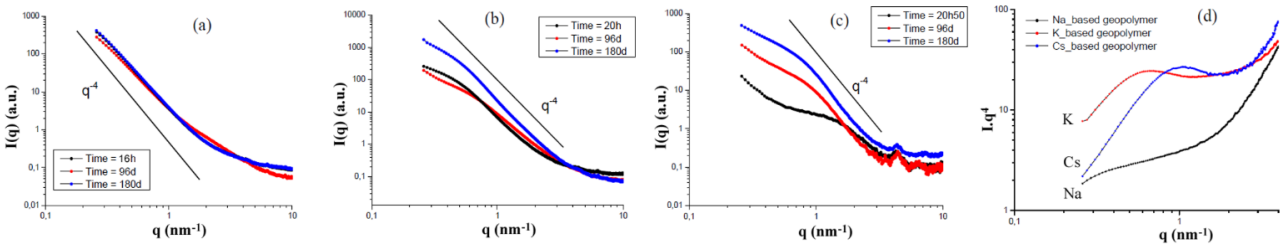

Figure 1.7: SAXS intensities data for Na, K and Cs-based geopolymers respectively in panels (a),(b) and (c). It shows the evolution of the paste structure with the setting time. In addition, the panel (d) shows the role of the alkaline ion on the final structure, set after 180 days. Reproduced from [29].

The role of setting conditions must also not be neglected : ambient temperature and relative humidity have been shown to highly influence the resulting pastes [29, 28].

1.3 Comparison between ordinary portland cement and geopolymers

Cement and geopolymers serve as binding materials in construction applications, but they have significant differences in their chemical compositions, production processes, and properties. They are made by mixing two phases, a solid and a liquid. The difference between the two is that water is enough to initiate the chemical reactions of cement whereas geopolymer require an alkali solution. This is due to the difference in dissolution reactivity of the cement powder and the aluminosilicate source material.

1.3.1 Micro-structure comparison

Geopolymers are made of aluminosilicate oligomers. Through the years, these structures have been identified and studied using ^{29}Si Nuclear Magnetic Resonance (NMR)[30]. Fig 1.8 (a) shows a plethora of possible stable molecules. The same process has been iterated to identify structures involving Al and Si atoms and so aluminosilicates. These structures are given in Fig 1.8(b).

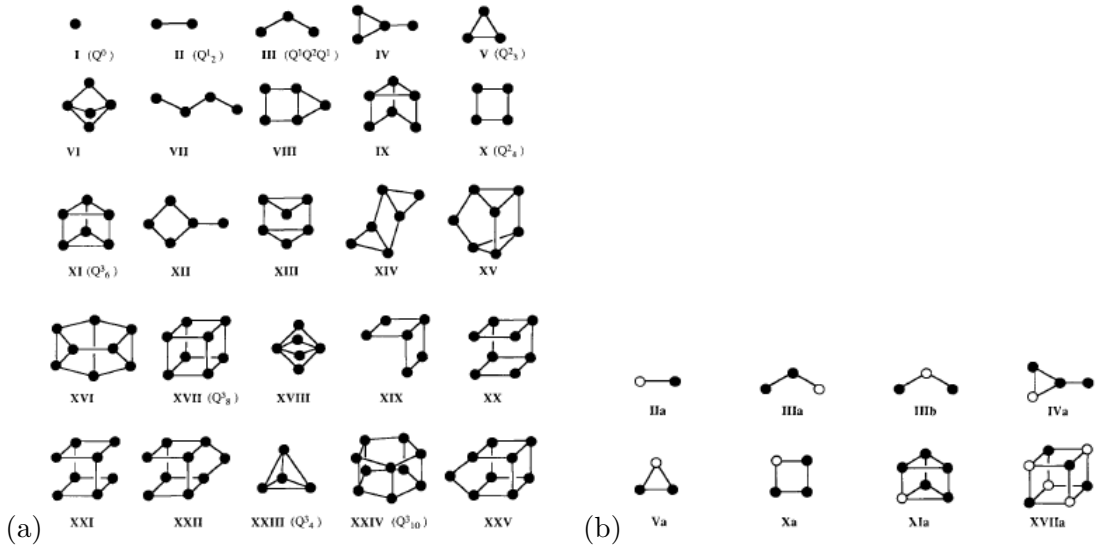

Figure 1.8: (a) Silicate and (b) aluminosilicate oligomers identified by ^{29}Si NMR and ^{27}Al NMR. Filled dots correspond to Si atoms while empty ones to Al atoms, each surrounded by 4 oxygen atoms. Reproduced from [30].

Cement and geopolymers undergo chemical reactions to form a solid matrix. Cement powder (the so-called clinker grains from the cement sac) primarily consists of Portland cement clinker, which is composed mainly of calcium silicates and aluminates. When mixed with water, these compounds undergo hydration reactions to form a solid made of the so-called CSH gel (85% in volume) and other hydration products (15% mainly Portlandite, CH)[31, 32]. Geopolymers on the other hand, are typically based on aluminosilicate materials such as metakaolin or fly ash, and form a three-dimensional polymeric network through geopolymerization reactions[21].

Both materials involve the formation of silicate- based structures, although the specific chemical bonds and structures vary. In cement, the primary nano-grains are considered to be calcium silicate hydrate (CSH) particles. CSH particles are formed during the hydration of Portland cement clinker and are responsible for the strength and durability of concrete[32]. In geopolymers, oligomers or short-chain polymers are formed during the geopolymerization process. These oligomers then cross link to form a three-dimensional network, which provides the binding properties of geopolymers. These oligomers can be considered as elementary nano-grains in geopolymers[21].

Fig. 1.9 shows the molecular structures from atomistic simulations of such materials. We note that CSH has the least ordered molecular structure compared to clays or zeolites. Geopolymer grains shows even less ordering, as a ramified structure.

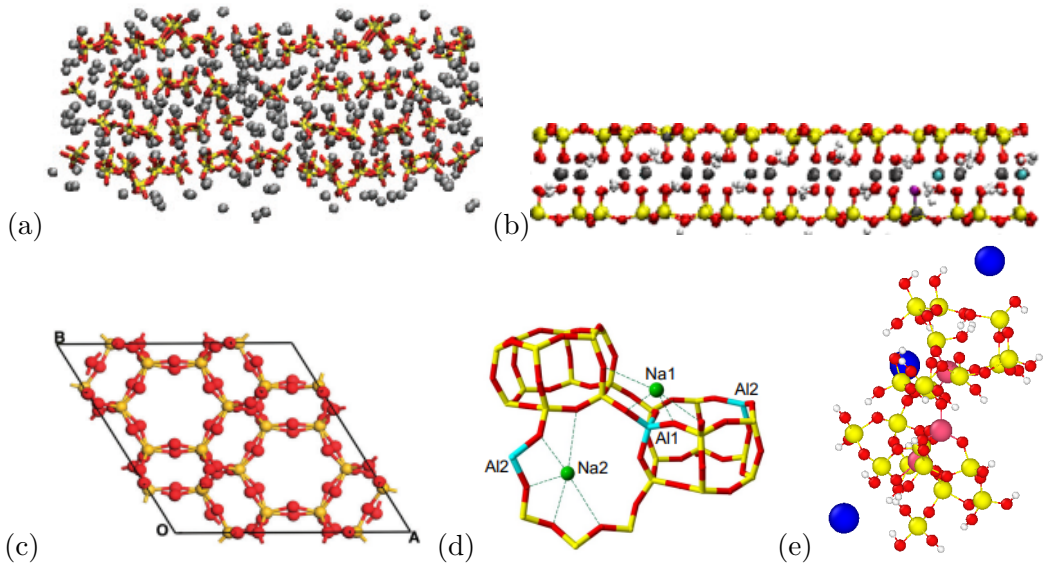

Figure 1.9: Different types of structures discussed in literature (a) : CSH platelet [33], with in red,yellow and gray respectively oxygen, silicon and calcium ions; (b) : clay grains [34] with in red,yellow, white and gray respectively oxygen, silicon, hydrogen atoms and calcium ions ; (c) Silicate zeolite amorphous structure, red and yellow display oxygen and silicates atoms [35], (d) Aluminosilicate zeolite amorphous structure [36], red and yellow correspond to oxygen and silicon while blue and green stands for aluminum and sodium atoms. (e) Geopolymer grain structure obtained from reactive molecular simulations [15] with red, yellow, pink, white and blue spheres corresponding to oxygen, silicon, aluminum, hydrogen and sodium atoms.

1.3.2 Comparison of the solidification process

Cement paste solidifies primarily through hydration/precipitation reactions, forming calcium silicate hydrates (CSH) gel, while geopolymers solidify through geopolymerization reactions, forming a polymeric network structure. The solidification process of geopolymers is typically slower than that of cement paste and involves the reaction of aluminosilicate compounds with an alkaline activator solution. In the following section, the two processes are described.

Cement paste formation

With the addition of water to cement powder (typically Portland cement), chemical reactions occur between the water and the cementitious compounds in the powder. The phenomenon is called hydration/precipitation. Calcium silicates and aluminates in the cement powder react with water to form calcium silicate hydrates (CSH) and calcium hydroxide (CH). CSH is the primary binding phase in concrete, providing strength and durability. The CSH gel forms a network of interlocking grains, which gradually hardens over time. This process is known as the setting and hardening of concrete. It involves both chemical reactions and physical processes such as precipitation and nucleation. After mixing, the cement paste undergoes a curing process to allow the hydration/precipitation reactions to continue and the cement to gain strength. Curing typically involves maintaining appropriate temperature and moisture conditions for a certain period[32].

Lootens *et al.*. [37] has studied the evolution of both elastic G' and shearing G^* moduli during the setting of cement pastes. Fig 1.10 (a) displays three regions : (i) under 1 minute, (ii) until 15 minutes (ii) after 15 minutes. The first step corresponds to the beginning of the dissolution reaction. After a minute, hydrates (CSH grains) start to precipitate at the surface of C_3S grains and water is consumed. This causes an increase of the moduli that reach a plateau as the material sets.

Fig. 1.10 (b) illustrates how conductivity and the thermal behavior monitor the setting of Ordinary Portland Cement (OPC) pastes. Under the simultaneous dissolution-precipitation mechanism during

the first minutes, ions are released in solution, inducing an increase in ionic strength that in turn increases the (ionic) conductivity C. As the cement gets into contact with water, massive precipitation starts, increasing the temperature (strong exothermic process) along with a fast decrease of C. As the moduli stabilize, the conductivity converges to 0, accounting for the formation of the porous solid network. Note that after 15 hours, a small peak of temperature is attributed to the formation of ettringite (a calcium sulfate that is a minor phase in the overall process). These results are supported by the heat flow analysis performed by Jansen *et al.*[38].

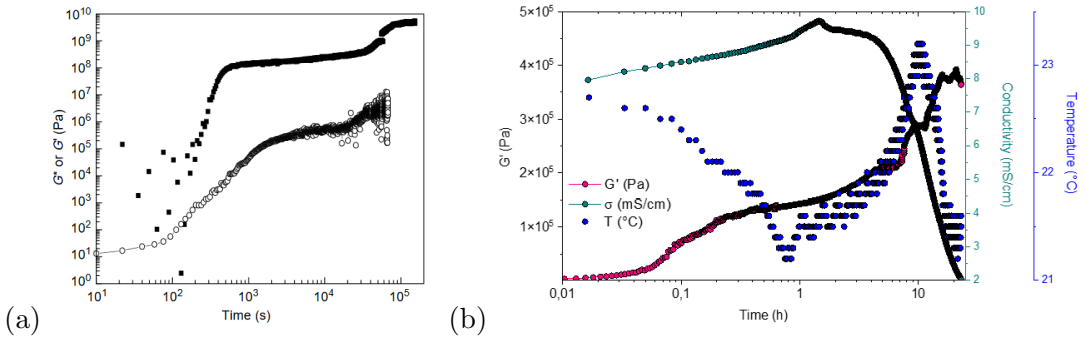

(a) (b)

Figure 1.10: (a) G' and G^*: elastic and shearing moduli respectively in dots and squares. Reproduced from [37]. (b) Elastic modulus measurement alongside conductivity and temperature during an OPC paste setting. Reproduced from [39].

Geopolymer formation

Geopolymers solidify through a process called *geopolymerization*. The source materials, such as metakaolin, fly ash, or slag, are mixed with an alkaline solution, typically a solution of sodium hydroxide (NaOH) or potassium hydroxide (KOH). The alkaline activator solution reacts with the aluminosilicate compounds in the source materials, forming polymeric chains or oligomers. Oligomers aggregation starts, giving rise to a porous network and binding properties of geopolymers. Geopolymerization typically occurs rapidly compared to the hydration process of cement. The mixture sets and hardens within hours, and the strength development continues over time as the geopolymer matrix undergoes further polymerization and curing. Fig. 1.11 displays the visco-elastic moduli during the setting of geopolymer pastes.

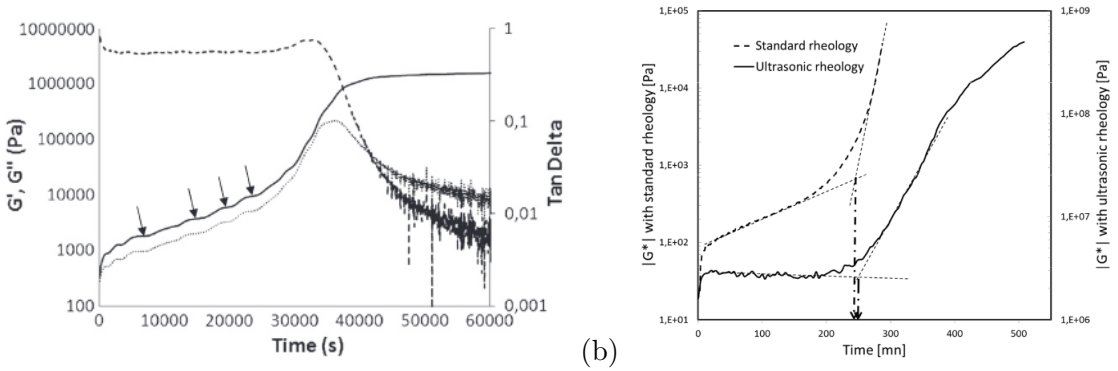

(a) (b)

Figure 1.11: (a) G' and G'', elastic and viscous moduli during a geopolymer paste setting, shown respectively in straight and dotted lines. The dashed lines corresponds to $\tan\delta = G''/G'$. Arrows shows the different levels of G' at the beginning of the reaction. Reproduced from [40]. (b) Shearing modulus measurement during geopolymer paste setting. Reproduced from [41].

From Fig. 1.11(a), one can observed that a 3-step process is recovered as that for the cement paste, see Fig. 1.10. At first, G' remains constant at the very beginning, it levels slightly for geopolymers,

as shown by black arrows. Then, moduli increase to reach a plateau, similarly as in Fig. 1.10(a). Characteristic times appears to be very different though. It takes 8h for G' to reach a plateau of 1MPa for geopolymer pastes while 15 minutes are required in the case of CSHs. In comparison to Fig. 1.10(a), the shearing modulus of geopolymer shown in Fig. 1.4 is similar, once again with a higher characteristic time (250min instead of around 100s).

The G'' modulus, accounting for viscous dissipation is also displayed. It shows a faster increase than G' between 7 to 8 hours. Illustrating the dominant role of viscous dissipation, this shows that interactions are, in the case of geopolymers, controlled by water: H_2O and OH^- are released in the system as the polycondensation occurs. As geopolymers are formed mostly from aluminates coming from the dissolution of solid metakaolin source that poly-condensate with silicates from the alkaline solution, oligomer interactions appear to be weaker than the interactions of CSH particles in cement. The Al-O-Si grains, as products from polycondensation remain suspended in solution. During the formation of geopolymers, no nucleation and growth of nano-grains is observed around the unreacted metakaolin. This is different than cement where the CSH particles precipitate close to the surface of un-hydrated cement grains and form the so called inner and outer CSH. These are area of CSH with high and low density respectively.

Fig. 1.12 summarizes the evolution of elastic modulus, conductivity and temperature alongside the different steps of paste setting, similarly as from Fig. 1.10 (c) but with longer characteristic times. At first, the conductivity decreases as OH^- complexes are consumed and Al^{3+} released. This induces a slight increase of visco-elastic moduli, that then diverge during polycondensation, up to a percolation time around 5h. After such time, aggregation and densification starts as observed from the decrease of the conductivity and increasing of scattering intensities.

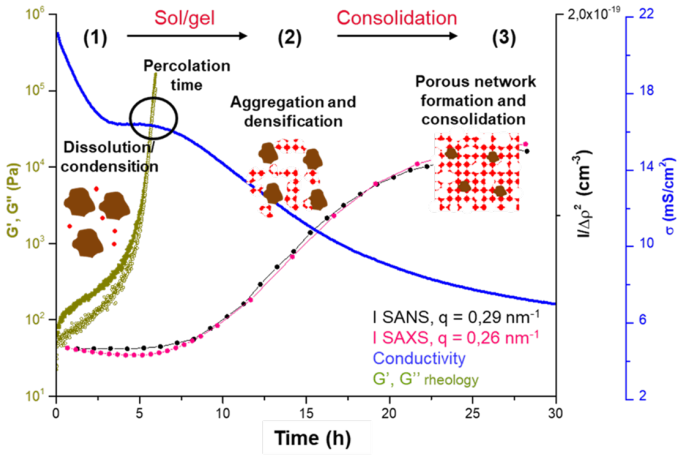

Figure 1.12: Summary of the experimental study of the geopolymerization process using a a cell that combines rheology, conductivity and thermal analysis. Different steps in the process are shown along with measurements of conductivity, elastic and loss modulus and scattering intensity. Data are given on the courtesy of Arnaud Poulesquen (CEA Marcoule).

The geopolymerization process occurs in different stages based on Nuclear Magnetic Resonance (NMR) and X-ray diffractograms, consistent with SEM observations [42, 43, 44]. These different stages are shown in Fig. 1.12 and, even though similar to cement, require more time to produce the final set material, mostly because of the release of water in the case of geopolymers instead of its consumption for cement.

1.4 Experimental characterization of geopolymers

At the macroscopic scale, geopolymers appear to be porous rocks showing very interesting characteristics in comparison to Portland cements[45]. Advanced characterization techniques such as scan-

ning electron microscopy (SEM), X-ray diffraction (XRD) and nuclear magnetic resonance (NMR) spectroscopy are often used to analyze the micro-structure of geopolymers. In addition, Nitrogen Sorption/Mercury Intrusion Porosimetry (NSP/MIP) and Small Angle X-ray/Neutron Scattering (SAXS/SANS) also gives major insights on material texture at the micro level. As the micro-structural features determine the mechanical performance of geopolymers, techniques such as compressive tests and nanoindentation are used for mechanical characterization.

In MIP, the structure in immersed in a mercury solution while a force is applied for the liquid to fill pore materials. Then, inserted volume is measured at each pressure point and related to pore sizes. It is usually used to investigate pores of sizes ranging from 3nm to a few hundreds of μm. Gas sorption methods as NSP complement these measurements to smaller pores (from mm to nm) with the evaluation of gas adsorption isotherms within a material, connected to specific surface areas according to the BET (Brunauer, Emmett and Teller) theory[46]. Pore size distributions can be obtained from desorption branches of the isotherms using the Barret–Joyner–Halenda (BJH) model[47].

Scattering experiments stand as a non-invasive method to study micro-structures. Intensity I and small angles variations of the deflected beams (under the form of wave vectors q) relate to the structure S and form factor P as $I(q) = S(q)P(q)$, giving information on characteristic sizes, shape or orientation of the structures. Fig. 1.13 displays the setting of a SAS experiment.

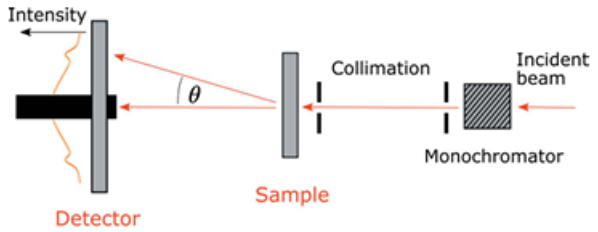

Figure 1.13: Sketch of the set up of a Small Angle Scattering (SAS) experiment. Reproduced from [48].

On mechanical tests, both compressive and nanoindentation are incremental methods that evaluate the response of a structure w.r.t. an imposed stress. They allow to measure, e.g. Young modulus, compression and hardness. Nanoindentation is used to measure mechanical properties of materials at small length scales, typically in the 100nm to micrometer range. It applies a controlled load or force using a sharp indenter, such as a diamond tip, onto the surface of a material and measures the resulting indentation depth or displacement. From the load-displacement data, various mechanical properties of the material can be determined, including hardness, elastic modulus and indentation creep.

1.4.1 Structural properties of geopolymers

Geopolymers exhibit a complex micro-structure characterized by a three-dimensional network of alumina-silicate gel. This gel structure is intertwined with a diverse pore network comprising macro-pores, meso-pores, and micro-pores, influencing properties like strength and permeability. Additionally, geopolymers may contain crystalline phases originating from unreacted precursors or secondary reactions during geopolymerization. Curing conditions, such as temperature and humidity, play a crucial role in shaping the final microstructure and properties of geopolymers. The following subsections present the characterization of hardened geopolymers paste via Mercury Intrusion/Nitrogen Sorption Porosimetry (MIP/NSP) and Small Angle Scattering (SAS) experiments.

Pore network in geopolymers

Porous structure of geopolymers relates to their mechanical, thermal, and transport properties [20, 28]. Geopolymers typically exhibit a range of pore sizes, including micropores (less than 2 nm), mesopores (2-50 nm), and macropores (greater than 50 nm). While the porosity is expected to be around

30%-40% , mean mesopore sizes are obtained around 10nm [28], confirmed by isotherm measurements [49, 50]. Controlling the pore structure is important to tailor properties such as strength, permeability, and durability.

For many pastes of meta-kaolin based geopolymers, Table 1.3 shows pore diameters obtained from both MIP and NSP tests. In addition, gyration radius and specific areas are also given, alongside the ones obtained from SANS measurements.

	Average pore diameter (Å)				Specific area ($m^2\,g^{-1}$)		
	Mercury intrusion	Nitrogen sorption	SAXS (R_g)	SANS	Mercury intrusion	Nitrogen sorption	SANS
Na-3.6-20	355	–	–	–	59	–	–
Na-3.6-15	154	120	–	–	96	67	–
Na-3.6-13	132	111	90	84	102	58	23
Na-3.6-11.5	117	88	70	74	92	53	28
Na-3.6-10	121	53	53	64	50	46	24
Na-4-13	160	88	80	68	78	64	31
Na-4-11.5	95	71	68	63	93	57	29
Na-4-10	98	51	60	50	51	40	26
K-3.6-11.5	208	85	49	54	64	101	63

Table 1.3: Average pore diameters or radius of gyration and specific areas for geopolymer pastes. First column denotes the paste compositions as M-SiO_2:M_2O-H_2O:M_2O, where M stands for the alkaline cation and the other terms for molar ratios. These values have been obtained for one-month-aged pastes *via* different techniques. After one month, the porosity still evolves but far slower than before. Gyration radius is evaluated thanks to SANS experiment using the Beaucage model described in the next subsection dedicated to scattering experiments. Reproduced from [28].

In complement to Fig. 1.14, this table shows that the pores and gyration radii increase with the water quantity (last number in pastes' name). This is attributed to more water being trapped within the material, and so, to the formation of larger pores. This is also illustrated in panel (d), with a H_2O:Na_2O ratio of 10. Distribution of the pores is thicker than at higher ratio, even after only 30 days. Despite mercury intrusion is less appropriate to account for smaller pore, the three method (MIP, NSP and SAXS) shows the same tendency and are complementary. Recalling Fig. 1.6(b), MIP probes micro and meso pore distributions while NSP captures nanopores (up to 50nm), probing a bi-modal porosity.

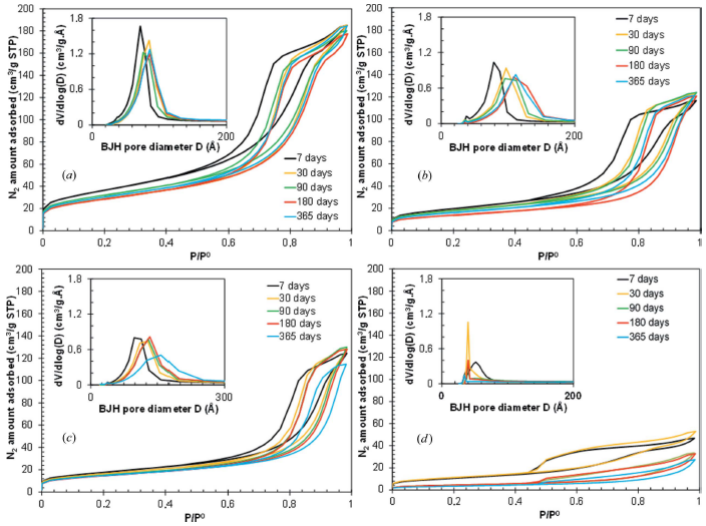

Figure 1.14: Time evolution of pore sizes for different geopolymer pastes. Main plots shows the nitrogen sorption isotherms for (a) K-3.6-11.5, (b) Na-4-13, (c) Na-3.6-13 and (d) Na-4-10 pastes, according to the nomenclature defined in Table 1.3. Insets are the associated pore distribution obtained with the BJH method[47]. The different colors stand for the curing days of the pastes. Reproduced from [28].

A SiO_2/Na_2O ratio of 4 suggests a decreasing of pore sizes in comparison to a ratio of 3.6. In addition, the use of bigger alkaline cations (K^+ vs Na^+) proves different results depending on the used methods. MIP suggests an increase of the pore size at the micron scale while NSP a decrease in the 1-50 nm range.

Overall, for Na-based materials, the quantity of water mostly monitors pore sizes distributions at fixed SiO_2:M_2O ratio. Geopolymer meso-porosity is in the range of [50-100] Å, largest values standing for a higher H_2O:M_2O ratio, i.e. more hydrated/diluted systems.

Scattering experiments

Scattering experiments in geopolymer and cement paste are used to probe its microstructure and properties. Neutron, X-ray (including small-angle and wide-angle X-ray), and light scatterings are among the common methods employed. These techniques provide insights into the arrangement of particle and cluster sizes, pores, and crystalline phases, shedding light on factors influencing strength, durability, and reaction kinetics. In this section, are briefly presented data from Small-Angle Neutron and X-ray Scattering (SANS/SAXS) for geopolymer pastes. Results from SANS [51] and SAXS [28] experiments for both cement and geopolymer are shown in Fig. 1.15.

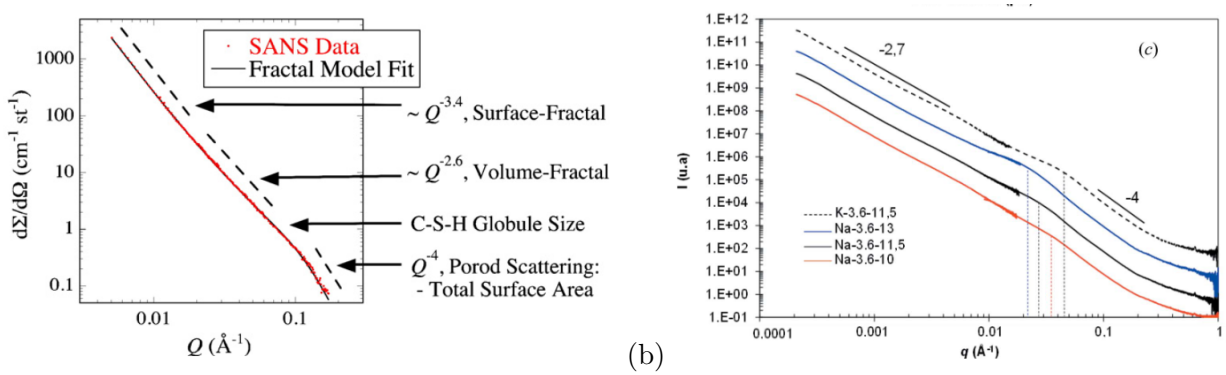

Figure 1.15: (a) SANS data for CSH. Reproduced from [51]. (b) SAXS data for geopolymer pastes. The different colors correspond to different paste compositions. Dotted lines show the different power law q^{-D}. Reproduced from [28].

Structural regimes

In some systems, scattering may follow a power-law relationship ($I \propto q^{-D}$), where the scattering intensity decreases with increasing scattering vector magnitude q. According to the value of D, different regimes can be characterized.

- With a non-integer exponent D. This regime is often observed in systems with fractal or self-similar structures. It arises from the lack of long-range order and heterogeneity.
- Power law of q^{-4}, also called Porod law: this regime typically occurs at intermediate scattering angles. In the Porod regime, scattering is dominated by interfaces between different phases, such as the interface between particles and the surrounding medium or the interface between different regions within a heterogeneous material. It provides information about the surface area and interfacial roughness.
- Constant I (usually power law of q^{-2} at low q-values): the Guinier regime occurs at very small scattering angles ($q \to 0$). It provides information about the size and shape of large well-defined particles or structures within the sample.

Gyration radius calculations

Small Angle X-ray Scattering experiments (SAXS) allows to characterize the structure of geopolymer pastes [28]. Thanks to the Beaucage model [52, 53] the scattering curves and structural parameters

of the material can be related. Involving both Guinier and Porod's contributions, it describes the scattering intensity $I(q)$ as :

$$I(q) = G \exp\left(\frac{-q^2 R_g^2}{3}\right) + \frac{C}{q^D}\left[\text{erf}\left(\frac{qR_g}{\sqrt{6}}\right)\right]^{3D}, \tag{1.2}$$

where R_g refers to the gyration radius, G to the Guinier scaling factor, d the Porod exponent and C the Porod scaling factor. This latter ensures a smooth transition from the Porod to the Guinier regime according to Eq. 1.3:

$$C = \frac{Gd}{R_g^d}\left[\frac{6d^2}{(2+d)(2+2d)}\right]^{d/2}\Gamma\left(\frac{d}{2}\right), \tag{1.3}$$

Γ being the gamma function. Note that in literature, N-levels Beaucage models can be used, writing as the sum of individual levels:

$$I(q) = \sum_{i=0}^{N} G_i \exp\left(\frac{-q^2 R_{g,i}^2}{3}\right) + \frac{C_i}{q^{D_i}}\left[\text{erf}\left(\frac{qR_{g,i}}{\sqrt{6}}\right)\right]^{3D_i}. \tag{1.4}$$

Scattering results discussion

Fig. 1.15(a) illustrates that at higher q-vectors, a Porod (q^{-4}) regime is observed for CSH, accounting for a sharp smooth interface that allows the definition of a specific area. Around the grain characteristic sizes, a -2.6 or -2.7 slope appears. Allen argues that this mass fractal regime arises from the low density of CSH at the surrounding of C_3S clinkers. At small angles ($q \to 0.01$Å), a rough surface appears in the continuity of the previously mentioned low CSH density.

Geopolymer pastes also probes a Porod regime at high q-values (around 1Å^{-1}). Fig. 1.15(b) also account for a volume fractal regime that extends to far small q-vectors (up to 0.0001Å^{-1}) and is attributed to badly defined correlation distances because of the grain polydispersity in the pastes. Especially, characteristic grain sizes are dependent of the water concentration and may correspond to a distance between partially dissolved metakaolin grains, illustrating the role of water and associated viscous effects in geopolymerization.

Comparing both pastes, the characteristic sizes of geopolymers materials are smaller than the one of CSH but remains within the same range of q vectors around a few nm. Both structures probes a sharp interface at sizes smaller than $2\pi/0.1 \approx 6.3$Å. Above, a power law in $D = -2.7$ is seen, as a volume-fractal accounting for less heterogeneous phases. The surface fractal slope seen for CSH has not been observed for geopolymer pastes, despite investigations at lower q-vector amplitudes.

1.4.2 Mechanical properties of geopolymers

Geopolymers exhibit a range of mechanical properties that make them attractive as alternatives to traditional cementitious materials like concrete. They can achieve high compressive strength, often comparable to or even exceeding that of Portland cement-based concrete. Geopolymers typically have a high elastic modulus, which reflects their stiffness and ability to resist deformation under applied loads. In the paragraph below literature results of compressive strength, Young modulus and nano-indentation are discussed.

Both compressive strength and Young modulus have been studied and converge to the results shown in Fig. 1.16 (a), with an order of magnitude at 40MPa for the compressive strength [54, 55, 19] while the Young modulus is found to be at the order of magnitude of 10GPa [41]. These latter results also combine well with the one of Fig. 1.16 (b). In both studies, an increase of the available pore volume results into a significant decrease of the strength.

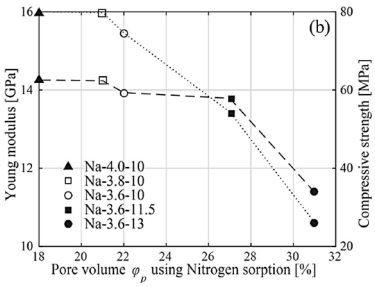

(a)

(b)

Sample Code	Open pore (%)	Compressive strength (MPa)	Density (gr/cm^3)
MK 1	23.31	38.32	2,109
MK2	21.37	40.03	2,069
MK3	25.8	27.65	2,069
MK4	26.5	12.57	1,870
MK5	27.1	4.73	1,830

Figure 1.16: (a) Experimental Young modulus and compressive strength measurements. Reproduced from [56]. (b) panel shows the relationship between mechanical resistance w.r.t. the porous network. As another example en compressive strength experimental measurements, it illustrates that more open pores leads to a smaller compressive strength. Reproduced from [57].

Apart from macroscopic mechanical characterization of geopolymers it is worth mentioning small scale mechanical characterization by nanoindentation, shown in Fig. 1.17 for both cement and geopolymers.

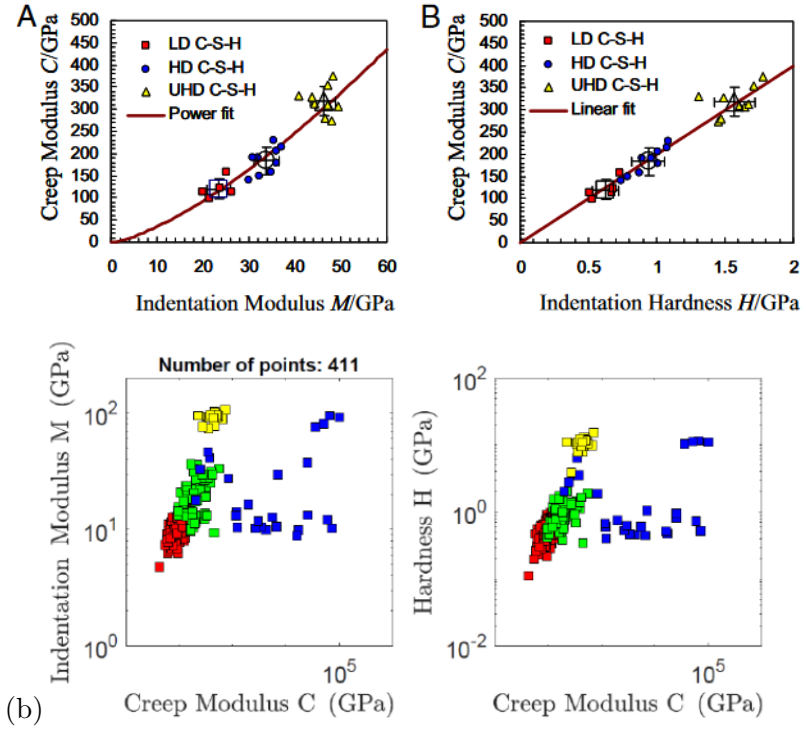

(a)

(b)

Figure 1.17: (a) Indentation and creep moduli of cement pastes obtained from nanoindentation, with a maximal load of 0.5mN. Red, blue and yellow colors refer to the CSH density, respectively low, high and ultra high. Reproduced from [58]. (b) Indentation and creep moduli of geopolymer pastes obtained from nano-indentation with a maximum applied force of 0.3mN. Yellow areas correspond to quartz and blue ones to the interface between geopolymer and quartz. Red and green dots are NASH structures. Unpublished data on the courtesy of Thibault Divoux (ENS Lyon).

At small creep values a linear behavior is observed for geopolymer materials, similar to the one of CSH over the same range of creep modulus. Green and red areas in Fig. 1.17(b) compares well with the low and high density CSH, displayed in red in Fig. 1.17(a) : low creep relates to smaller hardness and indentation modulus. As the creep modulus increases, so does the indentation modulus, linearly, as observed from the yellow squares, associated to quartz. Here is recovered the evolution from low to ultra high density for CSH. Major difference stands in the existence of a quartz-geopolymer interface at high creep. Such observations do not exist in the case of CSH and are mostly inherent to the suspension of aluminosilicate oligomers in solution.

1.5 Atomistic and coarse-grained simulations

Molecular simulations has played a major role in material sciences for the last 20 years, giving great opportunities to study both reaction paths and mechanical properties. Especially, grains interfaces, individual phases or very different mixtures have been explored to scales ranging from the nanometer to the micron-scale [59]. Within this range, atomic systems involving times up to the nanosecond can be studied while mechanical tests can also be performed at the engineering levels, i.e. up to seconds.

At the atomic scale, grains can be studied using either reactive or non-reactive potential. Performing equilibrium runs will give clues about the most probable structure (shape, size,...) of material grains. Then, the interaction between grains can be evaluated via different methods. With a sufficiently accurate description of interaction between grains, the agglomeration of these latter can be studied: mesoscale structures can be then obtained. From there, the texture of set of porous networks can be investigated and their mechanical properties tested using computer calculations.

Atomistic simulations deal with individual atoms, capturing their dynamics of interactions with outmost details. These simulations provide a microscopic view, unveiling the fundamental principles governing molecular dynamics and chemical reactions. At this scale, interactions are guided by weak and strong electrostatic interactions as Van der Waals or Coulombic interactions, usually modeled via inter-atomic force-fields/potentials.

Coarse-grained simulations adopt a larger scale approach, grouping atoms into larger entities to simplify the computational complexity while retaining essential features of the system. By zooming out, they offer understanding of phenomena that span longer timescales and larger spatial dimension. Both definition of coarse-graining lengths and effective interactions are of greatest importance to perform such simulations.

In this section, atomistic simulations of cement and clay from literature are presented with emphasis on the choice of force-fields. Upscaling simulations are then discussed before to move on a state of the art of performed simulations on geopolymer systems, at both atomic and meso-scales.

1.5.1 Cement and clay molecular simulations

At the atomic level, cement and clays are materials involving silicon network and alkaline ions. The physics of cement is based on the cohesion of CSH, as nano-platelet particles which surface charge is compensated by calcium ions. Clays are layered structures with a well-organized aluminosilicate structures. Local charge deficiencies due to the presence of $Al(OH)_3^-$ is compensated by sodium ions. Both their formation process is based on the dissolution of a solid raw material and the formation of grains in water. These latter are then condensing to form larger network to develop strong mechanical properties under a few minutes[60, 37].

As shown in Fig. 1.9 (a) and (b), CSH grains and clay platelets are usually modeled as layered silicate chains with charge compensating ions around. Thanks to these models, cohesion of cement pastes has been studied, allowing for a good understanding of most interaction involved at the colloidal level [61]. Layered grains have been employed to efficiently compute Potential of Mean Forces (PMFs) for both CSH [62] and clay [63] using a perturbative approach.

In this section, few examples of atomistic simulations for cement and clays are presented that are relevant either for their simulation approach or for the results obtained. With similar constitution and following a similar formation path as CSH and clays, literature of these nano-granular materials constitutes a starting point to our investigation into the cohesion of geopolymer oligomers/grains.

Force fields for cement and clays

Pair-potential between two atoms is driven by their chemistry on their local environment. Each atom carries a charge, inducing Coulomb interactions. Van der Waals interactions are also in action at short distance. But these (coulomb, Van der Waals) are usually referred to as non-bonded interactions as

they involve no electron sharing. The formation of covalent bonds (hence electron sharing processes can be modeled through various approaches starting with the most simple one, the Morse potential to the most advanced reactive force-field such as the ReaxFF force-field[64]. These accounts for the chemical bonding energies but also bonds length and angles (including dihedral (torsion)). Reactive force fields explicitly account for chemical reactions and bond breaking/forming events within a system. They incorporates a reactive potential energy surface that depends on the local atomic environment described through the so-called bond-order parameter. This allows these types of interatomic potentials to capture the dynamic evolution of chemical reactions and the rearrangement of chemical bonds during simulations.

Traditional force fields (ClayFF, IFF, CSH-FF,...)

The electrostatic (Coulombic) pair-potential between two particles i and j at a distance r_{ij} is described in Eq. 1.5

$$U_{\text{Coul}} = \frac{e^2}{4\pi\varepsilon_0}\frac{q_i q_j}{r_{ij}}, \tag{1.5}$$

where e stands for the elementary charge, $\frac{1}{4\pi\varepsilon_0}$ for the coulombic constant, q_i and q_j being the atomic charges.

For two particles σ_i and σ_j, Van der Waals interactions are usually approximated by Lennard-Jones potentials using distance and energy parameters σ_{ij} and ε_{ij} as in Eq. 1.6.

$$U_{ij} = \varepsilon_{ij,\text{VdW}}\left[\left(\frac{\sigma_{ij}}{r_{ij}}\right)^{12} - 2\left(\frac{\sigma_{ij}}{r_{ij}}\right)^{6}\right] \quad \text{or} \quad U_{ij,\text{VdW}} = \varepsilon_{ij}\left[2\left(\frac{\sigma_{ij}}{r_{ij}}\right)^{9} - 3\left(\frac{\sigma_{ij}}{r_{ij}}\right)^{6}\right]. \tag{1.6}$$

σ_{ij} and ε_{ij} respectively quantify the well zero-point and depth. 12/6 and 9/6 exponents describes the well width and their choice depends on the studied system.

Bonded interactions are also usually described using harmonic terms for bonds and angles as in Eq. 1.7.

$$E_{\text{bond}} = k_r(r_{ij} - R_0)^2 \quad \text{and} \quad E_{\text{angle}} = k_\theta(\theta_{ij} - \theta_0)^2, \tag{1.7}$$

where k_r and k_θ stand for the elastic constants, R_0 and θ_0 for equilibrium distance and angle respectively.

A force field corresponds to a set of parameters for chosen interactions. As a example, ClayFF[65] and Interface-FF[66] are defined as the sum of a Van der Waals and Coulomb potentials coupled with angles and bonds interactions as shown in Eq. 3.1, relating to Eq. 1.7.

$$E_{tot} = E_{\text{VdW}} + E_{\text{Coul}} + E_{\text{bond}} + E_{\text{angle}}. \tag{1.8}$$

Still, they differ from the definition of atomic charges. The first, had these fitted to DFT calculations while the second, evaluated them *via* dipole moments.

Water, can also be described different ways, either with the SPC/E model [67] or the TIP4P model [68]. The SPC/E model (used in this work) describes water molecules as rigid isosceles triangle between H-O-H atoms. Interactions within the molecules are the sum of Coulomb and a 12/6 Lennard-Jones interactions with the following parameters :

σ	ε	r_{OH}	θ_{HOH}	q_O	q_H
3.166Å	0.1554	1.0Å	109.47°	-0.82e	+0.41e

In overall, potential parametrizations can be different to study similar structure. They should be seen as a whole, encompassing all interactions at stake in a system.

A Reactive force field: ReaxFF

ReaxFF differs from the previously discussed interaction potentials, as it allows for reactions at the atomic level. i.e. bonds forming/bonds breaking based on the bond order parameter calculations. The bond order describes the electron density at the vicinity of interacting atoms. It quantifies the pair-potential energies via the strength of bonds between atoms[69]. At every simulation step, the update of atomic positions helps balancing the interactions and charges of each atoms are recomputed using charge equilibration methods as Qeq proposed by Rappé *et al.*[70]. In such a reactive field, each atom has a unique identity reflecting its local chemical environment. Therefore, ReaxFF is an extremely strong tool, based on initial quantum-DFT parametrization on representative but simpler situations (hence assuming a good degree of transferability). It is able to reproduce chemical reactions and transitions paths at the atomic scale with a smaller computational cost than direct *ab initio* calculations. However, compared to non-reactive potentials, it might be up to 10 times slower in simulations since it requires small timesteps and comport many subsequent calculations.

Mesoscale modeling of CSH and clays

In mesoscale simulations, the main elements are the grain definition, seen as a coarse-graining length and the effective interactions between the grains.

The mesoscale modeling efforts can be very much guided by concepts imported from colloids physics as in the end, we are dealing with charged objects and their cloud of counter ions in high pH conditions, all immersed in a solvent (water). Regarding the cement paste, water and ions get confined between CSH nanoplatelets. It is therefore legitimate to invoke the DLVO theory [71] that precisely deals with this situation but in the simplest way i.e. assuming that ions are point-charges and that the solvent can be modeled through a single dielectric constant) so to have an analytical mathematical solution. In short the DLVO theory handles the coulombic interactions though the Poisson-Boltzmann equation on the top of which a mesoscopic description of Van der Waals interactions are added using the Derjaguin approximation and a Hamaker constant. The outcome of the DLVO theory is a prediction on system cohesion or absence of cohesion; it is by all means a mean-field theory.

The Poisson-Boltzmann equation predicts a strong repulsion between two CSH platelets (or any charged colloids immersed in a electrolyte)[72] and augmented by van der Waals interactions will not allow to recover from the DLVO theory the observed strongly cohesive layer-to-layer interaction. This demonstrates the need of having the correct physical ingredients and approach to describe the behavior of charged objects as the nanolayers in CSH in a mesoscale modeling effort[71]. The proper CSH attracto/repulsive interactions are recovered as a function of ionic strength (and pH) provided the inclusion of ions position correlations together with the correct water dielectric constant [33, 73, 74] Interestingly enough the exact same conclusions were earlier reached by Carrier to explain clay cohesion making the colloidal physics approach to quantitatively agree the results from full atomistic simulations[34, 63]. AFM experiments found that in the case of CSH, this attraction phenomena is related to ionic concentration [75]. Both pH and calcium concentration appear as major parameters in the cohesion of cement pastes, accounting for either repulsion, attraction or attracto-repulsion between cement hydrates. The attracto/repulsive behavior between colloids were obtained through the interlayer pressure calculations that relates to the system free energy through an integration step. It is strictly equivalent to the so-called Potential-of-Mean-Force) approach (PMF) here below introduced.

The overall interaction between grains in solution can be evaluated under the scope of a free energy surface also called Potential of Mean Force (PMF). As a function of atomic/molecular coordinates, it quantifies the cohesive behavior of two entities immersed in a dielectric medium. From this definition, it stands as a way to move from the atomistic scale where the distance free-energy curve between grains is first established to the mesoscale describing an assembly of these grains in pairwise interactions. Defining the effective pair-potential of interaction at the mesoscopic level, the PMF can usually be

obtained from molecular simulations using different methods [33, 76].

A widely used approach to obtain the PMF for coarse grained system is the Free Energy Perturbation (FEP) technique. By sampling equilibria of grains at different distances, free energy variations can be estimated by applying small perturbation to the system. Once a model for interactions is proposed, precipitation of particles can be modeled thanks to Grand Canonical Monte Carlo (GCMC) simulations. Insights have been proposed on CSH and clays precipitation processes, based on transferable potentials as the Lennard-Jones, Yukawa or yet Gay-Berne potentials for spherical or ellipsoidal particles [77, 78, 79].

CSH particles interactions

At the colloidal level, Atomic Force Microscopy (AFM) allows measurement of surface interactions. In AFM experiments, interactions can be obtained between a CSH platelet and a CSH crystal[80]. Surface forces in such grains are dictated by the physico-chemical reactions at their interface as so AFM is a good way to quantify interface cohesion strength. The force between two grains presents a minimum and, depending on the Ca(OH)2 concentration, a maximum, both separated by a free energy barrier (as the force can be expressed as a variation of the free energy). Such a shouldered-shape of the force versus distance curve is attributed to the electrostatic correlation due to the charged surfaces of the grains[81, 82, 83]. Note that AFM experiments are very sensitive to the grain definition (shape, size)[84] and to the paste density[85, 86]. Thus, the obtained results may be used to model colloidal systems with a medium-range separations but not between inner layers of the grains.

Attractive inter-grain forces procure cement cohesion[80]. These are the direct consequence correlated movement of Ca^{2+} ions in-between CSH negatively charged grains immersed in a basic electrolyte as shown by experiments [87, 88] and simulations [89, 90].

Once the CSH grains have been defined from both their chemistry and size and the potential of interactions between them measured or calculated, the CSH paste can be modeled at the mesoscale using simulations techniques imported from Statistical Physics namely Molecular Dynamics (also used at the atomic scale) and Grand Canonical Monte Carlo. Masoero *et al.* proposed an effective potential for coarse-grained simulations of CSH based on molecular simulations [91]. According to experiments, as a function of the distance between two grains, this potential should fulfill three features: a minimum at short distances to ensure cohesion, a repulsive shoulder at medium range for adhesion and must go to zero as the distance increases. To reproduce only the well of interaction, they proposed a Mie potential (slightly modified Lennard-Jones potential)[92], with a well depending on the particles size so that a poly-disperse approach can be taken. Between two grains i and j of size σi and σj, the potential energy stands as:

$$U_{ij} = 4\varepsilon \left[\left(\frac{\sigma_{ij}}{r_{ij}} \right)^{2\alpha} - \left(\frac{\sigma_{ij}}{r_{ij}} \right)^{\alpha} \right], \text{ with } \sigma_{ij} = \frac{1}{2}(\sigma_i + \sigma_j), \tag{1.9}$$

where calibration of potential depth ε and the exponent α has been performed using mechanical measurements as the elastic modulus or the strain failures obtained from previous work [93, 94]. Ioannidou et *al.* [95] carried mono-disperse simulations using a combination of a Mie (short-range attraction) and a Yukawa (medium range repulsion) potentials as follow :

$$U_{ij} = 4\varepsilon_0 \left[\left(\frac{\sigma}{r_{ij}} \right)^{2\alpha} - \left(\frac{\sigma}{r_{ij}} \right)^{\alpha} \right] + A\frac{e^{-\kappa r_{ij}}}{r_{ij}}. \tag{1.10}$$

These simulations were mostly performed considering spherical particles. However, most PMFs calculations were obtained from the study of nanolayers/platelets [33, 62, 63]. To account for such geometry, coarse-graining simulations have been proposed for cement using a orientation-dependent

potential [96, 97] as the Gay-Berne potential [98] with disk-shaped particles [99, 100]. As an illustration, PMFs obtained for CSH, fitted with a Lennard-Jones and a Gay-Berne potential are shown in Fig. 1.18.

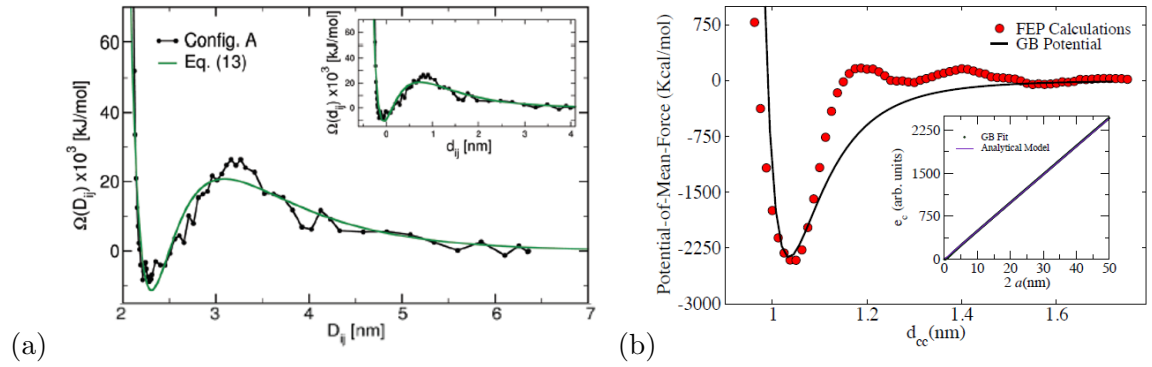

(a) (b)

Figure 1.18: PMF obtained for face-to-face interactions of CSH nanolayered particles as a function of the center-of-mass distance. (a) Fitted with a hybrid 12/6 exponent Lennard-Jones+Yukawa potential. In the inset are shown the curves w.r.t. the surface-to-surface distance. Reproduced from [33]. (b) Fitted with a Gay-Berne potential with oblate C-S-H particle with diameter of 10 nm. The inset shows the dependence of fitting parameters on the particle diameter. Reproduced from [101].

Both plots show a attractive well at a few nanometer distances followed with a repulsive shoulder. Attractive well from the fits mostly arise from the $-1/r^6$ in the LJ model, as the Gay-Berne model stands as an anisotropic form for the 12/6 Lennard-Jones potential. These results illustrates the ability for CSH layers to interact in water through an attracto-repulsive potential, accounting for cohesion.

Precipitation simulations of CSH

Having set up the coarse-graining lengths and effective potential of interaction, the precipitation of grains can be studied thanks to molecular simulations [102, 103]. In particular, cement mesostructures can be studied with regard to the precipitation kinetics/parameters.

Both attractive and attracto-repulsive effective potential have been proposed to study the evolution of CSH gels at the micro-level. Both roles of potential and kinetics on resulting structures are presented. As the potential mimics the pH (or lime concentration), its relation to pore size distributions is shown. Faster setting times are modeled using larger precipitation rates R as the ratio between molecular dynamics and Grand Canonical Monte Carlo steps. In overall it shows that increasing the lime concentration induces higher local coordination and so, stronger gels. This is seen from as slighter deceleration of precipitation at high pH.

Mesostructures also appear to be sensitive to precipitation kinetics. In addition to particle clustering studies, resulting porous network can be evaluated under the scope of pore size distributions and scattering intensities [78]. Such properties allow for a direct comparison with experimental measurements.

1.5.2 Geopolymer molecular simulations

Similarly as for CSH and clays, geopolymer materials are formed from the dissolution of a solid source and the agglomeration of nano-grains, motivating a coarse-grain approach to model the geopolymerization. Formed under high pH conditions, these aluminosilicate materials show a more amorphous microstructure, as a result of a complex simultaneous dissolution/condensation reaction. At the atomic scale, oligomers formation has been studied thanks to reactive potentials [104, 105, 15]. A few upscaling models for geopolymer gels were proposed to study the agglomeration process either on from a grain structure as a defective clay crystal structure [106] or as lattice/silicate cubic particle (accounting for the tetrahedron geometry)[107].

Atomic simulations: speciation using reactive potentials

With its strong ability to form and break bonds, ReaxFF has allowed to generate aluminosilicate structures in water and alkaline solutions, mimicking the dissolution/aggregation process of geopolymerization [107, 108, 15]. Yang *et al.* have presented the stability and the structure of key neutral aluminosilicate clusters [109]. In addition, favorable oligomer structures from geopolymer speciation have been obtained under different conditions [14, 105].

The formation of clusters of sizes greater than 4nm from monomers and dimers has been modeled thanks to reactive molecular dynamics[104]. Especially, regarding the free energies, they observed that the $AlSi(OH)_4Na$ dimer turns out to be the main reactant in cluster growth, which is consistent with previous experimental investigations[110, 111]. $AlSi(OH)_4Na$ also appeared to be more reactive than its silicate counterpart $Si(OH)_4Na$, making it sensitive enough to form Si/Al dimers, avoiding Loewenstein's rule violation [112] (according to which there should be no Al-O-Al bonds, even though this one is not strictly applying to geopolymers[113]). Further, beside experimental works [31, 114], it was noticed that temperature has only little impact on the thermodynamics of these aggregating reactions.

Parallel tempering techniques have been used to dissolve and speciate large aluminosilicate clusters, as illustrated in Fig. 1.19 [12, 15]. It was performed for pure silicate mix of aluminate and silicate, also illustrating how would the presence of aluminum in the system impacts the gel network. Alumina content, already known to enhance the whole geopolymerization process, allows larger structure to be formed, up to gyration radius of $R_g \approx 10\,\text{Å}$. Especially, these results are consistent with the gyration radius estimated around 2.1Å using the Guinier model from SAXS experiments [20].

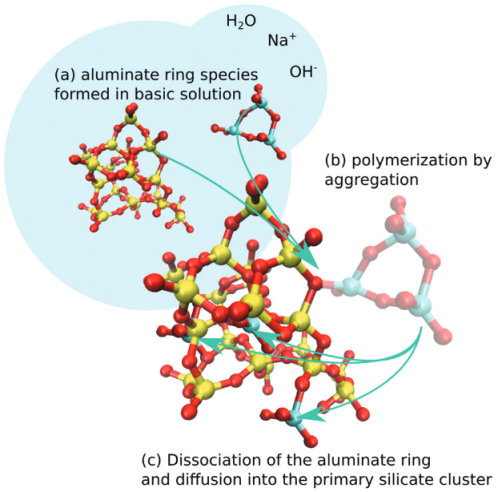

Figure 1.19: Different phases of the formation of an aluminosilicate species in an alkaline solution modeled in molecular simulations with a reactive potential. A silicate species merges with an aluminate ring species form in the solution before aluminum atoms diffuse into the structure to reach the more energetically favored structure. Red, yellow and cyan spheres display oxygen, silicon and aluminum atoms. Reproduced from [15].

The speciation process is shown to be highly dependent of the initial concentrations (either in the aluminosilicate sources or in the activating solution), the pH or the activating alkali.

Mesoscale simulation of geopolymers

A geopolymer gel is constituted of polydisperse aluminosilicate oligomers. Based on both quantum Density Function Theory (DFT) and Coarse-Grained Monte Carlo (CGMC) simulations, White *et al.* developed a methodology to study solid-gel transition in zeolites [115] and applied it to geopolymers [116]. Defining particles as silicate and aluminate monomers (tetrahedron of size around 3.1Å), they

used CGMC simulations to mimic dissolution, polycondensation and aggregation of species into nano-particles called *nano-precipitates*, in aluminosilicate gels [107]. This approach allowed to study a system within a box size of 9nm.

They studied the formation of clusters depending on the composition of the activating solution as seen from Fig. 1.20 (a). Especially, it turns out that without silicates in the solution, big clusters form continuously from the aggregation of mid-sizes clusters. On the contrary, introducing silicates in solution lead to more direct formation of big clusters, as an enhanced 3D-networking.

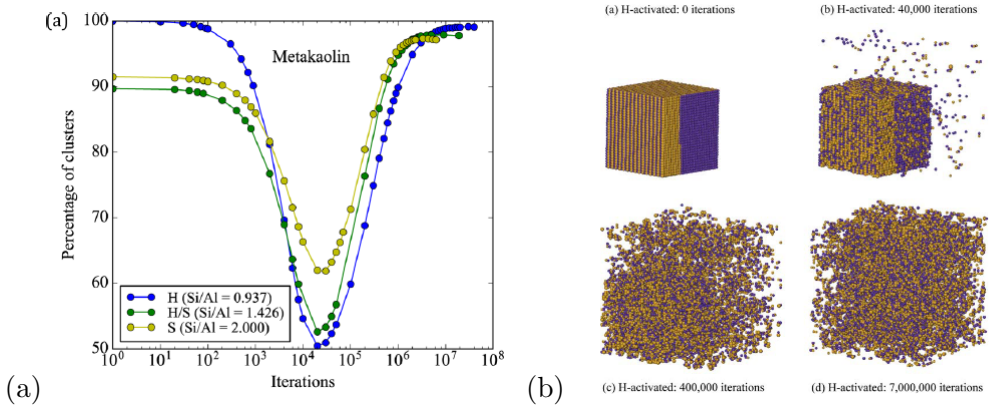

Figure 1.20: (a) Cluster formation with regard to the Si:Al ratio in CGMC. Reproduced from [107]. (b) Geopolymer gel relaxation using a coarse-grain Monte Carlo approach by White *et al.*. It shows the relaxation of hydroxide activated geopolymer with aluminate sites in yellow and silicate sites in purple. Reproduced from [116].

Multi-scale first trials

As proposed by Lolli et Masoero[117], a new model of defective crystal opened new insights in mesoscale simulations of geopolymers. Based on the fact that experimental studies of geopolymers showed both crystalline and amorphous structures [118, 119], they have decided to define a model as an intermediate state between these two latter, called defective crystal model, corresponding to a "pseudo-crystalline" structure[120]. Relating this structure to material mechanical properties allowed to account for average geopolymer particle sizes ranging from 5 to 50nm, seen as oligomer aggregates. Considering a polydisperse Lennard-Jones potential of interaction, Monte Carlo simulations have been performed for meta-kaolin based-geopolymers, activated with an alkaline aqueous solution[117]. Resulting structures encompass key features of mechanical properties, but underestimate effective forces at the mesoscale (compared from mechanical characterization of the mesostructures and the derivation of the used potential of interactions).

1.6 Conclusion and research questions

Even though geopolymer pastes stand alongside cementitious and clay materials, their formation process remains poorly understood. Still, experimental works brought many insights on their mechanical properties and how they do relate to raw materials constitutions.

On the first hand, aggregation of CSH grains and clay platelets have been deeply investigated from both experiments and simulations. On the other hand, despite their differences in time scales, their formation process shows many analogies with geopolymerization, leading to equivalent mechanical properties.

From a simulation point of view, forces at the origin of cement cohesion have been understood as a competition between electrostatic and Van der Waals interactions, arising from local charge exchange. These advances allowed the definition of mesoscale models based on the determination of both a coarse-graining length and an effective potential of interactions at the atomic scale. Mesostructures were so

obtained and validated according to experimental measurements. While a few attempts of mesoscale modeling have been proposed for geopolymer materials, none accounted for the use of an effective pair potential of interaction directly computed from atomistic simulations. Still, using reactive potentials, the coarse-graining length of geopolymer and oligomers properties have been discussed.

The next step toward a better understanding of the aggregation of oligomers in aluminosilicate gels is to use individual grain characteristics to evaluate the effective pair-potential, driving a path towards mesoscale simulations of geopolymers. This thesis stands there, digging into the nature of cohesion within geopolymer gels and their growth. It aims to better relate atomistic properties to mesoscale structures of these promising materials.

Chapter 2

Methodology

In this chapter, the methodologies that have been used in this work will be presented. First, statistical physics will be introduced. Then, we discuss the methods used to reconstruct the mean force potential from atomistic simulations: the perturbation theory approach and enhanced sampling approaches (metadynamics).

2.1 Statistical physics and molecular simulations

Statistical physics connect microscopic states to and the macroscopic states by giving a description of system with large number of particles. First introduced by Kelvin, Maxwell and Boltzmann with the study of gas kinetics (modeled as random collisions of particles due to Brownian trajectories for the atoms and molecules), the principles of statistical mechanics or also called *equilibrium thermodynamics* were formalized by Gibbs in 1902 [121].

Let us consider a system at the thermodynamic equilibrium. It is commonly accepted to describe it with macroscopical parameters as its density ρ, pressure P, temperature T or volume V. The purpose of statistical physics is to give a correct description of these parameters with regard to microscopic ones, such as the system energy, the chemical potential or the number of particles.

A system can be defined with variables that can be either extensive (system-size dependent such as pressure) or intensive (system-size independent such as volume). As shown in Table 2.1 for instance pressure and volume are conjugated variable. As an example, the macroscopic temperature T of a system is nothing less than a measurement of the microscopic kinetic energy of an ensemble of particles.

Extensive variable	**Intensive conjugated variable**
Internal Energy E	Temperature T
Volume V	Pressure P
Number of particles N	Chemical Potential μ

Table 2.1: List of thermodynamic state variables

2.1.1 Thermodynamic basics

In order to properly understand and manipulate the variables involved in the study of such thermodynamic state we come back to the first principle which stands that the energy E of the system is the sum of absorbed heat Q and the amount of work W done on the system :

$$E = Q + W. \tag{2.1}$$

It is important to note that E is a state function, meaning it does not depend on the chosen path,

while Q and W are not. Therefore, any change in Q or W must be considered along a differential path such that

$$\mathrm{d}E = \delta Q + \delta W \equiv \mathrm{d}Q_{\mathrm{rev}} + \mathrm{d}W_{\mathrm{rev}}. \tag{2.2}$$

While the differential amount of heat exchanged by a system is directly related to the differential entropy by $\delta Q = T\mathrm{d}S$, the differential work done by the system must be decomposed into a mechanical work $\mathrm{d}W^{\mathrm{mech}}$ and a chemical work $\mathrm{d}W^{\mathrm{chem}}$. The first one is subjected to the volume evolution according to $\delta W^{\mathrm{mech}} = -P(V)\mathrm{d}V \equiv P\mathrm{d}V$, where P is the system's pressure. The chemical work is related to the number of particles within the system. If we go from a set of N_1 particles to a state with N_2 particles ($N_2 > N_1$), the chemical work can be quantified as $W^{\mathrm{chem}} = \sum_{N_i=N_1}^{N_2} \mu(N_i)$, $\mu(N_i)$ being the chemical potential of the system comporting N_i particles. Thus, the differential chemical work is given by $\delta W^{\mathrm{chem}} = \mu(N)\mathrm{d}N \equiv \mu\mathrm{d}N$.

Finally, we obtain the relation between thermodynamic variables as

$$\mathrm{d}E = T\mathrm{d}S - P\mathrm{d}V - \mu\mathrm{d}N, \tag{2.3}$$

and so the differential entropy is

$$\mathrm{d}S = \frac{\mu}{T}\mathrm{d}N + \frac{P}{T}\mathrm{d}V + \frac{1}{T}\mathrm{d}E. \tag{2.4}$$

On the other hand,

$$S \equiv S(N,V,E) \Longrightarrow \mathrm{d}S = \left(\frac{S}{N}\right)_{V,E}\mathrm{d}N + \left(\frac{S}{V}\right)_{N,E}\mathrm{d}V + \left(\frac{S}{E}\right)_{N,V}\mathrm{d}E. \tag{2.5}$$

From identification we recover expressions for the thermodynamic variables T, P and μ as

$$\frac{1}{T} = \left(\frac{\partial S}{\partial E}\right)_{N,V} \quad ; \quad \frac{P}{T} = \left(\frac{\partial S}{\partial V}\right)_{N,E} \quad ; \quad \frac{\mu}{T} = \left(\frac{\partial S}{\partial N}\right)_{V,E}. \tag{2.6}$$

Since the energy can be expressed as a function of the system energy $E \equiv E(N,V,S)$, these can also be rewritten as

$$T = \left(\frac{\partial E}{\partial S}\right)_{N,V} \quad ; \quad P = -\left(\frac{\partial E}{\partial V}\right)_{N,S} \quad ; \quad \mu = \left(\frac{\partial E}{\partial N}\right)_{V,S}. \tag{2.7}$$

Equations 2.7 show relations between macroscopic observables and the energy of the microstates.

Thermodynamic ensemble

One macroscopic state may not be only defined by a single microscopic state. In fact, the fundamental postulate of statistical physics known as the *a priori* equiprobability postulate stands that :

Given an isolated system in equilibrium, the system has the same probability of being in any of the accessible microstates.

Thus, by denoting Ω the number of accessible microstates of a system, the probability for a system to be in a given microstate is $p = 1/\Omega$ and so, is uniform.

The ensemble of microstates is the thermodynamics ensemble and is defined by its variables. For instance, in the microcanonical ensemble, microstates are defined at a given number of particles N

inside a given volume V and at an energy E. Thus, the microcanonical ensemble is often referred as the (N, V, E) ensemble.

The function $\Omega \equiv \Omega(N, V, E)$ quantify the part of the phase space accessible by the system. It can be obtained from an integration over $6N-1$-dimensional constant-energy hyper-surface (defined from positions and momenta). Moreover, we recall that we work in the classical mechanics and so in a Hamiltonian framework. The Hamiltonian, $\mathcal{H}$, is therefore conserved over the phase space (see [122], chapter 1 and Eq. 1.6.15 for details).

By denoting $\mathrm{x} = (\mathbf{r}, \mathbf{p})$ a vector of such a phase space, we have

$$\mathcal{H}(\mathrm{x}) = E, \tag{2.8}$$

and the number of accessible state by the system reads as

$$\Omega(N, V, E) = \frac{1}{h^{3N} N!} \int \mathrm{dx} \delta(\mathcal{H}(\mathrm{x}) - E), \tag{2.9}$$

where h is the Plank constant.

Gibbs' entropy

While the macroscopic state of a system can be well defined by three parameters: e.g. P, T and V, microscopic states with N particles requires $6N$ parameters (x, y, z the position and v_x, v_y, v_z the velocity, for each particle). As a consequence, a lot of information is lost when moving from the microscopic to the macroscopic state. Even though considering very large system allow to consider such transitions, information remains lost and can be quantified by a quantity called entropy and denoted S.

In the framework of statistical physics, Gibbs defined the entropy as

$$S(P_i) = -k_B \sum_i^M P_i \ln(P_i), \tag{2.10}$$

where M is the number of accessible microstates with probability P_i. Note that if the probability is uniformly equal to $P_i \equiv P = 1/\Omega$ we recover $S = +k_B \ln(\Omega)$, which is the Boltzmann's entropy formula.

Ergodicity

Up till now, we have only discussed the microscopic states in a purely static sense : every state can be occupied with the same probability and the actual state can be seen as an *ensemble* average over all these states, i.e over the *phase space*.

The ergodicity principle states that time and ensemble averages are equivalent, i.e :

$$\lim_{N \to +\infty} \frac{1}{N} \sum_{k=1}^{N} F_k = \lim_{\tau \to +\infty} \frac{1}{\tau} \int_{t_0}^{t_0+\tau} F(t) \mathrm{d}t, \tag{2.11}$$

i.e

$$\langle F \rangle = \overline{F}. \tag{2.12}$$

A way to properly understand it is to see that with a sufficiently long time, a system at equilibrium will occupy most of the configurations that would correspond to the N duplicates one can consider. This is one of the key principles of Molecular Dynamics.

2.1.2 Other statistical ensembles

As already mentioned, a macroscopic state is defined by three parameters. Fixing such macroscopic parameters allows to define statistical ensembles (of microstates) that will be presented below. Each of these ensemble has its own definition of *partition function* (distribution of probability), entropy and so, relations between the macro and microscopic variables.

The canonical ensemble (NVT)

Now considering a system inside a thermostat T, i.e a macroscopic state at the temperature T, it is possible to define a *(canonical) partition function* Q for the ensemble (N, V, T), called the *canonical ensemble*.

Partition function $Q \equiv Q(N, V, T)$

By denoting i a possible microstate, we get the two key equations of the statistical mechanics, quantifying the probability for the state i to occur as P_i :

$$Q = \sum_i \exp\left(-\frac{E_i}{k_B T}\right) \quad ; \quad P_i \equiv \frac{\exp\left(-\frac{E_i}{k_B T}\right)}{Q}, \tag{2.13}$$

where E_i is the energy of microstate state i, k_B is the Boltzmann constant and T is the system temperature (which is fixed along the volume V and the number of particles N).

With regard to this density probability function $P_i(E_i)$, the canonical partition function $Q(N, V, T)$ can be related to the micro-canonical partition function $\Omega(N, V, E)$. In fact, in the canonical ensemble, the Hamiltonian is not conserved and so the energy changes according to a Boltzmann distribution (with mean E_0), allowing the system to access a new number of accessible microscopic states. Therefore, the canonical partition function is related to its micro-canonical counterpart as

$$Q(N, V, T) = \frac{1}{E_0}\int_0^\infty \mathrm{d}E \exp(-\beta E) M \int \mathrm{dx}\delta(\mathcal{H}(\mathrm{x}) - E) = \frac{1}{E_0}\int_0^\infty \mathrm{d}E \exp(-\beta E)\Omega(N, V, E). \tag{2.14}$$

Mean energy E and internal energy U

Many thermodynamics quantities can now be defined, starting with the system's mean energy reading as

$$E \equiv \langle E \rangle \equiv \sum_i E_i P_i = \sum_i E_i \frac{1}{Q} \exp\left(-\beta E_i\right) = -\frac{\partial \ln Q}{\partial \beta}, \tag{2.15}$$

where $\beta = 1/k_B T$ the inverse temperature (in inverse energy units). Note that in the thermodynamic limit, $E \equiv U$ is the *internal energy* of the system.

Entropy S and Helmholtz free energy A

Now using the definition of the entropy in Eq. 2.10 and Eq. 2.13, one gets $S \equiv S(N, V, T)$ for the canonical ensemble :

$$-\frac{S(N, V, T)}{k} = -\beta E - \ln Q \Longleftrightarrow S = \frac{E}{T} + \ln Q. \tag{2.16}$$

Recalling the definition of the Helmholtz free energy $A \equiv A(N,V,T) = E - ST$ (Legendre transform method to change the energy from a function of (N,V,S) to a function of (N,V,T)[122]), it relates to the partition function according to Eq. 2.35

$$A = -kT \ln Q = -\frac{1}{\beta} \ln Q. \tag{2.17}$$

One may recall that the free energy variation quantifies the amount of work a thermodynamic system can perform at constant T. A '+' sign refers to a favorable thermodynamic process while '−' refers to an unfavorable one.

The isothermal-isobaric ensemble (NPT)

Characterizing the system with the number of particles N, the pressure P and the temperature T defines the (N,P,T) ensemble, called the isothermal-isobaric ensemble. In this ensemble, the energy is defined and identified as the enthalpy $H = E' = E + PV$.

The partition function of this ensemble is given as the following integral over the volume similarly as the canonical partition function was over energy :

$$\Delta \equiv \Delta(N,P,T) = \frac{1}{V_0} \int_0^\infty Q(N,V,T) \exp(-\beta PV) \mathrm{d}V. \tag{2.18}$$

The grand canonical ensemble (μVT)

The *Grand Canonical* ensemble can be used to exchange particles with a fictitious reservoir with a chemical potential μ. It corresponds to the states for which the chemical potential μ, the volume V and the temperature T are fixed.

According to the first principle of thermodynamics, the energy E and the Helmholtz free energy A are given as

$$E = TS - PV + \mu N \quad ; \quad A \equiv E - TS = -PV + \mu N. \tag{2.19}$$

The *grand partition function* $\Xi \equiv \Xi(\mu,V,T)$ is therefore given by

$$\Xi = \sum_i \exp(-(E_i - \mu N_i)/k_B T) = \sum_{N=0}^{+\infty} \exp(\beta \mu N) Q(N,V,T), \tag{2.20}$$

where the sum is made over the microstates i composed of N_i particles, with energy E_i. $Q(N,V,T)$ is the canonical partition function.

By defining the Landau free energy (according to a Legendre transform) or here called the *grand potential* : $\Omega \equiv A(\mu,V,T) - N(\mu)\mu$, we recover the relation $\Omega = -k_B T \ln \Xi$ and similarly as for the previous ensembles, it allows to relate thermodynamic properties to microscopic properties. Note that we have $\Omega = -PV$ and so $PV = k_B T \ln \Xi$.

The Nosé-Hoover thermostat

All the previously discussed ensembles involve constant temperature T. However, for a system of N particles, temperature relates to the kinetic energy of the system (quantified from particles' velocities) according to:

$$\langle E_{\mathrm{kin}} \rangle = \frac{3}{2} N k_B T. \tag{2.21}$$

A *thermostat* is an algorithm that controls of the temperature of the system by introducing energy fluctuations. This can be done by coupling to system to an external heat bath. To do so, Andersen proposed a model based on stochastic collisions of particles)[123]. Another approach, taken by Nosé *et al.* is to introduce energy fluctuations as an additional term in the Hamiltonian of the system[124]. With the introduction of a virtual variable s accounting for the influence of the external system, on a system of N particles with masses m_i and momenta $\mathbf{p}_i$, the Nosé-Hoover Hamiltonian writes as:

$$H_{\text{Nosé}-\text{Hoover}} = \sum_{i=1}^{N} \frac{\mathbf{p}_i}{2m_i s^2} + \phi(\mathbf{q}) + \frac{p_s^2}{2Q} + gk_BT\ln(s), \tag{2.22}$$

where Q corresponds to an effective mass associated to the variable s and $\mathbf{p}_s$ its momentum. With this definition, equations of motion are slightly modified and so the system can account for associated energy fluctuations, controlling the temperature, i.e. acting as the thermostat.

2.1.3 Molecular simulations

As seen in §3, the thermodynamic properties of a system can be expressed as an average as an integral over the ensemble of accessible microstates, also called phase space. To calculate the macroscopic observables, it is necessary to know the microstates that can be reached by the system within a given thermodynamic ensemble. Simulations can be used to sample the ensemble of microstates of a system. Molecular dynamics (MD) and Monte Carlo (MC) approaches are efficient tools for sampling the microstates that have been widely used. While a Monte Carlo method will skim the phase space according to probabilistic algorithm, Molecular Dynamics is time-dependent and is based on Newton's laws. According to the ergodicity principle, both method are equivalent and can be coupled in order to study a great variety of systems.

Monte Carlo (MC)

In the Monte Carlo simulations, at each step of the simulation, a MC move is attempted. The acceptance of the refusal of the attempts are based on a probability of acceptance that depends on the energy of the system before the move and after the move.

Metropolis algorithm

The Metropolis algorithm can be used to determine the acceptance of the refusal of a MC move, within the framework of a Markov chain.

First, we denote π_{ij} the transition probability to move from a state i to a state j, while the probability to be in state i is denoted ρ_i. The Markov Chain corresponds to a sequence of independent states. Therefore, π_{ij} is the probability that if the n^{th} state of the chain is in state i, the state $n+1$ is in the state j. For our Markov Chain to be consistent, a few conditions must be satisfied :

- The transition matrix is stochastic : starting from a state i of the chain leads to a state in the chain : $\sum_j \pi_{ij} = 1$;
- Ergodicity : all accessible states are at equilibrium : $\sum_i \rho_i \pi_{ij} = \sum_j \rho_j \pi_{ji}$;
- Micro-reversibility : $\rho_i \pi_{ij} = \rho_j \pi_{ji}$.

Now, the transition probability is decomposed into two probabilities : $\pi_{ij} = \alpha_{ij} P_{ij}$, where α_{ij} is the probability to try the state change from i to j (and is symmetric) and P_{ij} is the probability to accept the trial. Such an approach allows to define a distribution of probability P_{ij} independent of the partition function. In fact, from the micro-reversibility condition :

$$\rho_i P_{ij} = \rho_j P_{ji} \Rightarrow \frac{P_{ij}}{P_{ji}} = \frac{\rho_j}{\rho_i} = \exp\left[-\beta(U_j - U_i)\right]. \tag{2.23}$$

There exist many possibilities to chose such distribution. Metropolis *et al.* chose the following :

$$P_{ij} = \begin{cases} \frac{\rho_j}{\rho_i} & \text{if} \quad \rho_j < \rho_i \\ 1 & \text{if} \quad \rho_j \geq \rho_i \end{cases} . \tag{2.24}$$

Thus, the transition matrix elements are

$$\begin{aligned} \pi_{ij} &= \begin{cases} \alpha_{ij}\frac{\rho_j}{\rho_i} & \text{if} \quad \rho_j < \rho_i \\ \alpha_{ij} & \text{if} \quad \rho_j \geq \rho_i \end{cases} . \\ \pi_{ii} &= 1 - \sum_{j \neq i} \pi_{ij} \end{aligned} \tag{2.25}$$

Monte Carlo simulation covers the phase space by moving from one state to another with regard to the energy difference between the states. As a consequence, the larger the energy difference is, the lowest the probability to visit the state is.

Molecular Dynamics (MD)

In Molecular Dynamics, equilibrated states are visited following the evolution of time and the mechanical laws of motion.

$$\mathbf{F}_i = m_i \mathbf{a}_i \equiv m_i \frac{\mathrm{d}^2 \mathbf{r}_i}{\mathrm{d}t^2}, \tag{2.26}$$

where m_i correspond to the mass of the atom i, $\mathbf{F}_i$ the force exercing on the atom i and $\mathbf{a}$ its proper acceleration.

For a given configuration of N atoms with coordinates $\mathbf{r} = \{\mathbf{r}_1, ...\mathbf{r}_N\}$, the energy E is quantified with regard to the motion of atoms *via* its kinetic energy K and with regard to their positions *via* its potential energy $V = V(\mathbf{r}_1, \mathbf{r}_2, ..., \mathbf{r}_N))$, also called *Potential Energy Surface* (PES). Thus, the atomic forces are defined according to

$$\mathbf{F}_i = -\nabla_{\mathbf{r}_i} V(\mathbf{r}_1, \mathbf{r}_2, ..., \mathbf{r}_N). \tag{2.27}$$

Interatomic interactions

For MC and MD algorithms, the interparticles forces have to be calculated. Within an atomic system, particles interact *via* intermolecular forces (Coulombic interaction, Van der Walls forces, covalent bonds, etc.). For atomistic systems, there are two ways of computing the forces: either using quantum approaches which are based on the calculation of the electronic density or using classical force fields.

For classical force fields, the PES is often computed from pairwise potentials $\phi(r_{ij})$ and requires the definition of a cut-off radius r_c above which interactions are null (i.e. particles are so far that their interactions can be neglected).

$$V(\mathbf{r}) = \sum_i \sum_{j>i} \phi(|\mathbf{r}_i - \mathbf{r}_j|) \equiv \sum_i \sum_{j>i} \phi(r_{ij}). \tag{2.28}$$

The Lennard-Jones Potential

One of the most basic pairwise potentials is the Lennard-Jones (LJ) potential, as plotted in Fig. 2.1 (a), which has an attractive contribution and a repulsive one. For instance, the attractive contribution can reproduce the Van der Waals forces while the repulsive contribution corresponds to the Pauli repulsion in an atomic system.

It is defined by ε, the potential depth, and σ the potential zero-point:

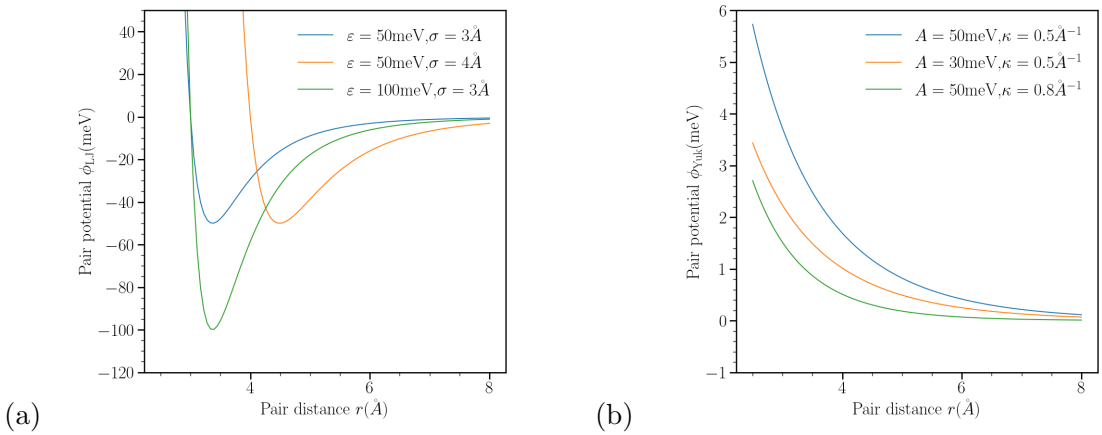

Figure 2.1: (a) Lennard-Jones and (b) Yukawa pair-potentials for different sets of parameters

$$\phi_{\mathrm{LJ}}(r) = 4\varepsilon \left[\left(\frac{\sigma}{r}\right)^{12} - \left(\frac{\sigma}{r}\right)^{6} \right]. \tag{2.29}$$

This potential is said to be *attractive* since it presents a well which is characterized by it depth ε and its zero distance σ.

The Yukawa Potential

Another example of pairwise potential, is the Yukawa potential, which is a purely repulsive potential given as:

$$\phi_{\mathrm{Yukawa}} = A\frac{e^{-\kappa r}}{r}, \tag{2.30}$$

where A is the amplitude and κ quantifies the range of interactions. Fig. 2.1 (b) illustrates its behavior with regard to the inter-atomic distance r.

Periodic boundary conditions

In order to account for larger system, periodic boundary conditions are often used in molecular simulations. These mimic a replication of the simulation box in chosen space directions (x,y and z). It has the strength to allow calculations to be performed with a smaller number of atoms.

Fig. 2.2 shows the replication of a cubic simulation box and the application of the Minimal Image Convention (MIC).

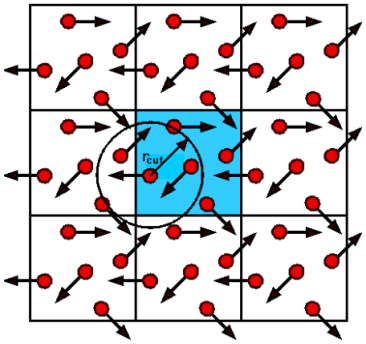

Figure 2.2: Periodic boundary conditions applied in two dimensions to a cubic simulation box containing spherical particles, filled in blue. Red dots shows the particles and the arrows the forces applied on them. The cut-off sphere of interactions is shown for an atom, illustrating the MIC. Reproduced from [125].

MIC stands that for an atom, its interactions are taken within the cut-off spheres of atoms according to box replication and not necessarily with the one its own cell. It ensures that all interactions are taken into account only once within the replicated system but requires the cut-off radius r_c to be taken smaller as half the simulation box size.

2.1.4 Potential of mean force

The Potential of Mean Force corresponds to the mean force of interaction between two atomic clusters. PMF can be computed from the free energy differences, itself computed from Thermodynamics Integration (TI). TI purpose it to compute the difference in a thermodynamic property (usually the free energy) of the system between some reference states and the state of interest. To measure the free energy change from initial to final state, thermodynamic parameters characterizing the system are changed along a continuous path keeping the system in an equilibrium. This ensures that the path is reversible, i.e., the same path can be traversed in the opposite direction.

The evaluation of the potential mean force can be done using a perturbative theory or enhanced sampling methods, such as nudge elastic band, umbrella sampling or metadynamics. Herein, we will present the perturbation theory approach as well as the metadynamics approach, account for a more direct potential energy calculations.

2.1.5 Theory of the perturbative approach

This perturbative method [126, 34, 62] is based on the thermodynamics integration principles. Along a perturbation coordinate (distance, angle, charge, etc.) λ, a large number of states are created. For each state, a trajectory is simulated to obtain a sample of configurations that are used to compute the free energy of a system by perturbing it around its equilibrium.

The free energy difference ΔA between two states i (unperturbed) and j (perturbed) can be quantified by

$$\Delta A(i \to j) = A_j - A_i = -k_B T \ln \left\langle \exp\left(-\frac{U_j - U_i}{k_B T}\right) \right\rangle_i , \tag{2.31}$$

where U is the state energy and the triangular brackets denotes the average over a simulation run for the state i.

Configuration space and importance sampling

This *perturbative* approach must remain, by definition, in a perturbative framework which must be properly defined. Considering a given state i, there exist a multitude of microstates that can cor-

responds to this state, also called *configurations*. The ensemble of such microstates can be called *configuration space* or *phase space*. When performing perturbative calculations between two states, we expect both states not to be too different from each other and so, they share the same configuration space Γ. It is commonly accepted in molecular simulations that states can be characterized by their respective energy. Let us then consider a state i. The perturbation will then generate two states, corresponding to a state i, L and a state i, H, respectively with a lower and a higher energy. Over a finite simulation run, both state will cover a set of micro-states belonging to the whole phase space Γ, that we can denote $\Gamma_{i,L}$ and $\Gamma_{i,H}$ for low and high energy states. These are called *important configurations* since they constitute direct transcriptions of all micro-state possibilities for initial and perturbed states.

In the perturbative approach, one expects these important configuration spaces to overlap so that the energy differences between two states is not too large (while differences are still required, otherwise it means that the perturbation was not sufficient to differentiate both states). In fact, the better the overlap is, the more accurate FEP calculations will be [127].On the counterpart, computational costs will be increased because of lowering the perturbation. An example of important configurations over a phase space is given in Fig. 2.3

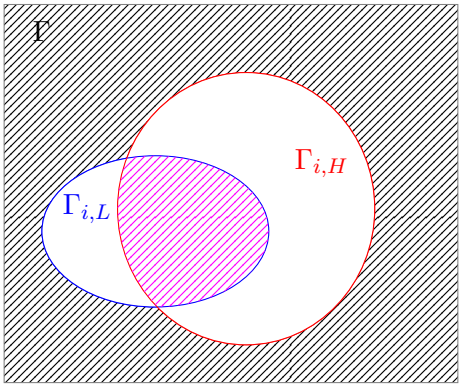

Figure 2.3: Schematic diagram of important configurations for a state i that is perturbed to run FEP calculations. $\Gamma_{i,L}$ in blue and $\Gamma_{i,H}$ in red correspond to the important configurations respectively to the low and high energy states while Γ denotes the whole configuration space. The intersection between both important configurations is represented with the magenta dashed lines.

A way to quantify the overlap between the important spaces is to study the distribution of energy for these states, since each of the micro-state can be characterized by its energy (or especially, by its entropy).

Let us now consider a given state i. In the following, the subscript i will be abandoned for clarity. There exist two states, of lower and high entropy/energy : by denoting the entropy difference $\Delta S \equiv S_L - S_H$, and by definition $\Delta S \leq 0$. Then, recalling Eq. 2.31 the free energy difference $\Delta A \equiv A_L - A_H$ is given according to :

$$\exp\left(-\beta \Delta A\right) = \exp\left(-\beta \Delta U\right) \equiv \exp\left(-\beta (U_L - U_H)\right), \tag{2.32}$$

where $\beta = \frac{1}{k_B T}$.

Assuming that the free energies differences from low to high energy states are distributed with regard to two distribution functions f and g such that

$$\begin{cases} \exp\left(-\beta \Delta A\right) = \int \mathrm{d}u \exp\left(-\beta u\right) f(u) \\ \exp\left(+\beta \Delta A\right) = \int \mathrm{d}u \exp\left(+\beta u\right) g(u) \end{cases}, \tag{2.33}$$

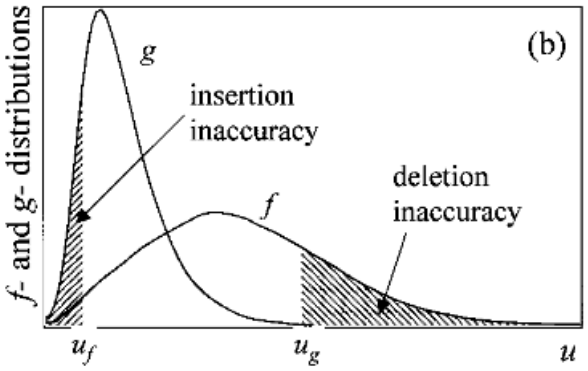

Figure 2.4: Examples of f and g distribution functions of the energy differences- between two states of lower and higher mean energy. Reproduced from [127].

u corresponding the energy difference between the two states, the integral being evaluated from $-\infty$ to $+\infty$. The accuracy of PMF calculations can be quantified according to the overlap of the f and g distributions. In fact, the tails of these ones will correspond to low and high energies of each of the lower and higher energy states as shown in Fig. 2.4. The more likely are the states, the more overlap the Gaussian will have. This indicates how much one works within the framework of a perturbative approach.

During a simulation, which runs for a finite time, not all the distributions are sampled and this is especially true for the Gaussian tails, generating inaccuracies (as non-visited states) in the calculations.

Overlap Sampling (OS) methods

As discussed above, the accuracy of PMF calculations depends on the overlapping of energy distributions between initial and the perturbed states, which requires long equilibria for each distributions to be well sampled. There are methods to improve the efficiency of these calculations [128]. In this former paper, Lu et Kofke have extended their study of the insertion/deletion FEP calculations by implementing different *Overlap Sampling* methods.

Let us consider two states, i and j with their respective Hamiltonian H_i and H_j. The key of OS methods is to consider an imaginary state M in between i and j. The Hamiltonian of state M can be reasonably taken as

$$H_M = -k_B T \ln w(\Delta H) + \frac{(H_i + H_j)}{2}, \ \Delta H = H_j - H_i, \tag{2.34}$$

w being a weight function that gives flexibility on the choice of M. Note that in the NVT ensemble, the free energy is related to the partition function Q as in Eq. 2.35 :

$$A = -kT \ln Q = -\frac{1}{\beta} \ln Q. \tag{2.35}$$

As the canonical partition functions Q is related to the Hamiltonian and especially to the free energy from Eq. 2.35, one can write

$$\exp(-\beta \Delta A) \equiv \frac{Q_j}{Q_i} = \frac{Q_M}{Q_i} \frac{Q_j}{Q_M}. \tag{2.36}$$

Since the partition function is defined with regard to the Hamiltonian, one obtains, by denoting $u = U_j - U_i$:

$$\exp\left(-\beta\Delta A\right) = \frac{\langle w(u)\exp\left(-\beta u/2\right)\rangle_i}{\langle w(u)\exp\left(+\beta u/2\right)\rangle_j}. \tag{2.37}$$

This equation differs from the one obtained by Direct Averaging (DA) discussed earlier. In fact, using the DA method, from Eq. 2.31 with the same notations :

$$\exp\left(-\beta\Delta A\right) = \langle\exp\left(-\beta u\right)\rangle_i. \tag{2.38}$$

The main difference is that the OS approach requires to average the energy differences over two different states. In the case of Eq. 2.38, only state i rules the calculations. U_j is obtained from perturbation applied to a system in state i in one energetic direction. However, it is known that energy distribution obtained from perturbation in one direction (e.g. from i to j) can widely differ from the one obtained in the other direction [129]. This generate a statistical bias that the OS method expect to palliate by taking both directions (called *forward* and *backward*) into account.

An important thing is to notice that Eq. 2.37 does not require any equilibrium of the intermediate state M but only involves its weighting function of the Hamiltonian w. Since w can be chosen arbitrarily, one might here identify different cases, corresponding to notable choices of w.

Simple Overlap Sampling : $w(u) = 1$ **for all** u

This corresponds to the simplest possible choice for the weight function. The free energy difference is directly obtained from

$$\exp\left(-\beta\Delta A\right) = \frac{\langle\exp\left(-\beta u/2\right)\rangle_i}{\langle\exp\left(+\beta u/2\right)\rangle_j}. \tag{2.39}$$

In fact, it corresponds to a choice of M at "equal distance" of states i and j as depicted in Fig. 2.5.

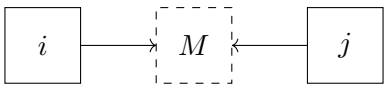

Figure 2.5: Illustration of the Simple Overlap Sampling case between two states i and j.

In terms of energies, this can be written as below

$$u \equiv U_j - U_i = (U_j - U_M) - (U_i - U_M) = \left\langle\frac{U_j - U_i}{2}\right\rangle_j + \left\langle\frac{U_j - U_i}{2}\right\rangle_i, \tag{2.40}$$

where the brackets denote the average over i and j states. These two averages correspond to perturbation performed forward and backward, differing from the DA case for which the energy difference u is taken as $u = \langle U_j - U_i\rangle_i$.

Application of the Simple Overlap Sampling (SOS)

Let us consider, between an initial and a final states 0 and 1, intermediate ones $i-1, i$ and $i+1$. The system is then perturbed to each states in the forward and backward directions, as pictured in Fig. 2.6.

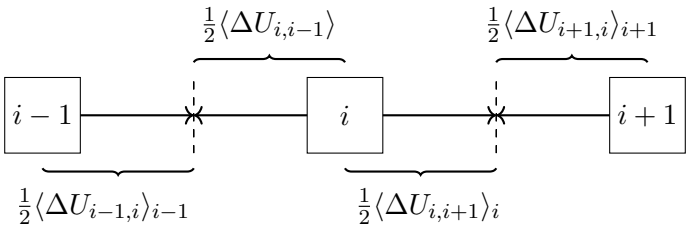

Figure 2.6: Scheme of the intermediate perturbed states in the SOS method. Three successive states are shown : $i-1$,i and $i+1$. Intermediate states as the perturbed ones are shown in dashed lines and energy differences associated to each perturbation shown.

With such sampling, Eq. 3.10 rewrites as :

$$\Delta A(i \to i+1) = A_{i+1} - A_i = -k_B T \ln \left[\frac{\langle \exp(-\Delta U_{i,i+1}/2k_B T)\rangle_i}{\langle \exp(-\Delta U_{i+1,i}/2k_B T)\rangle_{i+1}} \right], \tag{2.41}$$

and, assuming free energy additivity within the perturbative framework, the full free energy difference between states 0 and 1 writes as the sum of intermediate states free energy :

$$\Delta A(0 \to 1) = A_1 - A_0 = \sum_i \Delta A(i \to i+1). \tag{2.42}$$

2.1.6 Uncertainties calculations

Calculations involving free energies are subject to uncertainties that can be estimated using different statistical methods as proposed by Lu *et al.* [128]. Both jackknife and the bootstrap methods have been performed in the framework of this study in order to compare their relevance and efficiencies.

Jackknife bias estimation

Developed between 1949 and 1956 [130], the jackknife resampling method constitutes a strong tool to evaluate standard deviation and variance of estimators. Let us consider an estimator G, computed from a set of N sets of values : $G = f_N(x_1, ..., ...x_N)$, f_N being a functional that computes the estimator based on a set of N sets of observations. In our study, this corresponds to the calculations of the free energy variations $\Delta G(i \to i+1)$ as a function of $N = 500$ configurations for states i and $i+1$.

It is possible to compute $G = f_{N-1}(x_1, ..., ...x_{N-1})$, by removing one observation, i.e. to compute the energy difference using "only" $N = 499$ configurations. This way, one can get 500 values $G_{(i)} = f_{N-1}(\{x_{k\in[1,N],k\neq i}\})$ and compute a jackknife average :

$$G_{\text{jack}} = \frac{1}{N} \sum_{i\in[1,N]} G_{(i)}. \tag{2.43}$$

Finally, the standard deviation of G, taken over the total set of observables (configurations) is given by :

$$\sigma_{\text{jackknife}} = \left(\frac{n-1}{n} \sum_{i=1}^{n} (G_{(i)} - G_{\text{jackknife}})^2 \right)^{\frac{1}{2}}. \tag{2.44}$$

Bootstrap bias estimation

Inspired by the jackknife approach and published in 1979 by Efron [131, 132], the bootstrap technique relies on a probabilistic approach of standard deviation calculations. For an estimator G, the real values are not known but still, its standard deviation can be computed based on a probability distribution of its actual values. Therefore, by computing many values of the estimators based on many different sets of observations, it is possible to evaluate the distribution of this estimator.

For a given set of N observations, it is possible to build B sets, each composed of K observations, with $K < N$. The bootstrapping being a probabilistic method, the K observations are taken randomly among the total N of configurations. The estimator $G_b = f_K(x_1^b, ..., x_K^b)$, can be obtained for a given set b among the B so-generated.

In our case, we can, e.g., build $B = 200$ sets of $K = 100$ configurations for each states i and $i + 1$. Thus, we are able to compute 200 values of $\Delta G_b(i \to i + 1)$. Similarly as for the jackknife method, a bootstrap average of the estimator G is given as :

$$G_{\text{bootstrap}} = \frac{1}{B} \sum_{b=1}^{B} G_b, \tag{2.45}$$

and the associated standard deviation for the bootstrap method is :

$$\sigma_{\text{bootstrap}} = \left(\frac{1}{B-1} \sum_{b=1}^{B} (G_b - G_{\text{bootstrap}})^2 \right)^{\frac{1}{2}}. \tag{2.46}$$

2.2 Metadynamics and the Well-Tempered approach

The potential of mean force can also be constructed using metadynamics, which is an enhanced sampling method introduced by Laio and Parrinello in 2002 [133]. Metadynamics is using an adaptative bias potential in order to reduce the probability of the system to visit twice the same configuration. Within this framework, configurations are characterized by the so-called collective variables (CV).

Using metadynamics in molecular simulations allow PMF calculations based on an energy bias that is added during the run instead of using a thermodynamics integration approach. It has been shown that metadynamics and umbrella sampling (which is a thermodynamics integration approach [134]) give the same result, metadynamics being more efficient and having lower uncertainties [135]. Umbrella sampling is a method also commonly used to perform PMF calculations but is not at stake in this thesis.

2.2.1 Theoretical concept

Metadynamics is a molecular dynamics with an adaptative biased external potential. If V is the potential of the system, then the adaptative potential V' is

$$V' = V + V_{\text{bias}}, \tag{2.47}$$

where $V_{\text{bias}} \equiv V_{\text{bias}}(\overrightarrow{s})$ is the potential bias, a function of CV $\overrightarrow{s} \equiv \overrightarrow{s}(\{\overrightarrow{r_i}\}_i)$, themselves functions of all the positions of the system components. The key purpose of this bias is to change the potential energy of a system so that it is encourage visiting states it has not seen yet. In fact, during a simulation run, the system will spend more time in regions of the Potential Energy Landscape (PEL) within potential wells. Metadynamics allows to fill these gaps so that the system will have higher probability to visit other states and so on, encouraging it to explore more regions than without bias. Fig. 2.7 shows how can the free energy be estimated using a single collective variable x.

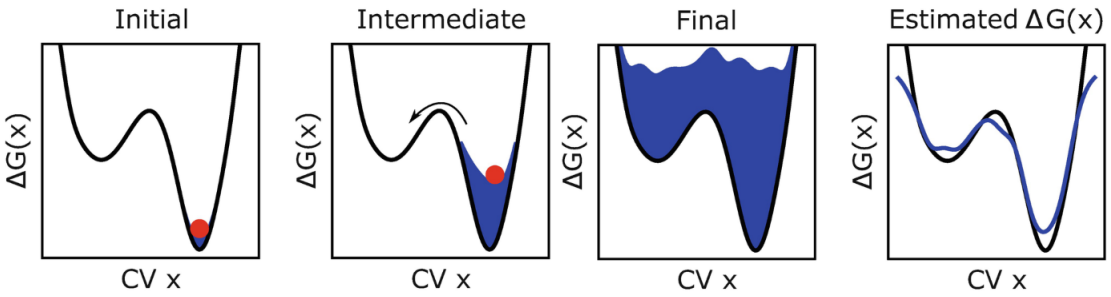

Figure 2.7: Illustration from the metadynamics approach. The black line corresponds to the actual free energy of a system as a function of a collective variable (CV) x. The red dot shows the corresponding state at initial, intermediate an final stages of the metadynamics run. The blue area illustrates the "filling" of the potential wells *via* the summation of biases. Last panel shows that the free energy can be estimated from so-added biases. Figure from [136].

The bias is a function of time and is updated according to a rate γ, under a distribution function δ with regard to the instantaneous CV $\overrightarrow{s_t}$ at time t such as

$$\frac{\partial V_{\text{bias}}(\overrightarrow{s})}{\partial t} = \gamma\delta(|\overrightarrow{s} - \overrightarrow{s_t}|) \Longrightarrow V_{\text{bias}}(\overrightarrow{s}) = \int_0^t \gamma\delta(|\overrightarrow{s} - \overrightarrow{s_t}|)\mathrm{d}t \equiv \gamma N(s,t). \tag{2.48}$$

For a run sufficiently long, the system is expected to reach its minimum "effective" potential of mean force A as most of the local potential minima have been filled by repulsive "hills" (biases). This means that the effective potential obtained at the final stages of the simulation is an estimator of the free energy A. Thus, the free energy of the system in a state with the CV $\overrightarrow{s}$ can be recovered, modulo a constant C, from

$$A(\overrightarrow{s}) = -\lim_{t\to+\infty} V_{\text{biais}}(\overrightarrow{s}) + C. \tag{2.49}$$

A common choice (and the one we use in this work) for the distribution δ is a multi-dimensional Gaussian function. This means that the potential energy of the system will be "filled" using Gaussian hills of energy. Note that th

2.2.2 Well-Tempered Meta Dynamics

By construction, metadynamics does not converge since constant bias is continuously being added to the system. An approach developed by Barducci *et al.* and proposed in 2008 [137] allows to change the bias in metadynamics simulations. The principles is that the bias added in a state that has already been visited will be reduced over time.

The bias is adding following:

$$\mathrm{d}V_{\text{bias,WT}}(\overrightarrow{s}) = \Delta T \ln\left(1 + \frac{\gamma V_{\text{bias,WT}}(\overrightarrow{s})}{\Delta T}\right), \tag{2.50}$$

where ΔT stand for the bias in temperature, γ is a chosen energy rate and $\vec{s}$ the set collective variables.

Well-Tempered Metadynamics simulations have a converging V_{bias}, meaning that after all states have been visited no more bias is added and the simulations is terminated. The choice of the bias is important to cover the PEL properly. Especially, in Well-Tempered Metadynamics, a too large bias would lead to a classical metadynamics while a too low will requires far more steps to converge.

2.3 Precipitation simulations

Molecular simulations of precipitation usually employ Grand-Canonical Monte Carlo simulations. It couples particle insertion/deletion in the μVT ensemble with Molecular Dynamics runs in the associated NVT ensemble, N being the number of particles in the simulation box. In a cubic box of size L^*, with periodic boundary conditions, particles are inserted and deleted according to the Metropolis Monte Carlo process, with a probability of

$$P(\text{insertion/deletion}) = \min\left[1, e^{-\beta(\mu_{\text{exc}} - \Delta U)}\right], \tag{2.51}$$

where μ_{exc} denotes the excess chemical potential. This excess chemical potential is defined w.r.t. the true μ and the ideal gas chemical potential μ_{id} as

$$\mu_{\text{exc}} \equiv \mu - \mu_{\text{id}}, \text{ where } \mu_{\text{id}} = k_B T \ln \rho\Lambda^3. \tag{2.52}$$

The ideal term corresponds to the ideal gas contribution to the chemical potential and is a function of ρ, the density of the fictitious ideal gas reservoir, Λ standing for the de Broglie wavelength as defined in 2.54.

Grand Canonical Monte Carlo (GCMC)

In this work, precipitation will be studied through the MC algorithm, applied within the framework of Grand Canonical Monte Carlo (GCMC) simulations. Within the Grand Canonical ensemble μVT, an excess chemical potential μ guides the equilibrium and the number of particles is allowed to fluctuate. Particles can be inserted/deleted to the system according to a MC algorithm with move acceptance probabilities defined as :

$$\begin{cases} acc(N \to N+1) = \frac{V\Lambda^{-3}}{N+1} \exp(\beta\mu) \exp(-\beta(U_{N+1} - U_N)), & \text{insertion} \\ acc(N \to N-1) = \frac{N}{V\Lambda^{-3}} \exp(-\beta\mu) \exp(-\beta(U_{N-1} - U_N)), & \text{deletion} \end{cases}, \tag{2.53}$$

where Λ is the de Broglie wavelength defined as

$$\Lambda = \sqrt{\frac{2\pi\hbar^2}{mk_BT}}, \tag{2.54}$$

m and T being respectively the atomic mass and the temperature. Under such definition of acceptation of either insertion/deletion probability, the probability goes to zero as the energy difference between the two states gets closer to the chemical potential μ.

2.4 Derjaguin-Landau-Verwey-Overbeek (DLVO) theory

The Derjaguin-Landau-Verwey-Overbeek (DLVO), shown independently by pairs Derjaguin and Landau in 1941 [71] and Verwey and Overbeek in 1948 [138], describes the interactions of charged colloidal particles/surfaces in an aqueous medium by quantifying both Van der Waals and Coulomb interactions.

Let us consider two spheres of radius R. Each carries a charge Z and both are immersed in a liquid medium with a dielectric constant ε_r.

Electrostatic interactions

Two charged objects at distance r in solution will generate an electrostatic potential $\psi(r)$ that obeys the Poisson-Boltzmann equation as:

$$\Delta\psi(r) \equiv \nabla^2\psi(r) = -\frac{\rho_e(r)}{\varepsilon_0\varepsilon_r}, \tag{2.55}$$

ε_0 standing for the vacuum permittivity. $\rho_e(r)$ denotes the local electric charge density that writes, for a solution composed of N ions of respective charges q_i and local concentrations $c_i(r)$:

$$\rho_e(r) = \sum_{i=1}^{N} q_i c_i(r) \equiv \sum_{i=1}^{N} q_i c_i^0 \exp\left(\frac{q\psi(r)}{k_B T}\right), \tag{2.56}$$

as the ions distribution is described by the Boltzmann statistics.

For simplicity and to remain within the framework of our study, we will consider only one type of cations in solution (corresponding to sodium is the cases discussed in the manuscript). Therefore, Eq. 2.55 rewrites as

$$\Delta\psi(r) = \frac{-Z}{\varepsilon_0\varepsilon_r} c_0 \exp\left(\frac{-Z\psi(r)}{k_B T}\right). \tag{2.57}$$

Under the Debye-Hückel theory [139], the equation linearizes as the Helmoltz equation,

$$\Delta\psi(r) = \kappa^2\psi(r), \text{ with } \kappa \equiv \sqrt{\frac{Z^2 c_0}{\varepsilon_0\varepsilon_r kBT}}. \tag{2.58}$$

Such an equation has an analytic solution, that, taking into account that the potential is null at infinite distance, writes as a Yukawa (or may also be referred as a *screened-Coulomb*) potential :

$$\psi(r) = A\frac{\exp(-\kappa r)}{r}. \tag{2.59}$$

Continuity of the forces at a distance $r = R$ imposes the constant A and the effective pair potential for our two spheres in the ionic solution is given as

$$\psi(r) = \frac{-Z}{4\pi\varepsilon_0\varepsilon_r}\frac{\exp(\kappa R)}{1+\kappa R}\frac{\exp(-\kappa r)}{r}. \tag{2.60}$$

From Eq. 2.60, the Debye screening length $\lambda_D \equiv 1/\kappa$ can be defined. It corresponds to the distance beyond which the charged objects are screened by the surrounding ions. Note also that this latter stands, in an electrolyte of ionic strength I, composed of N ion types with respective concentrations c_i and charges z_i, as :

$$\lambda_D = \sqrt{\frac{\varepsilon_0\varepsilon_r k_B T}{2NN_a e^2 I}}, \text{ with } I = \frac{1}{2}\sum_i^N c_i z_i^2. \tag{2.61}$$

Usually, for water at room temperature (20°C), the Debye length is related to the ionic strength as $\lambda(\text{nm}) = 0.3/\sqrt{I(\text{M})}$.

Within this medium, the electrostatic interaction between two elementary charges is equal to the thermal energy scale at the Bjerrum length λ_B [140]. Therefore, for two spheres at a distance $r = \lambda_B$:

$$E_p, \text{Coulomb} \equiv \frac{e^2}{4\pi\varepsilon_0\varepsilon_r\lambda_B} = k_B T \Leftrightarrow \equiv \lambda_B = \frac{e^2}{4\pi\varepsilon_0\varepsilon_r k_B T}. \tag{2.62}$$

Integrating the electrostatic potential from Eq. 2.60 over the surface of a sphere at distance r gives the Coulomb effective potential as

$$U_{\text{Coulomb}}(r) = \frac{1}{\beta} Z^2 \lambda_B \left(\frac{e^{\kappa R}}{1+\kappa R} \right)^2 \frac{e^{-\kappa r}}{r}, \tag{2.63}$$

where $\beta = 1/k_B T$.

Van der Walls interactions

Between two small species at distance r in solution, Van der Walls interactions can be calculated assuming an attractive pair-potential of the form $u_{\text{VdW}}(r) = -C/r^6$ [141]. In addition, we assume potential additivity : the interaction of a sphere with a surface is the sum of every sphere's particle interactions with the surface. Within a circular cross section $\mathrm{d}\sigma = 2\pi \mathrm{d}x\mathrm{d}z$ of a sphere of radius R, the number of particles is $\mathrm{d}N = \rho \mathrm{d}\sigma = 2\pi\rho z \mathrm{d}x\mathrm{d}z$. Geometry of the situation is shown in Fig. 2.8.

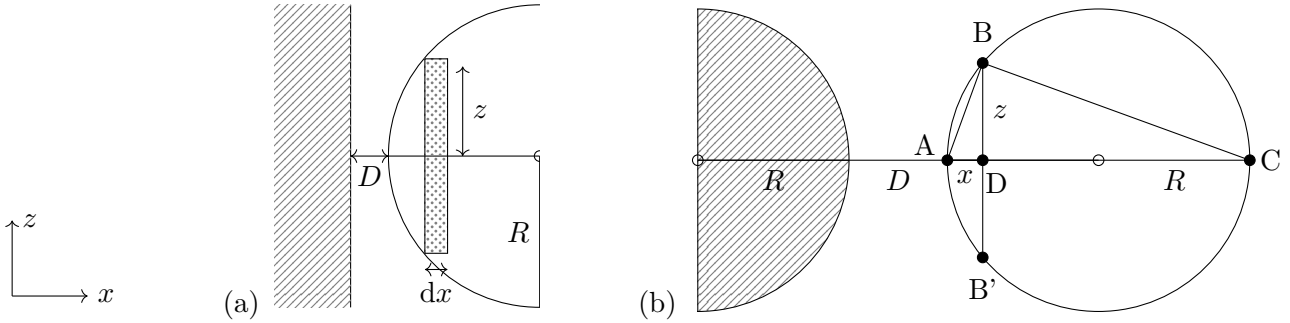

Figure 2.8: Scheme of geometrical considerations for charged (a) sphere-to-surface and (b) sphere-to-sphere Van der Walls interactions.

Thus, for a sphere at a distance D of a surface with infinite length as shown in Fig. 2.8 (a) :

$$u_{\text{VdW}}(D) = \int_N u_{\text{VdW}}(r_N)\mathrm{d}N = -2\pi\rho \int_{x=D}^{+\infty} \mathrm{d}x \int_{z=0}^{z=+\infty} \frac{z}{(\sqrt{x^2+z^2})^6} \mathrm{d}z. \tag{2.64}$$

First, we have

$$\int_{z=0}^{z=+\infty} \frac{z}{(\sqrt{x^2+z^2})^6} \mathrm{d}z = \int_{z=x^2}^{z=+\infty} \frac{1}{2} \frac{\mathrm{d}x^2}{(x^2)^3} = \frac{1}{4}\frac{1}{x^4}, \tag{2.65}$$

and then

$$\int_{x=D}^{+\infty} \frac{1}{x^4} \mathrm{d}x = \frac{1}{3}\frac{1}{D^3}. \tag{2.66}$$

It comes that the interaction between the sphere and the surface is given by :

$$u_{\text{VdW}}(D) = -\frac{\pi\rho C}{6D^3} \tag{2.67}$$

Let us now integrate the pair potential over a whole sphere by seeing the second one as a succession of surfaces of height $D \ll z$, that can be seen as infinite planes. First, we consider a circular section of area as shown in Fig. 2.8 (a) : in the y-plane, the circular cross section is $\mathrm{d}\sigma = \pi z^2 \mathrm{d}x$. From the Chord's theorem, using the notation of Fig 2.8 (b), one can write

$$|\mathrm{BD}| \cdot |\mathrm{DB}'| = |\mathrm{AD}| \cdot |\mathrm{DC}'|, \text{ i.e. } z^2 = x(2R - x). \tag{2.68}$$

Therefore, the cross section becomes $\mathrm{d}\sigma = \pi x(2R - x)\mathrm{d}x$ and contains $\mathrm{d}N = \rho \mathrm{d}\sigma = \rho\pi x(2R - x)\mathrm{d}x$ particles, where ρ is the particle number density within the cross section of thickness $\mathrm{d}x$.

The potential of interaction of a sphere at distance D of the second sphere's surface is the sum of all its components (each at a distance $D + x$ of the opposite surface) interactions. It is therefore given by :

$$U_{\mathrm{VdW}}(D) = \int_N u_{\mathrm{VdW}}(D + x)\mathrm{d}N = -\frac{2\pi^2\rho^2 C}{6} \int_{x=0}^{2R} \frac{x(2R - x)}{\sqrt{D + x}^6}\mathrm{d}x. \tag{2.69}$$

When the spheres are close, $D \ll R$ and only the smaller value of z account in the interactions, i.e these where $z \approx D$. The previous integral can then be evaluated by

$$\int_{x=0}^{2R} \frac{x(2R - x)}{\sqrt{D + x}^6}\mathrm{d}x \approx \int_{x=0}^{+\infty} \frac{2Rx}{\sqrt{D + x}^6}\mathrm{d}x = \int_0^{+\infty} \frac{z - D}{z^3}\mathrm{d}z = \frac{1}{D} - \frac{1}{2D} = \frac{1}{2D}. \tag{2.70}$$

Thus, the interaction between both spheres is :

$$U_{\mathrm{VdW}}(D) = -\frac{\pi^2\rho^2 RC}{6D} \equiv -\frac{A_H R}{6D}, \tag{2.71}$$

where we recall that ρ is the number particle density, R the spheres' radius and D the surface-to-surface distance. A_H is called the Hamaker constant [142]. Especially, A_H allows the calculation of the London Van der Walls parameter C without explicitly accounting for the medium the interaction occurs into.

Full DLVO potential

The DLVO theory couples Coulomb interactions and Van der Waals' one. For two spheres at a surface-to-surface distance r, the potential energy is

$$U_{\mathrm{DLVO}}(r) = U_{\mathrm{Coulomb}}(r) + U_{\mathrm{VdW}}(r) = \frac{1}{\beta} Z^2 \lambda_B \left(\frac{e^{\kappa R}}{1 + \kappa R}\right)^2 \frac{e^{-\kappa r}}{r} - \frac{A_H R}{6r}. \tag{2.72}$$

Chapter 3

Potential of mean force calculation for aluminosilicate grains

This chapter investigates the effective interactions between nano-grains of aluminosilicate species. This is a key step towards coarse-grain models of geopolymers to reach mesoscale (few hundreds of nm) simulations. The effective interactions between two nano-grains can be calculated *via* the Free Energy Perturbation (FEP) method. Based on the computation of free energy differences from Molecular Dynamics, Monte Carlo or Metadynamics simulations. It has been used successfully to evaluate effective interaction of calcium-silicate-hydrates [33] or clays [62].

In the first section of this chapter, the definition of geopolymer nano-grain is discussed as a first step to compute nano-grain interactions and the potential of interaction is described. Then, two grains are set in solution and molecular simulations are performed to sampled configurations required to implement FEP calculations. The results are presented and compared to metadynamics calculations. Finally, their limitations are discussed.

3.1 Initial setup of aluminosilicate nano-grains

The first step of geopolymerization process corresponds to the dissolution of the aluminosilicate solid source with an activation solution. As a consequence, bonds are broken within the solid network to form smaller species that will fuse to form the gel phase as oligomers in solution. This process involves bonds breaking/formation and is highly related to initial concentrations of the raw materials, either in silicates, aluminates and sodium.

3.1.1 Grain structuring

The initial structure for the aluminosilicate skeleton has been generated via MD simulations led by Dupuis et al.[15]. In their work, they used brief Parallel Tempering to reproduce the aggregation of aluminates and silicates into an aluminosilicate cluster at a Si:Al=50:6 ratio. An aluminate ring species formed in a basic solution polymerize with a higher degree silicate cluster. Then, the aluminum diffuses in the silicate structure to form a stable aluminosilicate skeleton composed of 20 Si and 3 Al atoms. It will be taken as a reference grain in this work and is shown in Fig. 3.1. So-generated aluminosilicate cluster has been measured with a gyration radius of 10 Å[15]. Note that remaining Si and Al atoms formed smaller structure in the solution (size estimated around 4 Å[15]). In this work, we have considered only the interaction between the largest grains for simplification but geopolymer precursor solutions are highly polydisperse.

3.1.2 ClayFF potential and adaptations

In the literature, the closest aluminosilicate structures that have been simulated using classical force fields are clays, for which ClayFF has been developed[65, 143]. Therefore, this potential can be chosen

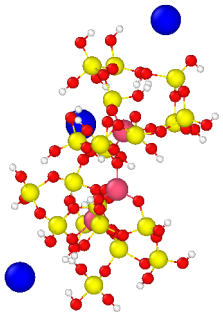

Figure 3.1: Geopolymer grain generated from reactive molecular dynamics [15]. Red, yellow, pink, white and blue spheres respectively represent oxygen, silicon, aluminum, hydrogen and sodium atoms.

and slightly adapted to perform our simulations.

This potential is defined as the sum of a Van der Walls and Coulomb potentials coupled with angles and bonds interactions as shown in Eq. 3.1.

$$E_{tot} = E_{\text{VdW}} + E_{\text{Coul,Wolf}} + E_{\text{bond}} + E_{\text{angle}}. \tag{3.1}$$

In the ClayFF potential, bond and angle energies are included with a harmonic model as given in Eq. 3.2:

$$E_{\text{bond}} = k_r(r_{ij} - R_0)^2 \quad E_{\text{angle}} = k_\theta(\theta_{ij} - \theta_0)^2, \tag{3.2}$$

where k_r and k_θ stand for the elastic constants, R_0 and θ_0 for equilibrium distance and angle respectively.

Parametrization

In ClayFF, the partial charge attributed to each atom has been developed only for entirely protonated species, i.e. SiO4H4, Si2O7H5, etc. However, in geopolymers, AlO4H4 clusters have are partially charged and are compensated by Na^+. This counter cations carries a partial charge of +1 whereas H+ carries a charge of +0.425 in ClayFF. As a result, to ensure electroneutrality, we have modified the partial charge on O atoms first neighbors of Al. Moreover, when the clusters are partially deprotonated, the charge on O- is adapted. The final parametrization of the ClayFF potential is given in Table 3.1

Species	$q(e)$	D_0 (kcal/mol)	R_0 (Å)	M (u)
O	-1.05	0.1554	3.5532	15.999
O(Al)	-1.175	0.1554	3.5532	15.999
Si	+2.1	1.8405e-6	3.7064	28.085
Al	+1.6	1.8405e-6	3.7064	26.9815
Na	+1.0	0.1301	2.6378	22.9898
Of	-1.0	0.1554	3.5532	15.999
Of(Al)	-1.075	0.1554	3.5532	15.999
H≡Hf	+0.425	0	0	1.0
Ow	-0.82	0.1553	3.166	15.999
Hw	+0.41	0	0	1.0

Table 3.1: Parameters of the ClayFF parameters to account for local deprotonation. O, Si, Al, Na and H stands for oxygen, silicon, aluminum, sodium and hydrogen atoms. The f subscript stands for atoms at the edges of the grains and the (Al) notation corresponds to oxygen included into a $Al(OH)_4^-$ tetrahedron.

Note that the parameters are mixed between two species i and j according to Eq. 3.3

$$D_{0,ij} = \sqrt{D_{0,i}D_{0,j}} \quad and \quad R_{0,ij} = \frac{1}{2}(R_{0,i} + R_{0,j}), \tag{3.3}$$

and that the parameters of water atoms corresponds to the Extended Simple Point Charge (SPC/E) model [67, 144, 143].

The SPC/E model describes water molecules as rigid isosceles triangle between H-O-H atoms. Interactions within the molecules are the sum of coulomb and Lennard-Jones interactions with the following parameters :

σ	ε	r_{OH}	θ_{HOH}	q_O	q_H
3.166Å	0.1554	1.0Å	109.47°	-0.82e	+0.41e

3.1.3 Implementation of the potential : the Ewald summation method

For numerical calculations, cut-off pair potentials are usually used. While the Lennard-Jones potential varies as $1/r^6$ and converges quickly to 0 as the atomic distance increase, Coulomb interactions varies as $1/r$ and can be considered as a very long-range potential. In practice, we consider a tail-correction for electrostatic interaction in simulations so that the energy "lost" by the cut-off implementation can be evaluated at a reduced computational cost.

One way to do so is the Ewald summation method, proposed by the physicist of the same name in 1921 [145]. As a purely mathematical approach, it allows to compute the contribution of electrostatic interactions above the cut-off radius by dividing the total electrostatic potential energy into two parts corresponding to the real space and the reciprocal space (from PBCs).

$$E_{\text{Coul}} = E_{\text{Coul},\mathbf{r}} + E_{\text{Coul},\mathbf{k}}. \tag{3.4}$$

In a simulation box of size L, containing N ions with associated charges q_i at positions r_i, by denoting $r_{ij} = |\mathbf{r_i} - \mathbf{r_j}|$ the distance between atoms, the Coulomb potential from a non-periodic system stands as

$$E_{\text{Coul}} \equiv \frac{1}{2}\sum_{i=1}^{N}\sum_{j\neq i=1}^{\infty}\frac{q_i q_j}{r_{ij}}. \tag{3.5}$$

Ewald's proposal is to use periodic image of the simulation cell $\mathbf{n} = (n_x, n_y, n_z)$ to rewrite this latter formula with regard to a convergence parameter α as

$$E_{\text{Coul}}^{\text{Ewald}} = \frac{1}{2}\sum_{i=1}^{N}\sum_{j=1}^{N}\sum_{\mathbf{n}=0}^{\infty}\frac{q_i q_j}{|\mathbf{r_{ij}} + \mathbf{n}L|}[\text{erfc}(\alpha|\mathbf{r_{ij}} + \mathbf{n}L|) + \text{erf}(\alpha|\mathbf{r_{ij}} + \mathbf{n}\text{L}|)]. \tag{3.6}$$

The $\mathbf{n}$ components correspond to the periodic images of each particles in the associated axes, reproducing an artificial periodicity of the interactions.

The error (erf) and the complementary (erfc) error functions correspond to the Gauss error function as

$$\text{erf}(\alpha r) = \frac{2}{\sqrt{2}}\int_0^{\alpha r}\exp(-t^2)\text{d}t, \text{ and } \text{erfc}(\alpha r) = 1 - \text{erf}(\alpha r). \tag{3.7}$$

In practice, the Ewald correction calculations has a computational complexity in $\mathcal{O}(N^2)$ that can be reduced to $\mathcal{O}(N^{\frac{3}{2}})$ with an well chosen convergence parameter. In addition, the Particle-Particle-Particle-Mesh (PPPM) method can be used to build up the reciprocal vectors basis, reducing the complexity to $\mathcal{O}(N\log(N))$[146].

Wolf summation

In Eq. 3.4, reciprocal contributions appears to be small [147, 148] . In order to improve the Ewald CPU performances, Wolf *et al.* to propose an adaptation of the Ewald summation as a shifted potential at the cut-off distance [149]. It stands as :

$$\varphi_{\text{Coul}}^{\text{Wolf}}(r_{ij}) = \frac{q_i q_j}{r_{ij}}\text{erfc}(\alpha r_{ij}) - \lim_{r_{ij}\to R_c}\left(\frac{q_i q_j \text{erfc}(\alpha r_{ij})}{r_{ij}}\right). \tag{3.8}$$

Such a formula recovers the Ewald summation if the cut-off is long enough (w.r.t. to the box size) and a convergence parameter small enough (i.e. that allows to take every box contributions into account).

3.1.4 Validation of the adapted potential

First, a relaxation of the reference grain (shown in Fig. 3.1) is performed in the NVT ensemble, placed within a large box of size $45\times53\times43$Å (which was chosen arbitrarily but respecting more than twice the grain size and the cut-off of defined interaction). This box is then filled with water to reach liquid water properties ($\rho\approx 1.0\text{g.cm}^{-3}$) at ambient temperature. The system is pre-relaxed for 0.1ns in the NVT ensemble with a timestep of 0.1fs so that the system can reach an equilibrium. Then, it relaxes in the NVT ensemble for 5ns with a timestep of 0.5fs. This procedure is applied using both our adapted ClayFF potential and a reactive force field for aluminosilicates (ReaxFF) [69, 150]. The cut-off for interactions is set to $r_c = 12$Å, according to the grain geometry. Resulting final structures are shown in Fig. 3.2.

Note that this adapted potential of interaction has also been successfully tested over a structure containing more aluminum atoms. By substitutions of some silicon into aluminum atoms and addition of sodium counter-cations for charge equilibration, a grain with Si:Al=16:7 (closer to the ratio of 2 of interest for the industry) have been produced.

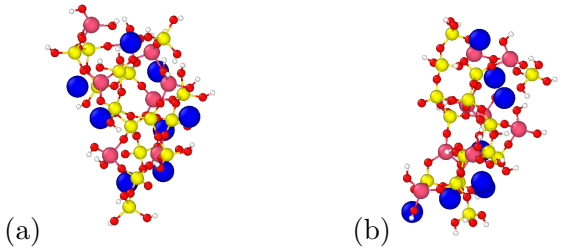

(a) (b)

Figure 3.2: Final structure after relaxation with the (a) adapted ClayFF and (b) ReaxFF (right) potentials. Red, yellow, pink, white and blue spheres respectively represent oxygen, silicon, aluminum, hydrogen and sodium atoms.

Final properties of the simulation box/grain structures are given in Table 3.2 and 3.3. Table 3.2 illustrates that the thermodynamics output from grain relaxation using either ReaxFF or the adapted ClayFF are similar. In addition, the radial distribution characteristics are gathered in Table 3.3.

	ReaxFF	ClayFF
E_p (kcal/mol)	-14250 ± 8.43	-17701 ± 313.45
P (atm)	-0.860 ± 168.63	-1.834 ± 112.6
T (K)	300.15 ± 22.09	299.97 ± 22.68

Table 3.2: Thermal parameters comparison between ClayFF and ReaxFF.

$g(r)$ ($r_{\text{peak}}/g(r_{\text{peak}})$)	Adapted ClayFF	ReaxFF
Si-O	1.55/9	1.55/163
Al-O	1.64/1	1.58/107
Na-O	2.35/0.03	2.32/33
O-O	2.55/9	2.55/42
Si-Si	3.08/2	3.1/40
Al-Al	4.05/0.1	4.06/8.00
Si-Al	2.95/4	2.95/71
O-H	1.05/21	1.05/160

Table 3.3: $g(r)$ comparison between our Adapted ClayFF and ReaxFF potentials

The structure of the grains generated from both potential are similar. In this work, since no chemical reactions are investigated, we will use the adapted ClayFF potential. The procedure described here will serve as a reference for further simulations, involving more grains.

3.2 Initial configurations for Free Energy calculations

The grand potential of interaction, or also called Potential of Mean Force (PMF) between two grains in solution is described by free energy change between two states. One of the states is when grains are in contact, the other state is when grains are separated. In this work, we are considering a inter-grain distance from 0 to 30 Angstroms and we aim to reproduce the PMF along this coordinate. We have presented before the structure of a single aluminosilicate grain in solution that can serve as a reference grain. The pair-potential of interaction between two such grains now needs to be evaluated w.r.t. their relative distance.

3.2.1 Box preparation : from one grain to water immersed interacting grains

First, the grain generated previously is duplicated and rotated giving us two grains. These two grains are set at an initial distance d_{COM} and immersed into solution with the `PACKMOL` package [151]. In this first part of the chapter, this immersion is performed as follow: after setting the grains at a given distance, ions are added to the box to compensate the local charge of the grain (that can vary depending on the protonation degree of the grain, as discussed later), the grains are relaxed in void before water addition to the simulation box.

3.2.2 Grain orientation

In solution, many grain geometries can be observed. While grains can deform, we first want to check that there is no energetically favored relative axial orientation between the two structures.

Then, the two grains are placed at a surface-to-surface distance of 3 Å (defined in this work as the minimum distance between two atoms of each grains), it is immersed in water and relaxed in the NVT ensemble for 3ns. Fig. 3.3 illustrates the simulation box with a relative angle $\theta = 0°$. Fig. 3.4 illustrates that the system potential energy is barely impacted from the grain rotation. Therefore, our simulations will be initiated with an orientation $\theta = 0°$.

3.2.3 States at different distances

Interaction between the grains in water is computed using the Free Energy Perturbation (FEP) method described in Chapter 2. Already applied to CSH and clay [34, 62], it has probed good results in free energy calculations for such systems. This methods requires to sample configurations at different distances, which energies must be close enough to remain within the perturbation framework.

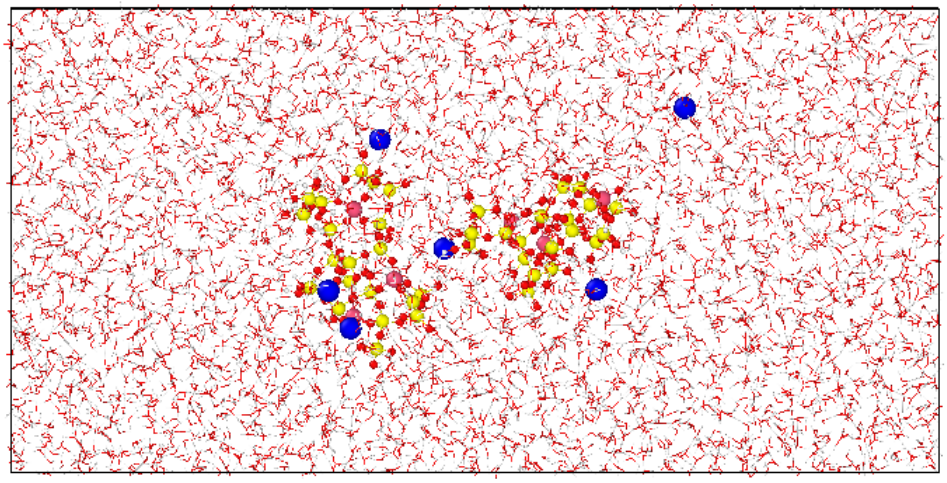

Figure 3.3: Two aluminosilicates in solution : yellow, pink, red, white and blue spheres correspond to the Si, Al, O, H and Na atoms of the aluminosilicate structures while the red and white branches are water molecules.

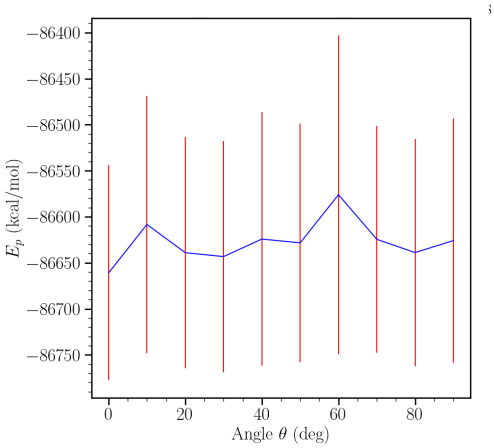

Figure 3.4: Potential energy as a function of angles between the two grains at a surface-to-surface distance of 3Å. The red lines are the error bars over the simulation run.

We recall here, that the free energy difference ΔA between two states i and j can be quantified by

$$\Delta A(i \to j) = A_j - A_i = -k_B T \ln \left\langle \exp\left(-\frac{U_j - U_i}{k_B T}\right)\right\rangle_i = \sum_{k=i}^{j-1} \Delta A(k \to k+1). \tag{3.9}$$

Generation of states at different distances

600 configurations have been created varying the distance from 0 to 30 angstroms with a step of $\delta d = 0.05$Å. Before each displacement step, a relaxation of the grains is performed for 0.1ns in the NVT ensemble at ambient temperature, with a timestep of 1.0fs. During this relaxation, grain COM remain fixed at their initial position but the grain are fully allowed to relax (so that the $d_{\text{COM}} = 0$Å distance can be reached). Each of these is associated to a distance $d_{\text{COM}} = r_i$.

Relaxation of the grains in water

For each state, water immersion is performed by the addition of 1200 water molecules, using the PACKMOL package[151]. Simulation box dimensions are of 80Å×40Å×40Å, and a NPT relaxation is performed at ambient conditions : $T = 300$K and $P = 0$atm. The final box dimensions remain the

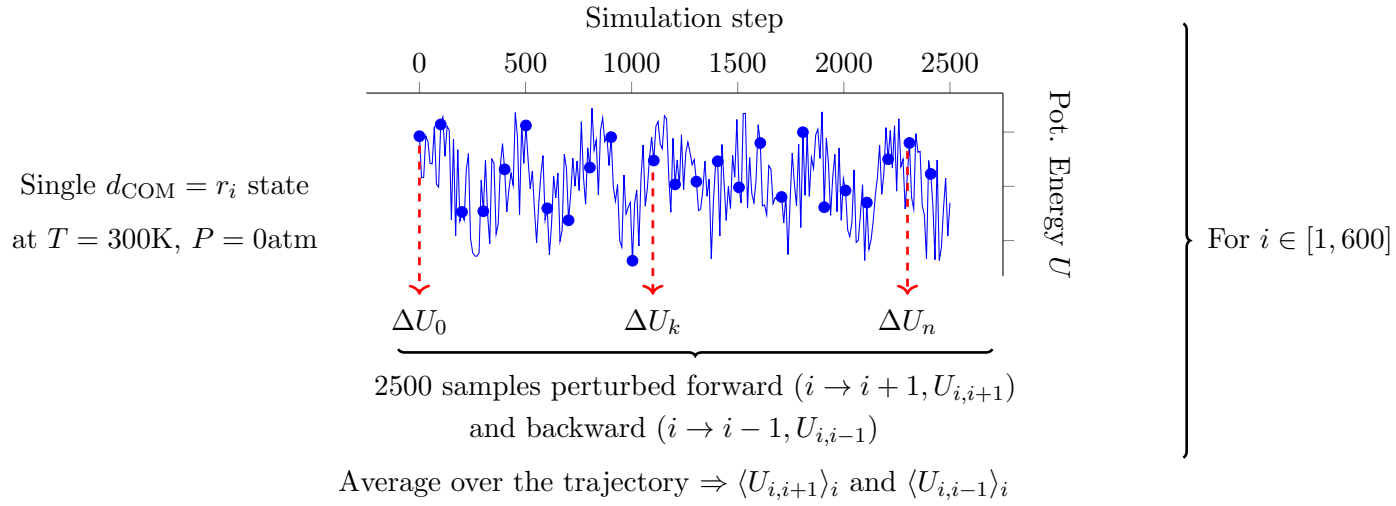

Figure 3.5: Scheme of the Free Energy Perturbation calculations. Configurations are sampled along the equilibrium trajectory, as a few are shown in blue dots. For each state i, the 2500 sampled configurations are perturbed in both forward and direction. 2500 values are obtained for each $\Delta U_{i,i+1}$ and $\Delta U_{i,i-1}$. $\langle U_{i,i+1}\rangle_i$ and $\langle U_{i,i-1}\rangle_i$ are obtained as averages over the 2500 energy differences for each perturbation direction, for a single state i. These calculations are performed over the 600 states.

same ± 0.1 depending on the distance, and the box density is $\rho = 1.05\mathrm{g.cm}^{-3}$ in average. It contains 12834 atoms, including the two aluminosilicate entities composed each of 117 atoms (grain+ions). Note that the number can increase if the grain gets deprotonated ($H^+ \leftrightarrow Na^+$ substitution).

Equilibrium of each state

A simulation is run for each state, in the NVT ensemble at ambient temperature and atmospheric pressure with a Nosé-Hoover thermostat. The NVT ensemble is applied to both water molecules and grains atoms. Both aluminosilicates center-of-mass (COM) remain fixed at their initial position so that the center of mass distance d_{COM} is kept constant. The timestep is set tot 1.0fs and Periodic Boundary Conditions (PBCs) are applied in every directions.

At each distance r_i, a 0.5ns equilibrium is performed in the NVT ensemble to reach equilibrium. Then, configurations are sampled over a 2.5ns production run every 1000 steps, i.e. 1000fs=1.0ps. This way, a total of 2500 configurations are extracted, for each state r_i.

Perturbation steps

Finally, for each of the 2500 saved configurations, a single perturbation step is performed both forward and backward with the associated δd, depending on the distance r_i, : the right grain is moved either in the right or the left direction by $\delta d = 0.05$Å. Both energy differences $\Delta U_{i,i+1}$ and $\Delta U_{i+1,i}$ w.r.t. the state i are computed. These can then be averaged over state i (considering N configurations among the 2500 sampled) and doing the same procedure for state $i+1$ allow to compute the free energy variation between states i and $i+1$: $\Delta G(r_i \to r_{i+1})$. Fig. 3.5 illustrates the methodology for a given state i. All the molecular dynamics simulations has been performed with LAMMPS [152].

3.3 Convergence of DA and SOS calculations

In order to improve the convergence of free energy perturbation calculations, we have applied the Simple Overlap Sampling (SOS) method. A first set of tests have been performed using configurations for which grains have been relaxed without interstitial water and both water and alkaline solution added a posteriori. The alkaline solution is modeled by replacement of 50 water molecules by $(OH)^-$+Na^+, accounting for a solution with $[Na^+]$=0.727 mol/L (vs 0.078mol/L in the case of water, because of the compensating sodium ions).

Fig. 3.6 displays the curves obtained from DA and SOS formula and one sees that the SOS is better converged as the DA since with DA, the resulting PMF depends on the sampling size.

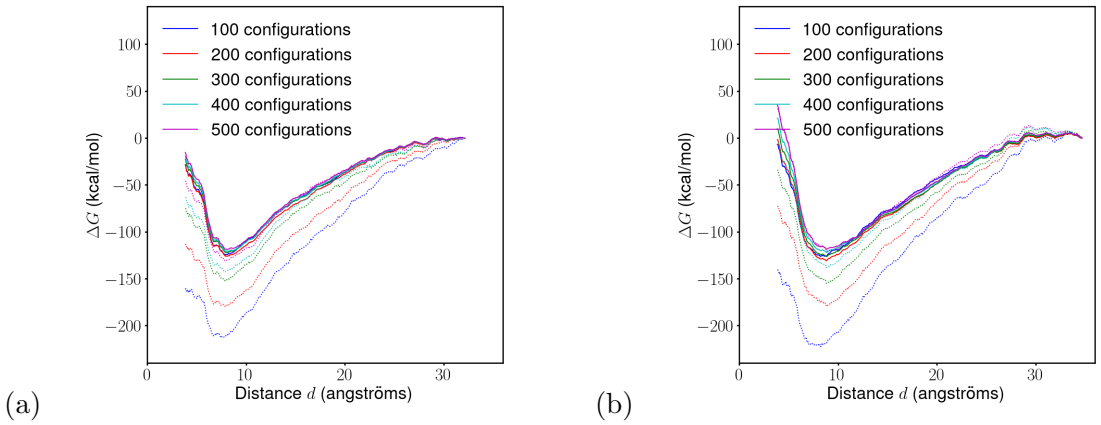

Figure 3.6: Convergence w.r.t. the number of configurations for the Potential Mean Force (PMF) of interaction between two grains (a) in water, (b) in an alkaline solution. DA results are plotted in dotted lines while continuous plots depicts SOS calculations.

Fig. 3.6 shows that DA calculations converge to the SOS one as the number of sampled configurations increases. Moreover, the independence of the SOS-computed PMF w.r.t. the number of configuration probes that this one is well set. With a number of 500 configurations, DA calculations fits well with the results obtained with SOS, using only a 100 of configurations.

Note that one can also check the stability of these results by sampling the configurations used in PMF randomly (instead of periodically over the sampling period). Taking randomly 100 configurations with 5 different seeds among the total set of samples give, for the SOS method, leads to Fig. 3.7, comforting on the convergence of the method.

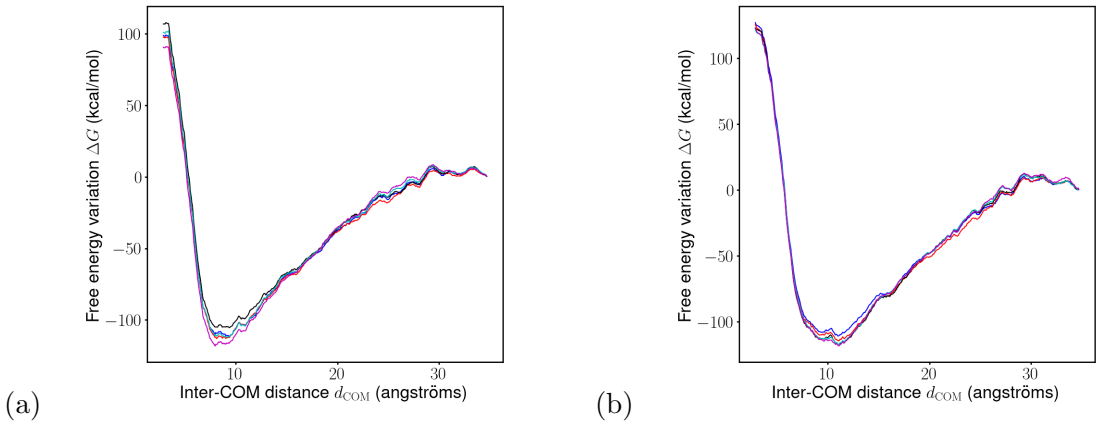

Figure 3.7: Plots of the Potential Mean Force (PMF) of interaction between two grains (a) in water, (b) in an alkaline solution. The PMF have been computed considering 100 configurations taken randomly among the total set of samples. Each set of 100 configurations corresponds to a color.

3.3.1 Estimation of PMF standard deviation

For both cases, we have performed standard deviation calculations using both jackknife and bootstrap methods as described in Chapter 2. They have been performed over 500 of the 2500 samples. Using the 500 available configurations, the jackknife method has been performed in two different ways, by

considering either the 100 or 500 configurations (periodically sampled from the total set). Note that the first way is only possible for the SOS calculations, since with 100 configurations, the PMF is far from converged with the DA method (cf. Fig. 3.6).

Comparison of the methods

For each $\Delta G(i \to i+1)$, the Jackknife standard deviation have been estimated from either 100 or 500 configurations. These are plotted w.r.t. the COM distance in Fig. 3.8 with the total ΔG standard deviation.

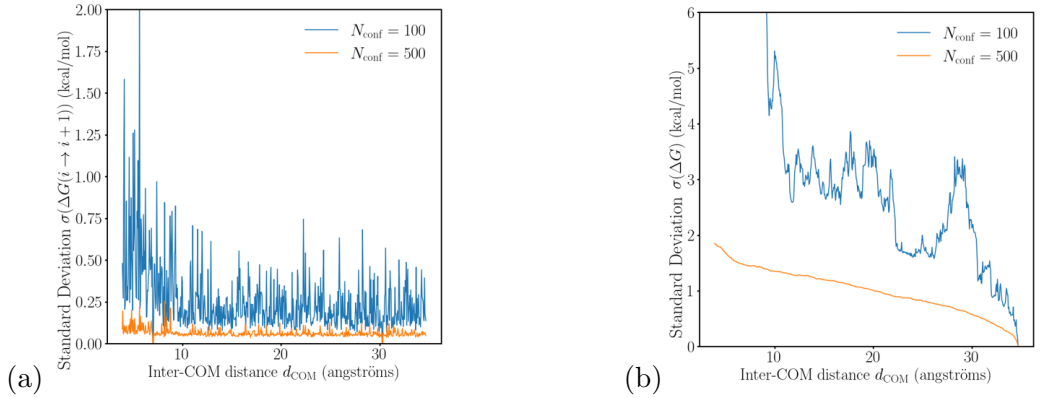

Figure 3.8: Jackknife standard deviation estimation over the PMF computed by the SOS sampling between (a) two successive states ($\Delta G(i \to i+1)$) and (b) initial to j states ($\Delta G(0 \to j) \equiv \Delta G(0 \to j)$),, as the sum of individual ones until state j.

As it requires on a sub-sampling of the configurations, the convergence of Bootstrap standard deviation on $\Delta G(i \to i+1)$ must be ensured by applying the procedure for different sets sizes B. According to Fig. 3.9, Considering $B = 100$ sets of configurations appears to be enough to reach a converged estimator standard deviation.

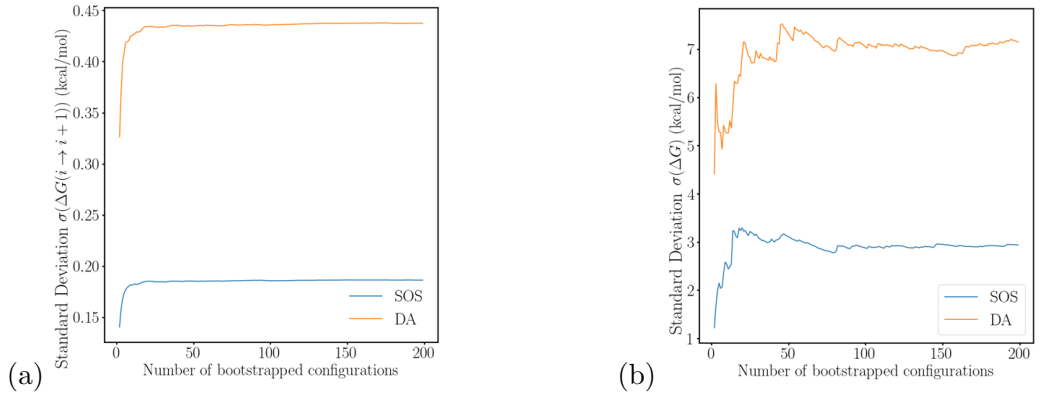

Figure 3.9: Convergence of the bootstrap standard deviation over PMF calculations using both DA and SOS methods between (a) two successive states ($\Delta G(i \to i+1)$) and (b) initial to j states ($\Delta G(0 \to j) \equiv \Delta G(0 \to j)$)

Both estimation of standard deviations can be compared from Fig. 3.10, probing that for smaller initial set of data, the bootstrap performs better than the jackknife, while considering a higher number of possible sets of data leads to a smaller standard deviation for the jackknife approach.

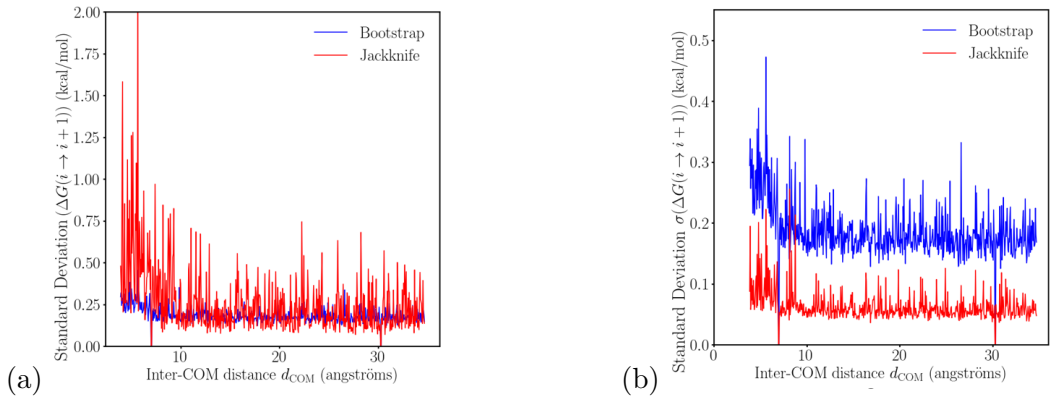

Figure 3.10: Comparison of jackknife and bootstrap method for different maximum sampling size N. Jackknife calculations are based on sets of (a) 100 configurations in total, (b) 500 configurations in total. Bootstrap standard deviations is still estimated considering 100 configurations among the 500 available.

Fig. 3.11 clearly shows that the bootstrap states a better standard deviation for $\Delta G(0 \to j)$, at less computational cost. The order of magnitude is the same for both method but the Jackknife approach requires more configurations and so calculations.

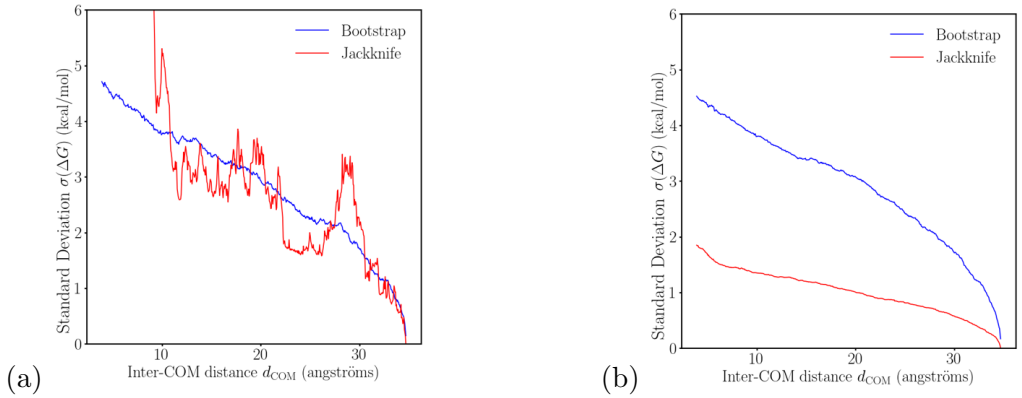

Figure 3.11: Comparison of jackknife and bootstrap methods for different maximum sampling sizes N. Jackknife calculations are based on sets of (a) 100 configurations in total, (b) 500 configurations in total. Bootstrap standard deviations is estimated considering 100 configurations among the 500 available.

The bootstrap has shown very good performances for a smaller number of sets of observations, e.g. for $B = 100$ in Table 6.1 from [132]. If the convergence of the method is ensured, it might therefore be more relevant to work with it rather than with the jackknife. This is our choice, which was also taken in studies similar to ours [62].

Results on the Potential of Mean Forces

Finally, it is possible to plot the converged PMF for both cases : grains in water and grains in the alkaline solution, with their respective standard deviations in Fig. 3.12. These PMFs show an attraction at short range for the grains, with a well around -120kcal/mol located at a distance of 8.5Å. At very short distances, a repulsive regime appears and the interactions go to zero to larger distances. The attraction well ranges between 5 to 24Å COM distances.

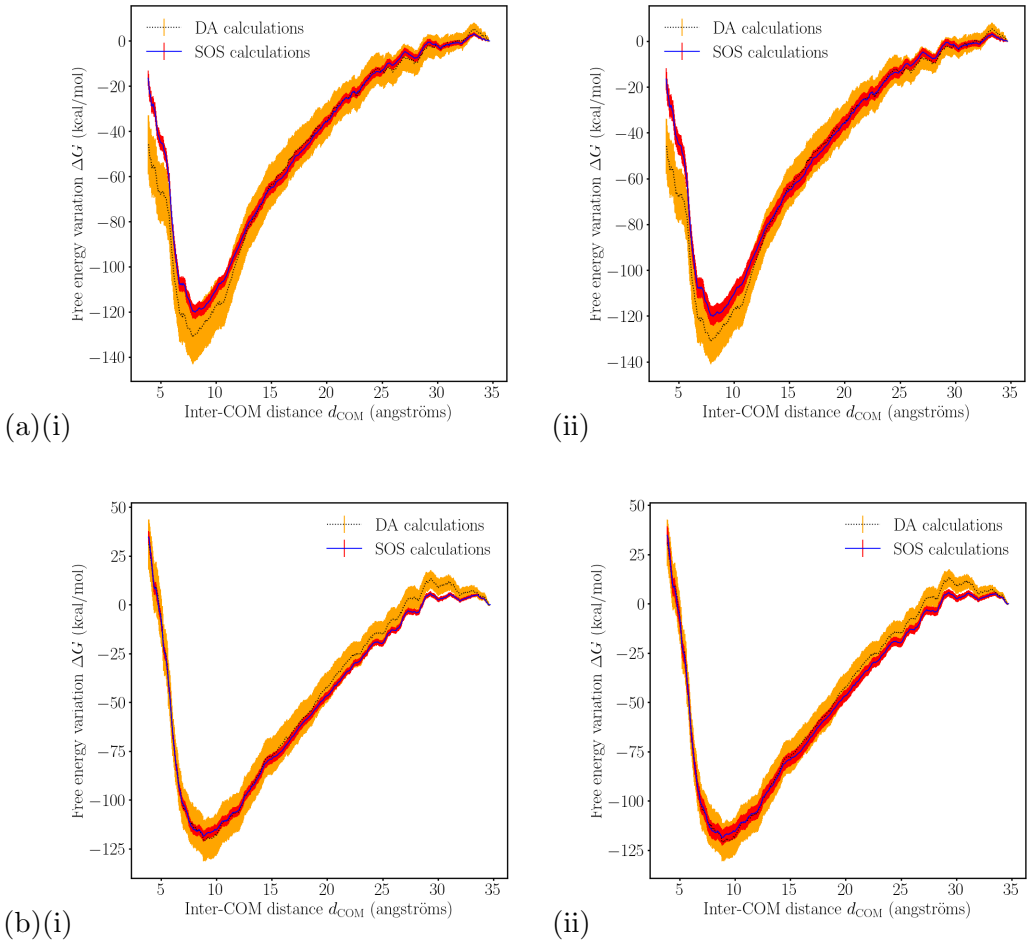

Figure 3.12: Potential of Mean Force for grains in (a) water and (b) in the alkaline solution with their respective standard deviation obtained with (i) the jackknife and (ii) the bootstrap methods.

3.4 Influence of simulation parameters

A good representation for grain-grain interaction requires a good grain representation but also a good quantification of physics at stake at the atomistic level. Pair-potential must be chosen wisely and so does all simulations parameters as the NVT parameters, the conditions of equilibrium and the perturbation step used for FEP calculations.

3.4.1 Choice of the pair-potential parameters

Until this point, the cut-off of pair interactions was set to $r_c = 12$Å, according to the grain geometry. This choice is important as it highly influences the CPU time if it is too large and may not be able to account for all interactions if taken too small. For the Lennard-Jones term, a few tests probed the 12Å value to be at good balance.

From an electrostatic point of view, in addition to the cut-off, a damping parameter is required to compute the potential energy. Fig. 3.13 shows the dependence of this latter on damping parameter α and the cut-off r_c involved in Wolf sum calculations.

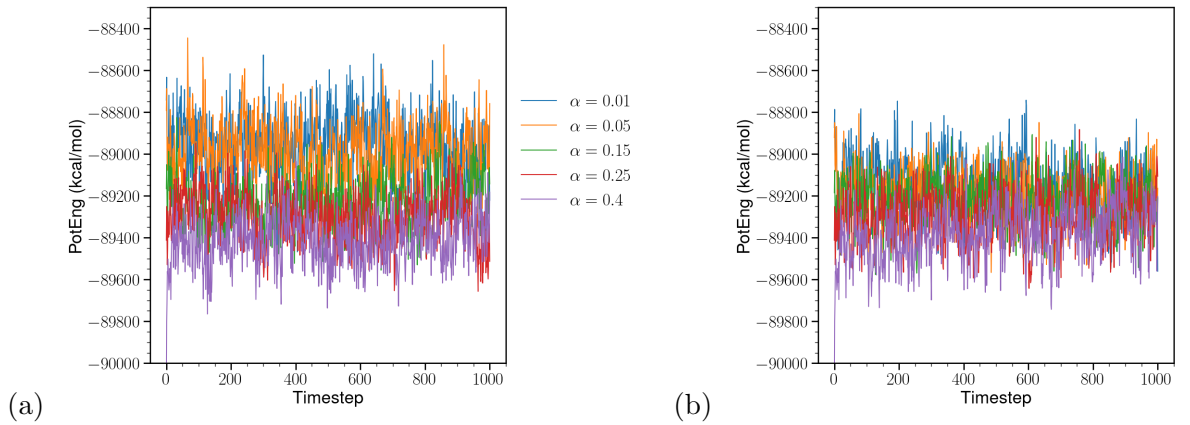

Figure 3.13: Potential energy of a box with two neutral grains at distance $d_{\mathrm{COM}} = 15$Å, during a run of 1000 steps of 1.0 fs. The electrostatic pair-potential is computed w.r.t. the wolf summation method with varying damping parameter α and a cut-off of (a) $r_c = 12\,$Å and (b) $r_c = 18\,$Å.

The damping does influence the potential energy of the system. The change in potential energy with damping changing from $\alpha = 0.25$ to 0.05 can be estimated to around 0.5% of the average value as shown in Fig. 3.13 (a). The change is also related to the cut-off used for Coulomb interactions. With a longer cut-off, this α-dependence decreases, according to Fig. 3.13 (b). This tells us that with a cut-off long enough, the damping parameter will not influence much the total potential energy. However, one must be aware of its role and still chose it small enough so that the wolf tail-correction has converged to the Ewald one, according to Fig. 3.14.

To study this, we introduce local grain deprotonation by remove hydrogen of the structure, so creating a surface charge. By substitution of an edging hydrogen atom with a sodium ion (and so, an adaptation of the edging oxygen charge to $-0.95-(1-0.425) = -1.525$), the grain electronic charge is increased. The deprotonation degree d is defined as the number of edging protons that have been randomly substituted. It relates to the grains charge $q_{\mathrm{grains}} = -d-3(e)$, since the grain already carries a charge of -3 due to the presence of aluminum in its structure.

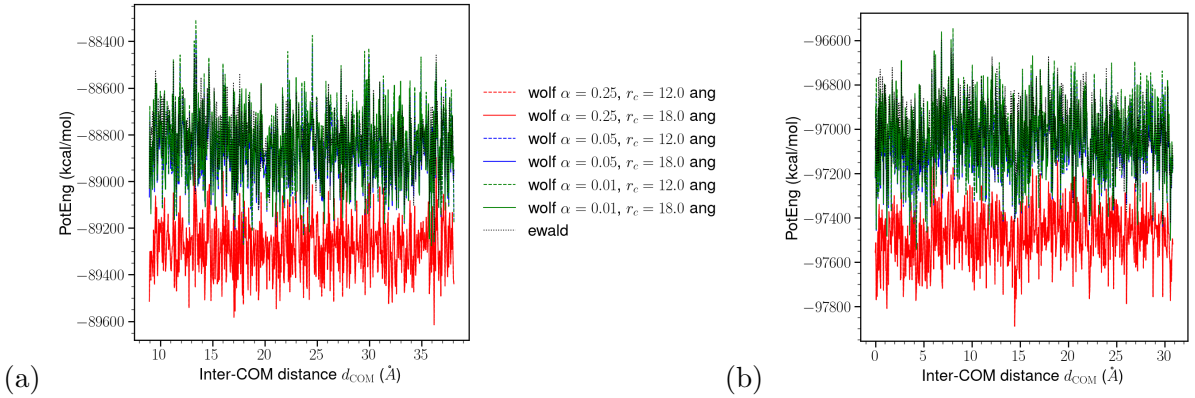

Figure 3.14: Potential energy for equilibrated configurations at different distances. The electrostatic pair-potential is computed w.r.t. the wolf summation method with varying damping parameter α and cut-offs r_c for (a) neutral grains and (b) highly charged grains ($q_{\mathrm{grain}} = -13e$).

Fig. 3.14 compares two cases, where the grains are neutral charges and one with high surface charges $q_{\mathrm{grain}} = -13e$ (grain surface charging is discussed in next subsection). The red curves confirm the previous statement that with a too short cut-off and a too important damping, the potential energy is not converged to the Ewald one. However, with a damping less than 0.05 and/or a cut-off of 12 Å, the

Wolf summation gives a tail-correction similar to the Ewald one. From a molecular simulation point of view, it may be relevant, if the CPU cost is reasonable, to work with the longest cut-off as possible. After a few tests, a cut-off of 18 Å will be applied to electrostatic interactions for further simulations. The damping not affecting significantly the computational cost, it will be set to 0.01.

3.4.2 Choice of the perturbation step

Applying a perturbative approach requires to study similar states. From a molecular dynamics point of view, a way to quantify the similarity of two states is to compare their respective potential energies.

Let us consider two states, i and $i+1$. In the framework of the SOS method, the convergence of the FEP calculations can be ensured by a sufficient similarity between state $i+1$ perturbed with regard to state i and state i perturbed with regard to state $i+1$. This condition directly arises from Eq. 2.41. To ensure this, we compute, for each state, the energy differences forward and backward (from i to $i+1$ and from $i+1$ to i) Fig. 3.15 (on next page) shows their distributions for three different grain charges and with different perturbation size δd.

Fig. 3.15 display smaller energy differences as the perturbation size decreases. Still, for these different δd, the overlap is higher than 50% and remains within the framework of the perturbative approach discussed by Lu and Kofke [127, 128].

In addition, the overlap percentage can be estimated as the overlapping area with regard to the full histogram coverage for all states. It is shown as a function of the COM distance between the grains as shown in Fig 3.16.

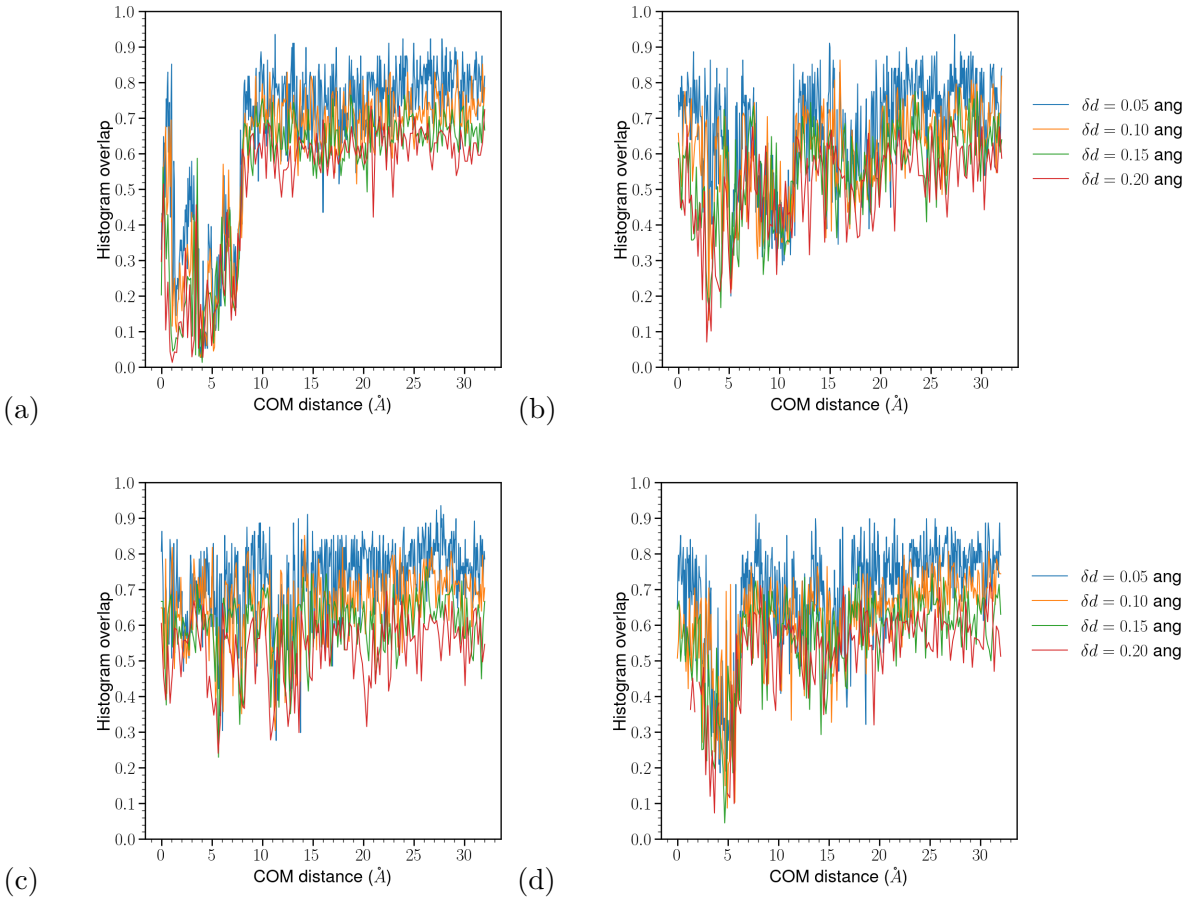

Figure 3.16: Overlap of δU overlap from both forward and backward perturbation for (a) neutral, (b) $q_{\text{grain}} = -6e$, (c) $q_{\text{grain}} = -8e$ and (d) $q_{\text{grain}} = -13e$ grains.

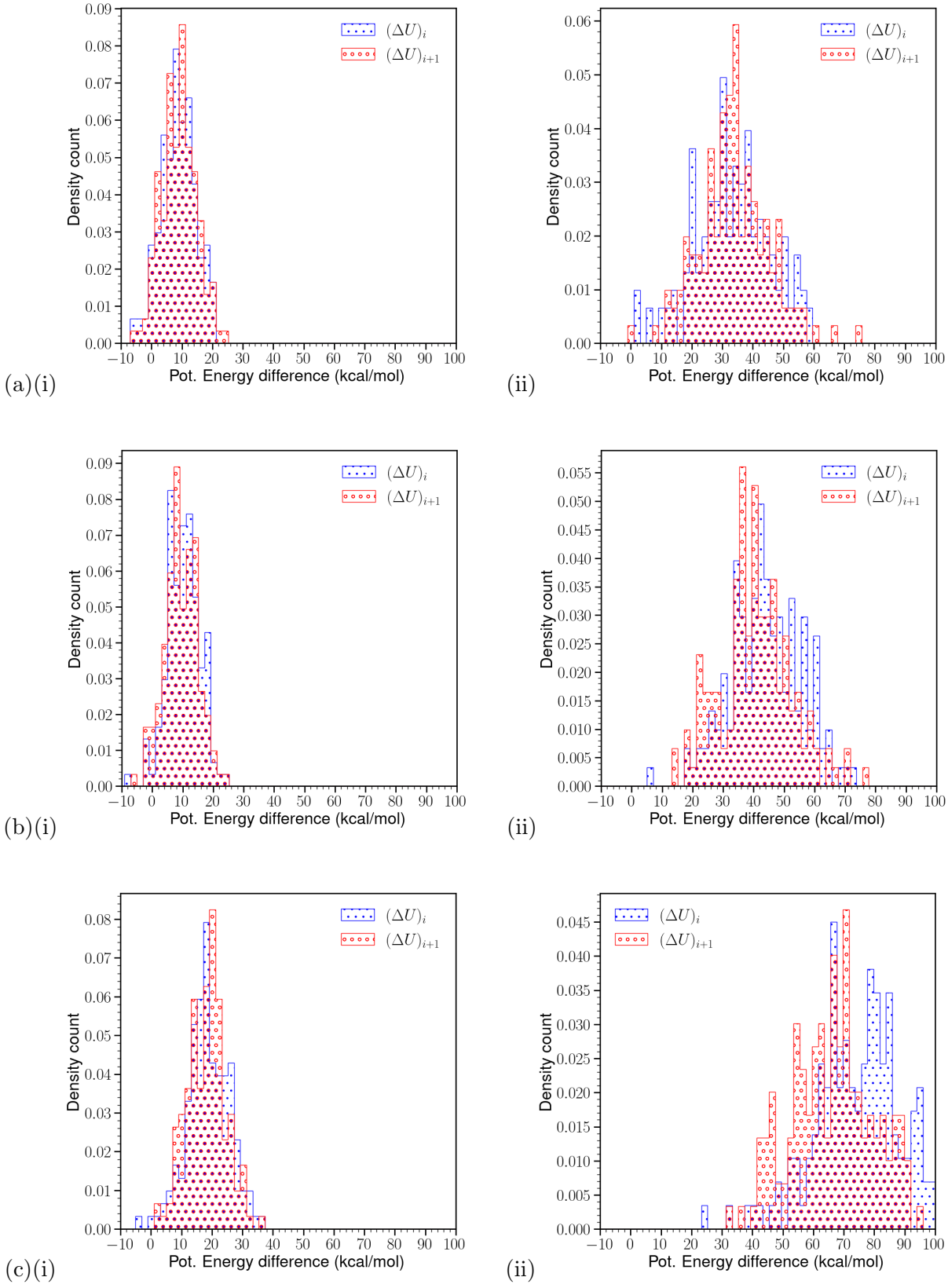

Figure 3.15: Energy differences in absolute values while performing the perturbation in both forward and backward directions. In blue, the system is moved from state i to $i+1$ (forward) and in red, the system is moved from state $i+1$ to state i (backward). The plots are done for systems at distance $d_{\mathrm{COM}} = 15\,\text{Å}$ for (a) neutral grains, (b) grains with a charge $q_{\mathrm{grains}} = -6e$ and (c) with charge $q_{\mathrm{grains}} = -13e$. (i) and (ii) plots respectively correspond to perturbation sizes of $\delta d = 0.1\,\text{Å}$ and $0.2\,\text{Å}$.

The smaller the perturbations are, better the overlap are. At short distances though, energy differences between both direction seems to differ more than at larger ones. Below 6 Å, grains are forced to be very close which induces necessarily important potential energy change when performing the perturbation. In overall, the energy overlap are robust enough to ensure the convergence of this perturbative approach.

Finally, the mean of each distribution is computed as $\langle \Delta U \rangle_i$ and $\langle \Delta U \rangle_{i+1}$ w.r.t. reference states (i.e. COM distances) and their differences are compared in Fig. 3.17, for the different deprotonation degrees.

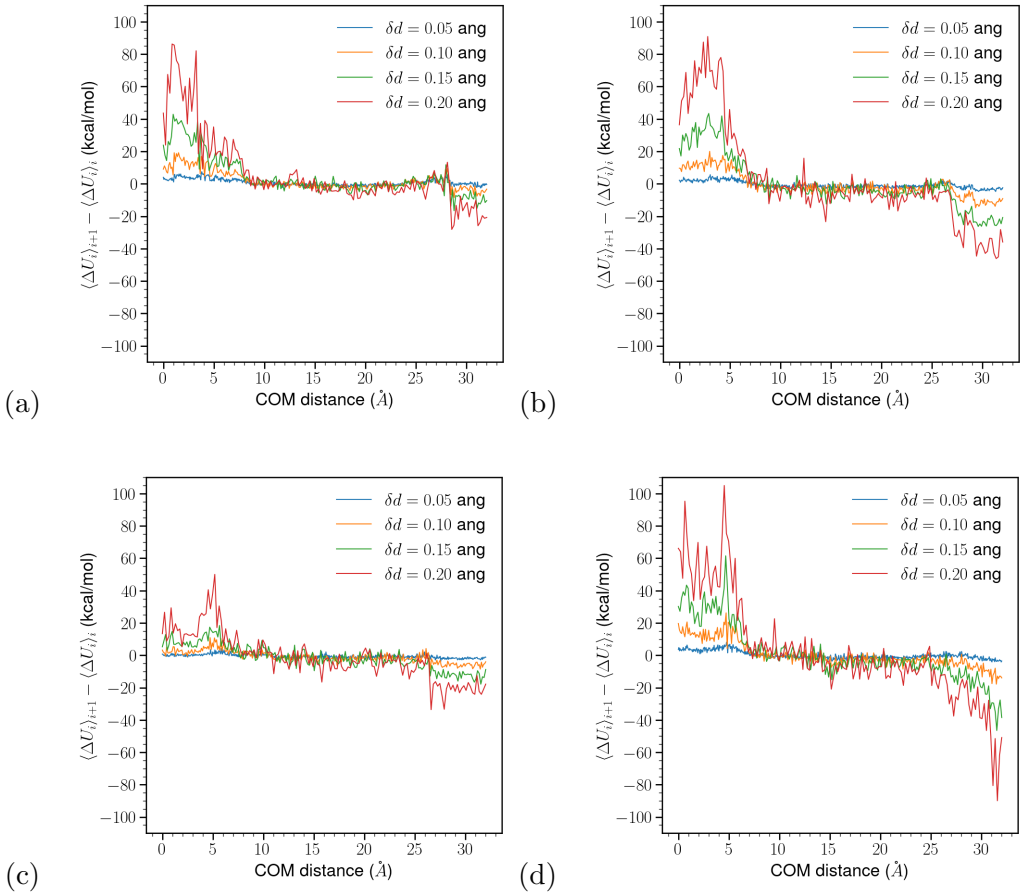

Figure 3.17: Overlap of δU overlap from both forward and backward perturbation for (a) neutral, (b) $q_{\text{grain}} = -6e$, (c) $q_{\text{grain}} = -8$ and (d) $q_{\text{grain}} = -13e$ grains.

The Simple Overlap Sampling (SOS) method involves calculations based on a ratio of two energy differences. Fig 3.17 depicts as δd increases, the energy differences gets larger, therefore impacting the free energy calculations, taken as an exponential of these potential energy changes according to Eq. 2.41 from Chapter 2. Smaller δd therefore lead to more accurate calculations.

Influence on the PMF

The perturbation size appears to highly influence the calculation of energy differences between perturbed states but not the overlap of ΔU distribution. Using the SOS method should therefore ensure that obtained results are consistent along this range of perturbation sizes. Fig. 3.18 shows the influence of the choice of δd on the final grand potential of interaction between two grains in water for many cases.

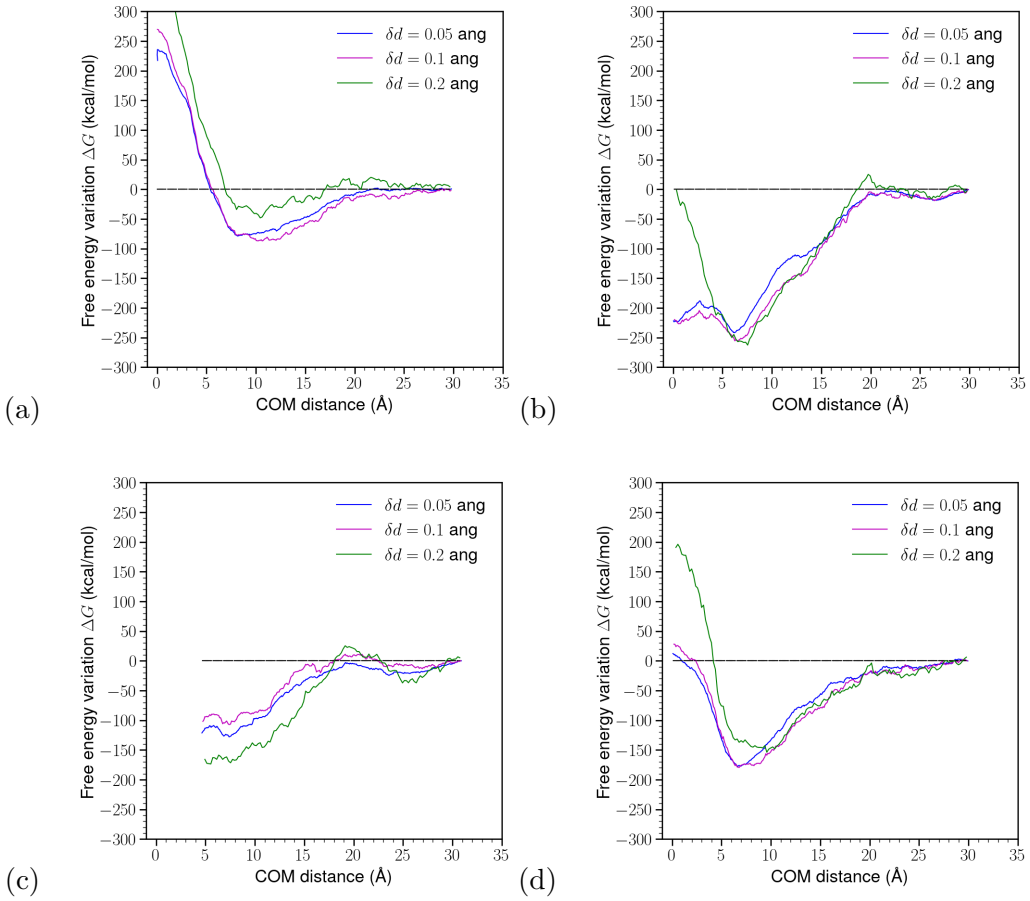

Figure 3.18: Potential of Mean Force (PMF) computed following the designed procedure, using different perturbation sizes, for (a) neutral, (b) $q_{\text{grain}} = -6e$, (c) $q_{\text{grain}} = -8e$ and (d) $q_{\text{grain}} = -13e$ grains. Note that these PMF have been computed with the initially described procedure but with the latest potential parameters discussed in this section (especially, the well for the fully protonated case (a) shows a wel less deep that it was from the first run, from Fig. 3.12). Note that Potential of Mean Forces obtained here for the fully protonated case (Fig. (a)) differing from the ones of Fig. 3.6 because of the electrostatic potential corrections. The associated well is shifted up of 30kcal/mol (slightly reducing its width) but has the same minimum location.

In overall, grains appears to attract each other no matter their deprotonation degree. Especially, the most deprotonated case is purely attractive within a range [0,30]Å. While electrostatic repulsion increases as the grains charge surface do, Van der Walls attractive interactions overwhelms coulombic forces. In fact, grain deprotonation make available O^- sites for the formation of non-covalent bonds (as hydrogen bonds), therefore increasing the Van der Walls contribution to the global interactions. Note that for most deprotonated grains, at most one proton per silicate is removed and therefore the surface still has OH groups.

In Fig. 3.18 (a) and (c), the well depth and width are dependent of the perturbation step. This enlighten that the interaction is not converged with a step that is not small enough. The global behavior of the interaction is not affected by the choice of the perturbation. However, a too large step may not allow to quantify the characteristic quantities of the pair-potential (well depth and location).

A perturbation of 0.1 Å might be sufficient to obtain a good estimate of interactions between our two grains in solution. However, a step of 0.05 Å might be preferable at short distances to avoid too large energy fluctuations within our system and properly quantify the grain-grain interaction. However, dividing by two the perturbation step requires to double the number of equilibrium to perform, i.e. the CPU cost of the calculations, according to the FEP model.

3.5 Calculation of the Potential Of Mean Force with Metadynamics

We propose to use a second approach of Free Energy calculations with Metadynamics. As discussed in Chapter 2, the Free Energy calculations using Metadynamics are based on the addition of the updated bias at every timestep and differs from a thermodynamic integration approach such as the small perturbation theory.

3.5.1 Metadynamics simulation details

In our case, the metadynamics simulation are performed using the inter-grain COM distance as the collective variable, i.e. the variable that will be biased and on which we can reconstruct the energy landscape. To get a good convergence, Well-Tempered Metadynamics (WT-MTD) is performed, in the NVT ensemble, at ambient temperature with a timestep of 0.1fs. We use the adapted ClayFF potential already discussed. Long-range Coulomb interactions are computed with the Wolf summation with a damping of 0.01 and a cut-off of 18 Å. Lennard-Jones cut-off interaction is set to 12 Å. All simulations are performed until PMF calculations are converged. Such a convergence is ensured that after additional runs, the PMF is not changed. In other terms, that added bias is too low to effectively disturbed the system. Well-Tempered Metadynamics aims to visit most states within important configurations (i.e at the edges of energetic distributions). Thus, when mostly converged, less biases are required to visit new states.

3.5.2 Discussion on the results

Fig. 4.2 displays the grand potential of interaction between the grains in water as they get deprotonated. Thanks to the zero line, two regimes can be observed : either attractive ($d = 0, 3, 5$) or repulsive ($d = 10$). Each curves is normalized with regard to its average values over the largest distances range: [24,25]Å.

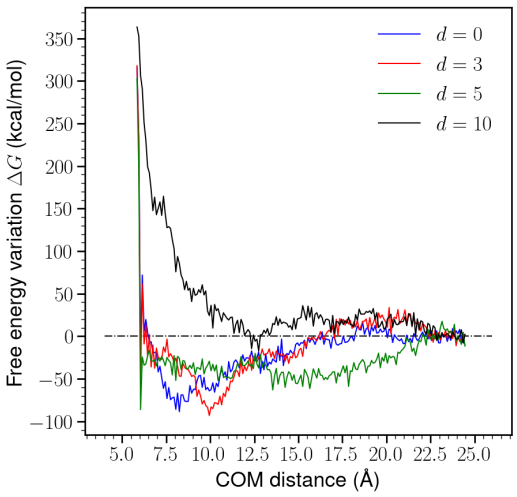

Figure 3.19: Potential of Mean Forces (PMFs) computed using Well-Tempered Metadynamics. Simulations have been performed for deprotonation degrees of $d = 0, 3, 5$ and 10 similarly as discussed in Fig. 3.18. The dashed black line corresponds to the zero line.

Fully protonated case: $d = 0$

Shown in blue in Fig. 4.2, interactions between the grains are attractive. The well with a minimum at -70kcal/mol accounts for an attraction when the two grains are away at a distance of 8Å. This attraction ranges until a COM distance of 15Å while a flat repulsive shoulder guides interactions above. At short distances, less than 6Å, a strong repulsive wall is recovered. Below 10Å grains are

merging. This will be a key point in the next discussions. Fig. 3.20 shows snapshots of the simulation box during Metadynamics simulations.

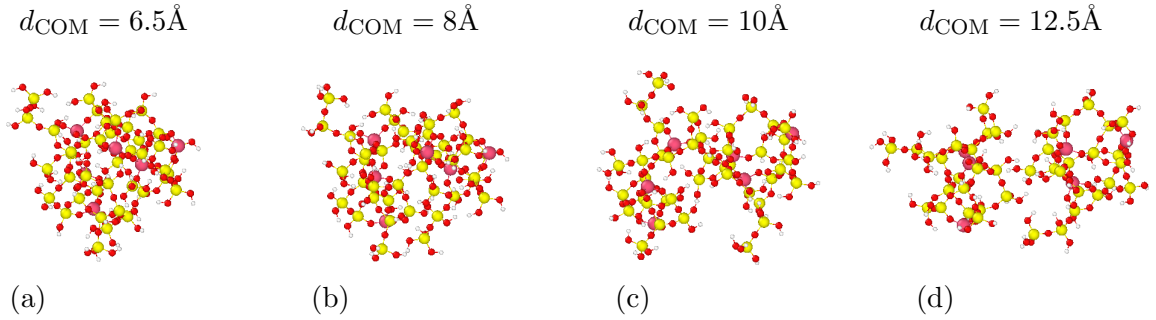

Figure 3.20: Successive snapshots of the protonated grains at different COM distances within the simulation box during metadynamics simulations. Red, yellow, pink and white spheres corresponds to Oxygen, Silicon, Aluminum and Hydrogen atoms. Water molecules and sodium ions are not displayed for clarity.

Fig. 3.20 illustrates the importance of grain deformation as they get closer. The four configurations belong to the attractive well but shows very different structures. As a recall, metadynamics run by adapting the potential of interactions to visit less-favorable states. A consequence is that for a given COM distance, very different configurations can be visited, illustrated in Fig 3.21 for two grains at the same distance $d_{COM} = 10$Å.

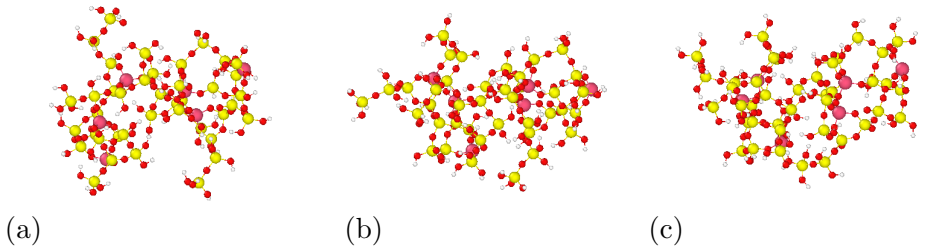

Figure 3.21: Snapshots of the protonated grains at $d_{COM} = 10$Å at different simulation times during metadynamics simulations. Red, yellow, pink and white spheres corresponds to Oxygen, Silicon, Aluminum and Hydrogen atoms. Water molecules and sodium ions are not displayed for clarity.

As the grains leave the attractive well, they appear to shown even more variety in the visited configurations. Atomic interactions between the grains are not influencing their shapes anymore. The study of grains geometry will be discussed in more details in the next Chapter.

Slightly deprotonated case: $d = 3$

As the grains get deprotonated, the interaction appears to be affected. Getting rid of three protons at each grain's vicinity, PMF calculations using potential biasing probe a shift in the well minimum location. With a value still around -70kcal/mol, grains shows the strongest cohesion at a COM distance of 10Å. In overall, the same attractive behavior is observed as for the fully protonated cases, with the same well width, ranging from 6 to 15Å with a slight repulsion at larger distances.

Midly deprotonated case: $d = 5$

Interestingly, the interaction between two grains with a deprotonation degree of 5, even though the values are negative, tend to have a neutral behavior with regard to each other. With a very large, almost flat, potential of interaction that minimize to -30kcal/mol (modulo the fluctuations due to the method), it probes that attraction is weaker. There is no clear well formation arising from the calculations. The well width also illustrates that there is not that much dependence of the interaction

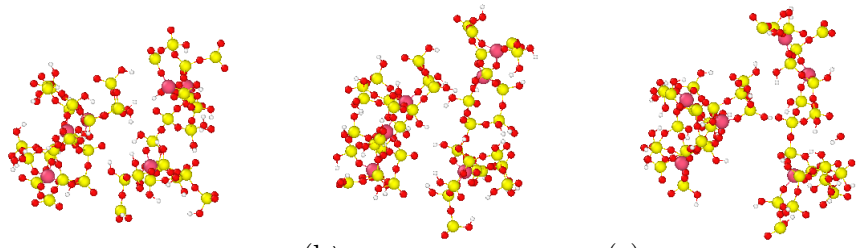

(a) (b) (c)

Figure 3.22: Snapshots of grains with a deprotonation degree of $d = 10$ at $d_{\mathrm{COM}} = 8$Å at different simulation times during metadynamics simulations. Red, yellow, pink and white spheres correspond to Oxygen, Silicon, Aluminum and Hydrogen atoms. Water molecules and sodium ions are not displayed for clarity.

global behavior on the COM distance. Both negative and positive value might arise from the renormalization, highly influenced by the fluctuations undergone by the system under this simulation framework.

Strongly deprotonated case: $d = 10$

Full repulsion is obtained for two grains with surface charges of $q = -13e$ (3 due to the presence of aluminates and 10 to the deprotonation). The black curves of Fig. 4.2 shows tat the repulsive wall starts at a distance of 12.5Å. Above, the interactions appears to be flat.

Fig. 3.22 shows that there is a clear deformation path for the right grain. In contrast with Fig. 3.20 (b), there is an avoidance of grain merging. This phenomenon arises from an opening of the grains arms to avoid inter-penetration. Chapter 4 will give a deeper insight on this point by a characterization of grains' geometry.

3.5.3 Comparison with FEP calculations

For low deprotonation degrees, the attractive behavior is recovered. Especially, both Fig. 3.18 and Fig. 4.2 display, in the fully protonated case, the similar wells with a minimum located at 8Å with a minimum of -70kcal/mol. Major difference stands in the well width that is 5Å larger for the FEP calculations, ranging up to $d_{\mathrm{COM}} = 20$Å. Both curves are plotted together in Fig. 3.23. Because of the grain pre-relaxation in void, shorter COM distances are available to FEP calculations. Still, both methods show a repulsive wall between 5 and 6Å.

While Fig. 3.18 (b) displays also attraction, it shows a well 3 times deeper than the one obtained with metadynamics, with a location that remains unchanged from the fully deprotonated case, around 8Å (to compare to 10Å with metadynamics).

The more the deprotonation degree increases, the more FEP and metadynamics PMFs differ. Panels (c) and (d) from Fig. 3.18 clearly show attraction while metadynamics do not. While FEP calculations accounts for only attraction between the grains, independently of its surface charge, metadynamics stands for a transition from attractive to repulsive regime as observed if Fig. 4.2.

In the following, we will try to understand what can induce such differences between the two methods and identify which is the most adapted to evaluate the grand potential of interaction between aluminosilicate species in water.

3.6 Role of the relaxation process in the perturbation approach

3.6.1 Grain relaxation

As detailed previously in this Chapter, the PMF is computed from equilibria of states generated with pre-relaxed grains in void (similarly as Zhu *et al.*[63], who added water after generating CSH

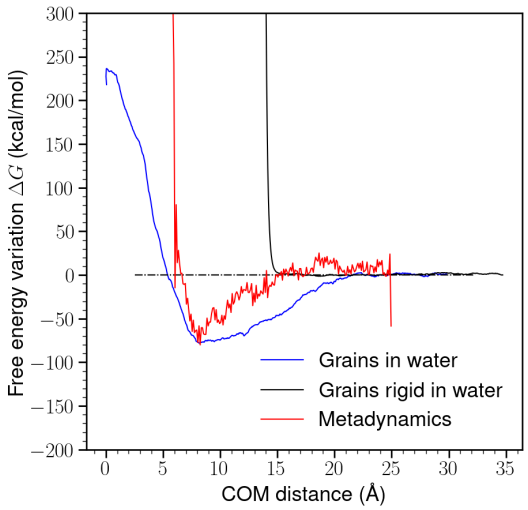

Figure 3.23: PMF obtained from equilibrium generated from pre-relaxed grains in water, rigid grains in water both with FEP and metadynamics calculations, respectively in blue, black and red. Note that in Metadynamics run, the grains are free to relax. These results are shown for grains fully protonated ($d = 0$).

grains configurations). In order to understand the effect of relaxation, we performed the perturbation approach using a rigid grain, in other words, no relaxation is performed and water is added immediately after displacing the grains. During the production run, grains are kept rigid by setting the forces acting on their composing atoms at 0. Resulting PMF is shown in Fig. 3.23.

Fig. 3.23 illustrates the role of relaxation in the materials' cohesion. The black curve, especially, shows that a hard wall of repulsion is reached as the grains have not yet fallen into the attraction well. Even though below distances of 15Å, both blue and red curves probe negative values, the rigidity does not allow such behavior. Grains are not interpenetrating each other, preventing short inter-grain distances and short-range phenomena as, e.g. the formation of H bonds that might be at stake according to the geometry of our oligomers. Note that the initial orientation of the grains have been chosen randomly, as discussed in §2.2 and shown in respective Fig. 3.3. In order to create cohesion, grain relaxation is required.

Therefore, the role of water/grain interaction on the relaxation of the grain appears essential and has, until that point, been strongly biased by the procedure to create the configurations. Indeed, since water is added after grain relaxation, the grains are attractive and reshape so that no water can be added in-between the grains at close distance. This explains the artificial attractiveness observed on all the PMF obtained by perturbation theory. Note that a dry interface would also contribute to ease the formation of non-covalent bonds.

3.6.2 Grain pre-relaxation

In the following, we are using a new procedure which consists in adding water molecules before relaxing the grains and water. Then, the same procedure of equilibration and production runs is used.

It was shown in most works involving FEP calculations, that water must be dealt with carefully at the grains interface [34, 97, 63]. Having water in the relaxation has a direct consequence on the available range for the COM distances. Indeed, water limits the contact between the grains and therefore, with a wet pre-relaxation, COM distances are taken to range from 2Å to 32Å, to keep 300 states. Both initial and this fore-mentioned procedure are detailed in Fig. 3.24.

Procedures described in Fig. 3.24 allow to perform equilibria of the 300 configurations in parallel. From a computational point of view, initiating these states (with water) for all 300 distances required

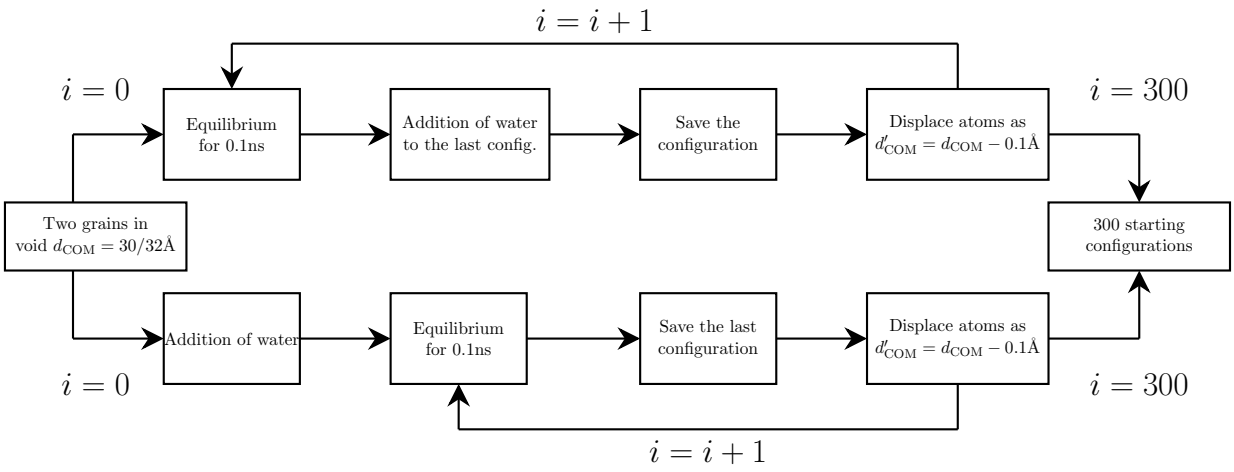

Figure 3.24: Scheme of the two pre-relaxation methods to initiate FEP calculations. The upper line corresponds to the initial path, for which grains are relaxed in void and the water added *a posteriori*: dry relaxation. The bottom line describes the pre-relaxation of grains with water added initially to the system: wet relaxation. The shared starting point is the simulation box with two aluminosilicate grains in void with their surrounding ions. At the end of both paths, 300 configurations of water immersed grains are obtained, each corresponding to COM distances ranging from 0Å to 30Å with a step $\delta d = 0.1$Å in the case of dry relaxation and from 2Å to 32Å with wet relaxation.

2 days of simulations. Therefore, the choice was taken to consider states equilibria in parallel rather than in series, which would have required around 400 days for a 2ns simulated time at each distance.

In the following, we consider, for FEP calculations, equilibria generated using this second pre-relaxation procedure. Free energy variations are computed using the exact same path as previously. Resulting PMFs are shown in Fig. 3.25 for the protonated ($q_{grains} = -3e$) and the high charged ($q_{grains} = -13e$) scenarios.

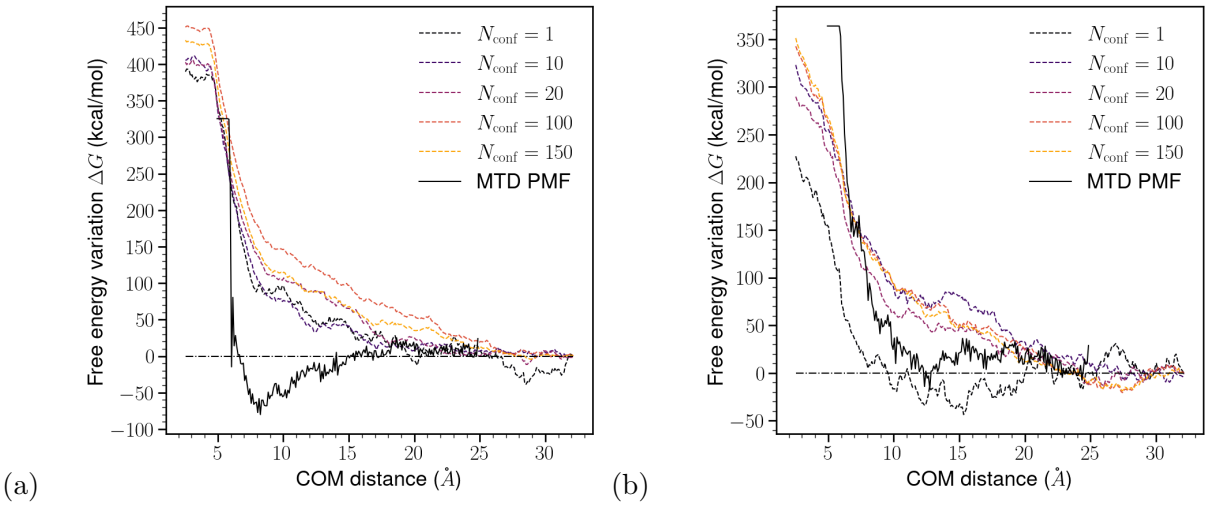

Figure 3.25: Potential of Mean Force computed *via* the FEP approach for the (a) protonated and (b) highly charged ($q = -13e$) cases. In black straight lines is plotted the PMF obtained from well-tempered metadynamics calculations. The configurations are taken randomly over the generated set of 150 configurations over a 0.15ns sampling (i.e. every 1.0ps).

Fig. 3.25 shows that PMF calculations are converged with only 150 configurations sampled every 1.0ps and that our grains repulse each other for both cases. This is not in favor of the polymerization process nor the results computed from metadynamics.

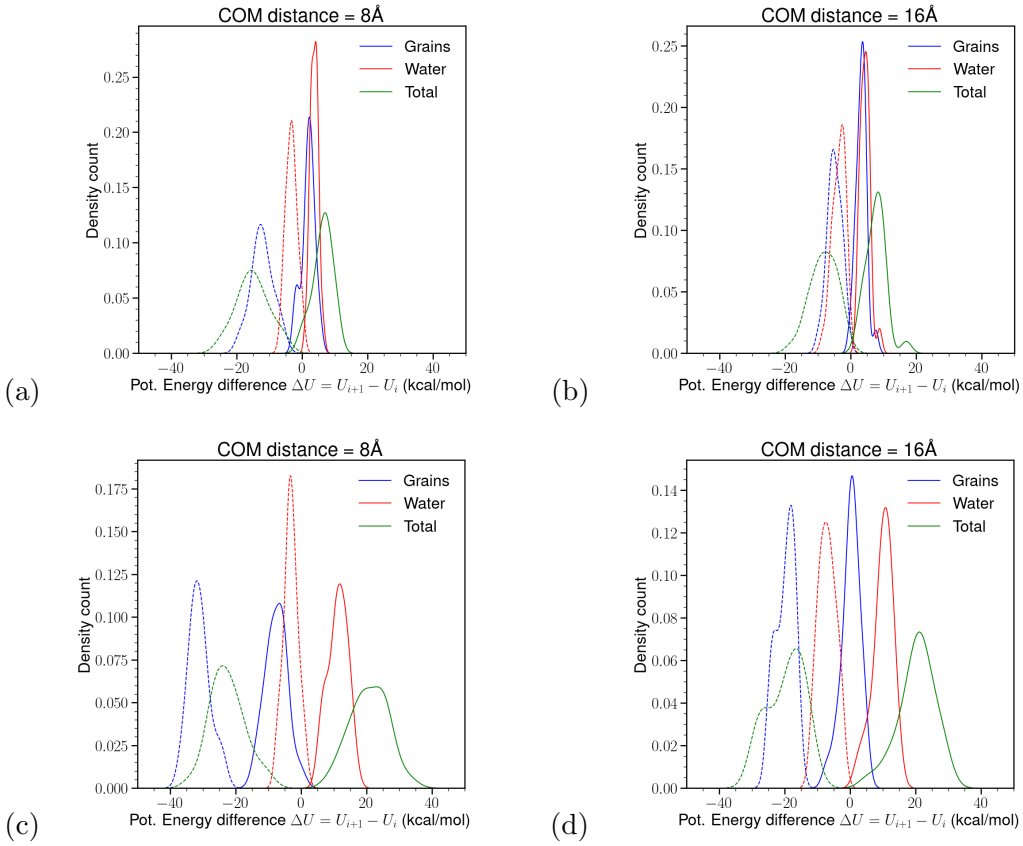

Figure 3.26: Kernel Density Estimation of the potential energy differences distributions for (a)/(b) the fully protonated case and (c)/(d) the highly deprotonated one ($d = 10$). Blue, red and green plots corresponds to the energy differences respectively felt by bot grains, water and total system. Straight line corresponds to $\langle U \rangle_i$,i.e energy differences obtained from i as the reference state (forward) and dashed lines to $\langle U \rangle_{i+1}$ (backward).

By comparing both FEP calculations, it appears that the way grains are relaxed before each equilibrium strongly influence the interactions between the grains. It appears that letting the grain approach each other allow the system to reach a configuration with a deep minimum of energy and stands within such energetic state. With water at the grain interface, there might not be such a deep potential energy minimum. Despite the flexibility of the grains, no attraction can be observed. These results are also in contradiction with the results obtained with the metadynamics approach. Moreover, it is unlikely that geopolymers form a cohesive material with purely repulsive inter-grain interactions.

3.6.3 Water energy correction

The main difference between Fig. 3.18 and 3.25 is the addition of the water during grain pre-relaxation. This step seems to be key in order to allow for either attraction or repulsion between the entities.

On the role of water in the perturbation

In theory $\langle U \rangle_i \equiv U_{i+1} - U_i$ and $\langle U \rangle_{i+1} \equiv U_{i+1} - U_i$ must have same sign : either i and $i+1$ state should be of higher energy. In our case, it appears not to be the case. Fig. 3.26 shows the distribution of potential energy differences for different distances and for both fully protonated ($d = 0$) and highly deprotonated ($d = 10$) cases.

Opposite signs illustrates that the forces applied by perturbing the system are the same in both forward and backward direction : $\langle \Delta U \rangle_i \equiv U_{i+1} - U_i$ and $-\langle \Delta U \rangle_{i+1} \equiv U_i - U_{i+1}$ are similar. These perturbations, as displacement of one grain closer and away to the other, should generated respectively an increase ($\langle \Delta U \rangle_i \geq 0$) and a decrease $-\langle \Delta U \rangle_{i+1} \leq 0$) of the potential energy. In both forward and

backward directions, the moved grain gets shifted from its position of a distance δd. It feels a shift in potential energy originating from its neighboring water molecules and the second grain. Since the magnitude of energy shift is of same order and same sign for different grain displacement directions, it probes that the energy difference caused by neighboring water overwhelms the grain-grain one.

Fig. 3.27 display the average energy variation $\langle \Delta U_i \rangle$ performing the perturbation. The average is made over the whole set of sampled configurations involved in the PMF calculations.

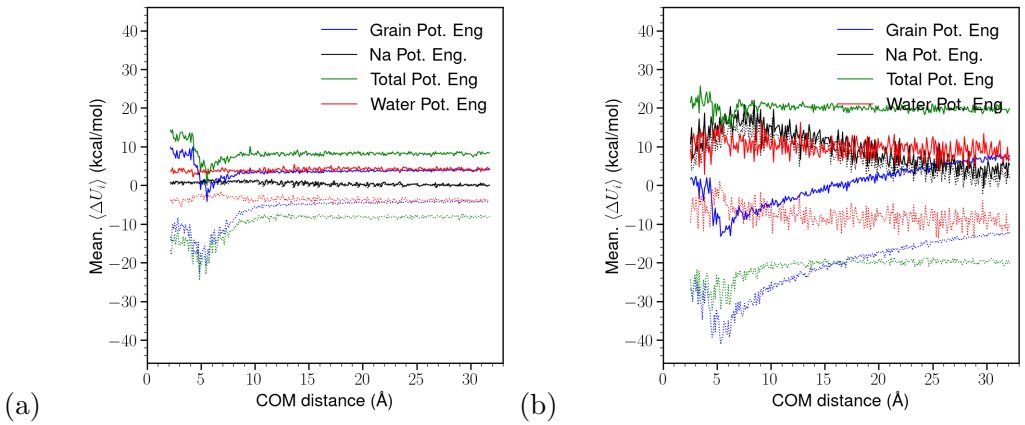

Figure 3.27: Mean energy differences when performing the perturbation with a step of $\delta d = 0.1$Å. The panel (a) corresponds to the protonated grains while panel (b) to deprotonated ones ($d = 10$). For both plots, the straight lines correspond to a perturbation of state i to $i+1$ (forward) and the dashed ones to a perturbation from state $i+1$ to i (backward). The different colors accounts for the energy felt by a group of atoms w.r.t. all the others (e.g. for the blue, as the sum of grain-grain, grain-water,grain-ions interactions).

Both energy variations and pressure present larger variation in the deprotonated case. According to the plots of grain energies, there is a well in energy differences, at distances between 5 and 10Å. As a system would favor a minimum of energy, this accounts for an attraction. Still, water and ions should also play a role in the grain-grain interaction. While in the protonated case, the perturbed energy of water and ions influence only a few the total potential energy differences (blue and green curves are very similar, only shifted by a constant), they play a more important role in the second case. As they undergo larger fluctuation, these ionic and water potential energies flatten the green curve, as a screening effect of grain-grain interaction that may even lead to a repulsion of the grains.

In literature, most potential of mean forces calculations showed to be water sensitive. Zhu *et al.* 2022 added water after the generation of states in the void [63], preventing the detrimental insertion of water at unfavored locations in clays PMF calculations. Masoumi *et al.* 2017 had to displace water molecule at box edges to limit the screening effect of water between CSH nanolayers [62]. Ebrahimi *et al.* 2014 [34] deleted the one too close to the interface of CSH platelets.

In these cases, interacting structures also had ionic adsorbed layers, which is not our case. The presence of ions at the grains vicinity may influence, because of electrostatic repulsion, the grains ability to deform and their interface. In the case of amorphous grains, the interstitial medium appears to be more complex, with insertion of water molecules in between grain branches and the non-formation of ionic layers, resulting into interstitial screening effects that can not be easily get ridden of.

Correction of the potential energy

We recall that the free energy perturbation ΔG is obtained using the total potential energy shift Δu of the system from

$$\exp\left(-\beta\Delta G\right) = \frac{\langle \exp\left(-\beta\Delta u/2\right)\rangle_i}{\langle \exp\left(+\beta\Delta u/2\right)\rangle_j}. \tag{3.10}$$

The influence of water

The energy u contains all potential energy interactions, i.e. grain-grain, grain-water, grain-ions, water-ions, water-water and ions-ions (and symmetric contributions). From the above discussion, water interactions may hide the effective shift in potential energy arising from grains interactions. Therefore, we propose to shift the system potential energy as follow :

$$(\Delta U(i \to i+1))' = \Delta U(i \to i+1) + \Delta U_{\text{water}}(i \to i+1). \tag{3.11}$$

Here, $\Delta U_{\text{water}}(i \to i+1)$ denotes the potential energy change due to water. This correction aims to cancel the constant slope that arise from calculations in the direct free energy calculations method (cf Eq. 2.31 in Chapter 2), shown from panels (a) and (c) in Fig. 3.28. In fact, for a given state transition, if a constant shift $\delta U = \langle \delta U \rangle$ is applied to ΔU so that $(\Delta U)' = \Delta U + \delta U$, the free energy variations transforms as

$$(\Delta G)' = -\frac{1}{\beta} \ln \left\langle \exp(-\beta(\Delta U))' \right\rangle = -k_B T \ln \langle \exp(-\beta(\Delta U)) \rangle - \delta U = \Delta G - \delta U. \tag{3.12}$$

In practice, this correction term is constant and corresponds to the potential energy shift obtained for the state at the longer distance. As the grains are the furthest away, the cut-off of interaction is smaller than the smallest distance between grain atoms to the other ones : only displacement with regard to water (and ions, even though they do not stand as close to the grains to the perturbation level) induces a change in potential energy. We hereby define a constant correction that can be applied according to Eq. 3.12 to the computed PMF.

Fig. 3.28 displays the PMF calculations using both Simple Overlap Sampling (SOS) and DA (Direct Averaging) with different ways of computing the ΔU energy difference (either forward, backward and average of both).

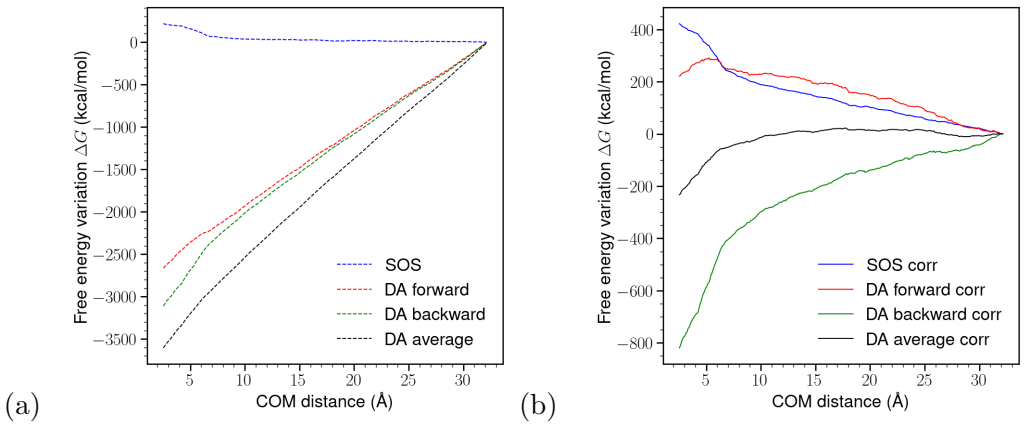

Figure 3.28: Correction of PMF calculations in the highly deprotonated cases ($d = 10$). The dashed lines/(a) panel represent the curves obtained from the perturbation theory. Straight lines/(b) panel shows the corrected curves. Correction is applied according to Eq. 3.12 and the value of energy shift at large distance. The different colors corresponds to the method used for free energy calculations. SOS refers to the SOS sampling as in Eq. 3.10 from Chapter 2. The different DA calculations have been performed with Eq. 2.38, where the energy difference is taken (in absolute value) in the forward ($\langle \Delta U \rangle_i$), backward ($\langle \Delta U \rangle_{i+1}$) and by average of both ($(\langle \Delta U \rangle_i + \langle \Delta U \rangle_{i+1})/2$).

Panels (a) displays curves with a constant slope, as an accumulation of a constant shift. In fact, applying the correction leads to panel (b) that do not show such linear behavior anymore. Despite this correction, there remains strong differences between the different approaches, accounting for a failure of our perturbative approach to evaluate the PMF for small aluminosilicate grains in water.

Symmetrization of the distributions

Perturbative theory requires likeness between the studied states as previously discussed, recalling Fig. 3.15. Still, from Eq. 2.33 in Chapter 2, our energy distributions of opposite sign should overlap, i.e. that their distributions of energy differences must be symmetric around 0kcal/mol.

We propose a symmetrization of potential energy shifts, aiming to artificially rebuilt the symmetry within the system. Both energy shift in the forward and backward direction are shifted from a mean value in order to make $\langle \Delta U \rangle_i$ and $\langle \Delta U \rangle_{i+1}$ symmetric according to Eq. 3.13. The associated PMF results are shown in Fig. 3.29

$$\begin{cases} \langle \Delta U \rangle_i = \langle \Delta U \rangle_i - \frac{\langle \Delta U \rangle_i + \langle \Delta U \rangle_{i+1}}{2}, \\ \langle \Delta U \rangle_{i+1} = \langle \Delta U \rangle_{i+1} - \frac{\langle \Delta U \rangle_i + \langle \Delta U \rangle_{i+1}}{2}. \end{cases} \tag{3.13}$$

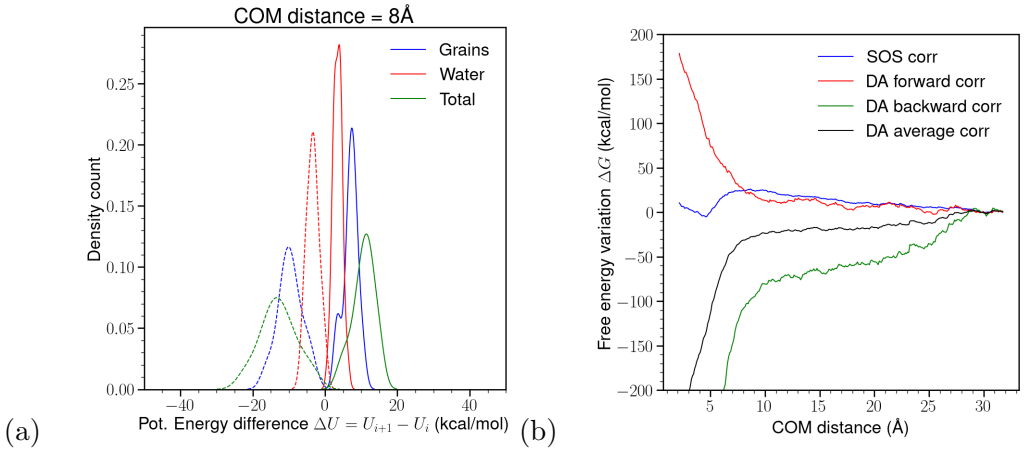

Figure 3.29: Correction of the potential energy difference distributions. Panel (a) shows an example of symmetrized potential energy variation distributions obtained from 3.13. The color refers to the energy felt by the different groups of atoms. Panel (b) displays the PMF obtained from these symmetrized energy differences. Different methods are displayed.

Even with potential energy centered (and so a good overlap of energy difference distributions), the obtained PMF depends on the used calculation technique. This illustrates that the calculations do not converge for our system. Despite canceling the error, at least partially, which can not be quantifies, the SOS approach fails to predict the switch between attractive/repulsive behavior upon pH modifications. This could be related to sampling issues at close distance.

3.7 On the role of the sampling

The FEP technique requires a good importance sampling, i.e. a sampling of very different configurations of the same microstates. Until now, it was shown that the overlap of potential energy differences are sufficient for the calculations to converge. At the difference with CSH grains and clay platelets, the amorphous structures have a flexibility that induces a very large number of possible microstates to visit and so, very long simulations to perform to visit. As a consequence, it may be more relevant to perform metadynamics simulation to compute free energy variations rather than run very long

equilibrium states to perform FEP calculations. As an enhancing sampling method, temperature bias prevent the system to remain within a too deep local minimum for a long time.

In order to investigate the effect of the sampling, we have extracted configurations from a metadynamics trajectory of 2ns every 5ps, each corresponding to a given COM distance ranging from 6 Å to 25 Å. Configurations are then binned within bins of size $\delta d = 0.1$ Å so that a perturbation of same size can be processed forward and backward and FEP calculations performed with the SOS method. FEP calculations are performed for grains with deprotonation degree of $d = 0, 4$ and 10 and the results plotted in Fig 3.30.

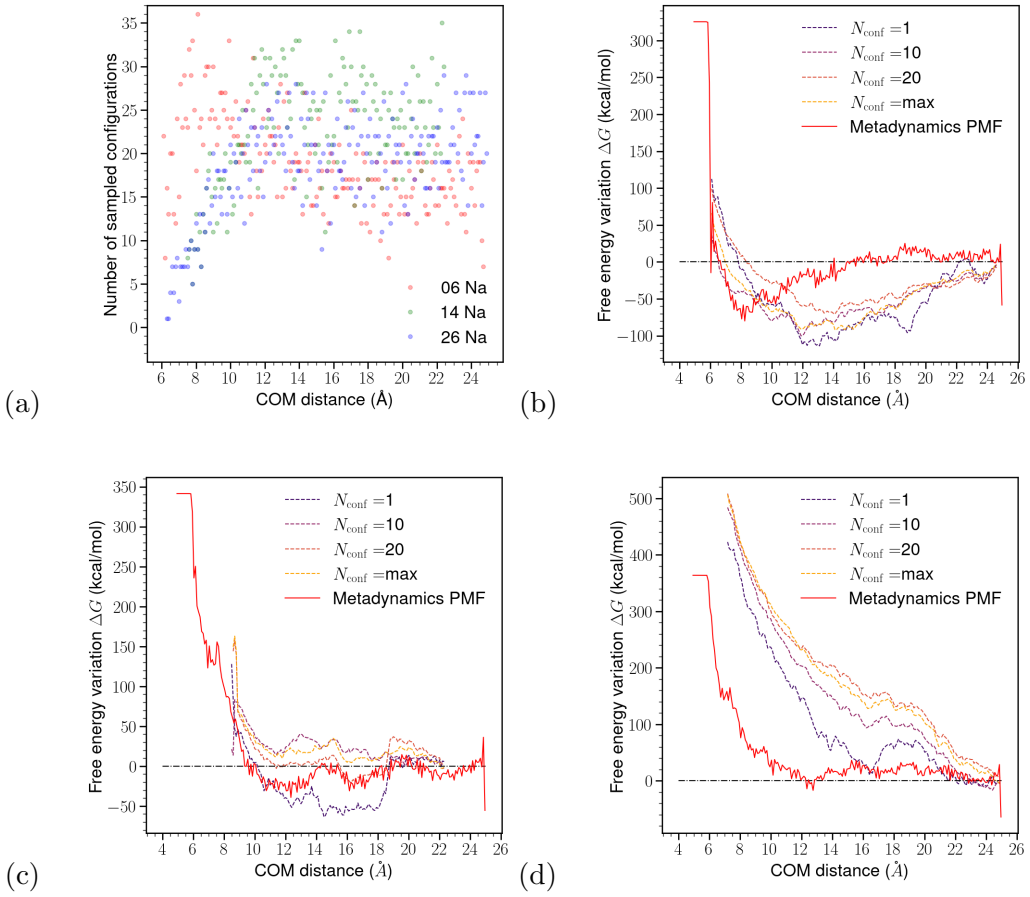

Figure 3.30: (a) Number of configurations per COM distance bin from metadynamics samplings. Red, green and blue colors correspond to deprotonation degrees of $d = 0, 4$ and 10. (b)/(c)/(d) panels are PMFs computed applying FEP calculations to configurations sampled with metadynamics with the SOS method for (b) protonated ($q = -3$), (c) $q = -7e$, and (d) $q = -13e$ grains. The plots are shown for a different number of configurations, "max" referring to the maximum number of configurations binned for each distance, shown in panel (a).

Using this approach, the FEP method is able to qualitatively reproduce either the attractive or repulsive behavior of interaction as metadynamics does. For the protonated case (panel (b)), the well locates around 13Å with a value around -100kcal/mol, contrasting with the one of -70kcal/mol obtained from the sum of the bias, at a COM distance of 8Å. For the most deprotonated grains, strong repulsion at 200kcal/mol is seen, at a distance of 14Å while metadynamics foresees it around 8Å.

Although the small number of configurations does not allow to carry a quantitative study, it seems to be consistent with metadynamics. Increasing the system charge increases the repulsion between the grains, which is physically expected from the presence of ions between the aluminosilicate grains. Note that with a sampling performed using metadynamics the sampled configurations shows far less correlation. During these simulations, the COM distance between aluminosilicate grains changes,

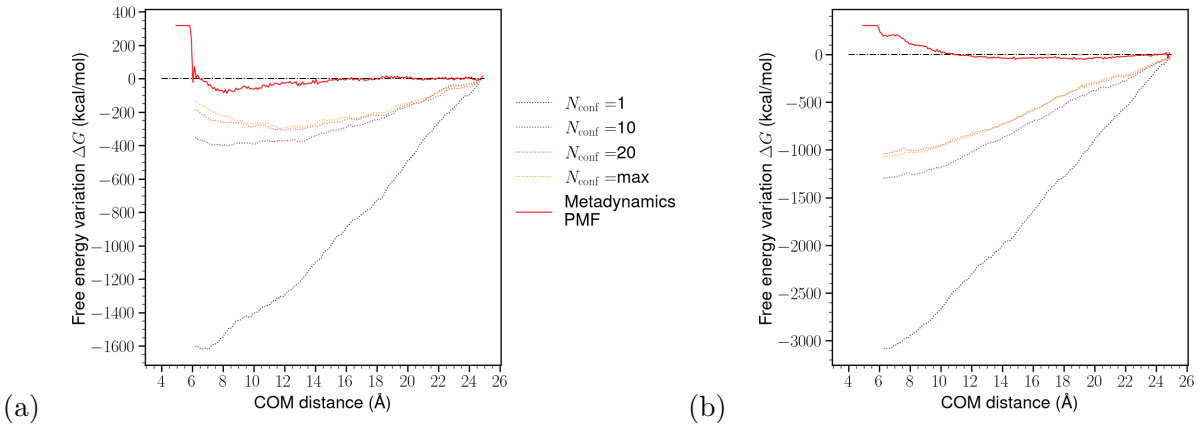

Figure 3.31: Potential of Mean Forces obtained from metadynamics sampling using the Direct Average (DA) calculations for (a) fully protonated and (b) highly deprotonated cases. The plots are shown for a different number of configurations, "max" referring to the maximum number of configurations binned for each distance, shown in Fig. 3.30 panel (a).

allowing for water molecules to insert/leave the grain-grain interface. This is not the case when performing equilibria at fixed COM distances. As previously mentioned, using the relaxation without water, we observed that the PMF were attractive using the FEP approach. On the opposite it has been extensively discussed that they are always repulsive using the configurations with a relaxation after adding the water. Seemingly, for the 26 Na cases, the metadynamics results show that the water remains in between the grains and therefore the potential is repulsive. However, in the 6 Na case, the water should be partially depleted fro m the interface. The fact that metadynamics trajectories are performed continuously with grains being approached and separated hundreds of times allows water to enter/exit the inter-grain region. In the opposite, when the system is relaxed in water, the water is being trapped at the interface and the PMF is made artificially repulsive. Performing a longer MD trajectory is not a solution. The most adequate solution is enhanced sampling.

Comparison of FEP and metadynamics

In terms of computational costs, the FEP approach requires about 600 trajectories of 2ns for each system while metadynamics requires a single 2ns simulation. As a result, metadynamics is about 500 times faster than FEP. Moreover, FEP requires complex data management with a large number of configuration files. On the other hand, metadynamics requires more testing of the meta parameters: bias temperature, Gaussian weights, etc. This needs to be done case by case to ensure that the system entirely explores the collective variable space at a reasonably slow pace to make sure that it probes all the minimum.

For our system the perturbation approximation overpass its limitations and despite testing different samplings, that can solve one of the issues, there is still systematic errors in direct averaging calculations as shown in Fig. 3.31. As described in this chapter, the systematic errors are most probably due to fact that moving the grain to the left or to the right results in the same interaction with water. For systems containing small grains in a liquid, it appears that the metadynamics approach is more reliable than the perturbation approach.

3.8 Literature PMFs of clays and CSH

While investigation of the PMFs for geopolymers using a FEP approach have, to our knowledge, never been performed, this method has already performed well on other systems such as clay and CSH [34, 33, 74, 97, 63]. Still, a difference is that geopolymers are formed by small ellipsoidal clusters that can interpenetrate.

As aluminosilicate systems, one might expect results comparable to the ones obtained in these previous studies, even though the shape and orientation of the clay platelets and CSH layered-nanoparticles can highly influence the order of magnitude of interactions. These results are discussed below and compared in Fig. 3.32.

3.8.1 Clay interactions

Ebrahimi et *al.* [34] has studied edge-to-edge and face-to-face interactions of two Wyoming Na-montmorillonite platelets immersed in water. Using such nano-layered grains, they built their simulations using finite-length layers with water in between each. The application of the FEP procedure allowed to obtain potential of interaction for both orientations.

In the edge-to-edge case, a single well is seen around $r_{\min} = 45\,\text{Å}$, with a depth of $\Delta G(r_{\min}) = -80\text{kJ/mol} = -19\text{kcal/mol}$. However, in the face-to-face case, the potential of interactions present two wells with depths around $\Delta G(r_{\min}) = -200\text{-}250\text{kJ/mol} = -50\text{-}60\text{kcal/mol}$. This study was carried out with grains of dimensions $20.9\,\text{Å} \times 36.3\,\text{Å} \times 6.7\,\text{Å}$. The well depth for the per-surface interaction are, for edge-to-edge and surface-to-surface estimated around : -0.17kcal/mol/Å^2 and -0.08kcal/mol/Å^2.

These results, obtained by Ebrahimi et *al.*, have been discussed by Zhu et *al.* [63] who computed Na-illite and Na-smectite PMFs. The first one has an attractive well of $-0.5\text{kJ/mol/Å}^2 = -0.12\text{kcal/mol/Å}^2$ at a center-to-center distance of 11 Å. The second appears to be fully repulsive. They have respectively been fitted with a Gay-Berne and a DLVO (Derjaguin, Landau, Verwey and Overbeek) model.

3.8.2 CSH interactions

Among the most recent works on CSH, we retrieve the one performed by Masoumi and Ebrahimi [74, 97].

In their early 2019 paper, layered-CSH globules of size $13.2\text{Å} \times 24.5\text{Å} \times 12.20\text{Å}$ are built and immersed in water to interact. Such globules are built with different Ca/Si ratio, allowing to studied the influence of the counter-cation concentration on the PMF. A common characteristic of the PMF obtained for all calcium contents is a well of $\Delta G(r_{\min}) = -110 k_B T\text{nm}^2 \approx -0.65\text{kcal/mol/Å}^2$ at ambient temperature. The well position is located around $r_{\min} = 12.3\,\text{Å}$ for Ca/Si$\leq$ 1.5 and moves backward to $r_{\min} = 10.5\,\text{Å}$ as the calcium content increase. It appears to be weaker when Ca/Si= 1.5, with a depth of $-45 k_B T/\text{nm}^2 \approx -0.27\text{kcal/mol/Å}^2$.

Performing a FEP on grains in water for face-to-face and edge-to-edge configurations [97] allowed to obtain an attracto-repulsive PMF for the first case with a minimum $\approx -30\text{kcal/mol/nm}^2 = -0.3\text{kcal/mol/Å}^2$ and a fully attractive one for the second, with a minimum of $\approx -5\text{kcal/mol/Å}^2 = -0.05\text{kcal/mol/nm}^2$ at 41 Å. These results have been fitted using a Gay-Berne potential.

3.8.3 Comparison of the PMFs

All the results obtained in literature are summarized in Table 3.4.

Comparing our results to the one from CSH and clay allows to see that our protonated geopolymer grains interaction stands between the one of clay and CSH. CSH tend to favor attracto-repulsive potentials while clays are mostly attractive. Thanks to their amorphous structure and flexibility, geopolymer grains are allowed to interpenetrate each other. This will shift the minimum of interactions at smaller distances than for layered-aluminosilicate materials which are geometrically restrained.

These geometrical considerations also plays a role on the strength of interactions. While interpenetrating, the Coulomb repulsion between the aluminosilicate chain components can increase, favoring a repulsion of the grains. In the cases of CSH and clay, the counter-cations between the layers may prevent such a strong repulsion and are even known to be at the origin of the cohesion [73].

$r_{\min}$	$\Delta G(r_{\min})$ (kcal/mol)		$\Delta G(r_{\min})$ (kcal/mol/Å^2)		Grain type and size ($x \times y \times z$ (Å^2))
(Å)	Face-to-face	Edge-to-edge	Face-to-face	Edge-to-edge	
11/45	-60.5	-23.8	-0.08	-0.17	Clay platelets, $20.9 \times 36.3 \times 6.7$ [34]
11	-91	×	-0.12	×	Clay platelets, $20.9 \times 36.3 \times 6.7$ [63]
10.5/41	-96.6	-16	-0.3	-0.05	CSH layers, $13.2 \times 24.5 \times 12.2$ [97]
10.2	-87	×	-0.27	×	CSH globules (Ca/Si= 1.5), $13 \times 24.5 \times 12$[74]
12.5	-209	×	-0.65	×	CSH globules (Ca/Si= 1.1), $13 \times 24.5 \times 12$[74]
	Flexible				
8	-66.4		-0.18		Geopolymer ellipsoid, $11.4 \times 16.6 \times 14$

Table 3.4: Summary of renormalized PMF calculations using molecular simulations for clay and CSH. Geopolymer grains have been modeled as a prolate ellipsoid with $a = 5.7$Å$, b = 8.3$Å$, c = 7$Å. The contact surface has been obtained according to Eq. 4.4 defined in Chapter 4. Details on the renormalization are discussed within the text.

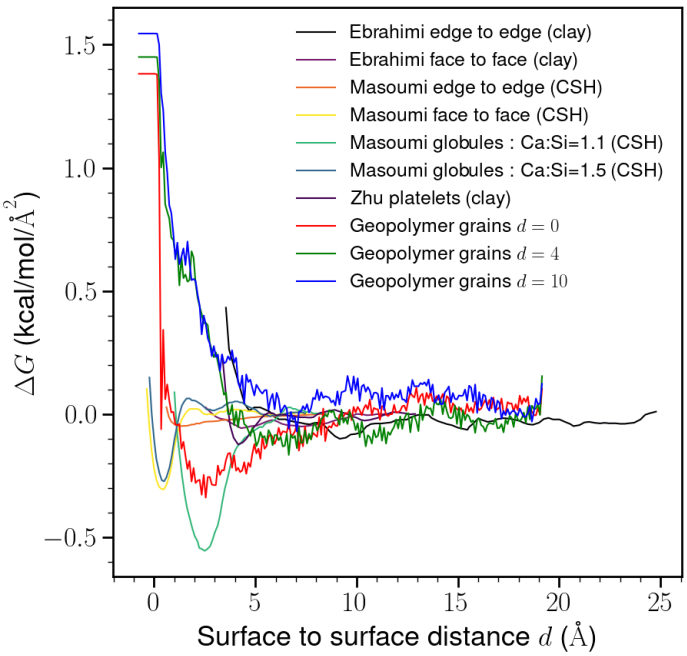

Figure 3.32: Comparison of PMFs previously obtained in the literature. Different systems have been studied, as clays and CSH. The curves are plotted as a function of the surface-to-surface distance and are normalized with regard to the particle surfaces for every case. Note that for CSH, charge-compensating ions are included in the size of the grains while for the study of clay they are not, inducing a shift in the surface-to-surface distance. In our case, the small number of ions and the flexibility of the grains do not generate such questioning. Details on key values are given in Table 3.4.

Both PMF for geopolymer and the one obtained for CSH by Masoumi et *al.* for smaller Ca:Si ratio have a minimum at the same surface-to-surface distance, around 2.8 Å. In terms of intensity, geopolymer attraction stands in the very in between clays and CSH. However, while this latter is tight (the well ranges from $[1, 6]$Å and present a small repulsive shoulder), our PMF for protonated grains is far wider and fully attractive, closer to the shape of the ones of clay. Such an widening of the curves can be attributed to the effects of surrounding ions, while these were included inside the grain definition in PMF calculations for CSH. In there, counteractions at the surface of the well shaped silicate network will create a so-called *surface charge*, acting as a repulsive barrier between the grains. For clay and, here, geopolymers, the ions may locate differently and so will not form a well-arranged barrier to generate repulsion between the two micro-structures. Further analysis from Chapter 4 will show that there is no ionic adsorption at the grain's vicinity, in opposition to clays and CSHs.

3.9 Conclusion

In this chapter are compared different ways to obtain the Potential of Mean Forces for aluminosilicate grains in solution. The first taken approach, motivated by similar works performed over clays and CSH is the Free Energy Perturbation technique, coupled with the Simple Overlap Sampling for a faster convergence of the calculations. While the convergence of the method is ensured with regard to different parameters in a case, we have realized that the way our configurations are initiated can strongly influence the resulting grain-grain interactions.

At first stance, grains are relaxed in void and can approach each other in a dry environment before the sampling of configurations is performed within water. Under this framework, attraction is observed at short range, for different degree of deprotonation of our grains. Adding the water before approaching the entities to initiate state equilibria then produce repulsive interactions, no matter what the grain surface charge is. A deeper investigation had us realize that water plays an important role in the potential energy difference obtained performing the perturbation and prevent them to properly reproduce the grain-grain interactions. A systematic error is found. Despite corrections applied to the calculations, there is no ability for the calculations to converge from both approach, to a consistent interaction regime. This is attributed to the small size of our amorphous aluminosilicate skeleton, that differs from layered materials platelets and globules previously discussed in the literature.

Metadynamics simulations allowed new calculation of the PMF, from a different approach, resulting in a transition from attractive to repulsive interaction as the grains' charge increases. These results are quantitatively recovered performing FEP calculations to configurations obtained from this enhanced sampling method. This enlightens that the complexity of our system should require far more sampling for the FEP calculations to converge. In overall, the metadynamics appear to be a better performing methods (either from a quantitative and CPU time point of view). Moreover, the found results stands within the order of magnitude of CSH and clays cohesive interactions.

Chapter 4

A metadynamics study of aluminosilicate interactions

While aluminosilicate oligomers stand as small and amorphous species, measuring their interactions in water appears to be a tedious task. The analogy with clays and CSH lead us use to the Free Energy Perturbation (FEP) method to evaluate how they may interact in water. However, from the previous Chapter, it is shown that such a method may not be the more efficient to evaluate Potential Of Mean Forces (PMFs) for small aluminosilicate grains. The use of Metadynamics has allowed a enhanced sampling that managed to evaluate PMFs based on both thermodynamic integration and on bias addition, confirming global tendencies of either attraction and repulsion depending on the grains' surface charge.

The role of grain flexibility has shown that relaxation is required (even in a dry relaxation case) in order to account for inter-grain cohesion. While we expect grain surface properties to influence its rigidity (and so, interactions), grain geometry will be studied within this chapter, over different deprotonation degrees. From a chemistry point of view, protons (H^+), oxygens (O^-) and sodium ions (Na^+) might have a strong effect on local interactions.

In the continuity of free energy calculations performed using Metadynamics, we use this method to study the effect of charge density on the grains in solution. The role of the deprotonation degree on the interaction is discussed alongside the ability for the grain to deform and reorganize. The contributions of the different types of interactions is presented, in order to originate either the attractive or repulsive behavior of our species in water. Thanks to a meta-grain approach, the key role of water in geopolymer cohesion is enlightened.

4.1 Grain deprotonation : influence of the ionic contribution

Previous chapter probed a dependence of aluminosilicates grains in water on their deprotonation degree and their flexibility. These dependence might relate to either their surface charge and/or an effect of surrounding ions. In this section, we discuss the influence of the deprotonation on grain geometry and analyze the behavior of ions to investigate how these two parameters can induce either attraction or repulsion.

Starting from our fully protonated grain, a surface charge is generated, by removing edge hydrogen atoms as discussed in Chapter 3. Fig. 4.1 shows a single grain that have been deprotonated at d random sites, and so, that has d Na^+ ions added to compensate for the charge deficit. We recall that the charge of edging oxygens is adapted from $0.95e$ to $0.95e - (+0.425e - 1e) = 1.525e$ according to the inter-atomic potential charge parameters.

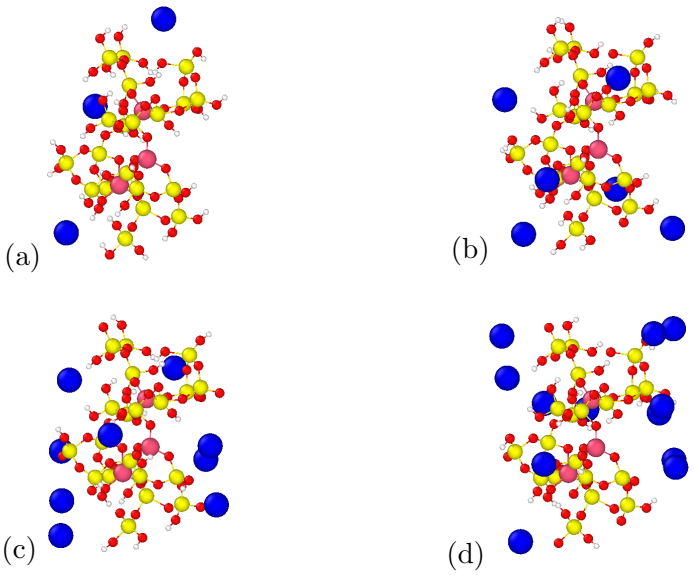

Figure 4.1: Representation of the grains with a deprotonation degree d of (a) 0, (b) 3, (c) 6, (d) 9. Note that the number of ions around the grain is given by $N_{\text{ions}} = d + 3$ as 3 ions are initially set to counter balance the $Al(OH)_3^-$ in the aluminosilicate structure.

4.1.1 Potential of mean force : a charge dependence

For each deprotonation degree, metadynamics molecular simulations are performed, resulting in PMFs shown in Fig. 4.2.

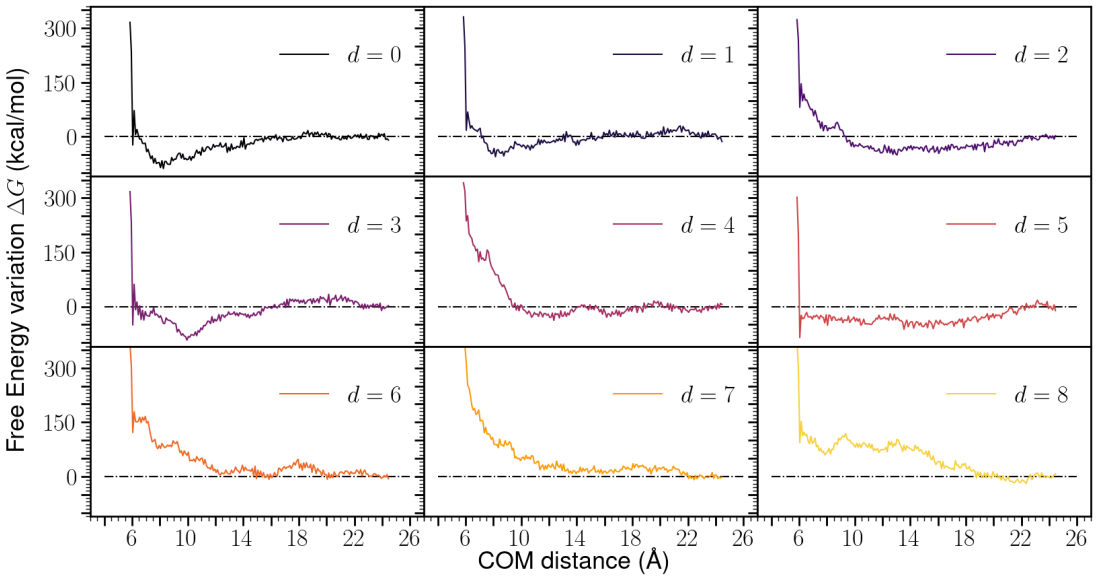

Figure 4.2: Potential of Mean Force computed using well-tempered metadynamics for different deprotonation degree d. The dash-dotted line shows the zero line, allowing the delimitation for either attraction or repulsion between the two grains.

There exists a transition path from an attractive to a repulsive behavior as the grains surface charge increases. With a surface charge higher than $\|q_{\text{grains}}\| = 9e$ (i.e. $d = 6$), the interaction are fully repulsive.

Three regimes can be seen: (i) fully attractive, (ii) transitional as a flat curve and (iii) fully repulsive.

This transition is counter-intuitive with respect to ionic correlation forces accounting for attraction between electrolytes as their charge increase. This is the case for CSH, in which cations are adsorbed at the grains interface, compensating surface charge.

4.1.2 Ion displacement

As amorphous materials, geopolymer grains do not present a linear surface charge that might induce ionic layer adsorption. However, one may wonder whether this is a propensity for ions to stands at the grain vicinity to compensate for local charge deficit. Starting from a configuration shown in Fig. 4.3, we analyze the trajectories of sodium ions at equilibrium.

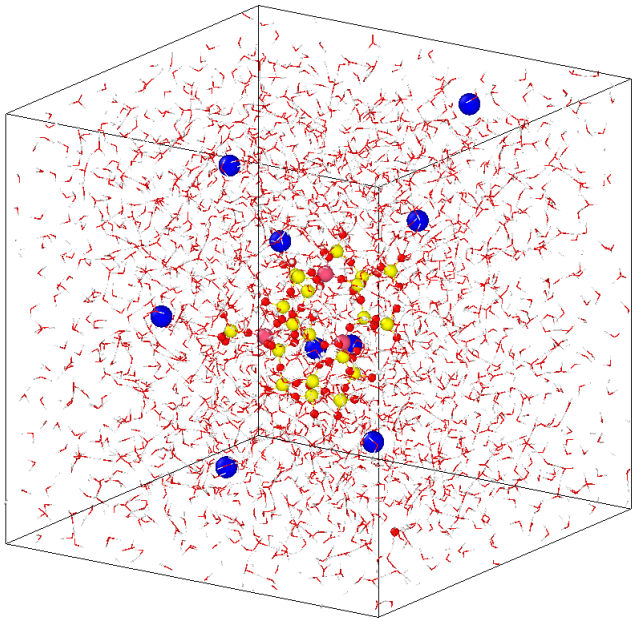

Figure 4.3: Snapshot of the simulation box with one grain ($d = 6$) immersed in water and ions. Red, yellow, pink, white and blue spheres respectively represent oxygen, silicon, aluminum, hydrogen and sodium atoms. Red and white lines are water molecules.

By placing a single grain in a box of size 40Å×40Å×40Å, filled with water, ions are set randomly within the simulation box. A NVT molecular dynamics run under ambient conditions ($T = 300$K and $P = 1$atm) is performed for 10ns. Data are sampled over the last 9ns. Simulations are performed for a deprotonation degree d ranging from 0 to 9.

Ionic trajectories

Trajectories of each ion (numbered from 1 to 9) can be analyzed w.r.t. its distance to the grain surface (as the minimum distance of the ion to any atom from the grain structure). It is shown in Fig. 4.4.

Fig. 4.4(a) shows, that ions can move freely within the simulation box. However, ions can be *captured*: standing close to the grain surface (distance decreasing to 0 Å, with low oscillations). As a example, it is the case for the 9th ion during most of the trajectory. After 7ns, ions 6 and 7 are also located close to the grain. Still, this captured state is not permanent. After 5ns, ion number 3 leaves the grain vicinity it has stand in for more than 2ns. The number of neighboring ions is not constant during the run. There is no need for the grain to be surrounded by a given number of ions. This may be counter-intuitive as one may expect ions to compensate the charge locally.

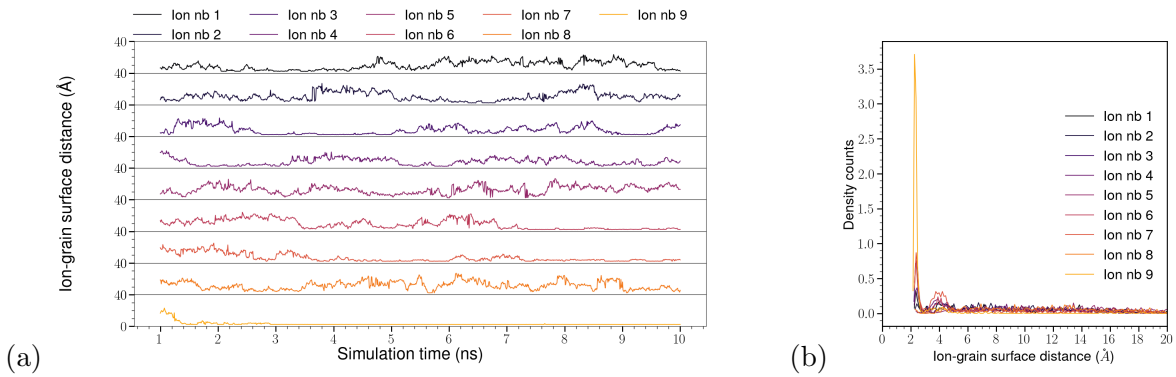

Figure 4.4: (a) Distance of each ion to the grain surface. (b) Radial distribution functions averaged over the full trajectory.

From the radial distribution of ions, in Fig. 4.4 (b), two distances seemed to be favored by the ions to sit close to the grain, at 2.5 and 4Å. Note that this value around 2.5Å is in good agreements with distances measured in glasses and crystals using either NMR, SAXS or Molecular Dynamics [153, 154, 155] and also between Na^+ ions and water oxygens in concentrated NaOH aqueous solutions [11] (consistent with both theory and experiment [156, 157]). A part of the sodium are acting as charge-compensating ions. Other ones are solvated. This result matches the discussion on the dissolution of aluminosilicate species in sodium hydroxides solution[105].

By considering an area ranging at a distance of 5Å from the grain surface (according to radial distribution functions from Fig. 4.4 (b)), it is possible to evaluate the average number of ions at a grain vicinity for each d, as shown in Fig. 4.5.

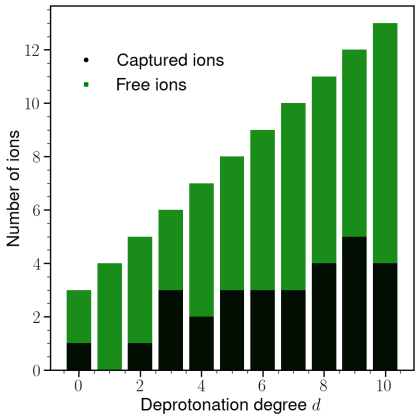

Figure 4.5: Proportion of ions captured by the grain during our simulations. In green is displayed the total number of ions and in black the one belonging within an area of 5Å around the grain surface. The number of ions in the 5Å area is computed at each timestep and averaged over the full trajectory.

Because of the increasing number of ions in our simulations, the number of captured ions by the grain can increase with the deprotonation degree. However, there does not appear to be an absolute relation between these quantities.

Ionic energies

Dynamics of ions is related to both its kinetic and potential energy . In Fig. 4.6 are shown potential energy distributions of each ions during equilibrium runs.

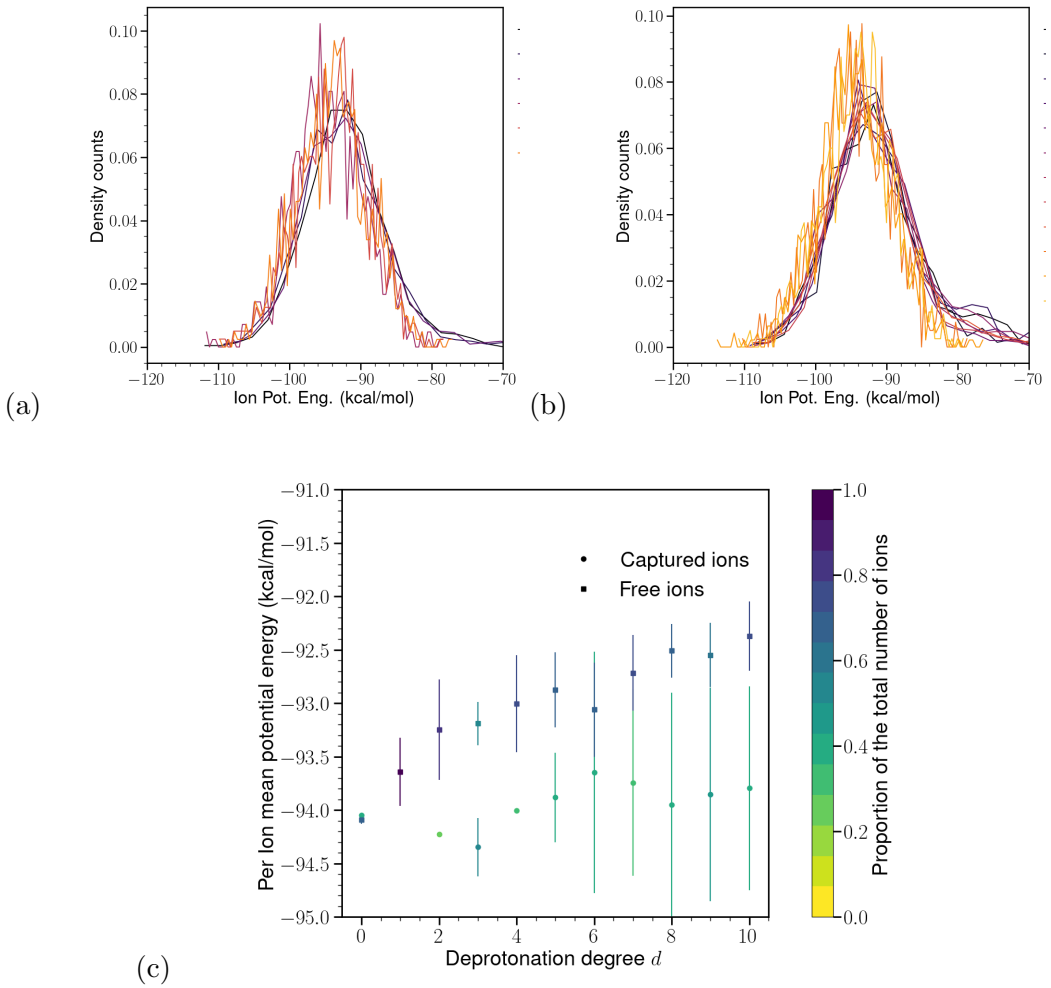

Figure 4.6: Distribution of potential energy of each sodium ion for a deprotonation degree d of (a): 3, (b): 9. Each color refer to an ion, according to coloring already defined in Fig. 4.4. (c) Mean potential energy for captured ions as a function of the deprotonation degree. The dots correspond to captured ions and the squares to free ones. Color map refers to the proportion of ions either in the captured or free state: darker color corresponds to a majority of ions in the associated state.

All energy distributions are Gaussian. Associated mean values slightly change with the deprotonation degree as it is shown in Fig. 4.6 (c). The energy difference between free and captured ions is less than 2kcal/mol and can be attributed to thermal fluctuations (at ambient temperature $k_BT = 0.6$kcal/mol). Still, we denote that captured ions undergo larger energy variations as it interacts with the grain. This relates to the less smooth distributions seen from panels (a) and (b).

4.1.3 Geometrical characterization

Previous Chapter, especially Fig. 3.20 and 3.21, showed that the regime of interactions is highly related to grains ability to deform. In order to quantify grain deformations, different geometrical parameters are computed as its elongation or its asphericity (arising from gyration tensor calculations). To perform these calculations, the grain core will be defined as the aluminosilicate core, including aluminum and silicon atoms.

Maximum elongation

Grain maximal elongation does not depend on a specific direction and is obtained by computing the maximum of distance separating two atoms of the aluminosilicate skeleton.

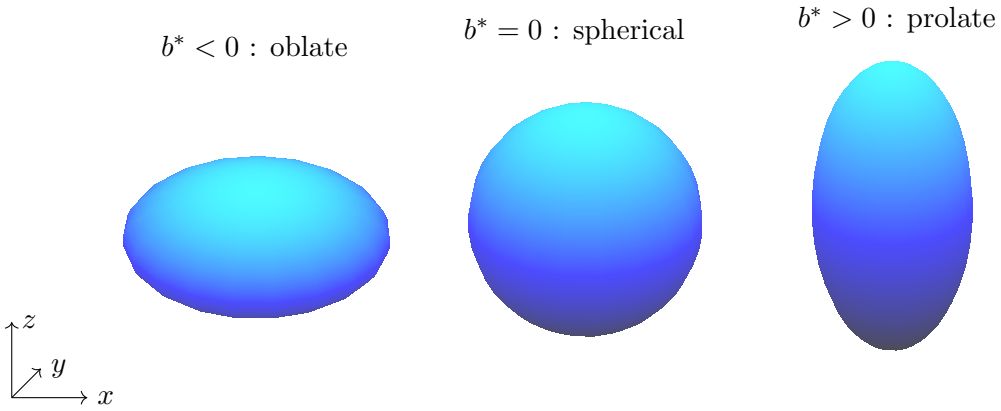

Figure 4.7: Deviation from spherical shape from normalized asphericity value

Gyration tensor

The morphology of a multi-particle system of size N can be studied with the gyration tensor. For two direction a and b in x, y or z, it is defined according to :

$$S_{ab} = \frac{1}{N}\sum_{i=1}^{N}\left[(r_a^i - r_{a,\mathrm{COM}})(r_b^i - r_{b,\mathrm{COM}})\right], \text{ with } \mathbf{r}_{\mathrm{COM}} = \frac{\sum_i^N \mathbf{r}^i m_i}{\sum_i^N m_i}, \tag{4.1}$$

$\mathbf{r}_{\mathrm{COM}}$ corresponding to the system center-of-mass.

From this gyration tensor, both gyration radius R_g and asphericity b (deviation from a spherical shape) can be computed, using S_{ab} eigen-values $\lambda_1, \lambda_2, \lambda_3$, sorted as $\lambda_1 \geq \lambda_2 \geq \lambda_3$:

$$R_g^2 \equiv \mathrm{Tr}(S_{ab}) = \lambda_1 + \lambda_2 + \lambda_3, \tag{4.2}$$

$$b \equiv \lambda_1 - \frac{1}{2}(\lambda_2 + \lambda_3). \tag{4.3}$$

From these two parameters, it is possible to characterize our grain shape w.r.t to a sphere using the normalized asphericity $b^* = \frac{b}{R_g^2}$. For a sphere, $b^* = 0$ while a positive (resp. negative) value refers to a prolate (resp. oblate) object as depicted in Fig. 4.7. Note that in 3D, with no constraint, it is possible to evaluate the deviation from a sphere with only positive value as a prolate ellipsoid turns out to be an oblate one from another angular point of view. As a consequence, only positive asphericities will be discussed in this work, to quantify the deformation.

In addition, we relate that for a prolate ellipsoid with parameters a, b, c, the surface is given as :

$$S_{\mathrm{prolate}} = 2\pi a^2 + 2\pi\frac{ac}{e}\arcsin e, \text{ where } e \equiv \frac{\sqrt{c^2 - a^2}}{c}. \tag{4.4}$$

Auto-correlation function

When considering a series of values, its auto-correlation corresponds to the correlation of its value at a time t with the value with a lag δt, i.e at a time $t - \delta t$. Considering a series X of length N, its auto-correlation function for a lag δt is given as

$$\mathrm{ACF}(\delta t) = \mathrm{E}\left[X(t)X(t-\delta t)\right] = \frac{1}{N\mathrm{Var}(X)}\sum_k (X(t)-\bar{X})(X(t-k\delta t)-\bar{X}), \tag{4.5}$$

where $\bar{X}$ designates the mean of the series $\bar{X} = \frac{1}{N}\sum_{k=1}^{N} X(t_k)$.

Correlation : the Pearson coefficient

Between two series X and Y, the correlation coefficient can be computed using the Pearson formula according to which

$$\mathrm{Corr}_{XY} = \frac{(X-\bar{X})(Y-\bar{Y})}{\sigma_X \sigma_Y}, \tag{4.6}$$

where $\bar{X}$ designates the mean of the series and σ_X is standard deviation, $\sigma_X = \sqrt{\mathrm{Var}(X)}$, i.e. $\sigma_X = \sqrt{\frac{1}{N}\sum_{k=1}^{N}(X_k-\bar{X})^2}$.

Grain geometry

An overall description of the grain geometry are shown Fig. 4.8.

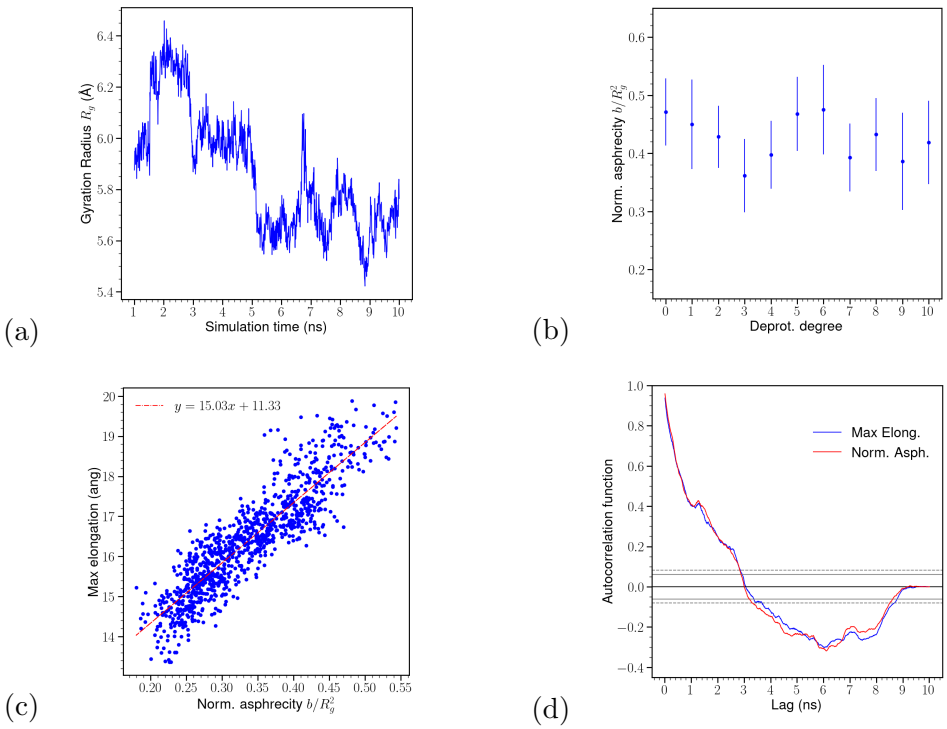

Figure 4.8: Geometrical characterization of a single aluminosilicate grain in water. (a) Gyration radius of the aluminosilicate core with regard to the simulation time for $d = 6$. (b) Normalized asphericity as a function of the deprotonation degree. Averages have been performed over the 9ns production runs. (c) Correlation between normalized asphericity and maximal elongation of the grain for $d = 6$. (d) Auto-correlation function of the series of geometrical characteristics over the simulation time. Colored lines corresponds to the geometric quantities, the gray ones either dashed and continuous display the 95% and 99% confidence interval respectively.

Panel (a) illustrates the ability of the structure to deform during an equilibrium. The gyration radius undergo fluctuations of 7% with regard to an average value of 5.9Å. Still, its average shape, related

to its asphericity/elongation, does not show any changing tendency w.r.t. the deprotonation degree as shown in panel (b). Note that panel (c) correlates asphericity to the maximal elongation.

According to Fig. 4.8 (d), there exists a correlation of the geometry at time t with its antecedent values. This plot reads as follow: if the function is within the 95%-confidence (resp. 99%) interval, there is a 95% (resp. 99%) probability that the series is not self-correlated. Out, there is 95% (resp. 99%) that it is. Here, both quantities are correlates with themselves. This illustrates that the way our grain shape evolve is path dependent during the simulation : there is no randomness and a latency in the grain deformation. If there was no auto-correlation the grain geometry would change mostly randomly (i.e. not depending on its shape at time $t - \delta t$), probing that it is very flexible. Fig. 4.8(d) probes the opposite: our grain has a certain degree of rigidity.

Role of the deprotonation

A deeper insight is taken over the auto-correlation functions (ACFs) for asphericity for each deprotonation degree and is shown in Fig. 4.9.

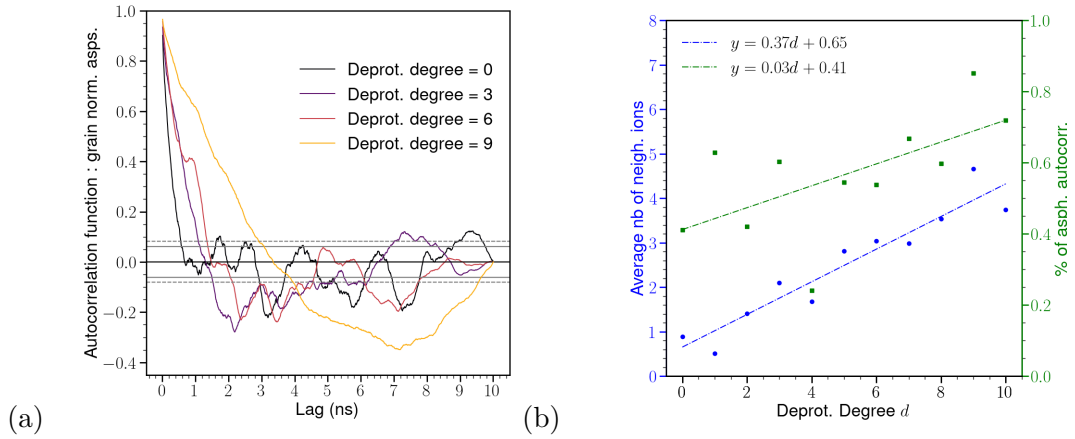

Figure 4.9: (a) ACFs of grain asphericity . (b) Number of neighboring ions and percentage lag out of the 95%-confidence interval as a function of the deprotonation degree.

As the deprotonation increases, the ACFs tend to spent less time within the confidence interval, accounting for less path-dependence of its asphericity. Fig. 4.9 (b) displays a linear evolution of the time spent out of of the 95% bands, illustrated in panel (a). This shows that the higher the surface charge is, the more rigid the grain becomes. This can also relates to the number of surrounding ions, which increases with grain deprotonation. Acting as local charge compensatory, these might cause the formation of O–Na–O, impacting grains structure.

Grain's rigidity can also be evaluated from the time required to reach a geometry that is completely uncorrelated from its initial one (corresponding to the initial slope of the ACF). Assuming that a geometry at time t becomes independent of grain's initial one when it enters the 95% confidence band, Table 4.1 can be drawn. The time required to reach an auto-correlation of 0 is also discussed.

Deprot. deg. d	0	1	2	3	4	5	6	7	8	9	10
Time decorr. (ns)	0.55	0.82	0.44	1.07	0.32	0.96	1.31	1.93	1.17	2.84	2.51
Full decorr. (ns)	0.81	0.90	1.35	1.27	0.38	1.02	1.41	3.36	1.21	3.28	2.79

Table 4.1: Minimum asphericity decorrelation time depending on the grains deprotonation degree. The decorrelation time is defined as the minimum time at which the ACF crosses the first (upper) 0.95 confidence band (dashed lines in Fig. 4.9(a)). Full decorrelation refers as the time required for the ACF to reach 0 (straight black line), i.e. a perfectly decorrelated state, for the first time.

Even though no linear relation between geometrical quantities and the deprotonation degree seems to appear, its relaxing ability is related to its surface charge: Protonated grains are more flexible and adapt quicker to change.

4.1.4 Interface medium

In the case of layered material as CSH, the role of water at the interface is primordial. Previous Chapter also probed that our systems can be strongly sensitive to its presence. As grains approaches, they deform, allowing or not for water molecules to insert/escape the interstitial area. Fig. 4.10 shows an overview of the interstitial environment as the number/density of water and ions.

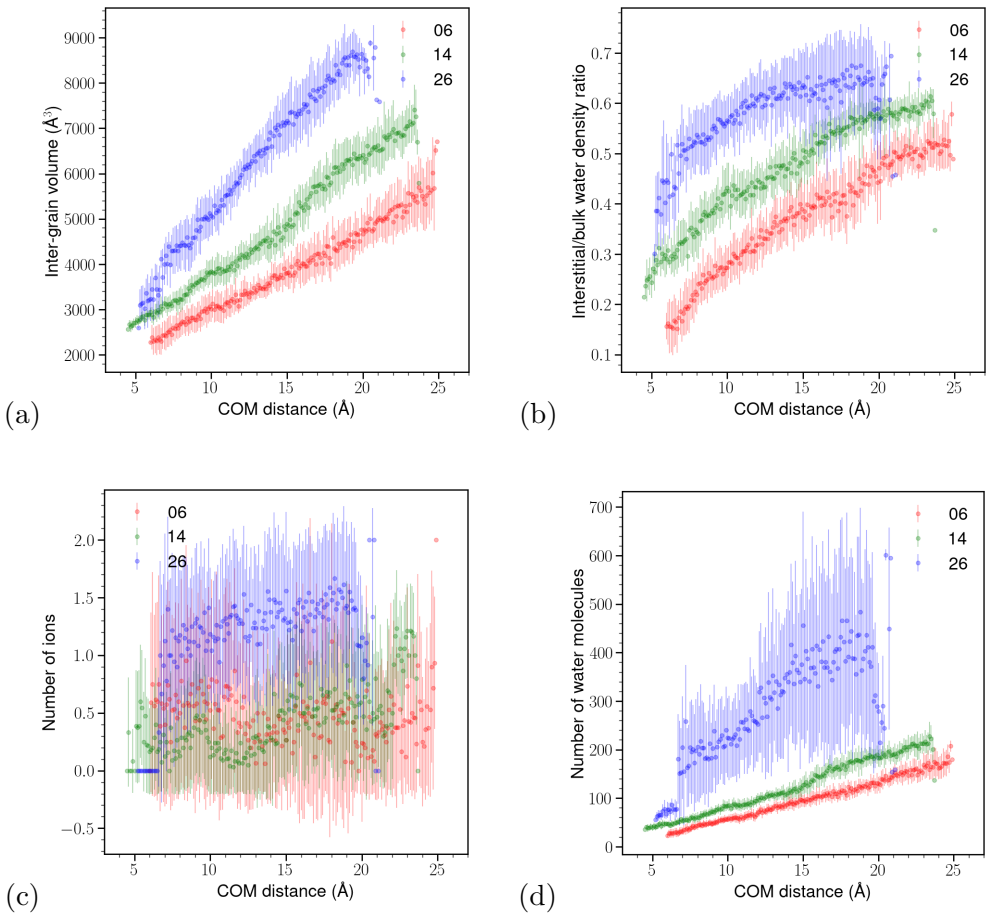

Figure 4.10: Analysis of the inter-grain area for the three cases 06, 14 and 26 respectively in red, green and blue. (a): Interstitial volume computed as a box volume based on grain elongations along the y and z axes and the COM distance (along the x-axis). (b): Water density normalized with the bulk one. (c) and (d): Number of ions and water molecules between the grains. Every quantities are computed for every configurations sampled over the metadynamics run averaged over COM distance bins of 0.1Å.

Fig. 4.10 (a) and (b) illustrate that both interstitial volume and water density between the grains are highly related to the deprotonation degree d. The increase of water molecule at the grains interface with d suggests a transition for a hydrophobic to a hydrophilic state. This transition relates to the ability of the grain to deform. With a high rigidity, grains do not deform much (see Fig. 3.21 in Chapter 3), i.e. do not let water molecules insert/leave the interface, as shown in Fig. 4.10(d). Note that at extremely close distances, the number of molecules is almost 0 since grains are almost merging.

In opposition to the case of CSH [89, 62] and clays [63], there does not seem to be any ion adsorption at the interface, echoing previous discussion from which these can move freely within the simulation

box.

4.1.5 Perturbation and metadynamics discussion

The discussion on water at the grain-grain interface echoes Chapter 3 PMFs obtained using three different approaches: (i) FEP calculations with a dry initiated interface ; (ii) FEP calculations with a wet initiated interface ; (iii) Well-tempered metadynamics. These are illustrated in Fig. 4.11. With dry initial interfaces, accounting for a hydrophobic regime, all the computed PMFs were attractive. In opposition, in the hydrophilic regime, interactions were always found to be repulsive.

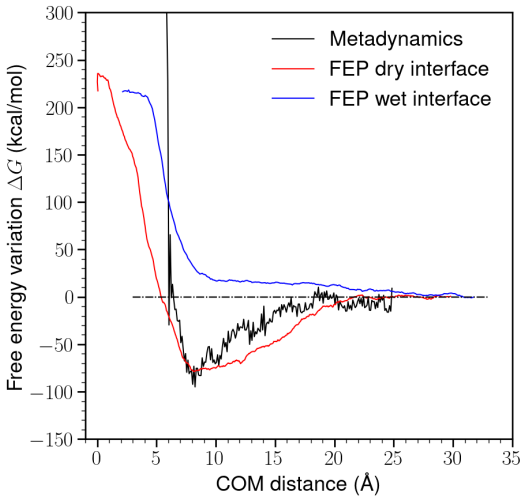

Figure 4.11: Potential of Mean Forces obtained with metadynamics and with FEP calculations in dry and wet interface scenarios as described in Fig. 3.24 in Chapter 3. The dash-dotted lines is the zero line.

As an enhanced sampling method, metadynamics allows to visit a large variety of states that our classical molecular dynamics equilibria may miss. This was illustrated from Fig. 3.22 in Chapter 3: very different configurations can be visited at a same COM distance. This accounts for a sampling of very different water quantities at the grain-grain interface, as seen from the largest standard deviations on Fig. 4.10(d). Indirect consequence is that this allows the system to chose whether it prefers an hydrophilic or hydrophobic interface, while this one was forced to one or another with the perturbative approaches.

Thanks to metadynamics enhanced sampling, the transition from attraction to repulsion between aluminosilicate grains can be put through to the grains ability to deform and relates strongly to a transition from a hydrophobic to hydrophilic interface.

4.2 Hydrogen bonds

Hydrogen non-covalent bonds exist between the two grains if a hydrogen of one grain gets close enough to an edge oxygen of the other one. These bonds might appear for distances shorter than 3.4Å if the H–O-H ranges between 120 and 180°[158]. Once these criteria have been set, it is possible to evaluate the bonds formation between the entities as a function of the distance as in Fig. 4.12.

Lower deprotonation allows the formation of more bonds. When deprotonating the grains, less hydrogen atoms are available at the grain-grain interface. Recalling Fig. 4.10 (b), it is also worth denoting that in the $d = 10$ case, shown in Fig. 4.12 (d), much water is located between the two aluminosilicate entities that for the two other cases. A direct consequence is the prevention of hydrogen bonds

forming, illustrated here. In addition, we denote that bonds form equivalently from the left grain to the right one and reverse.

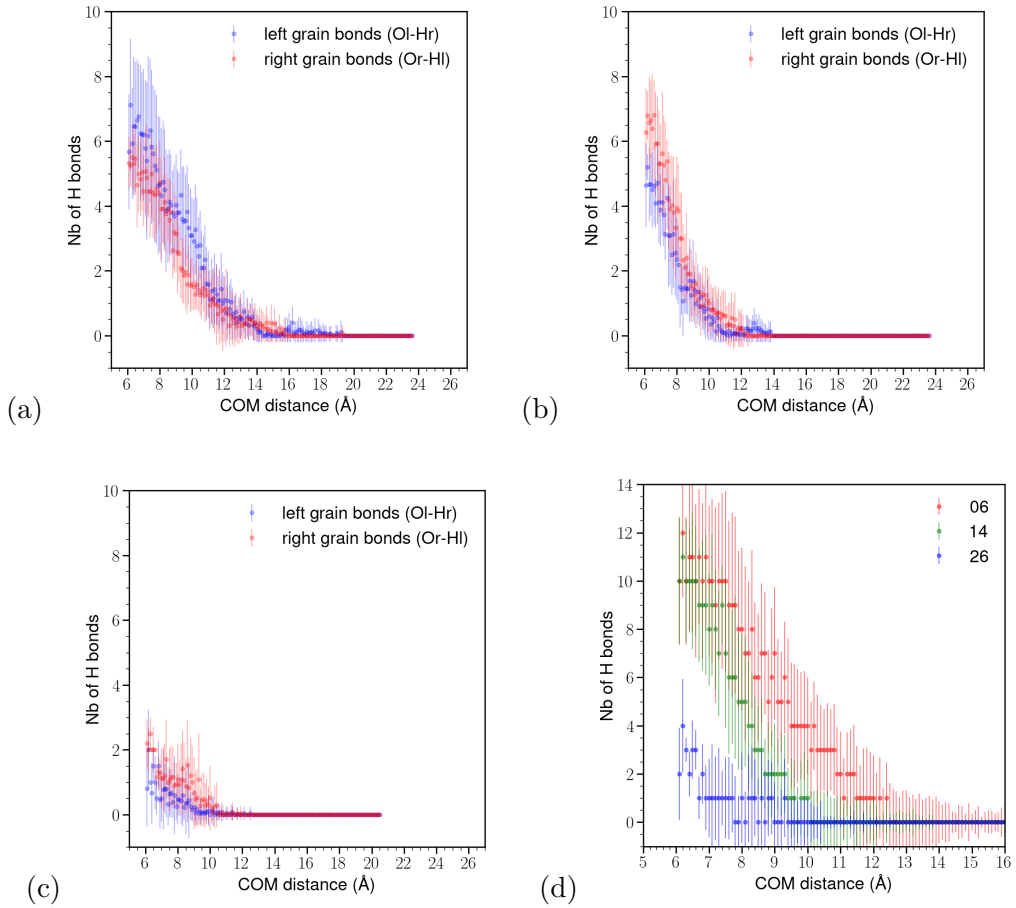

Figure 4.12: Number of hydrogen bonds for the different deprotonation degrees : (a) $d = 0$, (b) $d = 4$ and (c) $d = 10$. Panel (d) compares the total (summed) number of hydrogen bonds for the different cases. Each point correspond to an average of the quantity over binned configurations and the lines to the associated standard deviations.

Hydrogen bonds formation mostly relates on the interface medium, itself related to the grains geometry/deprotonation degree. Higher deprotonation leads to less flexibility, therefore leading to more water molecules at the grains' interface, preventing the formation of hydrogen bonds. Rather than a cause to attraction between our species, hydrogen bonds are a consequence of this interaction regime. As we are working with non reactive force field, no chemical reactions are allowed. However, the existence of these bonds relates both entities. Especially, within the alkaline solution, these H bonds might potentially turn into Si-O-Si or Si-O-Al bonds, connecting the species and so, fostering the polymerization process.

Such a behavior has already been discussed in literature an seen from experiments [159, 160]. Kai *et al.* has studied the silicate-geopolymers aggregates interface using reactive force field (ReaxFF). They denote that hydrogen bonds between the aggregates are the major interfacial bonding. In addition, tensile experiments were simulated over the system, observing two stages. A first one in which the strength decreases, with the breaking of Al-O-Si, Na-O and H bonding at the interface and a recovery one with the re-formation of Na-O and H-bonds (up to 0.5GPa). These results are supported by Brandvold *et al.* [160] who experimentally observed thixotropic restructuring associated to the reformation of hydrogen bonds between alumina and silica tetrahedra in the gel phase. OH groups from these tetrahedra would indeed induce attraction before to react with H^+ ions coming from either solution or a neighboring tetrahedron, so breaking and releasing water and enhancing

polymerization (e.g. forming a polysialate) *via* chemistry.

4.3 An atomic description to model interactions

Both grains consist of aluminosilicate skeleton immersed in water surrounded by sodium ions. As seen from Fig. 4.4(b), some ions can stand close to the grains at a surface distance less than 5Å. According to this, we can define two entities as {grain+close ions} that are set to interact in water. These correspond to charged systems interacting in water according to van der Waals and electrostatic interactions.

4.3.1 Defining the interactions

From an atomic point of view, our charged oligomers with ions can be seen as two clusters of charged particles interacting in water. Their electrostatic interactions are described by both coulombic and dipole-dipole pairing.

Coulombic interaction

Considering two punctual charges in water at location P_i and P_j, with charges q_i and q_j, the electrostatic force of a punctual charge q at location M stands as

$$\overrightarrow{F} = \frac{qq_i}{4\pi\varepsilon_0\varepsilon_r}\frac{\overrightarrow{P_iM}}{\|\overrightarrow{P_iM}\|^3}, \tag{4.7}$$

where ε_0 is the void permeability and ε_r the water dielectric constant.

Generalizing this equation to both left and right grains, Eq. 4.7 quantifies the electrostatic force felt by the right {grain+close ions} cluster on the left one as

$$\overrightarrow{F} = \sum_{i=1}^{N_{\text{left}}}\sum_{j=1,j\neq i}^{N_{\text{right}}}\frac{q_iq_j}{4\pi\varepsilon_0\varepsilon_r}\frac{\overrightarrow{P_iP_j}}{\|\overrightarrow{P_iP_j}\|^3}. \tag{4.8}$$

Adding the interaction with flying ions respectively for each cluster, the total resulting coulombic potential energy stands as

$$E_{\text{coul}} = \sum_{i=1}^{N_{\text{left}}}\sum_{j=1,j\neq i}^{N_{\text{right}}}\frac{q_iq_j}{4\pi\varepsilon_0\varepsilon_r}\frac{1}{\|\overrightarrow{P_iP_j}\|} + \sum_{i=1}^{N_{\text{left}}}\sum_{k=1,k\neq i}^{N_{\text{flying left}}}\frac{q_iq_k}{4\pi\varepsilon_0\varepsilon_r}\frac{1}{\|\overrightarrow{P_iP_k}\|} + \sum_{j=1}^{N_{\text{right}}}\sum_{k=1,k\neq j}^{N_{\text{flying right}}}\frac{q_jq_k}{4\pi\varepsilon_0\varepsilon_r}\frac{1}{\|\overrightarrow{P_jP_k}\|}, \tag{4.9}$$

where the subscripts "flying left/right" refer to the ions that are not considering within the left or right cluster respectively.

Dipole-dipole interactions

Each {grain+ions} system is so composed of a negative and a positive charge, inducing a local dipole. Dipole moments are computed according to the following procedure. Each specie, identified as a group of atoms (aluminosilicate skeleton + closest ions) is divided into two subgroups, composed of respectively atoms with positive and negative charges. For each of these subgroups, composed of atoms with mass m_i,charge q_i and coordinates $\mathbf{r_i}$, the COM is computed as

$$\mathbf{r}_{\text{COM}} = \frac{1}{M}\sum_{i\in\text{group}} m_i\mathrm{r}_i, \text{ where } M = \sum_{i\in\text{group}} m_i. \tag{4.10}$$

Then, a center of charge can be associated to both positive and negative charges according to

$$\mu_{\pm} = \sum_{\substack{i \in \text{group}, \\ \text{sign}(q_i)=\pm}} q_i(\mathrm{r_i} - \mathrm{r_{COM}}). \tag{4.11}$$

The moment dipole associated to a grain is finally obtained by

$$\mu_{\text{grain}} = \mathbf{r}_{\mathrm{Q}-} - \mathbf{r}_{\mathrm{Q}+}. \tag{4.12}$$

Between the two dipoles, the potential energy of interactions can be quantified according to the dipole-dipole part of the Stockmayer potential [161] as:

$$V_{\text{dip-dip}}(r) = -\frac{\mu_1 \mu_2}{4\pi\epsilon_0 \epsilon r^3} \left(2\cos(\theta_1)\cos(\theta_2) - \sin(\theta_1)\sin(\theta_2)\cos(\theta_{12})\right), \tag{4.13}$$

where μ_i and θ_i corresponds respectively to each grain dipole moment and angle relative to the inter-grain axis (here the x-axis). θ_{12} refers to the relative angle between both dipoles.

van der Waals interactions

The Lennard-Jones pair-potential is of common use in molecular simulation to account for van der Waals attraction forces. With our adapted ClayFF, their potential energy are expressed as a function of ε_i and σ_i parameters. Similarly as for the coulombic interactions, the van der Waals pair-potential energy can be obtained between our two {grain+ions} entities as

$$E_{\text{vdW}} = -\sum_{i=1}^{N_{\text{left}}} \sum_{j=1, j\neq i}^{N_{\text{right}}} 4\varepsilon_{ij} \left(\frac{\sigma_{ij}}{r_{ij}}\right)^6 - \sum_{i=1}^{N_{\text{left}}} \sum_{k=1, k\neq i}^{N_{\text{flying left}}} 4\varepsilon_{ik} \left(\frac{\sigma_{ik}}{r_{ik}}\right)^6 - \sum_{j=1}^{N_{\text{left}}} \sum_{k=1, k\neq j}^{N_{\text{flying right}}} 4\varepsilon_{jk} \left(\frac{\sigma_{jk}}{r_{jk}}\right)^6 \tag{4.14}$$

where σ_{ij} and ε_{ij} are set according to the discussion of §1.2 in Chapter 3.

Hard core repulsion

In addition, we propose a hard core repulsion at a COM distance $R_g = 6$Å corresponding to the aluminosilicate skeleton gyration radius computed earlier, with the form :

$$V_{\text{repulsion}}(r) = \frac{1}{(r-6)^{12}}. \tag{4.15}$$

4.3.2 Resulting interactions

All these interactions can be summed up, leading to the total potential energy of interaction, according to Eq. 4.16.

$$V_{\text{grain-grain,atomic}}(r) = V_{\text{Coulomb}}(r) + V_{\text{dip-dip}}(r) + V_{\text{vdW}}(r) + V_{\text{repulsion}}(r). \tag{4.16}$$

Resulting interactions are shown in Fig. 4.13 with the respective contributions in different colors.

It is interesting to denote that Coulombic interactions are mostly repulsive for charged cases and increase with grain deprotonation. When the grain is fully protonated, Coulomb forces becomes attractive below a COM distance of 10Å. Note that below this distance, grains deformation is forced, leading to proximity effects. According to Fig. 4.13(b), embedded dipoles interaction appears negligible w.r.t. the others.

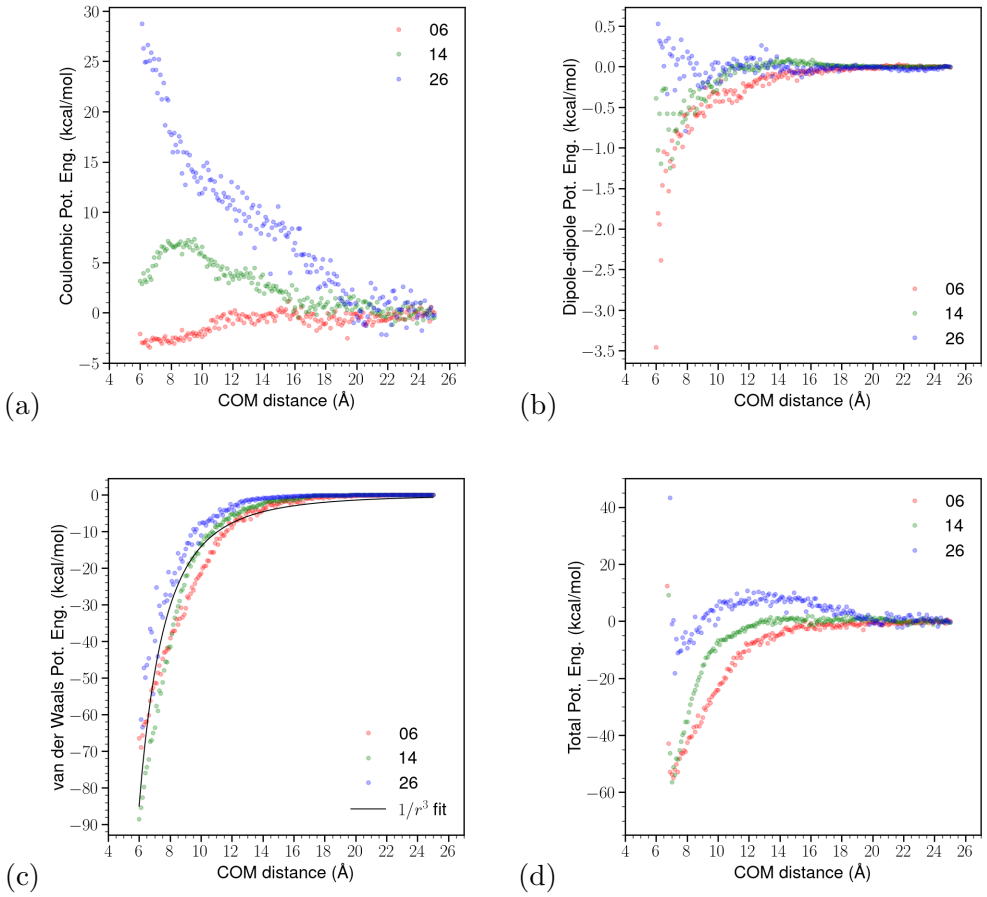

Figure 4.13: (a) Coulombic, (b) dipole-dipole and (c) van der Waals contributions to the pair-potential of interaction between our two atomic clusters {grain+ions}. In (c), a $1/r^3$ is shown with a black line. (d) Total pair-potential energy. Color refer to the different deprotonation degree case, with $d = 0, 4$ and 10, respectively accounting for 6, 14 and 26 sodium ions in solution.

Van der Waals potential energies show a interesting behavior. Especially, while accounting for a strong well of attraction, there appear to be independent on the deprotonation degree. As a sum of $1/r^6$ terms, the pair interaction shows a $1/r^3$ tendency, as for the dipole-dipole term.

Finally, Fig. 4.13(d) illustrates well a transition from an attractive to a repulsive regime as the surface charge of the oligomer increases. The fully protonated case displays a clear well of attraction within the range [6,16]Å with a minimum slightly higher than the one of metadynamics (-55 vs -75kcal/mol). Repulsion in the highly deprotonated case is not as strong as observed from metadynamics results illustrated in Fig. 4.2. However, we recall that the system is forced to close distances under 10Å and that in this highly protonated, the sampling is poor at shorter COM distances (see Fig. 3.30 in Chapter 3). In the mildly deprotonated case ($d = 4$), attraction starts below this distance 10Å. These results are consistent with metadynamics calculations, especially as the well is recovered in the protonated case and a repulsive regime in the highly deprotonated one, with the mildly charged case at the in-between.

While this approach requires atomic positions, it allows to get a simpler overview of the grain-grain interaction regime in solution. In the next section, we propose to upscale the approach by defining a model which do not involving inter-atomic properties.

4.4 Grains as charged meta-grains

There is a strong analogy between our aluminosilicate grains in water with flying ions and the atom, as an hard core with its electronic cloud. In this section, we propose to define a *meta-grain*, seen as a hard core aluminosilicate skeleton (which formulation depends on the deprotonation degree d: $[Si_{20}Al_3O_{61}H_{30-d}]^{(d-3)-}$), with its ionic cloud. Such a view permits the definition of different properties for the {grain+ions} complex, relating to grain-grain interactions at the mesoscale. In the following, three deprotonation cases will be discussed, of $d = 0, 4$ and 10, with respectively $6, 14$ and 26 sodium ions in solution.

4.4.1 Geometry of the grains

Over a simulation run, both grains are able to deform and reshape as already seen in §1.3 for a single grain in water. Fig. 4.14 illustrates that grains' geometry is influenced by the presence of a second one in solution. Despite the grains are similarly defined at the beginning of the simulation, their shapes undergo large fluctuation during the simulation. The different panels displays that not only grains asphericities depend on the deprotonation, but also on its proximity with the other grain.

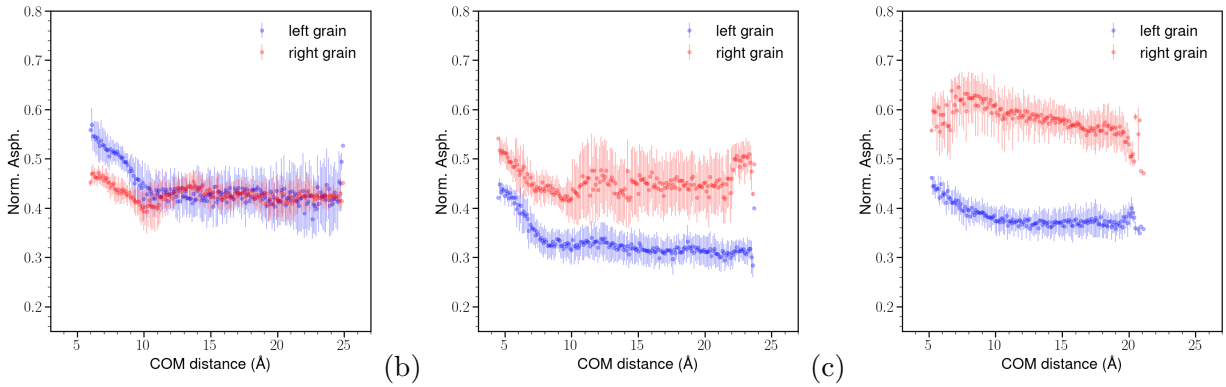

Figure 4.14: Evolution of the left (blue) and right (red) grain geometries as a function of the distance. The plots correspond to asphericities computed as defined in Chapter 2 . Each plot corresponds to a deprotonation degree of: (a) 0, (b) 4 and (c) 10. Every quantities are computed for every configurations sampled over the metadynamics run averaged over COM distance bins of 0.1Å.

At short distance, for all three cases, one grain as an asphericity close to 0.55 while the other stands as 0.45. However, only the fully protonated case display a convergence of both asphericities to the same values at largest distances. The higher the grain charge is, the more the shapes differ. This echoes the path dependence deformation of the grains already discussed from Fig. 4.9 and Table 4.1. For all the three cases, asphericities are mostly constant above 10Å, distances already discussed to be of extreme grains proximity, almost merging.

4.4.2 Meta-grains under different views

In the previous section, it was shown that sodium ions are allowed to move freely within the simulation box. Therefore ionic cloud associated to hard cores can be defined under different considerations. Two approaches are proposed here, both accounting for electro-neutrality of the whole system seen as two meta-grains in water.

(I) Splitting the box into a *left* and *right* parts from the middle of the meta-grains interface, attaching ions of each part to the respective grains ;

(II) Distributing ions to the closer grain in order to compensate for the charge deficit to obtain two meta-grains of null charge.

Fig. 4.15 illustrates how the ionic clouds are defined in both (I) and (II) cases. These two models will, in the following, be referred as the Half box (I) and Null charge (II) models.

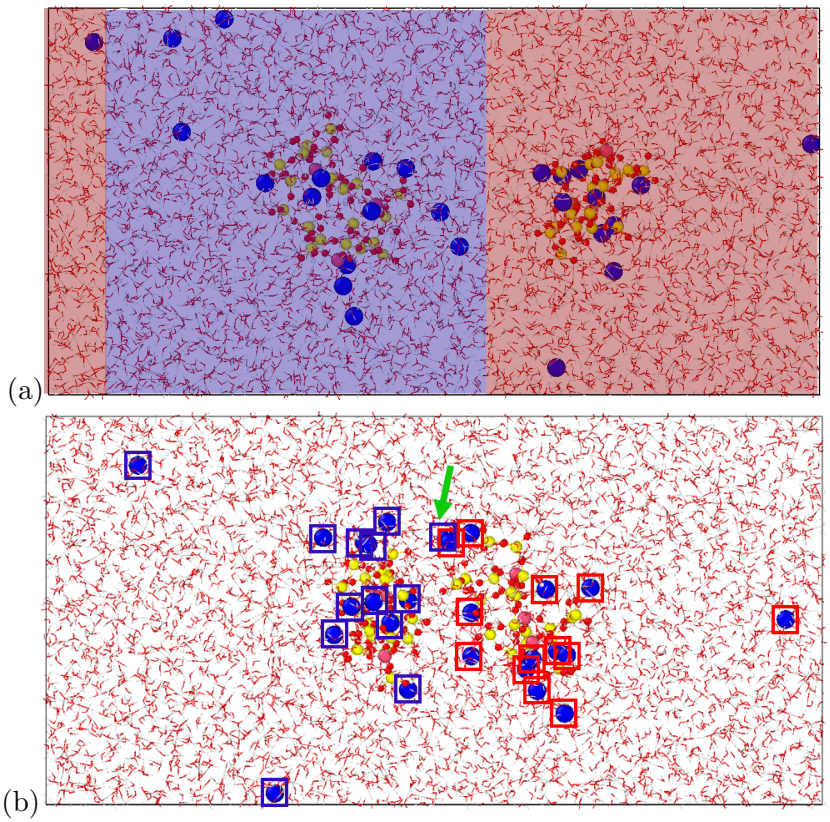

Figure 4.15: Ionic cloud definition under two perspectives : (a) the simulation box is split into two regions of same size (40Å×40Å×40Å) with regard to the middle of the COM distance between the grains (I). Blue and red regions are respectively defined with regard to the left and right grains. As the grains move along the x-axis, so do both regions. ; (b) atoms are attributed to either the left or right grain depending on their distance to grain surfaces to form {grain,ion} complex with null charge (II). The green arrow illustrates an ion that is attributed to the left grain while it is closer to the right one. This is a consequence that the right grain has more ions at its vicinity than the right one. In order to keep both structures neutral, this ion, being the closer non-belonging to the left entity, is attached to it.

4.4.3 Meta-grains characterization

Based on both approaches, our two meta-grains acquire electrostatic characteristics and geometric properties as charges, dipole norms and polarizabilities. These relate to dictate the interaction between the meta-grains in water.

Electric charge

The charge of a meta-grain is defined as the sum of the charge of its aluminosilicate skeleton, i.e. $-3-d$, d being the deprotonation degree, and its associated ions. We recall that a -3 charge is inherent to the grain because of the presence of aluminum ions in its core.

From its definition, model (II) ensures a null charge for both meta-grains. Since our models are thought to ensure electro-neutrality between the two meta-grains in water, both charges are of opposite signs.

Polarizability and Density Energy Transition

Within a meta-grain, the volumetric polarizability α can be computed as $\alpha = 4/3\pi\sigma^3$, with σ being

the distance of the furthest sodium ion to the grain center of mass. Such a definition gives rise, in first approach, to a Dipole Energy Transition (DET) η as

$$\eta = \sqrt{\frac{S}{\alpha}}, \tag{4.17}$$

S being the number of flying ions belonging to the ionic cloud, i.e. out of the grain vicinity (here taken further away from the grain of more than 6Å according to the ion pair correlation functions seen in Fig. 4.4(b)).

Average characteristics

For each model, the physical characteristics and geometrical properties can be obtained for both grains. Even though these might be distance dependent as discussed in next section, their dependence w.r.t. the model and the protonation degree is shown in Fig. 4.16. Note that the dipoles are defined similarly as in §3.1

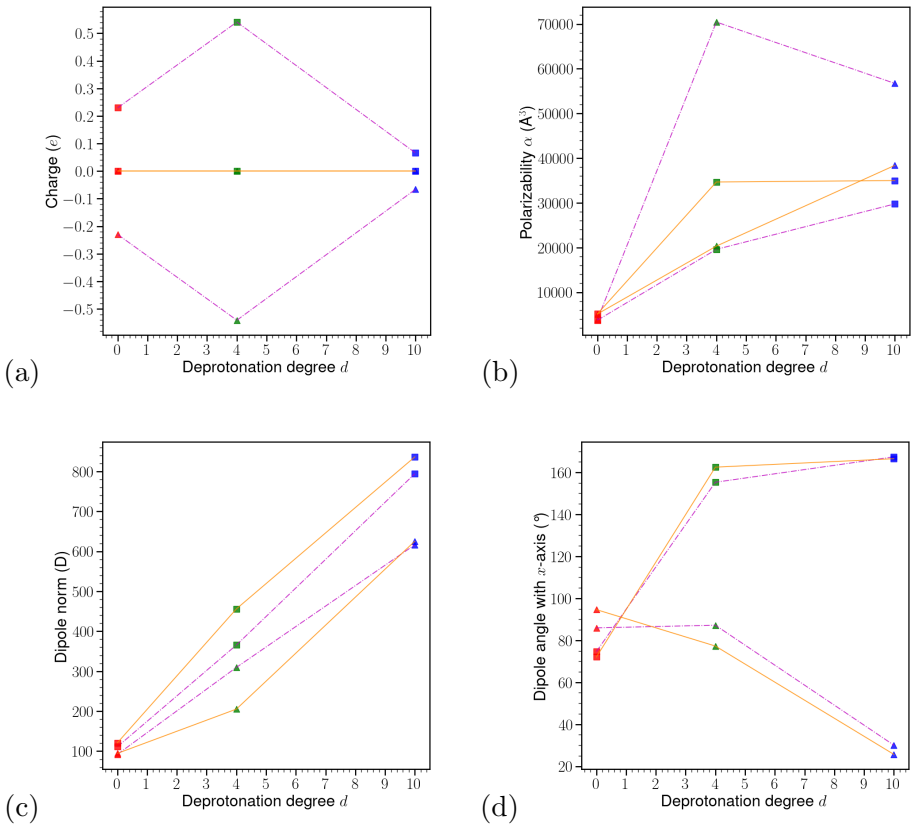

Figure 4.16: Electrostatic characterization of the meta-grains depending on the deprotonation degree d. All quantities are averaged over the full metadynamics trajectories, independently of the COM distances. (a): Charge, (b): Polarizability, (c): Dipole norm, (d): Dipole angle w.r.t. the x-axis. Triangles and rectangle shows the left and right grains. Magenta lines account for model (I) and the orange one to model (II). Red green and blue refers to the color code of Chapter 3 on the different deprotonation cases.

As expected, the charges of meta-grains with model (I) are opposite and remain null for model (II). The polarizability, expressed as a maximum distance between the aluminosilicate COM and the furthest ion, increases with deprotonation. However, the relation is not linear, since ions are allowed to move freely within the simulation box, according to Fig. 4.4. Deprotonating the aluminosilicate grains introduce a strong polarizability, without requiring a high surface charge.

As the deprotonation degree increases, meta-grains dipoles do too. This linear behavior is related to the increase of surface charge of the aluminosilicate grain alongside the increasing of the distance of ions to the grain. Both models display the same tendency for dipoles orientations. They go from almost perpendicular orientation to the x-axis to almost parallel, in opposite directions.

4.5 Meta-grains potential energy of interaction

Our meta-grains in solution are interacting in solution with three major types of interactions: 1. Coulombic interaction, depending on their respective charges; 2. Dipole-dipole interactions, from the fact that aluminosilicate skeleton is negatively charged and its ionic cloud positively; 3. Dispersion interactions (with analogy to the London dispersion force) accounted for from meta-grains polarizability.

These interactions, depending on the meta-grains characteristics, are discussed below and compared to Potential of Mean Forces obtained from metadynamics simulations.

4.5.1 Electrostatic repulsion

As seen from Fig. 4.15, model (I) allow charge exchange between the two meta-grains, therefore inducing a coulombic attraction. From the definition of model (II), meta-grains have null charge and so, are not subject to this type of interactions.

For two charges q_i and q_j at a distance r_{ij}, the coulombic interaction associated to their charges potential energy writes as

$$V_{\text{Coulomb}}(r_{ij}) = \frac{q_i q_j}{4\pi\epsilon_0 \epsilon r_{ij}}. \tag{4.18}$$

Fig. 4.17 shows the meta-grain charge evolution with the COM distance and the resulting coulombic interactions in model (I) description, according to Eq. 4.18.

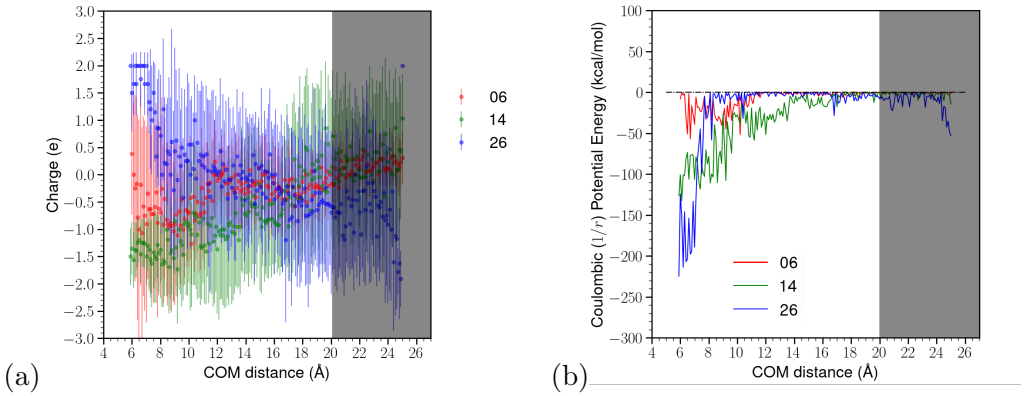

Figure 4.17: (a): Left meta-grain charge as a function of the COM distance between the grain. Dots corresponds to mean values and lines to standard deviations, taken over binned configurations (i.e. over time). Note that the charges computed here undergo very large fluctuations that are strongly related to the small number of available configurations, shown in Fig. 3.30(a) from Chapter 3. (b): Coulombic interaction between the two charged meta-grains. Both quantities are shown in the framework of model (I). All three deprotonation cases $d = 0, 4$ and 10 are shown with associated colors : red, green and blue. In this gray shaded area, above 20Å, meta-grains charges oscillates around 0. Because of the small number of sampled configurations (see Fig. 3.30(a) in Chapter 3), the average value is slightly different, therefore inducing numerical artifacts at larger distances, that do not have a physical sense.

4.5.2 Dipole-dipole interaction

Dipoles related to our meta-grains interact according to an embedded point dipole (within a dielectric sphere, as according to our modeling) interaction can be estimated from Eq. 4.13.

Fig. 4.18 shows the interactions obtained from dipole-dipole calculations according to Eq. 4.13.

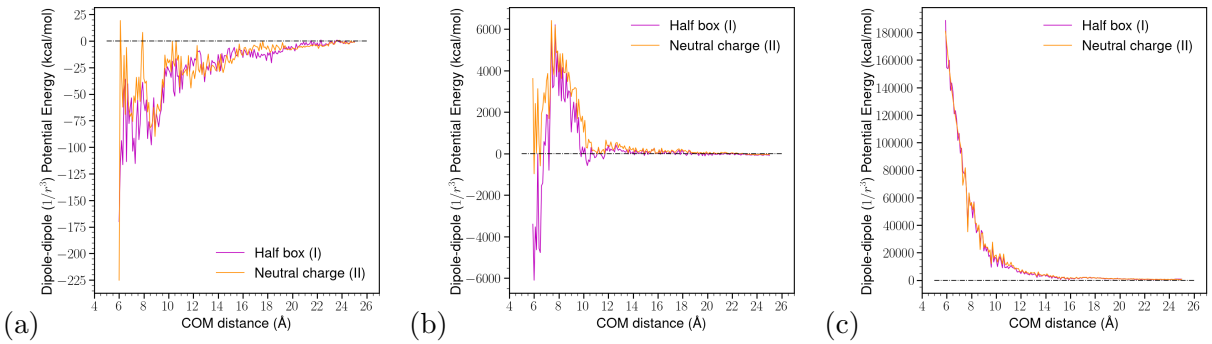

Figure 4.18: Dipole-dipole interaction contribution from the Stockmayer potential for (a): $d = 0$, (b) : $d = 4$ and (c): $d = 10$ respectively. Each color corresponds to a model for meta-grain definition

Without deprotonation, a attractive well is observed at very low distance, starting from 16Å. At distances lower than 10Å the aluminosilicate skeletons almost touch each other and so, the system undergo more fluctuation in their geometry (as seen from Fig. 4.14) due to their flexibility, causing oscillations in the computed quantities.

For the three cases, both model display the same behavior. Dipole-dipole interactions are attractive in the protonated case and strongly repulsion at high deprotonation degree. The middle case, however, shows a more sensitive behavior, even probing for a slight attraction between 10 and 14Å.

In order to get a better understand of this interaction regimes dipoles behavior can be analyzed *via* their norms and relative angles. Fig. 4.19 shows both these quantities in two cases

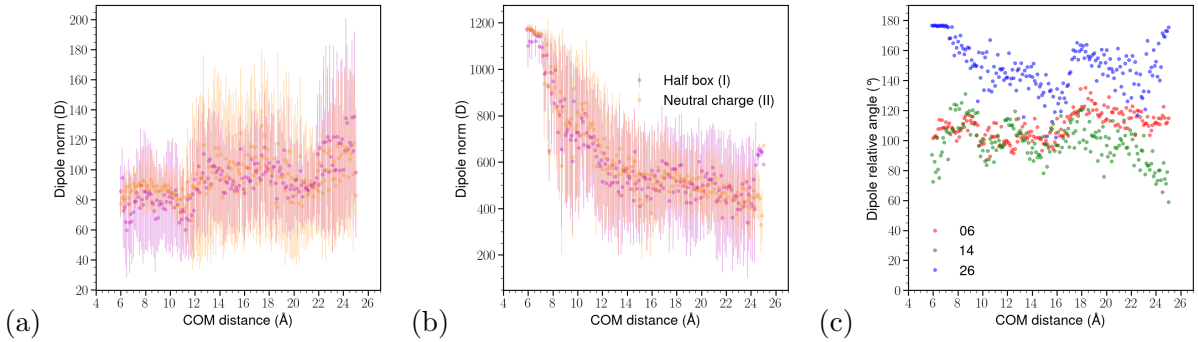

Figure 4.19: Analysis of meta-grains dipoles. Dipole norm of the left meta-grain norm obtained from the different model in the (a): protonated case; (b): highly deprotonated case. (c) Relative dipoles orientation for method (I), similar for (II). An angle of +180°corresponds to dipoles that have opposite directions and +90°to perpendicular ones.

Dipole-dipole repulsion appears to be characterized by the strong increase of the dipoles norms as aluminosilicates approach each other in high charge case. At higher deprotonation degree, we find more ions within the simulation box, which are more likely to be located far from the grain. This extend the dipole norm as seen from Fig. 4.15(c). The dipole norm increases as the grain gets closer. Since in the highly deprotonated case, dipole relative angle is around 150°, a strong repulsion is induced.

Both $d = 0$ and 4 embedded dipoles have relative orientations ranging between [100,120]° , suggesting almost perpendicular dipoles. According to Fig. 4.19(a), dipole norm is almost constant, even when the grains gets close. Its intensity is lower to the one of the mildly deprotonated case. However, as this one shows a repulsive regime of dipole-dipole interaction, it turns out that the intensity of its dipole is high enough to generate repulsion, weaker than the one of the 26Na because of the relative angles.

4.5.3 Dipole-induced dipole interaction : the dispersion approach

The dispersion effects contribution to the potential energy is of the shape

$$V_{\text{disp}}(r) = -\left(\frac{C_6}{r^6} + \frac{C_8}{r^8} + \frac{C_{10}}{r^{10}}\right), \tag{4.19}$$

where the C_n coefficient stands for the dispersion forces coefficients and r corresponds to the distance between the two interacting entities[162]. Note that Eq. 4.19 is expressed in reduced units, as $e = 1$, $1/4\pi\varepsilon_0 = 1$ and $\hbar = 1$[163]. They do account for instantaneous dipole-dipole quadripole-dipole and quadripole-quadripole/octopole-dipole interactions from $n = 6, 8$ and 10 respectively. In our case, the first term is of most interest and can be computed from grains polarizabilities.

The dipole-dipole coefficient C_6 is obtained from Density Energy Transitions η and polarizability α for two particles i and j in solution as :

$$\frac{3}{2}\frac{\eta_i\eta_j}{\eta_i + \eta_j}\alpha_i\alpha_j, \tag{4.20}$$

and so, the dispersion energy terms rewrites, in Hartree, as

$$V_{\text{dispersion}}(r_{ij}) = -\frac{3}{2}\frac{\eta_i\eta_j}{\eta_i + \eta_j}\alpha_i\alpha_j\frac{1}{r_{ij}^6}. \tag{4.21}$$

Arising from both quantities is the resulting dispersion interaction that is shown in Fig. 4.20.

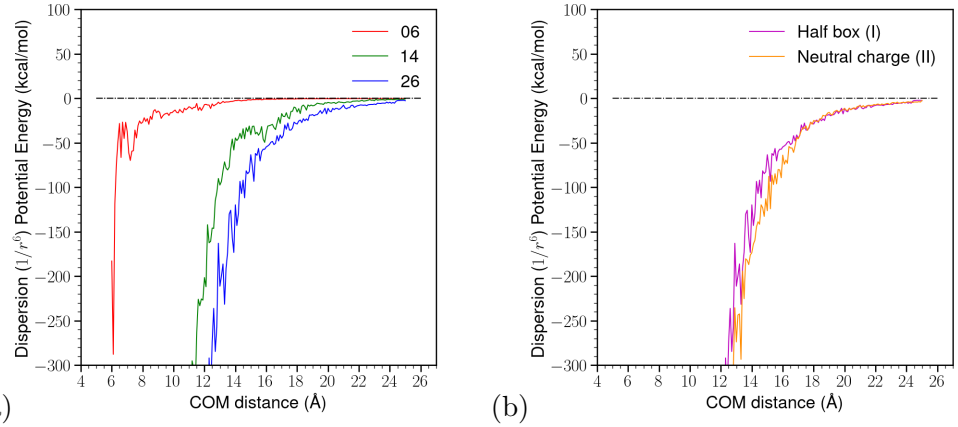

Figure 4.20: Dispersion contribution to the potential energy between the two meta-grains. (a) Interactions for different deprotonation degrees in the model (I). (b): Interactions in the highly protonated case $d = 10$ for both models.

In the opposite of dipole-dipole interactions shown in Fig. 4.18, the dispersion turns out to be strongly attractive. This is inherent to the grains strong polarizabilities as ions are flying in the entire box. This can be seen from both panels of Fig. 4.20. Panel (a) probes that attraction occurs at largest distances

as the deprotonation degree increases, i.e. more ions fly within the simulation box. In addition, panel (b) illustrates that both models are converging.

4.5.4 Total interactions

In this section, the grain-grain interactions have been thought under the scope of two meta-grains as {grain+ions} complexes, in which ions are included w.r.t. different models, involving or not aluminosilicate grain-ion distance. Meta-grains interactions have been seen under the scope of coulombic, dipole-dipole and dispersion interactions, in water. Once again, we apply a hard core repulsion at the COM distance $R_g = 6$Å according Eq. 4.15. All these interactions can be summed up, leading to the total potential energy of interaction, according to Eq. 4.22.

$$V_{\text{grain-grain,meta}}(r) = V_{\text{Coulomb}}(r) + V_{\text{dip-dip}}(r) + V_{\text{dispersion}}(r) + V_{\text{repulsion}}(r). \tag{4.22}$$

Resulting potential energies are shown in Fig. 4.21 and discussed below.

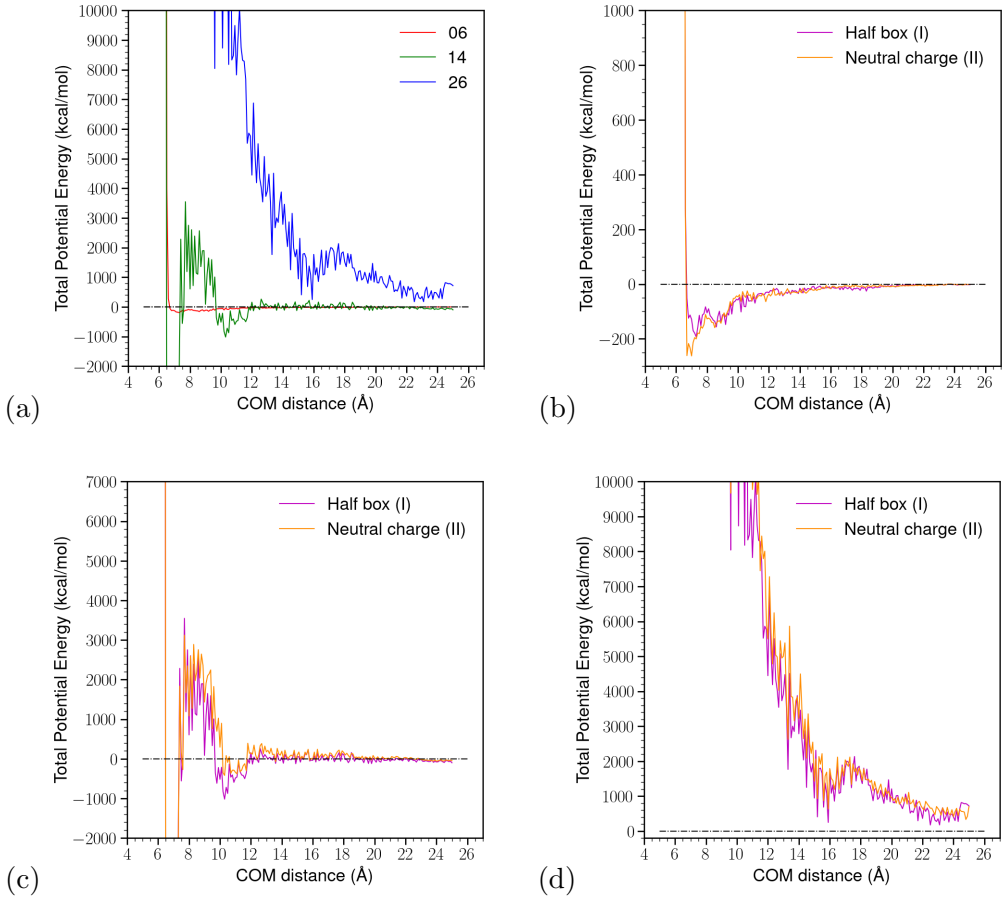

Figure 4.21: Total interactions computed from the different meta-grain models using Eq. 4.22. Panel (a) compares the potential energy for different deprotonation degrees in the second model (II). The results of both models are shown and compared in details in panels (b),(c) and (d), respectively for deprotonation degrees of $d = 0, 4$ and 10.

From Fig. 4.21 panels shows:

(b) attraction for the $d = 0$ case;

(c) a attracto-repulsion for $d = 4$;

(d) a strong repulsion for $d = 10$.

These results recall the one previously obtained from metadynamics and especially the transition from attractive to repulsive regime with the increase of grain deprotonation (see from Fig. 4.2). The different models shows a good ability to account for either attractive or repulsive regime for our system. However, the interactions here appears to be out of scale as the grain surface charge increases.

Rescaling the interactions

Up to this point, interactions have been computed in the void, i.e. with a dielectric constant $\varepsilon_r = 1$. However, section §1.4 showed that water must not be neglected at the grains interface. While the attractive well is recovered with the meta-grain approach, we recall that it showed a hydrophobic regime, i.e. a dry interface, consistent with a value of $\varepsilon_r = 1$. Fig. 4.10 (b) illustrates that it is not the case when the grains are deprotonated.

In fact, the water content at the grains interface is likely to influence the interactions as probed for clays and CSH charged materials by Carrier[164] and Goyal *et al.* 2021[73] respectively. In addition, Thoenen [165] studied the dependence of water dielectric constant in clays as a function on the water content. It results in an equation of the form:

$$\varepsilon(w) = \varepsilon_{\text{bulk}} - (\varepsilon_{\text{bulk}} - \varepsilon_{\text{adsorbed}}) \exp(-\alpha w), \tag{4.23}$$

where w stands for the water content, $\varepsilon_{\text{bulk}}$ and $\varepsilon_{\text{adsorbed}}$ being the dielectric constant for both bulk and adsorbed water. This function proposes a strong increase of ε a function of the water content, similar to the sigmoid function proposed to evaluated ε_r depending on CSH COM distance[73].

Under such view, we propose a rescaling of interactions according to the dielectric constant distribution shown in Fig. 4.22. According to Fig. 4.10, the water content per 100g of aluminosilicate grain can be evaluated.

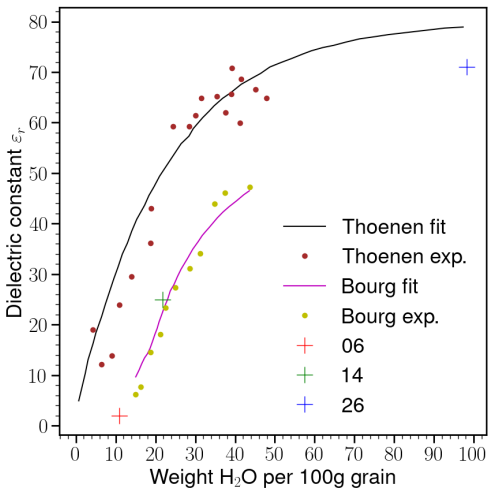

Figure 4.22: Dependence of the water dielectric constant ε_r on the water content. Dark red dots corresponds to experimental values obtained for clays and the black straight line to the associated fit, data reproduced from [165]. Yellow dots are the simulated values obtained for clay systems and the magenta line to the associated fit, data reproduced from [166]. These data are originally produced as a function of the d-spacing between two clay platelets. Here, water content is modeled linearly to the distance as equal to 0 at null spacing and of 100 (corr. to a $\varepsilon_r = 78$ from [165]) at $d = 8$Å. Colored crosses are the proposed values to rescale the interaction for our geopolymer grains, respectively 2,25 and 71 for deprotonation degrees of 0,4 and 10.

We proposed, for each deprotonation degree (and so, water content), a value of ε_r that rescales the meta-grain interactions to the same order of magnitude than the one of metadynamics. As seen from

Fig. 4.22, these follow a tendency similar to the one obtained experimentally for clays and fit well with the estimated curve from molecular simulations [166]. Resulting interactions are shown on Fig. 4.23 and compared to previously obtained PMFs.

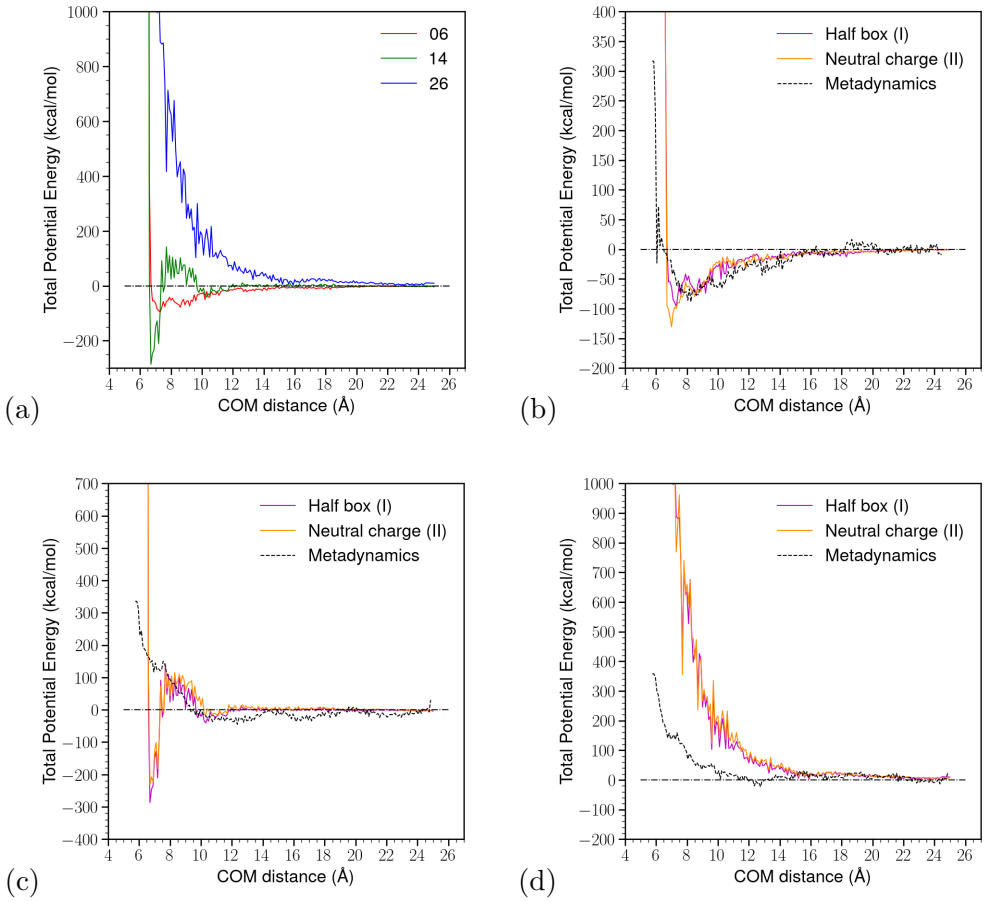

Figure 4.23: Total interactions computed from the different meta-grain models using Eq. 4.22. Panel (a) compares the potential energy for different deprotonation degrees in the second model (II). The results of both models are shown and compared in details in panels (b),(c) and (d), respectively for deprotonation degrees of $d = 0, 4$ and 10. The Potential of Mean Forces obtained from metadynamics simulations are shown in black lines.

With this rescaling, the details of interactions can be shown in Fig. 4.24. It displays the contributions of Coulombic, dipole-dipole and dispersion interactions for all the three cases.

In the three deprotonation cases, the total interactions is driven by the dipole-dipole interactions. These relate to a strong ionic correlation between the grains[164]. As the surface charge increases, the dielectric screening gets stronger, reducing ionic fluctuations and so, repulsion occurs.

No deprotonation $d = 0$

When the grain is fully protonated, a fully attractive potential is observed, starting around 16Å (see Fig. 4.23(b)). This attraction arises from a combination of both dipole-dipole and dispersion interactions.

According to MTD calculations, the attractive well starts around 16Å to reach a minimum at 8Å. Using the meta-grains models, this one reaches a minimum a bit later because of the strong dispersion attraction at short distances. At 8Å, the same values of metadynamics potential well are recovered around -80kcal/mol.

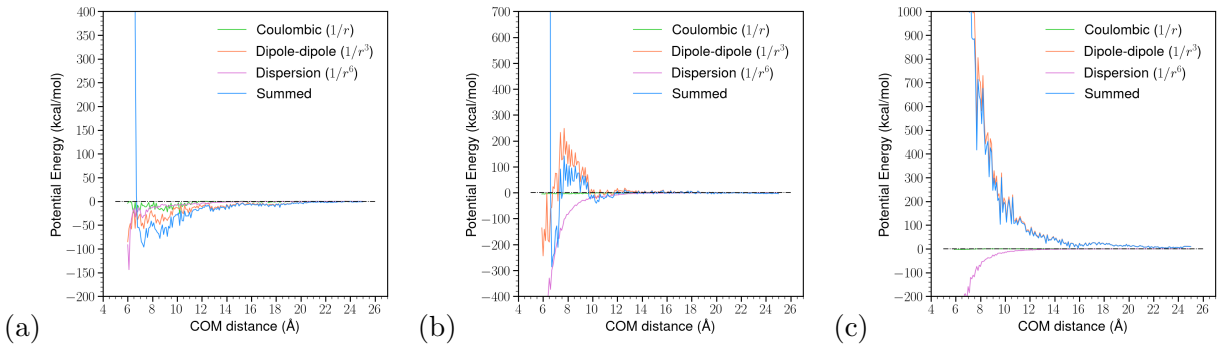

Figure 4.24: Details of the contributions to the total meta-grain-meta-grain interactions. The different colors corresponds to each interaction and the light blue is the total interaction as the sum of the different contribution and the repulsive wall as defined in Eq. 4.15. All contributions have been normalized w.r.t. ε_r according to Fig. 4.22. The dash-dotted black line is the zero line.

Mid-range deprotonation $d = 4$

Potential of interaction of this mildly deprotonated case displays a small attractive well between 10 to 12Å. Still, within the range 8-16Å dipole-dipole interaction undergo very slight fluctuations around 0kcal/mol before being strongly repulsive. The short-range repulsion starting at 10Å can be attributed to dipole-dipole interactions (see Fig. 4.19. This is explained by a combination of both the increasing of dipoles norms an their non-aligned disposition. For $d = 4$, even if the dipole norm increases as the COM distance decreases, both dipoles are not parallel (see Fig. 4.18) but rather parallel. Especially, Fig. 4.18 (c) probes that the dipoles relative angle undergo fluctuations over this range of distances. Mid-range attraction appears to originate from dispersion interactions, not overwhelmed by dipole-dipole repulsion at this distance range. Finally, state at COM distances smaller than 8Å are unfavored ones and have been poorly sampled with metadynamics (see Fig. 3.30 from Chapter 3). Therefore, results below this distance are assumed irrelevant.

With a gyration radius of the whole cluster around $R_g = 10$Å$= 1$nm[15], a spherical model for the aluminosilicate grains leads to an approximation of the surface charge as $7/4\pi R_g^2 = 0.006\text{e}/\text{Å}^2$ similar to the one of clays[164]. In the case of clays, the same behavior as found here have been discussed for nano-particles in water[166]. Especially, using metadynamics to model this system, they have found a well of attraction around $1\text{eV} = 26\text{kcal/mol}$, consistent with Fig. 4.23(c). According to their study, sodium ions are to leave the inter-grain region, promoting an hydrophobic interface (Donnan effect [167]). At a grain spacing distance ranging from 1.5 to 2.0nm, they estimated the water dielectric constant to $\varepsilon_r = 10$ to 30, similar to the value around 25 proposed here.

Meta-grains approach and metadynamics results converge. Both curves show a very potential of interaction, illustrating a transition regime, at the in between of repulsion and attraction.

High deprotonation $d = 10$

From both models (I) and (II), a strong dipole-dipole repulsion is recovered as for metadynamics, starting at 16Å COM distance instead of 12Å for the biasing method. Even though dispersion interactions account for attraction, it does not overwhelm the dipole-dipole term. Coulombic interaction, despite attractive, is too low to influence the total interaction.

In this case, the surface charge is about $0.01e/\text{Å}^2$. As immersed in almost bulk water ($\varepsilon_r = 71$, the dielectric water constant measured for SPC/E water model used in this work [168]), the grains Debye length is of 8.1Å, accounting for a high screening of its electrostatic effects. While low electrostatic coupling is the basis of the Poisson-Boltzmann equation, this repulsion regime aligns well with the DLVO theory (discussed in more details in Chapter 2)[71], using both metadynamics or the meta-grain approach.

Role of the water at the interface

Results on the protonated case echo §1.5 discussion and Fig. 4.11. In the dry interface (corresponding to $\varepsilon_r = 1$), the well of interactions is recovered by the perturbation technique. In opposition, while all cases deprotonation cases were found attractive in the dry interface case (see Fig. 3.18 in Chapter 3), both metadynamics and meta-grains approaches nuance these results with a transition to a repulsive regime as the surface charge increases. According to the current discussion, this strongly relies on role of the water content at the interface and is illustrated in Fig. 4.25.

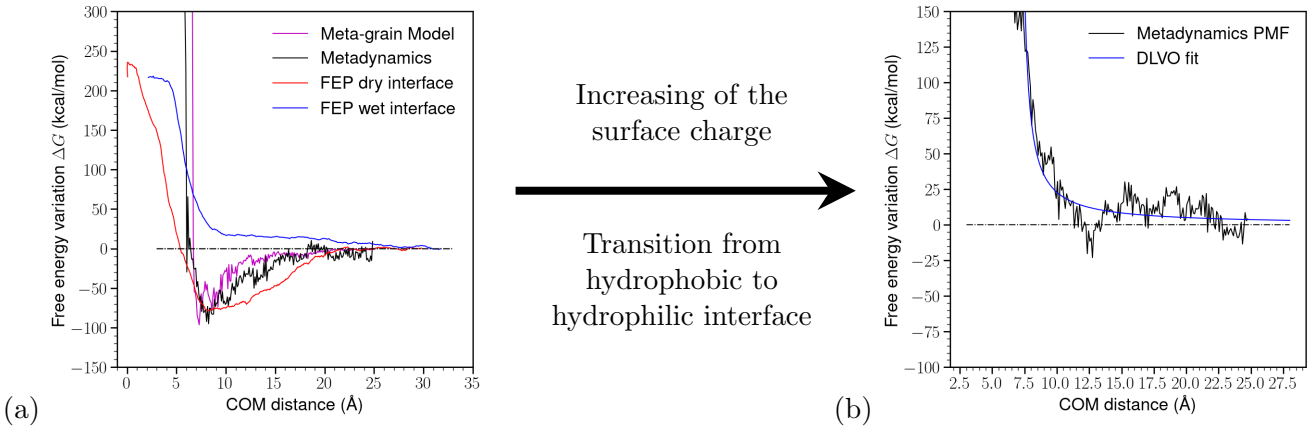

Figure 4.25: (a) PMFs obtained from four different techniques, echoing Fig. 4.11 with addition of the meta-grain model PMF. (b) Metadynamics and meta-grain model PMFs. The metadynamics curve has been fitted with a DLVO equation as described in Chapter 2, with a Hamaker constant of 8×10^{-20}J as measured for aluminosilicate materials[169, 170].

4.5.5 Reactivity at short distances for protonated grains $d = 0$

While high pH conditions (i.e. surface charge) seems to forbid the cohesion because of an induced hydrophilic regime, attraction turns out to occur when oligomers are fully protonated, at a dry interface.

Considering two grains at a COM distance of 8Å, we perform a well-tempered metadynamics run with, as a collective variable, the distance between a silicon atom of a grain and an oxygen atom from the other one. The run is performed in the NVT ensemble at ambient temperature with the ReaxFF potential [69] in order to account for either the formation or not of chemical bonds between the entities. Fig. 4.26 shows the PMF obtained w.r.t. the O-Si–O distances between the two oligomers.

Fig. 4.26(a) shows the formation of a Si-O–Si bond with a well of energy in the PMF. This PMF also display a strong well in the 3 to 5Å distance range, that may account for electrostatic bonds between the OH edge of a grain with the O^- and OH sites of the second one. Such equilibria is only possible at a dry interface and could act as a strong precursor to further geopolymerization (this process happen while geopolymerization has already started, especially allowing the existence of our studied oligomer). Entities link *via* the formation of a siloxane bond with the release of an OH^- group, *via* the following reaction process:

$$\text{R–O–H} + \text{O–R'} \rightarrow \text{R–O–R'} + OH^-,$$

where R and R' stand for either silicon (Si) or aluminum (Al) atoms.

This phenomenon can only happen with a dry interface between the two oligomers, i.e. under not too high pH conditions.

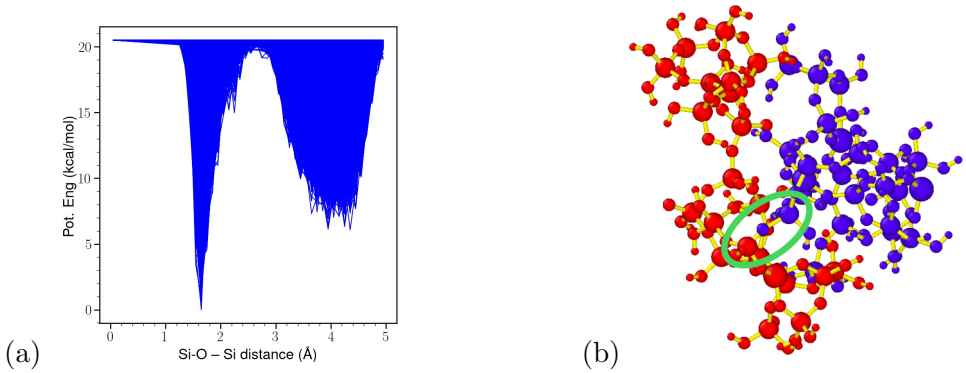

Figure 4.26: (a) Potential Energy as a function of the O-Si–O distances between two protonated aluminosilicate oligomers at a COM distance of 8Å. (b) Snapshot of the two bonded grains. In blue and red are shown the two grains and in yellow the bonds. The siloxane (Si-O-Si) bond formed during the simulation is shown in the green circle.

4.6 Conclusion

In this Chapter, the dynamics of ions have been discussed alongside the ability of the aluminosilicate grain to deform. Their flexibility have been quantified w.r.t. the deprotonation degree and appear to relate to effective interactions in solution. Higher grain surface charge account for less flexible grains and a repulsive regime.

An overall transition from attraction to repulsion between the oligomers in solutions is seen from metadynamics PMF calculations. These results probe a transition from a hydrophobic to hydrophilic interface that can be described with a dielectric screening theory. Effective interactions have been recovered by simplified atom/atom model and using a meta-grain approach, also supported by CSH and clay previous works.

Dielectric screening key role has been demonstrated in this meta-grains model. In the dry interface, pre-geopolymerization can start through an electrostatic cohesion between the two entities. In fine, cohesion is allowed if oligomers charges are low enough, i.e. at a pH that is not too high with the formation of Si-O-Si or Si-O-Al bonds. This echoes that with a too high pH in solution, geopolymer pastes do not set as observed experimentally at the CEA Marcoule from unpublished experiments and that aluminosilicate polycondensation is highly limited at high sodium concentration[171]. In addition, both experiments and simulations probed the existence of a maximal silicate oligomer size. At high pH, bigger grains are more deprotonated and so, may be less favorable to form Si-O-Si or Si-O-Al bonds with other oligomers within the gel.

Chapter 5

Mesoscale modeling of geopolymers

Gel phases involve oligomers of few nanometers size. In solution, oligomers with sizes up to 2nm are formed and interact with each other in order to form a larger oligomer network. This reaction path is called *polymerization*. Hardened material characteristics are highly related to the interactions between these oligomers as these rule the structuring of the paste at the meso-scale level.

From an atomic point of view, molecular dynamics simulations has allowed to quantify the grand potential of interaction between two aluminosilicate grains in solution using different techniques. As a matter of fact, these interactions appear to depend on their deprotonation degree. However, it remains, of a great interest to consider the structures that can be generated from the computed potentials, assuming an uniform distribution of aluminosilicate oligomers in solution.

To do so, in this Chapter, the Potential of Mean Forces (PMFs) obtained will be fitted to empirical potentials and implemented in Grand Canonical Monte-Carlo (GCMC) molecular simulations. Such a process aims to reproduce the aggregation of oligomers during precipitation, i.e. the formation of the meso-network from which the final material will arise. According to the previous discussion on grains geometry, a coarse-grained approach is proposed, with grain seen as spherical particles.

Because of the different Potential of Mean Forces (PMFs) obtained before, three types of potentials are discussed : an attractive one, corresponding to the fully protonated case (deprotonation degree $d = 0$ as defined in the previous chapter), one with a middle-range shoulder ($d = 4$) and a fully repulsive one ($d = 10$). These three case allow to study the resulting structures under the scope of pore size distributions and scattering intensity data, for geopolymer materials.

5.1 Aluminosilicate grains as particles

In order to define a coarse-grain model for geopolymer pastes, the geometry of a *geopolymer particle* must be identified. It would allow for the definition of coarse-graining length for mesoscale simulations. The average size of aluminosilicate oligomers has been evaluated using different approaches, either from experimental or in atomistic simulation. In addition, fitting the potential of mean force would also allow to define a characteristic size for the particle.

5.1.1 Scattering experiments

Performed by Steins *et al.* [20], Small Angle X-ray Scattering experiments (SAXS) allows to characterize the structure of geopolymer pastes. Thanks to the Beaucage model [52, 53] the scattering curves and structural parameters of the material can be related as described in Chapter 1. Gyration radius for oligomers was estimated around 2nm, in a geopolymer pastes.

5.1.2 Mesoscale Simulation literature

Two different models have been proposed to build up mesoscale simulations. Based on two distinct approaches, they have their own coarse-graining length and effective potential of interactions.

DFT calculations have allowed to understand the role of silicate addition to the activating solution at constant pH on the cluster formation from monomers in aluminosilicate materials[107]. In their simulation they used particles of size around 3.1Å corresponding to silicon and aluminum tetrahedron.

From measurement of mechanical properties of geopolymers pastes, an effective interaction potential between aluminosilicates nano-particles have been proposed under the form of a polydisperse Lennard-Jones potential. According to SAXS, MIP and TEM observations, a range of particles between 5 to 50nm is proposed to generate structure based on the agglomeration of oligomers and study their mechanics [108].

5.1.3 Reactive atomistic simulations

Recalling the grain model used in Chapter 3 and 4, a maximum gyration radius for an aluminosilicate grain containing 21 Si/Al atoms in solution has been estimated to 10Å [15]. With a Si-O distance of 1.6Å in silicates, this values is consistent with the 3.8Å gyration radius of silicate dimers or cyclic trimers.

5.1.4 Potential of Mean Force fitting

In Chapter 4, the grain geometry was discussed and it was shown that its asphericity oscillates between 0.3 and 0.6 according to Fig. 4.8 from Chapter 3. From a unique geometrical point of view, this characterization do not allow to model our grains as spherical particles.

Aluminosilicate grains appear to be highly amorphous w.r.t. their CSH and clay counterparts. Their geometry evolve alongside their Center-Of-Mass (COM) distance (also dependently on its deprotonation, as seen from Fig. 3.20 and 3.21 in Chapter 3). Therefore, there do not appear to be a straightforward geometrical model for aluminosilicate particles.

In this work though, we propose to account for spherical particles as a first approach and for simplicity. This choice has already been taken to study, e.g. CSH systems[102, 101] despite CSH grains are usually seen as platelets consisting of nanolayers[74, 33].

Pair-potentials for spherical particles

According to Chapter 3, without any deprotonation, the potential of interaction is fully attractive. When increasing grains deprotonation, it transits to a repulsive regime. Fig. 5.1 displays two types of inter-atomic potentials usually employed within molecular simulations : the Lennard-Jones and the Yukawa (see Chapter 2).

From the definition of the Lennard-Jones potential, σ corresponds to the distance that sets the potential energy to zero and can be seen as a "particle diameter", i.e. a characteristic particle size.

From the definition of σ as a parameter of the Lennard-Jones potential, transition from Fig. 5.1(a) to Fig. 5.1(b) is straight forward. With a particle size of 8Å, the well depth and location are retrieved. Increasing the particle size shift the well minimum to the right, meaning that with a bigger particle size, the actual well will not be accounted for. As a hard sphere model, a repulsive wall is imposed as the particles get in contact. Therefore, such potentials can not allow for grain deformation at very close distance that would result into sphere inter-penetration.

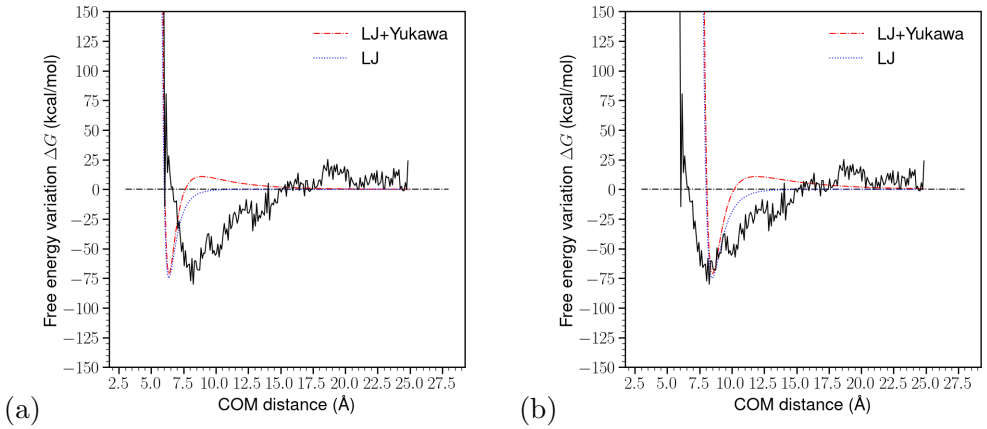

Figure 5.1: Fitting of the metadynamics Potential of Mean Force (PMF) obtained for the fully protonated case $d = 0$. The fit are proposed for either a single Lennard-Jones (LJ) potential or the sum of a Lennard-Jones and Yukawa (LJ+Yukawa) potentials. Panel (a) and (b) corresponds to particles sizes σ of 6Å and 8Å respectively. LJ energy parameter is taken as $\varepsilon = 75$kcal/mol for the (a) panel. It is set to $\varepsilon = 105$kcal/mol in panel (b), with Yukawa parameters as $A = \frac{4}{1.5}\varepsilon$ and $\kappa = 2/\sigma$. The black line is the metadynamics PMF.

A density approach

On the perspective of using a simple geometrical shape to design our geopolymer grains, a density approach is proposed here. Considering a single grain, by defining a minimal region according to its edges (in the x,y and z directions), the grain can be contained within a box. The volume of empty regions (containing no grain atoms) can be subtracted to the total, estimating a *grain-containing* volume, as illustrated in Fig. 5.2(a). This volume is estimated to be less than 60% of the box one.

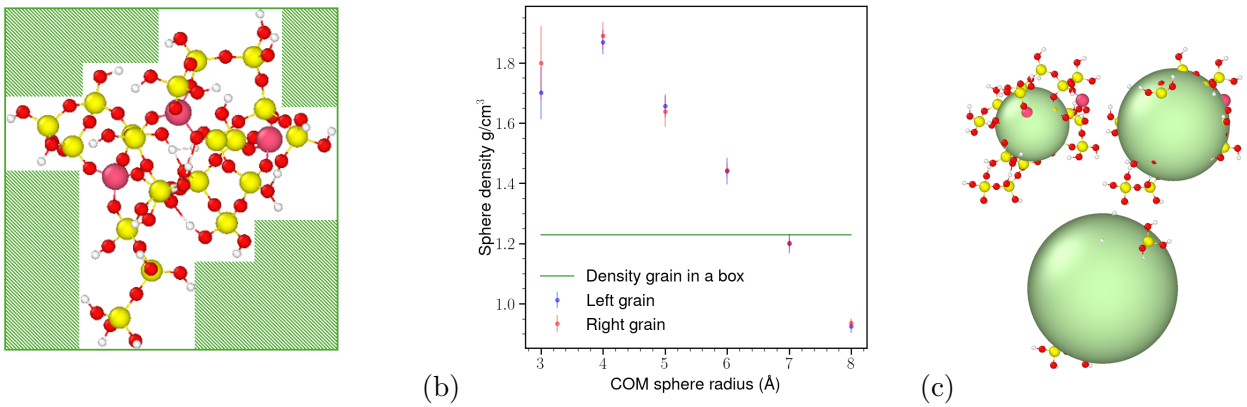

Figure 5.2: (a) Aluminosilicate grain within a box defined w.r.t. its edges atoms, shown in the $x - z$ plane. The green dashed rectangles show the volumes subtracted to the one of the box to estimate a local density of the grain. (b) Values of the density of aluminosilicate contained within a sphere taken at the COM of each grain. The values are shown in blue and red for the left and right grains, as a function of the sphere's radius in the case of two grains immersed in water. The green straight line correspond to local grain density obtained within the volume defined in (a). (c) Spheres at the center of a grain with radii of $4, 6$ and 8Å.

On the purpose of a spherical definition, because of the grains' flexibility, the distance that matters most is half the smallest accessible COM-distance (6Å), i.e. a minimum radius of 3Å. Fig. 5.2(b) shows the density of aluminosilicate grains at different COM distances. The density changes due to

the flexibility of grains. It shows a non monotonic behavior with maximum at 4Å. In fact, this 4Å sphere is able to encompass the denser part of the grains. Moreover, this density is higher than the one of the full grain, ensuring that we do not overestimate this volume.

Oppositely, using a sphere radius higher than 7Å would be too large. The volume of the spherical model should be as small as possible to account for deformation, i.e. attraction from a mesoscale point of view.

In overall, relating these results to Fig. 5.1, the choice of a spherical particle radius of 4Å is proposed for mesoscale modeling of geopolymer gels, in the framework of coarse-grained Monte Carlo simulations.

5.2 On the variety of pair-potentials

As a way to study the precipitation and aggregation of colloidal particles, precipitation simulation technique has been employed for reactive solution of CSH[102]. Coupling Grand Canonical Monte Carlo (GCMC) and Molecular Dynamics (MD), it mimics the reactive solidification of a paste. The precipitation is modeled *via* a GCMC procedure as defined in Chapter 2: our geopolymer particles are inserted with regard to a probability that depends on a excess chemical potential μ_{exc}. Similarly as for CSH, we assume that during precipitation, there is an excess amount of dissolved solute within the pores, and that the precipitation do not stop. As a consequence, μ_{exc}, accounting for the energy required to the formation of an oligomer (i.e. a particle), is taken to favor a full densification. MD runs are applied in between GCMC trials as it allow the system to aggregate and restructure dynamically.

Modeling precipitation reaction using Grand Canonical Monte Carlo requires an effective pair-potential for interactions. Variety of functions can describe potential energies as a function of the inter-particle distances, w.r.t. to physical model and types of particles. In this work, three types of interactions are discussed :

- A Lennard Jones (LJ) model: to model the attractive PMF ($d = 0$ case);
- A LJ+Yukawa model : to fit the transitive PMF ($d = 4$ case);
- A single Yukawa : to account for the DLVO repulsion ($d = 10$ case).

5.2.1 The Lennard-Jones model

An attractive inter-grain behavior can be modeled with a single Lennard-Jones (LJ) potential, considering particles as hard spheres. It is one of the most used and is well implemented in molecular simulation codes. Under its Mie form shown in Eq. 5.1, it can be parameterized in terms of well depth, location and width according to ε, σ and γ.

$$\phi_{\text{LJ}}(r) = 4\varepsilon \left[\left(\frac{\sigma}{r}\right)^{2\gamma} - \left(\frac{\sigma}{r}\right)^{\gamma} \right]. \tag{5.1}$$

Using a LJ model has the benefit to be highly transferable. From simulation performed with generic parameters (i.e. in so-called *LJ units*) $\sigma^* = 1$ and $\varepsilon^* = 1$, the results can be asset to any system by re-normalizing their values in S.I. units, according to Table 5.1 given in the next page.

Property	Dimensionless quantity	S.I. conversion
Length	r^*	$r = r^*\sigma$
Energy	E^*	$E = E^*\varepsilon$
Time	t^*	$t = t^*\sqrt{\frac{m\sigma^2}{\varepsilon}}$
Temperature	T^*	$T = T^*\varepsilon/k_B$
Pressure	P^*	$P = \frac{P^*\varepsilon}{\sigma^3}$
Density	ρ^*	$\rho = \rho^*/\sigma^3$

Table 5.1: Table for conversion of Lennard-Jones dimensionless units[172]

With a particle size $\sigma = 6$Å, taken as the gyration radius of our grain (see Fig. 4.8 in Chapter 4), Lennard-Jones pair-potentials are proposed with different γ exponents in Fig. 5.3, allowing to cover a good range of potential width. The $\gamma = 6$ and 12 potentials are the most commonly used while the 2.5 value was chosen to reproduce the well shape in the range [7,9]Å.

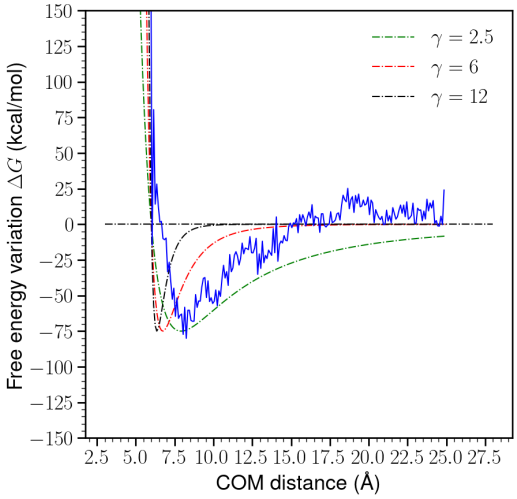

Figure 5.3: Fitting of the metadynamics PMF. Dashed-dotted lines stand for the LJ potential with different values of the γ exponent with a well depth $\varepsilon = 75$kcal/mol and a particle size of $\sigma = 6$Å. Note that the well can be distance-shifted by changing the value of σ as seen from Fig. 5.1. The blue line is the metadynamics PMF.

5.2.2 Morse model

Out of consideration of the particle sizes, the fore-mentioned PMF can be fitted using either a Lennard-Jones or a Morse potential, both accounting for Van der Walls interactions. The first one stands for a hard core modeling while the second allows to study soft systems (e.g. bonds equilibrium in biomolecules). Note that both potentials account for spherical particles.

The Morse pair-potential is defined as a

$$\phi_{\text{Morse}}(r) = D_e(1 - e^{-a(r-r_e)})^2, \tag{5.2}$$

where D_e and r_e denotes respectively the well depth and the equilibrium distance between the atoms. a is a width parameter that monitors the width of the well : this latter is wider as a increases. It is often normalized according to

$$\phi_{\text{Morse}}(r) = D_e\left(1 - e^{-a(r-r_e)}\right)^2 - D_e, \tag{5.3}$$

and can be rewritten as

$$\phi_{\text{Morse}}(r) = D_e(e^{-2a(r-r_e)} - 2e^{-a(r-r_e)}). \tag{5.4}$$

Comparison of the fit

Fig. 5.4 shows the fit performed for the Morse model defined above and an alternative Lennard-Jones potential.

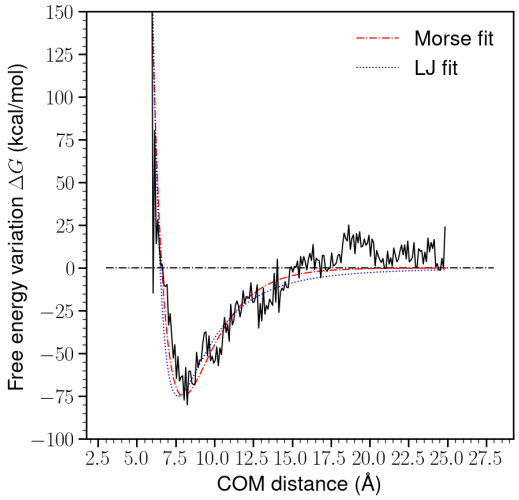

Figure 5.4: Fitting of the metadynamics PMF. Dashed-dotted line shows the LJ potential with $\varepsilon =$ 75kcal/mol, $\sigma = 6.5$Å and $\gamma = 4.2$. Morse fit is shown with the blue continuous line, with an amplitude of $D_e = 75$kcal/mol, a width parameter $a = 0.5$Å^{-1} and equilibrium distance $r_e = 8$Å. The black straight line is the metadynamics PMF and the dash-dotted one is the zero line.

The Morse potential is usually used to model molecule bonds or soft models as its behavior at short distances is less sharp than the LJ potential. As a consequence, even though it has a better ability to reproduce the shape of the grand potential of interaction, it does not probed interesting results at first stance in the framework of GCMC simulations.

5.2.3 Yukawa fitting

At high deprotonation degrees, the interaction between two grains appears to be repulsive, in consistence with the DLVO theory discussed in Chapter 2. Fig. 5.5 illustrates the fitting of the repulsive PMF with (a) the DLVO theory ; (b) a Yukawa potential. Note that as seen from Fig. 4.2 from Chapter 4, the deprotonation degree does not influence the shape of the pair-potential as soon as this one entered a repulsive regime (deprotonation degree higher than 6). Thus, most repulsive cases are concerned by this fitting.

From a technical point of view, the Yukawa potential is well implemented in molecular simulations codes. Therefore, it will be the one used in following coarse-grains simulations. Still, performing fore-mentioned simulations with a repulsive Yukawa potential as shown above results in a gas phase that do not reproduce a gel or solid phase.

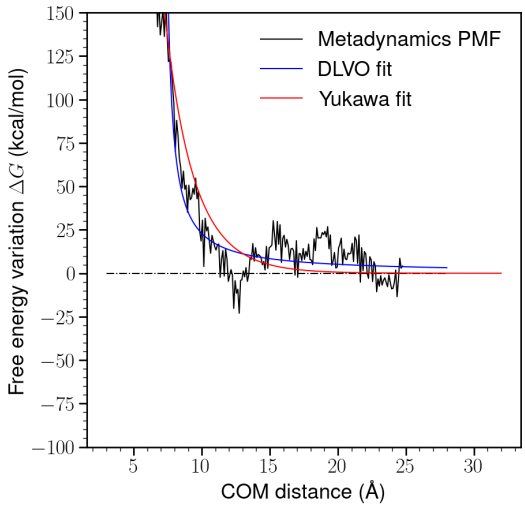

Figure 5.5: Fit of the repulsive potential of interaction between deprotonated grains in water with the DLVO formula with a Hamaker constant of 8×10^{-20}J as measured for aluminosilicate materials[169, 170] and a Yukawa potential with $A = 1.4e4$kcal/mol and $\kappa = 0.35$. The fits are performed for the highest charge system, i.e. a deprotonation degree $d = 10$.

5.2.4 Choice of the pair-potential

We dispose of four possibilities to model the effective pair-potential for GCMC simulations. According to the PMF discussed in Chapter 3 and 4, three regimes are obtained, that can be modeled either using a Lennard-Jones for the $d = 0$ case (cf Fig. 5.3 or 5.1), a combination of LJ and Yukawa (cf Fig. 5.1) for the $d = 4$ case and a repulsive Yukawa for the $d = 26$ case (cf Fig. 5.5).

In the following, we will proceed with these three options with a first study on the LJ potential and especially the role of its well width, before to propose different scenarios using both LJ and hybrid LJ and Yukawa pair potentials. Precipitation simulations will be performed with these potential used in reduced LJ units, ensuring transferable results to different coarse-graining lengths. Note that the repulsive Yukawa not being able to account for a hardened material, it will not be discussed further.

5.3 Reactive solidification for aluminosilicates

Building up a mesoscale model requires two main ingredients : particles morphology and an effective potential of interaction. From atomistic simulations, aluminosilicate grains have been designed and their geometry characterized (ellipsoidal shape, gyration radius). In addition, using different methods, the grand potential of interaction between such grains in water have been evaluated as the PMF. Both allow the study the aggregation of many aluminosilicate grains in solution thanks to hybrid GCMC+MD simulations.

In the following, two discussions are presented. The first one compares the Lennard-Jones potentials with different γ parameters as shown in Fig. 5.3. It evaluates the role of the pair-potential width on the mesostructure. The second one proposes three different scenarios of precipitation, based on the LJ and hybrid LJ+Yukawa potentials. Such a description aims to highlight the role of the pH on effective interactions that must be taken into account to buildup mesoscale simulation of geopolymer nano-particles.

This work differs from previous attempts of mesoscale simulations for geopolymers materials as it is based on a PMF obtained from fully atomistic simulations.

5.3.1 Simulation details

In the following, we perform precipitation simulations within a cubic box of length L^* (and so volume $V^* = L^{*3}$), defined at constant temperature $T^* = 0.15$. As discussed in §2, the excess chemical potential μ^*_{exc} is taken to ensure full densification of the system (and this, for every pair-potentials discussed). The timestep is set to $\delta t^* = 0.0025$. The packing fraction, corresponding to the percentage of volume occupied by our particles, is estimated from the particle number density ρ as $\varphi \approx \rho\pi/6\sigma^3$. It is set initially to $\varphi^* = 0.0005$ [95]. The * subscript denotes reduced Lennard-Jones units.

The kinetics of aggregation influences the resulting structures. When performing these hybrid simulation in the Grand Canonical ensemble, the Monte Carlo process of particle insertion/deletion is coupled with time-dependent relaxation. Thus, we define a precipitation rates as the ratio between Monte Carlo (MC) and Molecular Dynamics (MD) steps $R \equiv N_{MC}/N_{MD}$. Note that to respect the dynamics when increasing the box size, the volumic precipitation rate R/V^* must be kept constant. Therefore, as the box size increases, so does R, by increasing the number of MC calls (more particles inserted).

5.3.2 Kinetics of the Mie potentials

Let us first discuss the three Mie potentials shown in Fig. 5.3. Simulations are performed at a precipitation ratio $R = 0.5$, with 50 Monte Carlo trials performed every 100 Molecular Dynamics steps. These are carried out in a simulation box of size $L^* = 34\sigma$. The excess chemical potential is taken at a value $\mu^*_{\text{exc}} = -1.0$.

Densification

The precipitation kinetics of our simulations are shown and compared in Fig. 5.6. The evolution of the number of trials (a) and the convergence of precipitation rates to 0 (b) ensure that the system does not densify further.

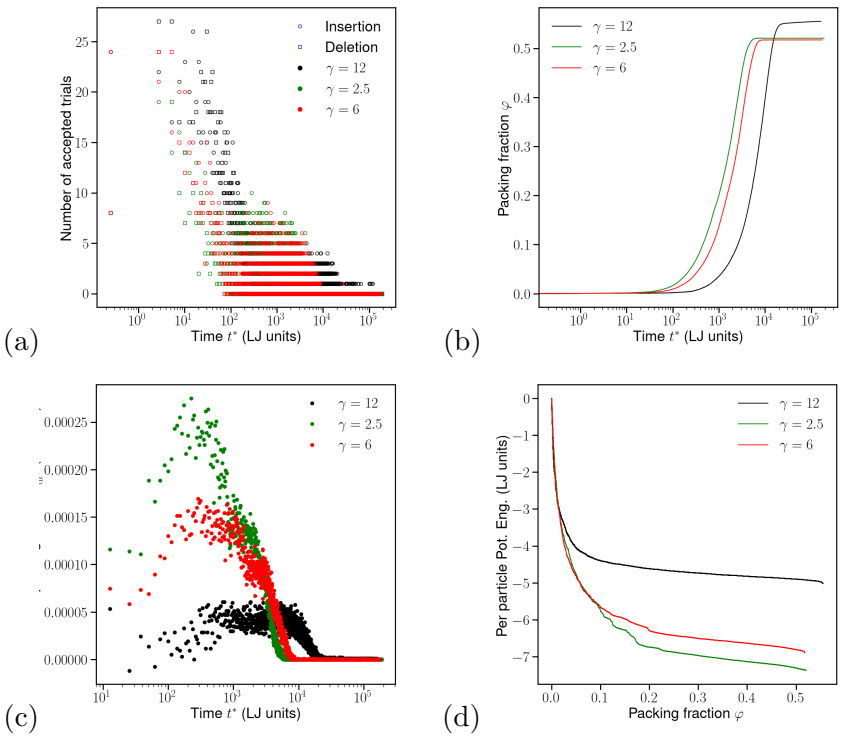

Figure 5.6: (a) Accepted trials of insertion and deletion of particles. Empty dots correspond to the number of accepted insertions and empty squares to accepted deletions. (b) Evolution of the packing fraction w.r.t. simulation time. (c) Packing precipitation rate during the run and (d) Potential energy as a function of the packing fraction. The colors refer to the values of γ.

The potentials with $\gamma = 6$ and $\gamma = 2.5$ reach similar final packings, the case $\gamma = 12$ shows a more packed structure, at a given $\mu^* = -1.0$. Recalling Fig. 5.3 it reads that a narrower well potential for short distances favors more packed structures. A wide well allow clusters of particles to be formed at larger distances : atoms maybe be attracted to a cluster without necessarily being at the minimum of the potential. This also directly relates from Fig. 5.6 (c): packing precipitation rate is lower for the narrower potential. This illustrates that the system requires more time to equilibrate. In fact, supposing an infinitely narrow potential, a particle would be either in or out of the well. Therefore, the addition of new particle would generate stronger energy difference whether it is added close or not of other particles. On the opposite, with a wide well, inserted particle can transit to the minimum of potential continuously, accounting for a more smooth precipitation. According to Fig. 5.6 (d), structure stability (under the scope of lower per particle potential energy) is increased according alongside two parameters : (i) the pair-potential width ; (ii) the packing fraction.

5.3.3 Kinetics of the attracto-repulsive potential

Fig. 5.1 (b) shows two pair-potentials, corresponding to an attractive and a attracto-repulsive regimes which kinetics is discussed here.

As the precipitation rate R for CSH simulation was taken between 0.2 and 4[102], geopolymers probed a slower setting time (see Chapter 1). Therefore, we chose to study aggregation with a precipitation rate of $R = 0.1$. This value is set to R for $L^* = 20$ and is adapted for different box sizes $L^* = 25, 34$ and 50 to keep R/V^* constant. The excess chemical potential is set to $\mu^*_{\text{exc}} = -1.0$ for the attractive potential and to -0.21 for the attracto-repulsive one.

Densification

Fig. 5.7 shows both the evolution of the packing fraction as a function of the simulation time, expressed in Lennard-Jones units and the potential energy per particle as a function of the packing. Simulations are performed over different box sizes L^* (expressed in LJ units) ranging from 20 to 50σ. As expected, Fig. 5.7 illustrates that the precipitation kinetics does not depend on the box size.

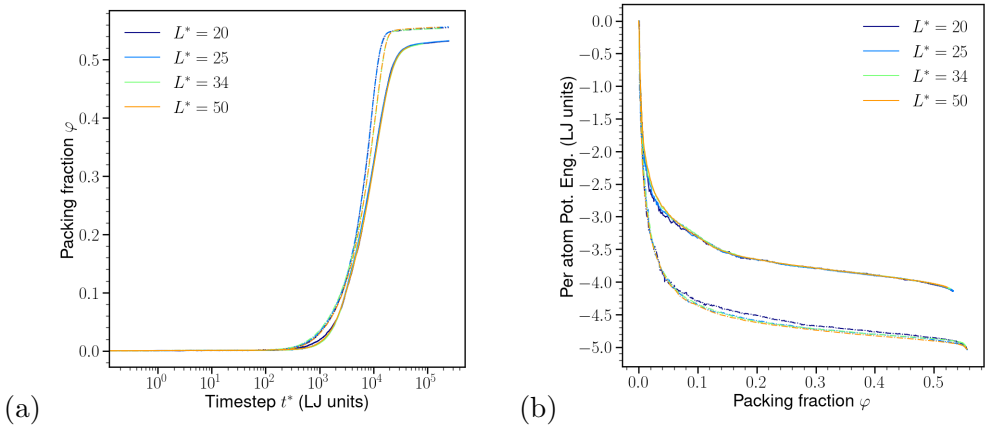

Figure 5.7: (a) Increasing of the packing fraction with simulation time. (b) Per particle potential energy as a function of the packing fraction. Each color refer to a box length. The straight lines corresponds to the attracto-repulsive potential (Lennard Jones + Yukawa) while the dash-dotted to the attractive one (Lennard Jones).

Considering chemical potential that allows to reach a packing fraction φ higher than 0.5 (but still less than 0.64 because of the spherical packing), both potential probes similar precipitation kinetics. The studied simulations allow the sampling of structure with φ varying from 0.1 to 0.5. Panel (b) shows that the potential energy per particle is smaller for the attractive potential, accounting for a more, thermodynamically speaking, stable structure.

5.4 Microstructure results for Mie potentials

In this section are discussed the influence of the width of the pair-potential of interaction on the overall structure. Especially, structures are analyzed with regard to their Pores Sizes Distributions (PSDs) and small angle scattering data.

5.4.1 Structure dependence on the well width

Fig. 5.8 shows the evolution of the global structure within the simulation box of size $L^* = 34\sigma$ for the Mie potential with respectively, $\gamma = 2.5, 6$ and 12.

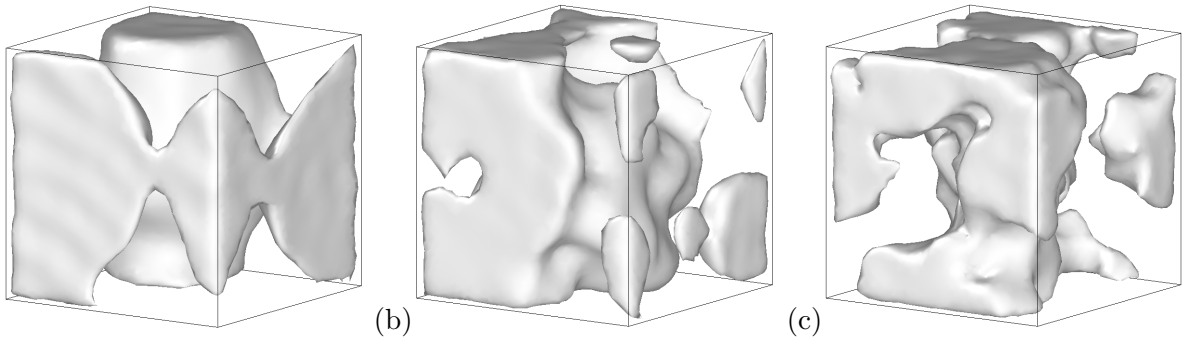

Figure 5.8: Surface mesh structures of configurations based on GCMC simulations with $\gamma =$ (a) 2.5, (b) 6 and (c) 12, at a packing fraction of $\varphi^* = 0.3$. Surface areas can be estimated based on the alpha-shape algorithm [173] implemented in Ovito [174] and stands, in LJ units, as 6494, 6601 and 7231 with increasing γ.

Transition from (a) to (c) illustrates that if particle precipitates with narrower interaction well the final form irregularities. This is illustrated from the increase of the mesh surface: narrower potential induces the formation of more locally packed particle clusters. Note that the structures obtained here would also be dependent on the precipitation rate initially chosen according to number of MC trials performed every MD steps.

5.4.2 Pore Size Distribution (PSD)

For packing fractions ranging from 0.1 to 0.3, the PSDs can be compared to discuss the influence of the γ parameter. Fig. 5.9 displays the PSDs with regard to γ at fixed packing fractions, ranging from $\phi \simeq 0.18$ (at which the system percolates) to $\phi \simeq 0.3$. Computations have been performed using a Monte Carlo process of particles insertion thanks to Bhattacharya *et al.* code [175], based on the Solvopt algorithm [176].

Both $\gamma = 6$ and $\gamma = 12$show a peak at small values which are the pores within the first neighbor shell. Overall, there is an a more important distribution of pores within the range $[4,8]\sigma$, with a maximum around 6σ. However, these distributions are not Gaussian. Fig. 5.9 (a) and (b) illustrate the densification of the system as the PSDs shift to smaller sizes as ϕ increases. This is seen with an increase of the proportion of $[0,3]\sigma$ pore diameters.

Fig. 5.9(b) shows a very discontinuous distribution. This is illustrated from Fig. 5.8(c): a narrow well for interactions leads to a less smooth surface. From Fig. 5.9 (d) wide potential may not favor the formation of small pore sizes. As seen from Fig. 5.8(a), particles aggregate into a big cluster.

We recall here Table 1.3 in Chapter 1 [28], referring to the obtained gyration radius of aggregates within a range of [60,100]Å for Na-based geopolymers. Especially, with a particle diameter of $\sigma = 8$Å, this size of pores is recovered here. In fact, with such a definition, we simulate a box of size $L = 34\sigma = 272$Å. Fig. 5.8 displays a huge pore that size can be estimated $\simeq 9\sigma = 72$Å from Fig. 5.9.

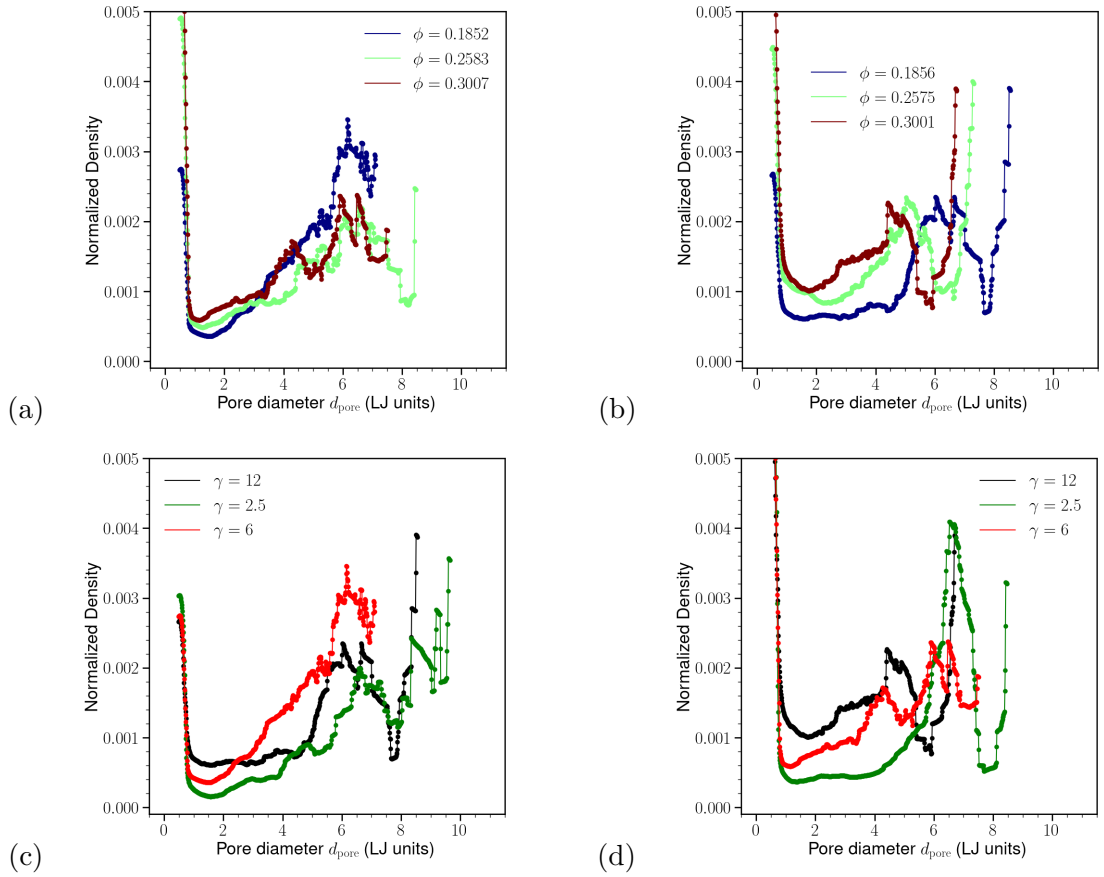

Figure 5.9: Pore Size Distributions for (a) $\gamma = 6$, (b) $\gamma = 12$, (c) $\phi \simeq 0.18$, (d) $\phi \simeq 0.3$. Test particles radius is taken at 0.01 in LJ units and diameter bins with a size of 0.01. A rolling mean is applied to the results.

5.4.3 Discussion on the role of the well width

In overall, with a wide well of interaction, the generated structure tends to form bigger pores. The contributions to nanopores smaller pores (less than 2σ) is lower than with a γ parameter of 6 and 12. As γ increases, the structure appears more rough, with pore distributed less continuously, i.e. probing a more complex porous network.

Still, according to Fig. 5.3, it is the wider well of potential the fits the best our obtained PMF. In addition, previous discussion related the observed dominant pore size to the experimental pores close to 10nm (see Table 1.3 in Chapter 1).

Fig. 5.10 shows the PSDs obtained from the potential but with a simulation box of size $L^* = 50$ and a snapshot of the simulation box illustrating the percolation of the system, happening at a packing fraction of $\varphi = 0.25$.

From Fig. 5.10(a), shows a strong distribution of pores with diameter of ranging from 4σ to 10σ, i.e. around a mean of 70Å, considering a particle size of $\sigma = 8$Å. It illustrates the ability of a wide well potential to reproduce pore sizes as obtained from sorption experiments [28]. Still, as observed from Fig. 5.10, larger simulation box may be required to a more complete investigation of the porous network. Fig. 5.10(b) and (c) illustrates the way the porous network forms. Particles aggregate to form big local clusters, inducing large pores within the meso-structure.

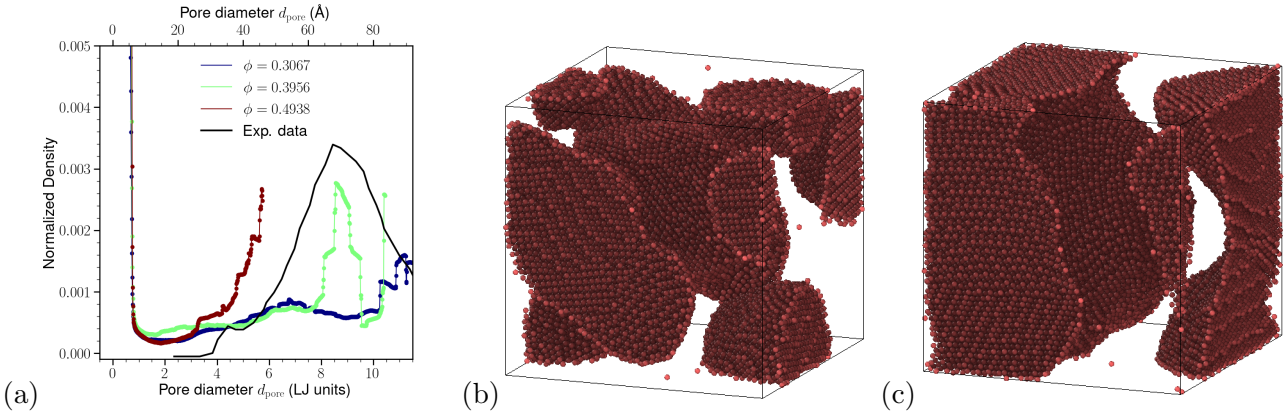

Figure 5.10: (a) Pore Size Distributions for $\gamma = 2.5$ at different packing fraction φ in a simulation box of size $L^* = 50\sigma$. The black straight line shows nitrogen sorption porosimetry data [28]. The upper axis refers to the pore diameter with a particle of size $\sigma = 8$Å. (b) and (c) Snapshots of the simulation box before (b) $\varphi \approx 0.2$ and after $\varphi \approx 0.3$ (c) percolation. Red dots account for the particles and the shading shows the ambient occlusion

Fig. 5.11 shows the porous network at different packing fractions under the view of a surface mesh. As the system densifies, the porous network closes.

In the framework of geopolymer gels and under the view of Chapter 4 results, geopolymer oligomers agglomerate with a dry interface. The precipitation observed here can be seen as the local formation of aluminosilicate glasses that expel water molecules out, therefore inducing the formation of large pores, similar to a demixing process.

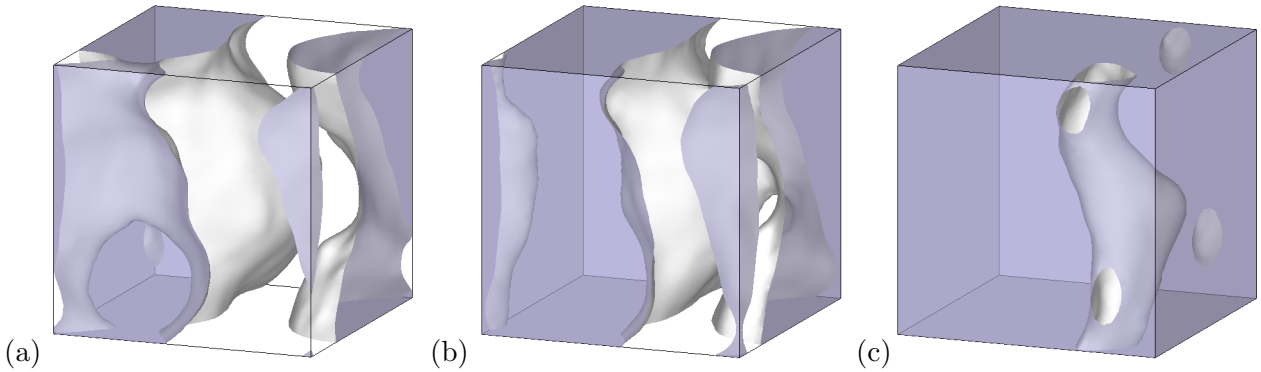

Figure 5.11: Surface mesh structures of configurations based on GCMC simulations with $\gamma = 2.5$ at packing fraction φ of (a) 0.3, (b) 0.4 and (c) 0.5. The box faces are blurred to display the system porosity. Surface areas can be estimated based on the alpha-shape algorithm [173] implemented in Ovito [174] and stands, in LJ units, as 15174, 16299 and 16413 with increasing φ.

5.5 Results for attractive and attracto-repulsive scenarios

As grain-grain cohesion depends on the pH (i.e. the grain deprotonation degree), previous discussions highlighted that interactions can either be in a attractive or attracto-repulsive regime. Both cases are discussed here and a third scenario of switching potential is proposed.

The influence of the box size on the final structure is discussed and PSDs and small angle scattering data are presented.

5.5.1 Three different scenarios

During the gel phase, both dissolution and polycondensation occur. Activation from the alkaline solution deprotonates the grains, influencing the interactions within the gel. Assuming a fully attractive potential within our particles may not reflect the complex aggregation phenomenon, related to the pH.

In this work, we propose to use the potential of the form only Lennard-Jones and Lennard-Jones+Yukawa to perform the aggregation of the grains, as shown in Fig. 5.1 (b), for their ability to fit the well depth. In addition, we propose a third scenario, switching from the attracto-repulsive potential to the attractive one and relax the structure at the same temperature. This mimics a decreasing of the pH as the material sets, when most hydroxyl groups have been consumed. This case will be referred as *switching* in the following.

Grand Canonical Monte Carlo (GCMC) simulations are performed according to the procedure described in Chapter 2. Structures with different packing fraction ϕ can then be extracted for each scenario and studied.

5.5.2 Structural characterization

As seen on Fig. 5.12, the three different precipitation scenarios lead to different structures. These can be characterized in terms of pore size distributions and scattering intensities. For the different length and packing fraction, both PSDs and scattering intensities can be computed.

From sampled structures with the attractive potential, 1000000 additional steps and a minimization at 0 temperature are performed in the NVT ensemble after switching the potential to generate the third scenario structures *switching*. Fig. 5.12 shows snapshots of the structures at different packing fractions, for both potentials and the so-relaxed case.

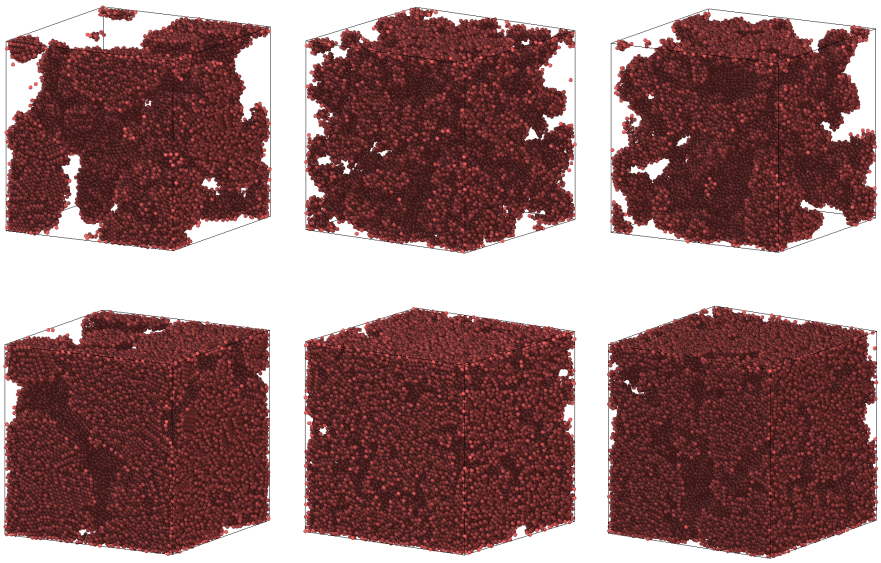

(a) (b) (c)

Figure 5.12: Snapshots of the structures for the three scenarios (a) attractive, (b) attracto-repulsive, (c) switching. Red dots accounts for the particles and the shading shows the ambient occlusion. The first line corresponds to a packing $\varphi = 0.2$ and the second one to $\varphi = 0.4$. Structures are shown for a box size of $L^* = 50\sigma$.

Pore Size Distributions (PSDs)

Fig. 5.12 displays porous mesostructures with different pore sizes distributions that can be investigated similarly as in §2.

Dependence on the box size

We performed a system size analysis using 4 box sizes. As the structures that are formed are heterogeneous, larger system size might capture better heterogeneities and show larger pore sizes. Fig. 5.13 displays the dependence of the PSD on the simulation box size.

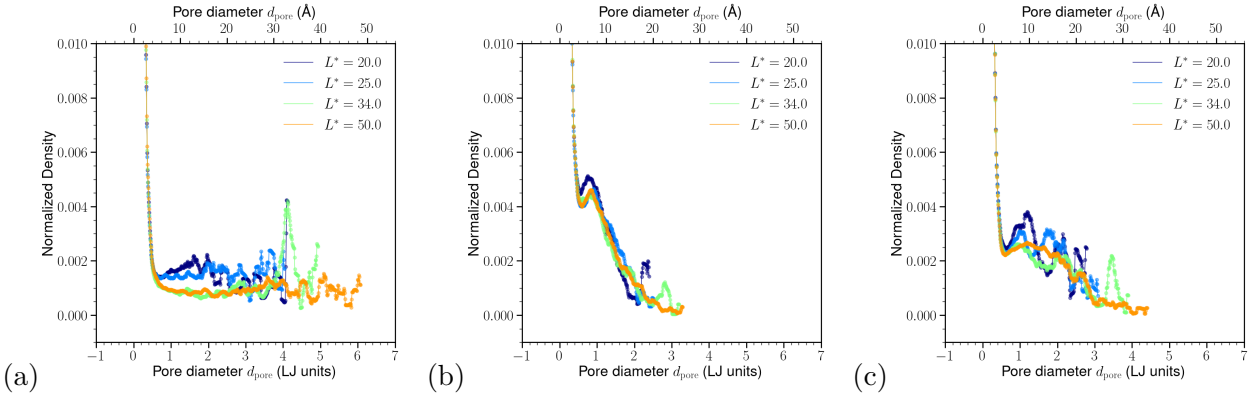

Figure 5.13: Pore size distributions for various box sizes L^* in the three different scenarios as (a) attractive, (b) attracto-repulsive, (c) switching. On the top of the graphs are shown the pore diameters w.r.t. particles of size (diameter) of 8Å. The calculations have been performed for a packing fraction of $\varphi^* = 0.4$. A rolling mean per 20 bins (0.2Å) have been performed over the raw data. The peak at 0.01Å corresponds to closely packed particles.

In most cases, the distributions cover the same range of pore diameters: [0,40]Å. Moving from panel (b) to (c), we observe that the relaxation flattens the pore distribution, accounting for the formation of a few larger pores. With a size of $L^* = 50\sigma$, more pore sizes are accessible by the system in the attractive case. In overall, it probes a complex continuum in pore size distributions while smaller box sizes may lack information. As a consequence, further study will be based on structures obtained with this larger box size.

Comparison of the scenarios

As the packing fraction increases, Fig. 5.12 shows that the porous network evolves. In fact, this latter is expected to close with densification: the number of bigger pores should decrease and the number of smaller increase. Fig. 5.14 illustrates such a behavior, reading from left to right.

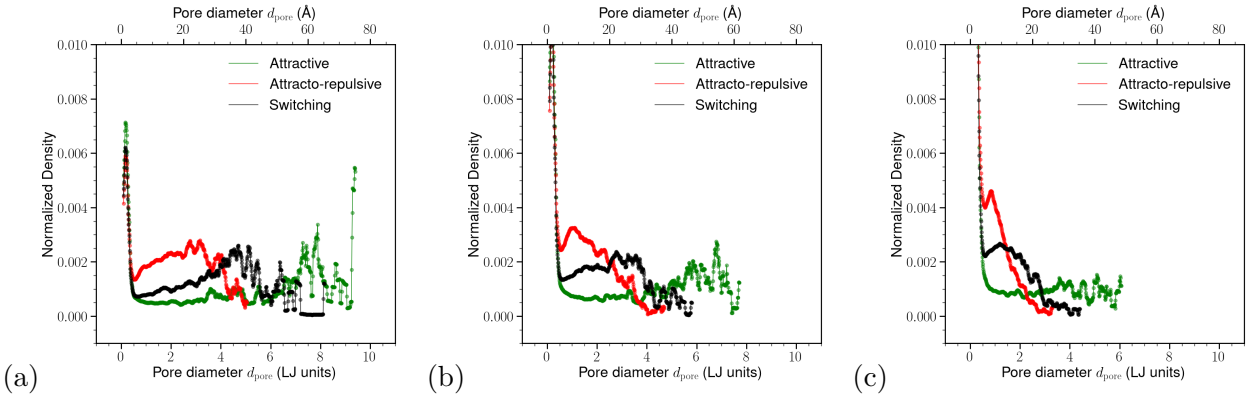

Figure 5.14: Pore size distributions of the three different scenarios for different packing fraction (a) $\phi = 0.2$, (b) $\phi = 0.3$, (c) $\phi = 0.4$. On the top of the graphs are shown the pore diameters w.r.t. particles of size (diameter) of 8Å. A rolling mean per 20 bins (0.2Å) have been performed over the raw data.

At every packing fraction, the switching scenario stands at the in-between of the two others. While

the attractive potential leads to a pore distribution centered on [0,4]σ, the addition of a repulsion shoulder allows the formation of pores up to 6σ at a packing fraction of $\phi = 0.4$. Fig. 5.14 illustrates that switching from the attracto-repulsive regime to the attractive one increases the pore size, i.e. shrinks the structure. This is well shown from Fig. 5.12, transiting from panel (b) to (c).

Considering particle size of $\sigma = 8$Å, PSDs range goes from [0,40Å] to [0,60Å]. These ranges of pores are of the same order of magnitude than the one obtained by Benavent [24], even if a bit smaller. Especially, this can be attributed to the choice of the particle size to 8Å (4Å radius), while its gyration radius is estimated around 6Å (but may not be able to account for attraction in a simplified model as proposed here). Note also that this model is monodisperse while geopolymer pastes tend to be highly polydisperse. In fact, experimental measurement estimated, thanks to a modeling with a two-levels Beaucage model (see Chapter 1, §4 for details), the gyration radius of particle within a range of [50,90]Å.

The attracto-repulsive potential stands for the formation of local clusters that stabilizes at an equilibrium distance dependent on the potential shoulder, accounting for a mid-range attraction and the formation of small pores. However, at high deprotonation degree, we found out that interactions can be strongly repulsive. According to Fig. 5.1, the repulsive should is light, not exceeding 15kcal/mol (in opposition to a -75kcal/mol well). With a stronger repulsion, the equilibrium distance between the formed clusters might increase, leading to bigger pore sizes.

In overall, there appears to be a net difference between the attracto-repulsive and the attractive cases with almost a factor two in pore sizes. Still, the switching case illustrates that a change in the interaction between the grains can influence a lot its porous network.

Scattering intensities

In addition to PSDs, scattering intensities can be computed to investigate the texture of our generated structures in the three discussed scenarios.

Atoms coordinates within the simulations box can be explicitly used to compute the scattering intensity as obtained from SAXS and SANS experiments. This one is defined as

$$I(q) = \phi V^2 \Delta\rho^2 P(q) S(q), \tag{5.5}$$

where $q = 2\pi/d$ denotes the modulus of the scattering vector, with d the scattering distance, ϕ the packing fraction and, V the particles' volume and $\Delta\rho$ the scattering contrast. Both $P(q)$ and $S(q)$ refers to the form and structure factors of the particles at a given scattering vector modulus.

In our simulations, spherical particles of diameter σ are used, i.e. of radius $R = \sigma/2$ are used. For a sphere, the form factor writes as

$$P(q) = \left[3 \frac{\sin(qR) - qR\cos(qR)}{(qR)^3} \right]^2. \tag{5.6}$$

The structure factor, mostly relevant for concentrated systems, is a function that can be obtained directly from a set of N particles coordinates $\{\mathbf{r}_i\}_{i=1\ldots N}$ according to:

$$S(q) = \left\langle \frac{1}{N} \sum_{i,j} e^{-i\mathbf{q}(\mathbf{r}_i - \mathbf{r}_j)} \right\rangle_{\mathbf{q}, \|\mathbf{q}\| = q}, \tag{5.7}$$

the bracket denoting the average over the wavevectors $\mathbf{q}$ that share the same norm q. Note that this structure factor is nothing less than the Fourier transform of the pair correlation function $g(r)$. As a consequence, it can be computed either directly from the set of coordinates or by Fourier transformation of this pair correlation function, this second methods have been used to validate our calculations.

Dependence on the box size

Different box sizes could produce different structures, as seen from PSDs, even though the dependence on the box size is light. Fig. 5.16 shows that for all scenarios, there is no dependence on scattering data from the simulation box size.

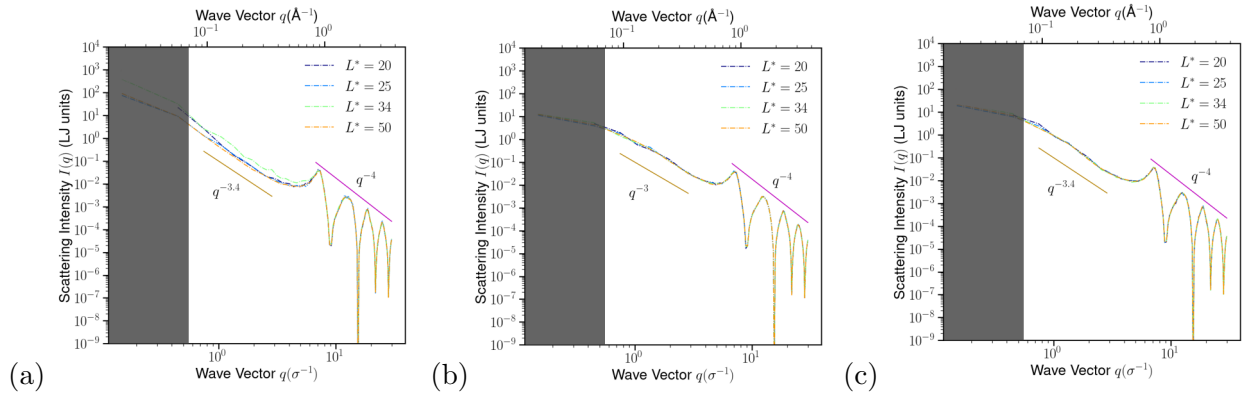

Figure 5.15: Scattering intensities at a packing fraction $\phi = 0.4$ for different box sizes, in the three different scenarios: (a) attractive, (b) attracto-repulsive, (c) switching. On the top of the graphs are shown the q-vector amplitudes w.r.t. a particles of size (diameter) of 8Å. Calculations have been performed from Eq. 5.7 and 5.6, with a scattering factor $\Delta\rho^* = 1$ in reduced units. q^{-D} slopes are shown to illustrates the main regimes encountered. Oscillations at largest q-vector amplitudes come from the system monodispersity. The left area is blurred for its poor q-vector sampling as it reaches the simulation box size.

A Porod regime of q^{-4} is recovered a highest q-vectors. At smaller q-vectors, three q regimes are observed depending on each scenario.

Comparison of the scenarios

Fig. 5.16 shows the scattering intensities obtained from the generated structures over the three scenarios. It illustrates that the intensity slightly depends on the packing fraction and the scenario.

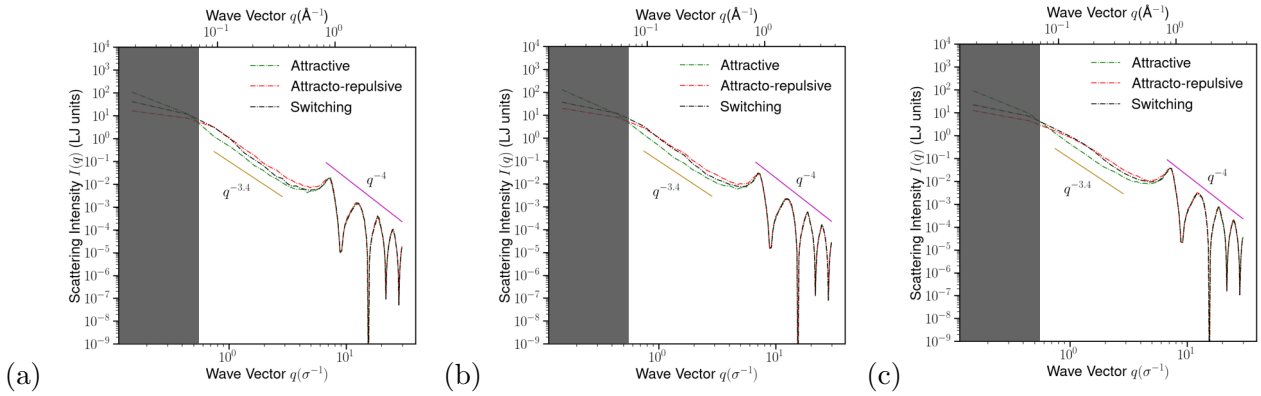

Figure 5.16: Scattering intensities for the three scenarios at different packing fractions: (a) $\phi = 0.2$, (b) $\phi = 0.3$, (c) $\phi = 0.4$. On the top of the graphs are shown the q-vector amplitudes w.r.t. a particles of size (diameter) of 8Å. Calculations have been performed from Eq. 5.6 and 5.7, with a scattering factor $\Delta\rho^* = 1$ in reduced units. q^{-D} slopes are shown to illustrates the three main regimes encountered. Oscillations at largest q-vector amplitudes come from the system monodispersity. The left area is blurred for its poor q-vector sampling as it reaches the simulation box size.

At highest q-vector amplitudes, structures are similar. At lowest values, the addition of repulsion between the grains flattens the slopes. In the mid-range (around $[0.5, 5.0]\sigma^{-1}$) of visited q-vector

amplitudes, the same behavior is seen, from panel (a) to (b), slopes exponent change from -3 to -3.4. Still, we denote that a regime of $q^{-3.4}$ is recovered when switching the interaction potential from attracto-repulsive to an attractive one. q-vectors at which the transition between two regimes occur are slightly shifted to higher values as repulsion is introduced, leading to smaller characteristic sizes: more attraction leads to the formation of bigger clusters (big oligomers).

Transition regimes with exponent varying as non-integers around -3 account for heterogeneity and a lack of order at this q-vectors scales, i.e. sizes of $d = 2\pi/q \in [1.26, 12.6]\sigma$. In opposition to SAXS and SANS experiments discussed in Chapter 1, no -2.7 exponent regime is seen here. In Fig. 1.15 (b) from Chapter 1, this regime is expected within the q range $[0.0001, 0.01]$Å^{-1}=$[0.018, 1.8]\sigma^{-1}$ with a particle size $2R_g = 2 \times 90$Å, as discussed in §1[28]. Despite the value of -2.7 is not obtained, a less-ordered structure is recovered over this range of sizes. Note that the same transition from the Porod ($q = -4$) to a -3.4 regime has been seen from CSH, and attributed to a surface fractal regime, as shown in Fig. 1.15 (a) from Chapter 1[51].

5.5.3 Discussion on the scenarios

From both PSDs and scattering intensities, the three scenarios leads to different mesostructures. Structural characterization shows that if the structure is generated with an attracto-repulsive potential before relaxation with an attractive one, it shows smaller pore sizes and a larger specific aggregate size than if there is no possible repulsion. Ongoing discussion illustrates the role of the repulsion on the formation of the porous network.

From the PMF results discussed in the previous Chapters, an aggregation with only attraction between the grain would correspond to a geopolymer gel in which the oligomers are not deprotonated. This would be the case at very low pH (or very high water content). Increasing the pH in solution would induce an ability of the interaction to cover both attractive and repulsive regimes.

Chapter 4 showed that water strongly influences the grains interactions and that repulsion is related to the omnipresence of water at the interface. In addition, experiments probed [24] that an increase of the water content leads to bigger pore sizes. These results are consistent and converging to say that a too large water content (or very low pH in solution) would induce very large pores and so, weaker mechanical properties.

On the opposite, increasing of the pH/lowering of the water content induces a strong dissolution of the solid aluminosilicate into an homogeneous gel of small oligomers, with a high degree of deprotonation [105]. This is also consistent from simulation performed with a fully repulsive potential (discussed below), corresponding to highly deprotonated grains.

As a matter of fact, there do not exist a linear relation between the porous structure and the water content. Under a given range of water content/pH, geopolymer oligomers in the gel will react with varying deprotonation degrees. As a consequence, their interactions will highly fluctuate, forming structures with a complex porosity at different levels within the mesoscale.

5.6 Conclusion

The mesoscale models proposed in this work give a few insights on the key challenges to build up a consistent model to study geopolymerization *via* molecular simulations. According to the PMF calculations from our previous work, different forms of the Mie potential have been used to model to precipitation of geopolymer oligomers thanks to a coupled Molecular Dynamics and Grand Canonical Monte Carlo molecular simulations. Fitting the potential well with a single Lennard-Jones pair-potential allowed to recover similar pore sizes as from experiments lead on geopolymer pastes. With a large well pair-potential, a scenario of local glass packing is observed. The implementation of simulation in larger box sizes may probed interesting results but would require more computational time.

With a monodisperse approach of spherical particles, three precipitation scenarios have been proposed, accounting either for a full attraction, attracto-repulsion or a path-dependent attractive interaction between aluminosilicate grains. On the one hand, Pore Sized Distributions and Scattering Intensities have been obtained and probed, that the ability of a potential to account for oligomers repulsion influences the porous network. With no repulsion, the pore sizes are larger and so does the characteristics aggregate sizes. On the other hand, fully repulsive potential does not lead to a formation of a stable paste. Under the view of these results, there appear to be a necessity for the oligomers in solution to show both attractive and repulsive interaction regimes.

Even though these models do not encompass the whole complexity of geopolymerization, it gives a good overview on how this process can be studied thanks to molecular simulations. Previous Chapter discussed the role of the grain flexibility on oligomer interactions. For the most part, these appear to be strongly related to their surface deprotonation which is highly influenced by the raw material constitution. During the dissolution of the solid metakaolin and the first steps of polymerization, it was experimentally probed that a lot of chemistry influence the structure of the oligomers (both sizes and deprotonation) and so, the nature of interactions within the gel. In the view of this work, including polydispersity and variety of pair-potential of interactions appears to be key parameters towards an improvement of geopolymer mesoscale simulations.

Conclusion and perspective

Thoroughly investigated through the scope of molecular simulations, geopolymer materials are promising materials, probing many similarities to cement and clays both in structure and in mechanical properties. At the nanoscale, cohesion is causing the aggregation of charged grains in an electrolyte. However, the amorphous shape of aluminosilicate oligomers complexifies the modeling of the geopolymerization at small length scale and long time scale.

This thesis proposes a new approach on the modeling of geopolymer materials at both the atomistic and the mesoscale. Based on aluminosilicate oligomers obtained from reactive molecular dynamics, a potential of interactions for amorphous aluminosilicates has been proposed adapted from ClayFF, first designed for clay systems. It allowed the calculation of Potential of Mean Forces (PMFs) between two oligomers in solution via a perturbative approach: the Free Energy Perturbation (FEP). The results have been compared to the one obtained from an enhanced sampling method: Well-Tempered Metadynamics. Despite the use of the Simple Overlap Sample in FEP calculations, it was shown that this technique requires far longer equilibrium to reflect the actual water behavior at the grain interface, while the bias introduced in the metadynamics algorithm led to a better description of the phase space. The comparison of PMF obtained with wet and dry interfaces probed the important role of interstitial-water on the potential of interaction. From the sampling of metadynamics configurations used to apply the FEP technique, PMFs were qualitatively retrieved. Overall, the order of magnitude of these effective interactions stand in the same range as the one discussed for clays and CSH.

Interaction between aluminosilicate grains in solution is related to their charge. An increase of grain deprotonation showed the transition from an attractive to a repulsive regime strongly related to the transition from a hydrophobic to hydrophilic grain-grain interface. This relates to a dependence of the grain flexibility on its deprotonation degree (and to its size and associated pK_a). While its overall geometry (gyration radius, maximum elongation) does not vary a lot, the branched shape accounts for a strong grain reorganization, especially at short distances, leading to attraction under the scope of a dry interface. At close distances a pre-geopolymerization can start, leading to chemical reactions and merging oligomers over Si-O-Si and Si-O-Al bonds. High pH relates to a wet interface. In this case, a strong repulsive regime is found, consistent with high electric screening in electrolytes and the DLVO theory. Upscaling the system, interactions have been quantified under the view of meta-grains, seen as two {grain+ions} bigger particles interacting in water with different dielectric constant, that depends on the grains deprotonation, i.e. on the pH. From this view, the PMFs are recovered from a theoretical description based on molecular physics. This allows to propose an engineering approach relying on non fudge parameters (only physical ones) to evaluate the global behavior of interactions at a given $[OH^-]$ concentration.

Geopolymer coarse-grained simulations first attempts have been performed in small simulations boxes, based on the fully atomistic PMFs obtained. Assuming grains as dense spherical particles, it is possible to capture the physical properties of the aluminosilicate oligomers and perform Grand Canonical Monte Carlo aggregation according to either attractive, attracto-repulsive or repulsive potential using monodisperse particles. The dependence of the attractive well width on meso-structure is discussed. Especially, fitting the PMF with a wide well Lennard-Jones pair-potential allowed to describe the nanoporous network as a demixing process. To model local pH variation with geopolymer gels, different scenarios of attractive/attracto-repulsive potentials were proposed. Generated meso-structures were

also discussed in the scope of pore size distributions and scattering intensities. However, there is no homogeneous interaction regime in geopolymer pastes, as seen from the dependence of interactions on deprotonation. As an insight, many potential simulations must be carried out. Additionally, polydispersity might also be a key feature since geopolymer gels are made of a large variety of oligomer sizes.

Focusing on a monodisperse study of grains in water, this thesis has given new insights on the geopolymerization process at the nano and mesoscale levels. Comparison of different methods allowed to chose metadynamics as an efficient technique to evaluate the PMF for aluminosilicate grains in solution. While this work focused of monodisperse interactions, further work may aim to quantify the interaction between grains of different sizes and/or different compositions (Al/Si ratio). Experimental works provided also many data on the use of heavier alkaline cations as potassium or cesium, which can be used with the same procedure defined in this work. While the systems discussed were highly diluted and deprotonation manually performed, it might be interesting to model the system in an alkaline solution and allow the grain to naturally deprotonate with the introduction of a reactive potential. Mesoscale simulations can be highly improved with larger box sizes and mechanical tests might be implemented to characterize mechanical properties of so-generated structures.

Bibliography

[1] École Polytechnique Fédérale de Lausanne. Limestone Calcined Clay Cement. `https://lc3.ch/`, 2020. [Online; last updated 29 September 2023].

[2] Meenakshi Sharma, Shashank Bishnoi, Fernando Martirena, and Karen Scrivener. Limestone calcined clay cement and concrete: A state-of-the-art review. *Cement and Concrete Research*, 149:106564, November 2021.

[3] B Muzeau, M Le Flem, D Rébiscoul, L Stefan, A Darquennes, and P Volovitch. DECIMAL - Phenomenological description of the corrosion and its impact on the durability of encapsulated magnesium wastes in hydraulic binders. 2018.

[4] S. Petlitckaia, Y. Barré, T. Piallat, O. Grauby, D. Ferry, and A. Poulesquen. Functionalized geopolymer foams for cesium removal from liquid nuclear waste. *Journal of Cleaner Production*, 269:122400, October 2020.

[5] United States Environmental Protection Agency. National Overview: Facts and Figures on Materials, Wastes and Recycling. `https://www.epa.gov/facts-and-figures-about-materials-waste-and-recycling/national-overview-facts-and-figures-materials`, 2024. [Online; last updated 2024].

[6] J.S. Damtoft, J. Lukasik, D. Herfort, D. Sorrentino, and E.M. Gartner. Sustainable development and climate change initiatives. *Cement and Concrete Research*, 38(2):115–127, February 2008.

[7] Peter Duxson, John L Provis, and Grant C Lukey. The role of inorganic polymer technology in the development of 'green concrete'. *Cement and Concrete Research*, page 8, 2007.

[8] Sébastien Lasvaux, Guillaume Habert, Bruno Peuportier, and Jacques Chevalier. Comparison of generic and product-specific Life Cycle Assessment databases: application to construction materials used in building LCA studies. *The International Journal of Life Cycle Assessment*, 20(11):1473–1490, November 2015.

[9] Joseph Davidovits. Solid-Phase Synthesis of a Mineral Blockpolymer by Low Temperature Polycondensation of Alumino-Silicate Polymers: Na-poly(sialate) or Na-PS and Characteristics. *IUPAC Symposium on Long-Term Properties of Polymers and Polymeric Materials, Stockholm 1976, Topic III*, 1976.

[10] Geopolymer Institute. What is a geopolymer ? Introduction. `https://www.geopolymer.org/science/introduction/`, 2006. [Online; last updated August 17,2012].

[11] Amaury Coste. *Modélisation moléculaire de solutions silicatées en milieux alcalins*. PhD thesis, November 2019.

[12] Romain Dupuis, Donatien Gomes Rodrigues, Jean-Baptiste Champenois, Roland J-M Pellenq, and Arnaud Poulesquen. Time resolved alkali silicate decondensation by sodium hydroxide solution. *Journal of Physics: Materials*, 3(1):014012, January 2020.

[13] G Engelhardt and D Michel. High-resolution solid-state nmr of silicates and zeolites. 1 1987.

[14] Romain Dupuis, Laurent Karim Béland, and Roland J.-M. Pellenq. Molecular simulation of silica gels: Formation, dilution, and drying. *Physical Review Materials*, 3(7):075603, July 2019.

[15] Romain Dupuis, Seung Ho Hahn, Adri C. T. van Duin, Roland J.-M. Pellenq, and Arnaud Poulesquen. Condensation and growth of amorphous aluminosilicate nanoparticles *via* an aggregation process. *Physical Chemistry Chemical Physics*, 24(16):9229–9235, 2022.

[16] Ján Šefčík and Alon V. McCormick. Thermochemistry of aqueous silicate solution precursors to ceramics. *AIChE Journal*, 43(S11):2773–2784, 1997.

[17] Edet F. Archibong, Neelum Seeburrun, and Ponnadurai Ramasami. Geometric and electronic structure of AlO4 and AlO 4 -. *Chemical Physics Letters*, 481(4-6):169–172, October 2009.

[18] John L. Provis and Jannie S. J. van Deventer. *Geopolymers Structure, processing, properties and industrial applications*.

[19] Mo Zhang. *Geopolymer, Next Generation Sustainable Cementitious Material - Synthesis, Characterization and Modeling*. PhD thesis, 2015.

[20] Prune Steins, Arnaud Poulesquen, Olivier Diat, and Fabien Frizon. Structural Evolution during Geopolymerization from an Early Age to Consolidated Material. *Langmuir*, 28(22):8502–8510, June 2012.

[21] P. Duxson, A. Fernández-Jiménez, J. L. Provis, G. C. Lukey, A. Palomo, and J. S. J. van Deventer. Geopolymer technology: the current state of the art. *Journal of Materials Science*, 42(9):2917–2933, May 2007.

[22] Joseph Davidovits. Geopolymers: Inorganic Polymeric New Materials. 37:1633–1656, 1991.

[23] Prune Steins. *Discipline : Matériaux Céramiques et Traitements de Surface*. PhD thesis, 2014.

[24] Virginie Benavent. *Caractérisation de la porosité des géopolymères : évolution temporelle et étude de l'eau confinée*. PhD thesis, 2016.

[25] Virginie Benavent, Prune Steins, Isabel Sobrados, Jesus Sanz, David Lambertin, Fabien Frizon, Sylvie Rossignol, and Arnaud Poulesquen. Impact of aluminum on the structure of geopolymers from the early stages to consolidated material. *Cement and Concrete Research*, 90:27–35, December 2016.

[26] Prune Steins, Arnaud Poulesquen, Fabien Frizon, Olivier Diat, Jacques Jestin, Jérémy Causse, David Lambertin, and Sylvie Rossignol. Effect of aging and alkali activator on the porous structure of a geopolymer. *Journal of Applied Crystallography*, 47(1):316–324, February 2014.

[27] Mo Zhang, Tahar El-Korchi, Guoping Zhang, Jianyu Liang, and Mingjiang Tao. Synthesis factors affecting mechanical properties, microstructure, and chemical composition of red mud–fly ash based geopolymers. *Fuel*, 134:315–325, October 2014.

[28] Virginie Benavent, Fabien Frizon, and Arnaud Poulesquen. Effect of composition and aging on the porous structure of metakaolin-based geopolymers. *Journal of Applied Crystallography*, 49(6):2116–2128, December 2016.

[29] Jaroslav Melar, Guillaume Renaudin, Fabrice Leroux, Adeline Hardy-Dessources, Jean-Marie Nedelec, Christine Taviot-Gueho, Elodie Petit, Prune Steins, Arnaud Poulesquen, and Fabien Frizon. The Porous Network and its Interface inside Geopolymers as a Function of Alkali Cation and Aging. *The Journal of Physical Chemistry C*, 119(31):17619–17632, August 2015.

[30] Thomas W Swaddle, Julian Salerno, and Peter A Tregloan. Aqueous Aluminates, SiIicates, and AluminosiIicates. page 7.

[31] S. Mintova, N. H. Olson, V. Valtchev, and T. Bein. Mechanism of Zeolite A Nanocrystal Growth from Colloids at Room Temperature. *Science*, 283(5404):958–960, February 1999.

[32] S. Mindess and J.F. Young. *Concrete*. Prentice-Hall civil engineering and engineering mechanics series. Prentice-Hall, 1981.

[33] Patrick A. Bonnaud, Christophe Labbez, Ryuji Miura, Ai Suzuki, Naoto Miyamoto, Nozomu Hatakeyama, Akira Miyamoto, and Krystyn J. Van Vliet. Interaction grand potential between calcium–silicate–hydrate nanoparticles at the molecular level. *Nanoscale*, 8(7):4160–4172, 2016.

[34] Davoud Ebrahimi, Andrew J. Whittle, and Roland J.-M. Pellenq. Mesoscale properties of clay aggregates from potential of mean force representation of interactions between nanoplatelets. *The Journal of Chemical Physics*, 140(15):154309, April 2014.

[35] Cui Wen, Lu Geng, Lina Han, Jiancheng Wang, Liping Chang, Gang Feng, Dejin Kong, and Jianwen Liu. A comparative first principles study on trivalent ion incorporated SSZ-13 zeolites. *Physical Chemistry Chemical Physics*, 17(44):29586–29596, 2015.

[36] Rachel E. Fletcher, Sanliang Ling, and Ben Slater. Violations of Löwenstein's rule in zeolites. *Chem. Sci.*, 8(11):7483–7491, 2017.

[37] D. Lootens, P. Hébraud, E. Lécolier, and H. Van Damme. Gelation, Shear-Thinning and Shear-Thickening in Cement Slurries. *Oil & Gas Science and Technology*, 59(1):31–40, January 2004.

[38] D. Jansen, F. Goetz-Neunhoeffer, B. Lothenbach, and J. Neubauer. The early hydration of Ordinary Portland Cement (OPC): An approach comparing measured heat flow with calculated heat flow from QXRD. *Cement and Concrete Research*, 42(1):134–138, January 2012.

[39] Jean-Baptiste Champenois, Celine Cau Dit Coumes, Arnaud Poulesquen, Patrick Le Bescop, and Denis Damidot. Beneficial use of a cell coupling rheometry, conductimetry, and calorimetry to investigate the early age hydration of calcium sulfoaluminate cement. *Rheologica Acta*, 52(2):177–187, February 2013.

[40] A. Poulesquen, F. Frizon, and D. Lambertin. Rheological behavior of alkali-activated metakaolin during geopolymerization. *Journal of Non-Crystalline Solids*, 357(21):3565–3571, November 2011.

[41] Julien Rouyer, Arnaud Poulesquen, and Fabien Frizon. Viscoelastic monitoring of curing geopolymer by ultrasonic rheology. In *2013 IEEE International Ultrasonics Symposium (IUS)*, pages 1895–1898, Prague, Czech Republic, July 2013. IEEE.

[42] Ana Fernández-Jiménez, Angel Palomo, Isabel Sobrados, and Jesús Sanz. The Role Played by The Reactive Alumina Content in The Alkaline Activation of Fly Ashes. *Microporous and Mesoporous Materials*, 91:111–119, April 2006.

[43] Peter Duxson, John L. Provis, Grant C. Lukey, Seth W. Mallicoat, Waltraud M. Kriven, and Jannie S.J. van Deventer. Understanding the relationship between geopolymer composition, microstructure and mechanical properties. *Colloids and Surfaces A: Physicochemical and Engineering Aspects*, 269(1-3):47–58, November 2005.

[44] John Lloyd Provis. *Modelling the formation of geopolymers*. PhD thesis, Chemical & Biomolecular Engineering, University of Melbourne, March 2006.

[45] N. Ganesan, Ruby Abraham, S. Deepa Raj, and Divya Sasi. Stress–strain behaviour of confined Geopolymer concrete. *Construction and Building Materials*, 73:326–331, December 2014.

[46] Stephen Brunauer, P. H. Emmett, and Edward Teller. Adsorption of Gases in Multimolecular Layers. *Journal of the American Chemical Society*, 60(2):309–319, 1938. _eprint: https://doi.org/10.1021/ja01269a023.

[47] Elliott P. Barrett, Leslie G. Joyner, and Paul P. Halenda. The Determination of Pore Volume and Area Distributions in Porous Substances. I. Computations from Nitrogen Isotherms. *Journal of the American Chemical Society*, 73(1):373–380, 1951. _eprint: https://doi.org/10.1021/ja01145a126.

[48] Cedric J. Gommes, Sebastian Jaksch, and Henrich Frielinghaus. Small-angle scattering for beginners. *Journal of Applied Crystallography*, 54(6):1832–1843, December 2021.

[49] Ehsan Negahban, Ali Bagheri, and Jay Sanjayan. Pore structure profile of ambient temperature-cured geopolymer concrete and its effect on engineering properties. *Construction and Building Materials*, 406:133311, November 2023.

[50] Shikun Chen, Shengqian Ruan, Qiang Zeng, Yi Liu, Mingzhong Zhang, Ye Tian, and Dongming Yan. Pore structure of geopolymer materials and its correlations to engineering properties: A review. *Construction and Building Materials*, 328:127064, 2022.

[51] Andrew J. Allen and Jeffrey J. Thomas. Analysis of C–S–H gel and cement paste by small-angle neutron scattering. *Cement and Concrete Research*, 37(3):319–324, March 2007.

[52] G. Beaucage. Approximations leading to a unified exponential/power-law approach to small-angle scattering. *Journal of Applied Crystallography*, 28(6):717–728, 1995.

[53] Boualem Hammouda. Analysis of the Beaucage model. *Journal of Applied Crystallography*, 43(6):1474–1478, December 2010.

[54] Matthew Rowles and Brian O'Connor. Chemical optimisation of the compressive strength of aluminosilicate geopolymers synthesised by sodium silicate activation of metakaolinite. *Journal of Materials Chemistry*, 13(5):1161–1165, April 2003.

[55] Ross P. Williams, Robert D. Hart, and Arie van Riessen. Quantification of the Extent of Reaction of Metakaolin-Based Geopolymers Using X-Ray Diffraction, Scanning Electron Microscopy, and Energy-Dispersive Spectroscopy: Quantification of the Extent of Reaction of Metakaolin-Based Geopolymers. *Journal of the American Ceramic Society*, 94(8):2663–2670, August 2011.

[56] Julien Rouyer and Arnaud Poulesquen. Evidence of a Fractal Percolating Network During Geopolymerization. *Journal of the American Ceramic Society*, 98(5):1580–1587, May 2015.

[57] Puput Risdanareni, Poppy Puspitasari, Edi Santoso, and Edo Prasetya Adi. Mechanical and physical properties of metakaolin based geopolymer paste. *MATEC Web of Conferences*, 101:01021, 2017.

[58] Matthieu Vandamme and Franz-Josef Ulm. Nanogranular origin of concrete creep. *Proceedings of the National Academy of Sciences*, 106(26):10552–10557, June 2009.

[59] Katerina Ioannidou, Christophe Labbez, and Enrico Masoero. A review of coarse grained and mesoscale simulations of C–S–H. *Cement and Concrete Research*, 159:106857, September 2022.

[60] Encyclopedia Britannica. Cement : Manufacture of cement. `https://www.britannica.com/technology/cement-building-material/The-major-cements-composition-and-properties`, 2008. [Online; last updated Mar 07, 2021].

[61] Roland .J-M. Pellenq and Henri van Damme. Why Does Concrete Set ? : The Nature of Cohesion Forces in Hardened Cement-Based Materials. 29(5):319–323, 2004.

[62] Saeed Masoumi, Hamid Valipour, and Mohammad Javad Abdolhosseini Qomi. Intermolecular Forces between Nanolayers of Crystalline Calcium-Silicate-Hydrates in Aqueous Medium. *The Journal of Physical Chemistry C*, 121(10):5565–5572, March 2017.

[63] Hejian Zhu, Andrew J. Whittle, and Roland J.-M. Pellenq. Potential of Mean Force for Face–Face Interactions between Pairs of 2:1 Clay Mineral Platelets. *Langmuir*, 38(43):13065–13074, November 2022.

[64] Adri C. T. van Duin, Siddharth Dasgupta, Francois Lorant, and William A. Goddard. ReaxFF: A Reactive Force Field for Hydrocarbons. *The Journal of Physical Chemistry A*, 105(41):9396–9409, October 2001.

[65] Randall T. Cygan, Jian-Jie Liang, and Andrey G. Kalinichev. Molecular Models of Hydroxide, Oxyhydroxide, and Clay Phases and the Development of a General Force Field. *The Journal of Physical Chemistry B*, 108(4):1255–1266, January 2004.

[66] Hendrik Heinz, Tzu-Jen Lin, Ratan Kishore Mishra, and Fateme S. Emami. Thermodynamically Consistent Force Fields for the Assembly of Inorganic, Organic, and Biological Nanostructures: The INTERFACE Force Field. *Langmuir*, 29(6):1754–1765, 2013. _eprint: https://doi.org/10.1021/la3038846.

[67] H. J. C. Berendsen, J. R. Grigera, and T. P. Straatsma. The missing term in effective pair potentials. *The Journal of Physical Chemistry*, 91(24):6269–6271, November 1987.

[68] William L. Jorgensen, Jayaraman Chandrasekhar, Jeffry D. Madura, Roger W. Impey, and Michael L. Klein. Comparison of simple potential functions for simulating liquid water. *The Journal of Chemical Physics*, 79(2):926–935, July 1983.

[69] Adri C. T. van Duin, Alejandro Strachan, Shannon Stewman, Qingsong Zhang, Xin Xu, and William A. Goddard. ReaxFF $_{\text{sio}}$ Reactive Force Field for Silicon and Silicon Oxide Systems. *The Journal of Physical Chemistry A*, 107(19):3803–3811, May 2003.

[70] Anthony K. Rappe and William A. Goddard. Charge equilibration for molecular dynamics simulations. *The Journal of Physical Chemistry*, 95(8):3358–3363, April 1991.

[71] B Derjaguin and L Landau. Theory of the stability of strongly charged lyophobic sols and of the adhesion of strongly charged particles in solutions of electrolytes. *Progress in Surface Science*, 43(1-4):30–59, May 1993.

[72] Jacob N Israelachvili. Intermolecular and Surface Forces.

[73] Abhay Goyal, Ivan Palaia, Katerina Ioannidou, Franz-Josef Ulm, Henri van Damme, Roland J.-M. Pellenq, Emmanuel Trizac, and Emanuela Del Gado. The physics of cement cohesion. *Science Advances*, 7(32):eabg5882, August 2021.

[74] Saeed Masoumi, Siavash Zare, Hamid Valipour, and Mohammad Javad Abdolhosseini Qomi. Effective Interactions between Calcium-Silicate-Hydrate Nanolayers. *The Journal of Physical Chemistry C*, 123(8):4755–4766, February 2019.

[75] Samuel Lesko, Eric Lesniewska, André Nonat, Jean-Claude Mutin, and Jean-Pierre Goudonnet. Investigation by atomic force microscopy of forces at the origin of cement cohesion. *Ultramicroscopy*, 86(1-2):11–21, January 2001.

[76] Konstantinos Keremides, Mohammad Javad Abdolhosseini Qomi, Roland J. M. Pellenq, and Franz-Josef Ulm. Potential-of-Mean-Force Approach for Molecular Dynamics–Based Resilience Assessment of Structures. *Journal of Engineering Mechanics*, 144(8):04018066, August 2018.

[77] Davoud Ebrahimi, Roland J.-M. Pellenq, and Andrew J. Whittle. Mesoscale simulation of clay aggregate formation and mechanical properties. *Granular Matter*, 18(3):49, June 2016.

[78] Katerina Ioannidou, Konrad J. Krakowiak, Mathieu Bauchy, Christian G. Hoover, Enrico Masoero, Sidney Yip, Franz-Josef Ulm, Pierre Levitz, Roland J.-M. Pellenq, and Emanuela Del Gado. Mesoscale texture of cement hydrates. *Proceedings of the National Academy of Sciences*, 113(8):2029–2034, February 2016.

[79] Igor Shvab, Laurent Brochard, Hegoi Manzano, and Enrico Masoero. Precipitation Mechanisms of Mesoporous Nanoparticle Aggregates: Off-Lattice, Coarse-Grained, Kinetic Simulations. *Crystal Growth & Design*, 17(3):1316–1327, March 2017.

[80] Cedric Plassard, Eric Lesniewska, Isabelle Pochard, and Andre Nonat. Nanoscale Experimental Investigation of Particle Interactions at the Origin of the Cohesion of Cement. 21(16):7263–7270, 2005.

[81] Lars Guldbrand, Bo Jönsson, Håkan Wennerström, and Per Linse. Electrical double layer forces. A Monte Carlo study. *The Journal of Chemical Physics*, 80(5):2221–2228, March 1984.

[82] Roland Kjellander and Stjepan Marčelja. Correlation and image charge effects in electric double layers. *Chemical Physics Letters*, 112(1):49–53, November 1984.

[83] Bo Jönsson and Håkan Wennerström. Ion–ion correlations in liquid dispersions. *The Journal of Adhesion*, 80(5):339–364, 2004.

[84] T.L. Hill. *An Introduction to Statistical Thermodynamics*. Addison-Wesley series in chemistry. Dover Publications, 1986.

[85] S. Alexander, P. M. Chaikin, P. Grant, G. J. Morales, P. Pincus, and D. Hone. Charge renormalization, osmotic pressure, and bulk modulus of colloidal crystals: Theory. *The Journal of Chemical Physics*, 80(11):5776–5781, June 1984.

[86] A A Louis. Beware of density dependent pair potentials. *Journal of Physics: Condensed Matter*, 14(40):9187–9206, October 2002.

[87] Patricia M. Dove and Colin M. Craven. Surface charge density on silica in alkali and alkaline earth chloride electrolyte solutions. *Geochimica et Cosmochimica Acta*, 69(21):4963–4970, November 2005.

[88] Christophe Labbez, Bo Jönsson, Michal Skarba, and Michal Borkovec. Ion-Ion Correlation and Charge Reversal at Titrating Solid Interfaces. *Langmuir*, 25(13):7209–7213, July 2009.

[89] Christophe Labbez, Bo Jönsson, Isabelle Pochard, André Nonat, and Bernard Cabane. Surface Charge Density and Electrokinetic Potential of Highly Charged Minerals: Experiments and Monte Carlo Simulations on Calcium Silicate Hydrate. *The Journal of Physical Chemistry B*, 110(18):9219–9230, May 2006.

[90] Christophe Labbez, Isabelle Pochard, Bo Jönsson, and André Nonat. C-S-H/solution interface: Experimental and Monte Carlo studies. *Cement and Concrete Research*, 41(2):161–168, February 2011.

[91] Enrico Masoero, Emanuela Del Gado, Roland J.-M. Pellenq, Sidney Yip, and Franz-Josef Ulm. Nano-scale mechanics of colloidal C–S–H gels. *Soft Matter*, 10(3):491–499, 2014.

[92] Gustav Mie. Zur kinetischen Theorie der einatomigen Körper. *Annalen der Physik*, 316(8):657–697, 1903.

[93] E Masoero and E Del Gado. Nanostructure and Nanomechanics of Cement: Polydisperse Colloidal Packing. *Physical Review Letters*, page 5, 2012.

[94] E Masoero, H Jennings, F Ulm, E Del Gado, H Manzano, R Pellenq, and S Yip. Modelling cement at fundamental scales: From atoms to engineering strength and durability. In Nenad Bícanić, Herbert Mang, Günther Meschke, and René de Borst, editors, *Computational Modelling of Concrete Structures*, pages 139–148. CRC Press, March 2014.

[95] Aikaterini Ioannidou. *Precipitation, gelation and mechanical properties of Calcium-Silicate-Hydrate gels*. PhD thesis, ETH Zurich, 2014. Artwork Size: 122 p. Medium: application/pdf Pages: 122 p.

[96] Zechuan Yu and Denvid Lau. Nano- and mesoscale modeling of cement matrix. *Nanoscale Research Letters*, 10(1):173, December 2015.

[97] Saeed Masoumi, Davoud Ebrahimi, Hamid Valipour, and Mohammad Javad Abdolhosseini Qomi. Nanolayered attributes of calcium-silicate-hydrate gels. *Journal of the American Ceramic Society*, 103(1):541–557, January 2020.

[98] J. G. Gay and B. J. Berne. Modification of the overlap potential to mimic a linear site–site potential. *The Journal of Chemical Physics*, 74(6):3316–3319, March 1981.

[99] R. Berardi, C. Fava, and C. Zannoni. A generalized Gay-Berne intermolecular potential for biaxial particles. *Chemical Physics Letters*, 236(4-5):462–468, April 1995.

[100] Roberto Berardi, Carlo Fava, and Claudio Zannoni. A Gay–Berne potential for dissimilar biaxial particles. *Chemical Physics Letters*, 297(1-2):8–14, November 1998.

[101] Enrico Masoero and Giovanni Di Luzio. Nanoparticle simulations of logarithmic creep and microprestress relaxation in concrete and other disordered solids. *Cement and Concrete Research*, 137:106181, November 2020.

[102] Katerina Ioannidou, Roland J.-M. Pellenq, and Emanuela Del Gado. Controlling local packing and growth in calcium–silicate–hydrate gels. *Soft Matter*, 10(8):1121–1133, 2014.

[103] Tran Thi Bao Le, Aaron R. Finney, Andrea Zen, Tai Bui, Weparn J. Tay, Kuhan Chellappah, Matteo Salvalaglio, Angelos Michaelides, and Alberto Striolo. Mesoscale Simulations Reveal How Salt Influences Clay Particles Agglomeration in Aqueous Dispersions. *Journal of Chemical Theory and Computation*, 20(4):1612–1624, February 2024.

[104] Chao-Shiang Yang, José Miguel Mora-Fonz, and C. Richard A. Catlow. Modeling the Polymerization of Aluminosilicate Clusters. *The Journal of Physical Chemistry C*, 116(42):22121–22128, October 2012.

[105] Romain Dupuis, Roland Pellenq, Jean-Baptiste Champenois, and Arnaud Poulesquen. Dissociation Mechanisms of Dissolved Alkali Silicates in Sodium Hydroxide. *The Journal of Physical Chemistry C*, 124(15):8288–8294, April 2020.

[106] Francesca Lolli and Enrico Masoero. A defective crystal model for the molecular structure of geopolymers as a baseline for multiscale modelling. page 9, 2019.

[107] Kengran Yang and Claire E. White. Modeling the Formation of Alkali Aluminosilicate Gels at the Mesoscale Using Coarse-Grained Monte Carlo. *Langmuir*, 32(44):11580–11590, November 2016.

[108] Francesca Lolli, Hegoi Manzano, John L. Provis, Maria Chiara Bignozzi, and Enrico Masoero. Atomistic Simulations of Geopolymer Models: The Impact of Disorder on Structure and Mechanics. *ACS Applied Materials & Interfaces*, 10(26):22809–22820, July 2018.

[109] Chao-Shiang Yang, José Miguel Mora-Fonz, and C. Richard A. Catlow. Stability and Structures of Aluminosilicate Clusters. *The Journal of Physical Chemistry C*, 115(49):24102–24114, December 2011.

[110] Julius Ciric. Kinetics of zeolite A crystallization. *Journal of Colloid and Interface Science*, 28(2):315–324, October 1968.

[111] Jimin Shi, Michael W. Anderson, and Stuart W. Carr. Direct Observation of Zeolite A Synthesis by in Situ Solid-State NMR. *Chemistry of Materials*, 8(2):369–375, January 1996.

[112] Walter Loewenstein. The Distribution of Aluminium in the Tetrahedra of Silicates and Aluminates. *American Mineralogist*, 39(1-2):92–96, 1954.

[113] Peter Duxson, John L. Provis, Grant C. Lukey, Frances Separovic, and Jannie S. J. van Deventer. ^{29} Si NMR Study of Structural Ordering in Aluminosilicate Geopolymer Gels. *Langmuir*, 21(7):3028–3036, March 2005.

[114] Monique Smaihi, Olivier Barida, and Valentin Valtchev. Investigation of the Crystallization Stages of LTA-Type Zeolite by Complementary Characterization Techniques. *European Journal of Inorganic Chemistry*, 2003(24):4370–4377, December 2003.

[115] Claire E. White, John L. Provis, Thomas Proffen, and Jannie S. J. van Deventer. Quantitative Mechanistic Modeling of Silica Solubility and Precipitation during the Initial Period of Zeolite Synthesis. *The Journal of Physical Chemistry C*, 115(20):9879–9888, May 2011.

[116] Claire E. White, John L. Provis, Thomas Proffen, and Jannie S. J. van Deventer. Molecular mechanisms responsible for the structural changes occurring during geopolymerization: Multiscale simulation. *AIChE Journal*, 58(7):2241–2253, July 2012.

[117] F. Lolli and E. Masoero. Towards a mesoscale model of geopolymers: Interaction potential from the molecular scale. In Günther Meschke, Bernhard Pichler, and Jan G. Rots, editors, *Computational Modelling of Concrete Structures*, pages 87–91. CRC Press, 1 edition, January 2018.

[118] Claire E. White, Katharine Page, Neil J. Henson, and John L. Provis. In situ synchrotron X-ray pair distribution function analysis of the early stages of gel formation in metakaolin-based geopolymers. *Applied Clay Science*, 73:17–25, March 2013.

[119] W. M. Kriven, M. Gordon, and J. L. Bell. Geopolymers: Nanoparticulate, nanoporous ceramics made under ambient conditions. *Microscopy and Microanalysis*, 10(S02):404–405, 2004.

[120] John L. Provis, Grant C. Lukey, and Jannie S. J. van Deventer. Do Geopolymers Actually Contain Nanocrystalline Zeolites? A Reexamination of Existing Results. *Chemistry of Materials*, 17(12):3075–3085, June 2005.

[121] Josiah Willard Gibbs. *Elementary Principles in Statistical Mechanics: Developed with Especial Reference to the Rational Foundation of Thermodynamics*. Cambridge Library Collection - Mathematics. Cambridge University Press, 2010.

[122] Mark E. Tuckerman. *Statistical mechanics: theory and molecular simulation*. Oxford University Press, Oxford ; New York, 2010. OCLC: ocn551495372.

[123] Hans C. Andersen. Molecular dynamics simulations at constant pressure and/or temperature. *jcp*, 72(4):2384–2393, February 1980.

[124] Shuichi Nosé. A unified formulation of the constant temperature molecular dynamics methods. *jcp*, 81(1):511–519, July 1984.

[125] University College London. Democtrituc: Periodic boundary conditions. `https://www.ucl.ac.uk/~ucfbasc/Theory/pbc-mi.html`, 2023. [Online].

[126] C. Y. Lee and H. L. Scott. The surface tension of water: A Monte Carlo calculation using an umbrella sampling algorithm. *The Journal of Chemical Physics*, 73(9):4591–4596, November 1980.

[127] Nandou Lu and David A. Kofke. Accuracy of free-energy perturbation calculations in molecular simulation. I. Modeling. *The Journal of Chemical Physics*, 114(17):7303–7311, May 2001.

[128] Nandou Lu, David A. Kofke, and Thomas B. Woolf. Improving the efficiency and reliability of free energy perturbation calculations using overlap sampling methods. *Journal of Computational Chemistry*, 25(1):28–40, January 2004.

[129] Christophe Chipot, Andrew Pohorille, A. W. Castleman, J. P. Toennies, K. Yamanouchi, and W. Zinth, editors. *Free Energy Calculations: Theory and Applications in Chemistry and Biology*, volume 86 of *Springer Series in Chemical Physics*. Springer Berlin Heidelberg, Berlin, Heidelberg, 2007.

[130] M H Quenouille. Notes on Bias in Estimation.

[131] Efron B. Bootstrap Methods: Another Look at the Jackknife. *The Annals of Statistics*, 7(1):1–26, 1979.

[132] Bradley Efron and Robert J. Tibshirani. *An Introduction to the Bootstrap*. Springer US, Boston, MA, 1993.

[133] Alessandro Laio and Michele Parrinello. Escaping free-energy minima. *Proceedings of the National Academy of Sciences*, 99(20):12562–12566, October 2002.

[134] Daan Frenkel and Berend Smit. *Understanding Molecular Simulation.* Academic Press, Inc., USA, 2nd edition, 2001.

[135] Davide Bochicchio, Emanuele Panizon, Riccardo Ferrando, Luca Monticelli, and Giulia Rossi. Calculating the free energy of transfer of small solutes into a model lipid membrane: Comparison between metadynamics and umbrella sampling. *The Journal of chemical physics*, 143(14):144108, October 2015. Place: United States.

[136] Joseph Clayton, Lokesh Baweja, and Jeff Wereszczynski. Peptide Dynamics and Metadynamics: Leveraging Enhanced Sampling Molecular Dynamics to Robustly Model Long-Timescale Transitions. In Thomas Simonson, editor, *Computational Peptide Science: Methods and Protocols*, pages 151–167. Springer US, New York, NY, 2022.

[137] Alessandro Barducci, Giovanni Bussi, and Michele Parrinello. Well-Tempered Metadynamics: A Smoothly Converging and Tunable Free-Energy Method. *Physical Review Letters*, 100(2):020603, January 2008.

[138] E J W Verwey. Theory of the Stability of Lyophobic Colloids.

[139] Typeset by Michael J Braus Translated. 'The theory of electrolytes. I. Freezing point depression and related phenomena' (Debye & Hückel, 1923). 1923.

[140] Obituary: Professor niels j. bjerrum. *Trans. Faraday Soc.*, 55:X001–X003, 1959.

[141] F. London. The general theory of molecular forces. *Trans. Faraday Soc.*, 33:8b–26, 1937.

[142] H.C. Hamaker. The London—van der Waals attraction between spherical particles. *Physica*, 4(10):1058–1072, October 1937.

[143] Randall T. Cygan, Jeffery A. Greathouse, and Andrey G. Kalinichev. Advances in Clayff Molecular Simulation of Layered and Nanoporous Materials and Their Aqueous Interfaces. *The Journal of Physical Chemistry C*, 125(32):17573–17589, August 2021.

[144] Swaroop Chatterjee, Pablo G. Debenedetti, Frank H. Stillinger, and Ruth M. Lynden-Bell. A computational investigation of thermodynamics, structure, dynamics and solvation behavior in modified water models. *The Journal of Chemical Physics*, 128(12):124511, March 2008.

[145] P. P. Ewald. Die Berechnung optischer und elektrostatischer Gitterpotentiale. *Annalen der Physik*, 369(3):253–287, 1921.

[146] R. W. Hockney and J. W. Eastwood. *Computer simulation using particles.* 1988.

[147] J. Braunstein, Gleb Mamantov, and G. P. Smith, editors. *Advances in Molten Salt Chemistry.* Springer US, Boston, MA, 1975.

[148] Charles Kittel. *Introduction to solid state physics.* Wiley, Hoboken, NJ, 8th ed edition, 2005.

[149] D. Wolf, P. Keblinski, S. R. Phillpot, and J. Eggebrecht. Exact method for the simulation of Coulombic systems by spherically truncated, pairwise r-1 summation. *The Journal of Chemical Physics*, 110(17):8254–8282, May 1999.

[150] Thomas P Senftle, Sungwook Hong, Md Mahbubul Islam, Sudhir B Kylasa, Yuanxia Zheng, Yun Kyung Shin, Chad Junkermeier, Roman Engel-Herbert, Michael J Janik, Hasan Metin Aktulga, Toon Verstraelen, Ananth Grama, and Adri C T van Duin. The ReaxFF reactive force-field: development, applications and future directions. *npj Computational Materials*, 2(1):15011, November 2016.

[151] L. Martínez, R. Andrade, E. G. Birgin, and J. M. Martínez. PACKMOL: A package for building initial configurations for molecular dynamics simulations. *Journal of Computational Chemistry*, 30(13):2157–2164, October 2009.

[152] Aidan P. Thompson, H. Metin Aktulga, Richard Berger, Dan S. Bolintineanu, W. Michael Brown, Paul S. Crozier, Pieter J. in 't Veld, Axel Kohlmeyer, Stan G. Moore, Trung Dac Nguyen, Ray Shan, Mark J. Stevens, Julien Tranchida, Christian Trott, and Steven J. Plimpton. Lammps - a flexible simulation tool for particle-based materials modeling at the atomic, meso, and continuum scales. *Computer Physics Communications*, 271:108171, 2022.

[153] Alex C. Hannon, Shuchi Vaishnav, Oliver L. G. Alderman, and Paul A. Bingham. The structure of sodium silicate glass from neutron diffraction and modeling of oxygen-oxygen correlations. *Journal of the American Ceramic Society*, 104(12):6155–6171, December 2021.

[154] F Angeli and P Faucon. Influence of glass chemical composition on the Na±O bond distance: a 23Na 3Q-MAS NMR and molecular dynamics study. 2000.

[155] Helen E. A. Brand, A. Dominic Fortes, Ian G. Wood, and Lidunka Vočadlo. Equation of state and pressure-induced structural changes in mirabilite (Na2SO4·10H2O) determined from ab initio density functional theory calculations. *Physics and Chemistry of Minerals*, 37(5):265–282, May 2010.

[156] Johan Mähler and Ingmar Persson. A Study of the Hydration of the Alkali Metal Ions in Aqueous Solution. *Inorganic Chemistry*, 51(1):425–438, January 2012.

[157] Takashi Ikeda, Mauro Boero, and Kiyoyuki Terakura. Hydration of alkali ions from first principles molecular dynamics revisited. *The Journal of Chemical Physics*, 126(3):034501, January 2007.

[158] Daniel Herschlag and Margaux M. Pinney. Hydrogen Bonds: Simple after All? *Biochemistry*, 57(24):3338–3352, June 2018.

[159] Ming-Feng Kai and Jian-Guo Dai. Understanding geopolymer binder-aggregate interfacial characteristics at molecular level. *Cement and Concrete Research*, 149:106582, November 2021.

[160] Allison S Brandvold and Waltraud M Kriven. Geopolymers as Alternatives to Cements.

[161] W. H. Stockmayer. Second Virial Coefficients of Polar Gases. *The Journal of Chemical Physics*, 9(5):398–402, May 1941.

[162] Geoffrey Maitland, Maurice Rigby, E. Brian Smith, William A. Wakeham, and D. Austin Henderson. Intermolecular Forces: Their Origin and Determination. *Physics Today*, 36:57–58, 1983.

[163] Wikipedia. Atomic units. `https://en.wikipedia.org/wiki/Atomic_units`, 2024. [Online; last updated March 2, 2024].

[164] Benoît Carrier. Influence of water on the short-term and long-term mechanical properties of swelling clays : experiments on self-supporting films and molecular simulations. page 230.

[165] T Thoenen. The Dielectric Constant of Water in Compacted Clays.

[166] Xinyi Shen and Ian C. Bourg. Molecular dynamics simulations of the colloidal interaction between smectite clay nanoparticles in liquid water. *Journal of Colloid and Interface Science*, 584:610–621, February 2021.

[167] F. G. Donnan. Theorie der Membrangleichgewichte und Membranpotentiale bei Vorhandensein von nicht dialysierenden Elektrolyten. Ein Beitrag zur physikalisch-chemischen Physiologie. *Zeitschrift für Elektrochemie und angewandte physikalische Chemie*, 17(14):572–581, July 1911.

[168] M. Rami Reddy and M. Berkowitz. The dielectric constant of SPC/E water. *Chemical Physics Letters*, 155(2):173–176, February 1989.

[169] Lennart Bergström. Hamaker constants of inorganic materials. *Advances in Colloid and Interface Science*, 70:125–169, 1997.

[170] G Lefèvre and A Jolivet. Calculation of Hamaker Constants Applied to the Deposition of Metallic Oxide Particles at High Temperature. 2009.

[171] Julien Aupoil, Jean-Baptiste Champenois, Jean-Baptiste d'Espinose de Lacaillerie, and Arnaud Poulesquen. Interplay between silicate and hydroxide ions during geopolymerization. *Cement and Concrete Research*, 115:426–432, January 2019.

[172] Wikipedia. Lennard-jones potential. `https://en.wikipedia.org/wiki/Lennard-Jones_potential`, 2024. [Online; last updated May 6, 2024].

[173] Alexander Stukowski. Computational Analysis Methods in Atomistic Modeling of Crystals. *JOM*, 66(3):399–407, March 2014.

[174] Alexander Stukowski. Visualization and analysis of atomistic simulation data with OVITO-the Open Visualization Tool. *Modelling and Simulation in Materials Science and Engineering*, 18(1), January 2010.

[175] Supriyo Bhattacharya and Keith E. Gubbins. Fast Method for Computing Pore Size Distributions of Model Materials. *Langmuir*, 22(18):7726–7731, August 2006.

[176] Franz Kappel. An Implementation of Shor's r-Algorithm. *Computational Optimization and Applications*, 15:193–205, 2000.